

ALTERATION EXPERIMENTS  
ON GEOTHERMAL RESERVOIR ROCKS  
OF THE UPPER RHINE GRABEN

Zur Erlangung des akademischen Grades eines  
DOKTORS DER NATURWISSENSCHAFTEN

von der KIT-Fakultät für  
Bauingenieur-, Geo- und Umweltwissenschaften  
des Karlsruher Instituts für Technologie (KIT)  
genehmigte

DISSERTATION

von  
M.Sc. Roman Berthold Schmidt  
aus Donaueschingen

Tag der mündlichen Prüfung:

05. 02. 2019

Referentin: Prof. Dr. Ingrid Stober  
Korreferentin: PD Dr. Kirsten Drüppel

Karlsruhe 2019

---

## ABSTRACT

---

Geothermal heat provide huge amounts of energy, inexhaustible in human periods of time. Therefore, geothermal energy is suitable to play a major role in the development of a sustainable energy supply and the German energy system transition.

The Upper Rhine Graben (URG) offers favorable conditions for geothermal energy utilization due to an elevated heat flow, which results in temperatures of  $\geq 200$  °C in 4–5 km depth. The geothermal reservoirs for deep geothermal energy in the URG are mainly the Bunter sandstone formations and the crystalline basement. Enhanced geothermal systems (EGS) are suitable for an effective exchange of heat from deep fractured reservoir rocks to the circulating fluid. The natural fracture network is enhanced by stimulation activities to increase the permeability and enlarge the rock surface for an effective heat exchange. Fluid composition of the deep reservoirs are mostly highly saline brines with the main constituents Na, Ca, and Cl and total dissolved solids of  $\geq 100$  g kgw<sup>-1</sup>.

These brines are commonly used as transport medium in the geothermal circuit. In EGS the brine directly contacts the surfaces of unaltered rock, exposed to the brine by natural seismicity or artificial stimulation activity. Thereby, geochemical-mineralogical alteration processes will be initiated, which are able to affect the geothermal circuit to high extent. Therefore, a better knowledge of the alteration process in geothermal reservoirs are crucial for a sustainable operation and the lifetime of geothermal installations.

The aim of this thesis is to contribute to the understanding of geochemical-mineralogical alteration processes in the context of geothermal installations and their impact on the geothermal circuit, especially under the conditions found in the URG. Therefore, three experimental studies have been conducted with typical reservoir rocks and fluid compositions of the URG.

In the **first study** (Ch. 4) alteration experiments on two different arkosic sandstones with a synthetic 2 M Na-Cl solution (XX) at temperatures of 200 °C and 260 °C have been performed. Sandstone samples with a fresh surface and an intact rock fabric were used, representing natural fracture surfaces.

The sandstones show a high reactivity during the experiments. Quartz grain surfaces exhibit deep dissolution features and all reaction fluids were saturated with respects to quartz. Illite and kaolinite from the primary sandstone cementation completely dissolved from the sample surface. Perfectly euhedral crystals of analcime formed during the experiment covering the sample surface. The overall net transfer process dissolves quartz + illite + kaolinite ± K-feldspar and precipitates analcime + chlorite ± albite. The process is accompanied by a total volume increase of the solids of 20–30 vol.%. The experiments show changes on the rock surface, leading to an increase of the aperture of a single fracture during the early phases of reaction and later to a decrease as the fluid-rock reaction progresses. Alteration of the fracture surface also generates loose fragments and altered minerals, which may efficiently reduce the aperture along the fracture.

---

The **second study** (Ch. 5) comprise alteration experiments on granite samples under the same conditions as the first study (Na-Cl solution, 200 °C and 260 °C) to reproduce and comprehend the initial granite alteration processes and compare the results to the sandstone experiments.

One of the major mineral reaction is the dissolution of quartz at the (sub-)surface. Biotite chloritization is the most reactive process in the experiments. Partly chloritized biotites of the initial samples completely transformed into chlorites at sample surfaces. Thereby, hydrobiotite and a corrensite-like mineral phase occur as intermediate phases. The chloritization accompanies with a delamination of the phyllosilicate sheets and an expansion of the mineral grains. Feldspars show only minor reactions in the experiments.

In accordance with the observations of alteration features in natural deep crystalline basement rocks (KTB, Soultz-sous-Forêts) following inferences can be made: (1) Quartz dissolution and biotite chloritization are the main mineral reactions in the early stages of fracture alteration in deep crystalline basement rocks under geothermal conditions. (2) In these early stages rock fabric will be further weakened by the mineral-brine reactions, resulting in a propagation of the fracture into the adjacent rock and thus, an increased fluid permeability in the early period of the fracture alteration.

The experiments of the **third study** (Ch. 6) have been performed on sandstone samples and three different solutions (2 M Na-Cl, Na-Ca-Cl, and Ca-Cl), which are closer the natural URG brine composition. Additionally, the experiments have been conducted in time series lasting up to 128 days at temperatures of 200 °C.

According to the experiments with pure Na-Cl solution, quartz dissolution and the removal of illite from the cementation are the major reaction processes of the primary mineral assemblage. But, K-feldspar showed a high degree of dissolution in the Ca-Cl solution. Again, massive amounts of zeolites precipitated during the experiments on the sample surfaces, whereby the type of zeolite depends on the solution composition. Analcime has been formed at high to intermediate Na/Ca ratios whereas wairakite at intermediate to low Na/Ca ratios. Additionally, sporadic epistilbite formed in the pure Ca-Cl solution.

The transformation of clay minerals (and quartz) to different zeolite phases are accompanied with a total volume increase of solids. Zeolite cementation in several natural sandstone formations indicate the potential of this alteration process for healing and clogging of pore space. Transferring these findings to a geothermal fracture network, a reduction of fluid pathways by zeolites precipitation is able to hamper the fluid circulation in the geothermal circuit.

Conclusively, different alteration processes depending on the initial rock type and the fluid composition could be described and their effects on the geothermal circuit were derived. The observed processes in the sandstones have the potential to hamper the fluid flow and decrease the efficiency of geothermal installations. Whereas the alteration in the granite rather have the potential to increase fluid pathways, at least in the initial stage of the granite alteration.

This thesis contributes to a better understanding for alteration processes in granitic and sandstone reservoir rocks, controlling the hydrothermal efficiency of the geothermal fracture network and therefore, the sustainable operation of geothermal installations.

---

## KURZFASSUNG

---

Geothermische Wärme liefert eine große Menge an Energie, unerschöpflich in menschlichen Zeiträumen. Daher ist geothermische Energie geeignet eine große Rolle in der Entwicklung zu einer nachhaltigen Energieversorgung und der deutschen Energiewende zu spielen.

Der Oberrheingraben (ORG) bietet durch einen erhöhten Wärmefluss gute Bedingungen für die Nutzung von Geothermie. Temperaturen von  $\geq 200$  °C werden in Tiefen von 4–5 km angetroffen. Die Reservoirs für tiefe Geothermie im ORG sind hauptsächlich Sandsteinformationen des Buntsandsteins und das kristalline Grundgebirge. *Enhanced geothermal systems* (EGS) ermöglichen einen effektiven Wärmeaustausch zwischen dem geklüfteten Reservoirgestein und dem zirkulierenden Fluid. Das natürliche Kluftnetzwerk wird dabei durch Stimulation erweitert, was zu einer erhöhten Permeabilität und einer vergrößerten Gesteinsoberfläche führt und letztendlich zu einem effektiven Wärmeaustausch. Die Zusammensetzung der tiefen Formationsfluide sind meist hoch saline Lösungen mit den Hauptbestandteilen Na, Ca und Cl und insgesamt  $\geq 100$  g kg<sup>-1</sup> gelöster Stoffe.

Diese Fluide sind für gewöhnlich auch das Transportmedium in EGS-Kreisläufen und stehen in direktem Kontakt mit durch natürliche Seismizität oder künstliche Stimulation erzeugte nicht-alterierten Kluftoberflächen des Reservoirgesteins. Dadurch werden geochemisch-mineralogische Alterationsprozesse initiiert, welche den geothermischen Kreislauf in hohem Maße beeinflussen können. Daher ist ein besserer Kenntnisstand von Alterationsprozessen innerhalb des Geothermiereservoirs essenziell für einen nachhaltigen Betrieb und eine hohe Lebensdauer von Geothermieanlagen.

Ziel dieser Arbeit ist zum Verständnis von geochemisch-mineralogischen Alterationsprozessen im Zusammenhang mit Geothermieanlagen und deren Einfluss auf den Geothermiekreislauf, unter Berücksichtigung der Bedingungen des ORG, beizutragen. In diesem Zuge wurden drei experimentelle Studien mit typischen Reservoirgesteinen und Fluidzusammensetzungen des ORG durchgeführt.

In der **ersten Studie** (Ch. 4) wurden Alterationsexperimente an zwei unterschiedlichen arkosischen Sandsteinen mit synthetischer 2 M Na-Cl-Lösung bei Temperaturen von 200 °C und 260 °C durchgeführt. Es wurden Sandsteinproben mit einer frischen Oberfläche und einem intakten Gesteinsgefüge verwendet, die eine natürliche Kluftoberfläche darstellen sollten.

Die Sandsteine zeigen eine hohe Reaktivität während der Experimente. Die Oberfläche von Quarzkörnern zeigt tiefe Lösungsmerkmale und die Fluide sind gesättigt im Bezug zu Quarz. Illit und Kaolinit aus der primären Sandsteinzementation wurden komplett von der Probenoberfläche gelöst. Perfekt idiomorphe Analcime bildeten sich während des Experiments, die die gesamte Probenoberfläche bedecken. Der gesamte Alterationsprozess beinhaltet die Auflösung von Quarz + Illit + Kaolinit  $\pm$  Kalifeldspat und die Bildung von Analcim + Chlorit  $\pm$  Albit. Er geht einher mit einem Volumenzuwachs der Festphasen von 20–30 vol.%.

---

Die Experimente zeigen Veränderungen der Gesteinsoberfläche, die zu einer erhöhten Öffnungsweite einer Kluft in der ersten Phase und eine Erniedrigung in einer späteren Phase der Fluid–Gesteins-Reaktionen führt. Die Alteration der Kluftoberfläche produziert ebenfalls lose Fragmente und alterierte Minerale, die die Durchlässigkeit entlang der Kluft wirksam verringern können.

Die **zweite Studie** (Ch. 5) umfasst Alterationsexperimente an Granitproben unter den selben Bedingungen wie bei der ersten Studie mit den Sandsteinproben (Na-Cl-Lösung, 200 °C und 260 °C). Hierbei soll der anfängliche Alterationsprozess von Graniten reproduziert und verstanden und mit den Ergebnissen der Sandsteinexperimente verglichen werden.

Eine der Hauptmineralreaktionen ist die Lösung von Quarz an der Probenoberfläche. Biotitchloritisierung ist der reaktivste Prozess dieser Experimente. Teilweise chloritisierter Biotit der frischen Probe hat sich an der Probenoberfläche vollständig in Chlorit umgewandelt. Dabei kommen Hydrobiotit und eine Corrensit-ähnliche Phase als Zwischenprodukt vor. Die Chloritisierung geht einher mit der Delamination der Phyllosilikate und einer dadurch erzeugten Expansion der Mineralkörner. Die Feldspäte zeigen in den Experimenten einer nur geringfügige Reaktion.

Im Einklang mit Beobachtungen von Alterationsmerkmalen in natürlichem tiefen kristallinen Grundgebirge (KTB, Soultz-sous-Forêts) können folgende Aussagen gemacht werden: (1) Quarzlösung und Biotitchloritisierung sind die wichtigsten Mineralreaktion in frühen Phasen der Kluftalteration unter geothermischen Bedingungen in tiefen Kristallingesteinen. (2) In diesen frühen Phasen wird das Gesteinsgefüge durch die Mineral–Fluid-Reaktionen gelockert, was zu einer Fortsetzung von Rissen in das angrenzende Gestein führt und dadurch die Fluidpermeabilität in der frühen Phase der Kluftalteration erhöht.

Die Experimente der **dritten Studie** (Ch. 6) wurden mit Sandsteinproben und drei unterschiedlichen Lösungen (2 M Na-Cl, Na-Ca-Cl und Ca-Cl) angesetzt, welche näher an die natürliche Zusammensetzung der ORG-Fluide herankommt. Die Experimente wurden in Zeitreihen mit einer Dauer von maximal 128 Tagen, bei einer Temperatur von 200 °C durchgeführt.

Wie bei den Experimenten mit reiner Na-Cl-Lösung sind Quarzlösung und das Verschwinden von Illit aus der Zementation die Hauptreaktionen der primären Mineralvergesellschaftung. Kalifeldspat zeigt in den Experimenten mit Ca-Cl-Lösung einen hohen Lösungsgrad. Während den Experimenten bildeten sich wieder große Mengen von Zeolithen auf den Probenoberflächen, wobei die Art der entstandenen Zeolithphase von der Lösungszusammensetzung abhängt. Analcim bildete sich bei hohen bis mittleren Na/Ca-Verhältnissen, wohingegen Wairakit bei mittleren bis niedrigen Verhältnissen vorkommt. In der reinen Ca-Cl-Lösung bildete sich vereinzelt Epistilbit.

Die Umwandlung von Tonmineralen (und Quarz) zu verschiedenen Zeolithphasen geht einher mit einer Nettozunahme des Volumens der Festphasen. Zeolithzementation in verschiedenen natürlichen Sandsteinformation zeigen das Potential dieser Alterationsprozesse zur Ausheilung und Zusetzung von Porenraum. Übertragen auf das geothermische Kluftnetzwerk zeigt dies, dass die Zeolithbildung zu einer Reduktion der Fluidzirkulation und damit einer beeinträchtigung des geothermischen Kreislaufs führen kann.

Es wurden unterschiedliche Alterationsprozesse, abhängig von Gestein und der Lösungszusammensetzung, beschrieben und erklärt und ihre Auswirkungen auf den Geothermiekreislauf diskutiert. Die beobachteten Prozesse in den Sandsteinproben bergen das Potential den Fluidfluss in geothermischen Anlagen zu beeinträchtigen, wohingegen die Alteration von Graniten eher zur Erhöhung der Fluiddurchlässigkeit führt, zumindest in den frühen Stadien der Granitalteration.

Diese Arbeit trägt bei zu einem besseren Verständnis von Alterationsprozessen in granitischen und Sandstein-Reservoirgesteinen, welche die Eigenschaften eines Kluftnetzwerkes und somit der nachhaltige Betrieb von Geothermieanlagen fundamental beeinflussen.

---

---

# CONTENTS

---

ABSTRACT	II
KURZFASSUNG	IV
1 INTRODUCTION	1
1.1 Deep geothermal energy in the URG . . . . .	1
1.2 Motivation . . . . .	3
1.3 Structure of thesis . . . . .	4
2 FUNDAMENTALS OF ROCK ALTERATION	6
2.1 Definition of alteration . . . . .	6
2.2 Alteration processes . . . . .	11
2.3 Mineral groups, important in alteration reactions . . . . .	14
3 FUNDAMENTALS IN GEOCHEMISTRY	27
3.1 Reaction mechanisms . . . . .	27
3.2 Fundamentals of aqueous geochemistry . . . . .	29
3.3 Experimental studies . . . . .	34
4 EXPERIMENTAL INTERACTION OF HYDROTHERMAL NA-CL SOLUTION WITH FRACTURE SURFACES OF GEOTHERMAL RESERVOIR SANDSTONE OF THE UPPER RHINE GRABEN	36
Abstract . . . . .	36
4.1 Introduction . . . . .	37
4.2 Material and methods . . . . .	38
4.3 Results . . . . .	41
4.4 Discussion . . . . .	50
4.5 Conclusion . . . . .	62
Acknowledgments . . . . .	62
5 EXPERIMENTS ON GRANITE ALTERATION UNDER GEOTHERMAL RESERVOIR CONDITIONS AND THE INITIATION OF FRACTURE EVOLUTION	63
Abstract . . . . .	63
5.1 Introduction . . . . .	64
5.2 Material and methods . . . . .	66
5.3 Results . . . . .	68
5.4 Discussion . . . . .	78
5.5 Conclusion . . . . .	89
Acknowledgments . . . . .	89

---

---

6	EXPERIMENTS ON SANDSTONE ALTERATION UNDER GEOTHERMAL RESERVOIR CON- DITIONS AND THE FORMATION OF ZEOLITES	90
	Abstract . . . . .	90
6.1	Introduction . . . . .	91
6.2	Methods . . . . .	92
6.3	Results . . . . .	96
6.4	Discussion . . . . .	107
6.5	Conclusion and perspective . . . . .	115
	Acknowledgements . . . . .	115
7	CONCLUSION	116
7.1	Major findings of the research . . . . .	117
7.2	Effects of alteration reactions on fluid permeability . . . . .	118
7.3	Outlook . . . . .	119
	REFERENCES	121
	DECLARATION OF AUTHORSHIP	137
	PUBLICATIONS	139
	ACKNOWLEDGMENTS	142

---

---

## INTRODUCTION

---

Geothermal heat provide a huge amount of energy, inexhaustible in human periods of time. It is mainly independent from diurnal, seasonal, and atmospheric variations. Therefore geothermal energy is suitable to play a major role in the development of a sustainable energy supply and the German energy system transition.

Shallow geothermal energy installation are suitable for heating and cooling purpose in private and public buildings. They work reliable and are prevalent in many European countries. The installations run with a closed geothermal circuit (e.g. borehole heat exchanger (BHE), collector fields, heat pumps) and also with open well systems (aquifer utilization), relatively space saving, and do not need necessarily an unusual elevated geothermal gradient (Stober & Bucher, 2012).

The generation of process heat for industrial application or electrical power generation needs higher amounts of energy from the geothermal reservoir. Therefore, higher temperatures and a larger rock volume are necessary for a sustainable operation.

### 1.1 DEEP GEOTHERMAL ENERGY IN THE UPPER RHINE GRABEN

In areas of without highly elevated geothermal gradients, the necessary temperatures for geothermal usage are reached in relatively great depth, which requires deep boreholes. A large heat exchanger volume is achieved by the use of open-cycle systems, where the production fluid passes a natural or enhanced fracture network with direct contact to the reservoir rock. The production hole(s) and the re-injection hole(s) are typically drilled sidetracked in opposite direction (after some 100s of m vertical) to achieve a large distance between the open-hole sections of both (or more) holes (Fig. 1.1).

The natural fracture network often is enhanced by stimulation activities to increase the rock surface and to elevate the efficiency of heat exchange between rock and fluid. This type of geothermal installation is designated as *enhanced geothermal system* (EGS, Fig. 1.1; Schindler et al., 2010).

In the Upper Rhine Graben (URG), a Mesozoic graben structure (Behrmann et al., 2003; Illies, 1972) in the border area between southwest Germany and east France, the geothermal gradient is elevated to a level, where economic profitable EGS systems can be installed. Temperatures up to 200 °C can be reached in depths of  $\leq 5$  km (e.g. Dezayes et al., 2008). Therefore, several geothermal facilities have been built in the URG in France, Germany, and Switzerland, e.g. Soultz-sous-Forêts (Genter et al., 2010), Rittershoffen (Baujard et al.,

---

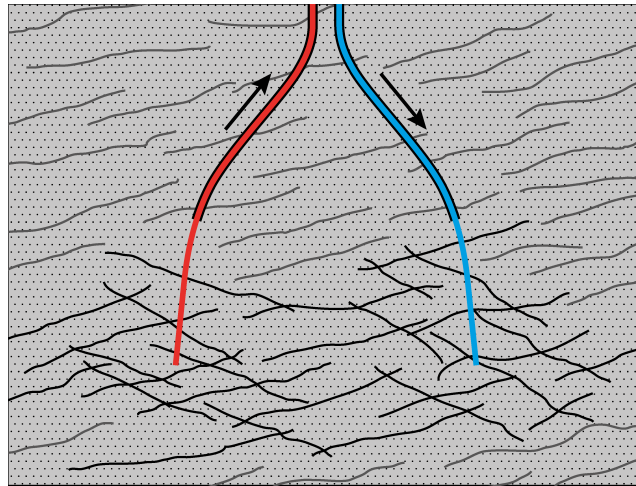


**Figure 1.1** – In enhanced geothermal system hot fluid is extracted from a production well (red) to the surface. Heat energy is extracted from the fluid (direct heat, electricity) and the chilled fluid re-injected through another well back to the reservoir (blue). Within the reservoir the fluid circulates through a fracture network in direct contact with the reservoir lithology.

2017), Riehen (Schill & Klingler, 2010), and Bruchsal (Herzberger et al., 2010).

In the URG geothermal reservoirs are located in the crystalline basement with granitic and gneissic rocks, in the overlaying sedimentary formation of the Triassic *Bunter* and Upper *Muschelkalk* (Fig. 1.2). Suitable reservoir rocks need a high matrix permeability or a well-developed fracture network. In the URG the sedimentary rocks provide the required fluid pathways and occur in accessible depth with temperatures high enough for geothermal usage. Crystalline basement rocks, mostly granitic and gneissic rocks, offer equal properties in the URG. Here permeability is mainly given by a (enhanced) fracture network.

The production fluid in EGS systems of the URG is the natural fluid stored for thousands of years in the reservoir formation. It is fed by surface water from the graben shoulders Black Forest in the East, and the Vosges in the West. The typical morphology of the graben structure drive the fluid flow in deeper parts of graben, where it is heated up to elevated temperatures (Pribnow & Schellschmidt, 2000) and raises due to the gradient in higher layers or even towards the surface (Fig. 1.2; Stober & Bucher, 2014).

On the pathway of the fluid from surface to the graben center, it concentrates in many substances from several lithologies it passes through. In the deeper part of the graben the fluid is a highly saline brine with numerous constituents and partly high degrees of gaseous components (Pauwels et al., 1993; Stober & Bucher, 2014). The total dissolved solids (TDS) can reach values markedly higher than  $200 \text{ g kgw}^{-1}$  (Sanjuan et al., 2016; Stober & Bucher, 2014). Main dissolved species are Na, Ca, Cl, often with elevated concentrations of K, Ba,  $\text{SO}_4$ , and  $\text{HCO}_3$  (Aquilina et al., 1997; Stober & Bucher, 2014). The main gaseous phase is  $\text{CO}_2$  and significantly lesser  $\text{N}_2$ .

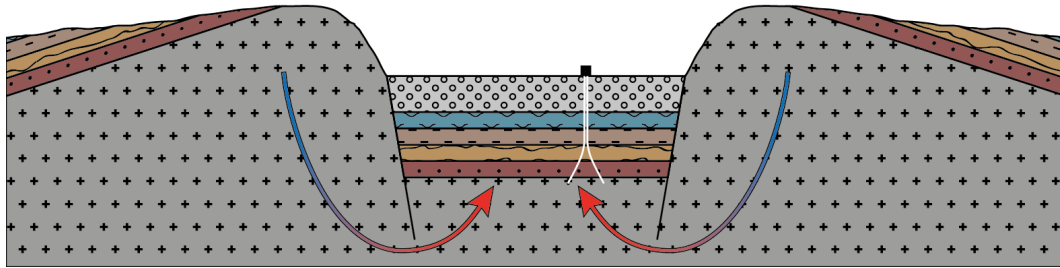


**Figure 1.2** – Graben structure of the URG with fluid flow (arrows) and a geothermal power plant in the graben center.

## 1.2 MOTIVATION

Alteration reaction of the reservoir rocks and the perfusing brine occur inevitably where the natural system is disturbed by exploration actions for geothermal energy usage. The geochemical-mineralogical conditions in EGS give a combination of partly extreme conditions, which interact complexly and affect each other in different ways.

Properties of altered rocks differ to high extend from fresh, unaltered, and solid rocks (e.g. Meller & Kohl, 2014; Wintsch et al., 1995). The influence of alteration on rock mechanics, hydraulic permeability, heat transfer, and chemical stability is vast. The efficiency and lifetime of geothermal installations are directly dependent on an unhampered fluid circulation and an optimal heat transfer from the rock to the production fluid. Especially in EGS, where initial investment cost are relatively high, it is essential to preserve the geothermal reservoir operable over a long time period (Bertrand et al., 1994; Milodowski et al., 1989; Morrow et al., 2001).

Conditions found in URG reservoirs provide many properties, which accelerate alteration reactions. Important parameters for alteration processes are:

- ◊ Elevated temperatures of  $>200\text{ }^{\circ}\text{C}$
- ◊ Highly saline brines with TDS of  $>200\text{ g kgw}^{-1}$
- ◊ Natural rocks with multi-phase mineral assemblages
- ◊ Varying mineral compositions
- ◊ Often high gas contents

The combination of extreme conditions complicate an easy prediction of fluid–rock interaction and alteration reactions. Calculations overstrain most modelling codes and the underlying databases for the complex systems. Thus, the forecast of geochemical fracture behavior can not be modelled with the present available codes and databases.

Hydrothermal alteration has a major influence on the rock properties, both, mechanical as well as hydraulic, and the characteristics and qualities of a geothermal reservoir (Meller & Kohl, 2014; Meller & Ledésert, 2017). Therefore, a better knowledge of the geochemical-mineralogical alteration reactions, proceeding in the geothermal reservoir, are crucial for a sustainable operation of a geothermal installation.

### 1.3 STRUCTURE OF THESIS

The thesis pursue to retrace and explain the first steps of fracture alteration on initially fresh rock surfaces in geothermal reservoirs. In natural systems, fractures often evolve from a fresh, highly permeable fissure towards a completely sealed and impermeable vein. Thus, it is essential to know, which alteration processes occur within the geothermal reservoir lithologies and how they influence the fracture aperture in the geothermal circuit.

Fundamentals of rock alteration and their potential influence on the geothermal circuit in EGS are provided in Chapter 2. Here, the definition and classification of alteration and alteration processes will be given, and the most important mineral types and their specific properties will be introduced. A short introduction in reaction mechanisms and geochemical background in aqueous systems is given in Chapter 3 and different approaches will be introduced.

The main research is published in or submitted to international scientific journals. The three parts are shortly presented below.

**SANDSTONE ALTERATION (CHAPTER 4)** The first study shows alteration reactions under typical geothermal conditions found in the URG in sandstone reservoirs. Two different sandstone samples, representing the surface of a fracture in a geothermal reservoir, have been hydrothermally altered in an autoclave system. Here a simplified solution composition (2 M Na-Cl) has been used, representing the main fluid components in deep sandstone reservoirs. For an understanding of the complex alteration processes in natural systems, it is necessary to narrow down the complexity of the involving geochemical components in this initial study. Main findings are alteration reactions involving primary quartz and clay minerals producing large amounts of analcime. The geochemical-mineralogical system is regarded and the influence for the geothermal reservoir discussed.

This study has been published in *Applied Geochemistry*.

**GRANITE ALTERATION (CHAPTER 5)** Granitic basement rocks are the second important reservoir lithology for EGS in the URG. Therefore, experiments under the same conditions as in Chapter 4 have been performed with granite samples. Alteration reaction differ strongly from the processes seen in sandstones. Primary phyllosilicates and quartz are the most reactive phases. Initial biotite alters completely to chlorite in the sample sub-surface. The rock fabric is weakened to large extend influencing the properties of the granitic reservoir rock.

This study has been published in *European Journal of Mineralogy*.

**SANDSTONE ALTERATION WITH VARIOUS SOLUTIONS (CHAPTER 6)** Based on the findings in the first study (Ch. 4), alteration experiments at 200 °C on sandstones with different solutions closer to the natural brine composition have been performed. Therefore, a Na-Ca-Cl solution with a Na : Ca ratio of 85 : 15 have been used, which is typical for URG brines. Furthermore, identical experiments with pure Na-Cl and pure Ca-Cl has been performed, too, for the end-member composition. The experiments have been conducted in time series up to 60 days, for a better insight into the first steps of the alteration reactions. Additionally, long-term experiments up to 128 days were taken out to pursue the brine–rock interaction to later stages. Different zeolite minerals precipitate on the sandstone surface, depending

on the initial fluid composition, at the expense of clay mineral cementation and initial quartz. The results are discussed in the context of URG sandstone reservoirs.

This study has been submitted to *European Journal of Mineralogy*.

---

---

## FUNDAMENTALS OF ROCK ALTERATION

---

Rock alteration is one major process in the global geological cycle. It takes place in every geological setting and therefore in a wide range of temperature and pressure conditions. Every type of rock can be exposed to changes in its environment, perturbing the conditions its mineral assemblage has been stabilized. Getting out of equilibrium, various geochemical-mineralogical reactions will be initiated, adjusting the chemical bulk composition, types of minerals, mineral composition as well as the compounds and properties of an involved fluid. Thereby the hydrological, mechanical, and geophysical properties of the rock may change tremendously.

### 2.1 DEFINITION OF ALTERATION

Alteration reactions under geothermal conditions connect processes which are part of the disciplines *metamorphism*, *hydrothermal alteration*, *metasomatism*, as well as *water-rock interaction* and *geochemical weathering*.

#### 2.1.1 WATER-ROCK INTERACTION

*Water-rock interaction* (WRI), or *fluid-rock interaction*, comprise a large field of geochemical processes and includes many of the disciplines introduced above. Reactions between a solid mineral phases and a fluid, mostly water with different dissolved components, and in various concentrations comprise this field of geochemistry. Limitation in temperature, pressure, chemical diversity and scale of systems do practically not exist.

The scale of WRI range from huge processes at the global geological cycle and reaches down to the nm scale, where the interaction of single atoms with the mineral surface and the co-existing fluid are dealt with. Within this large range of scales, WRI affect the global water compositions, as the groundwater, river and lake water, and oceans, but also the composition of fluids in hydrothermal systems, highly saline lakes as well as magmatic fluids and formation waters in fissures and veins. In the solid rock material WRI has an influence on the mineral and rock properties in natural and technical environments, and changes the types of minerals and their composition.

---

### 2.1.2 METASOMATISM

*Metasomatism* is the re-equilibration of a mineral assemblage to a changed chemical environment when a fluid enters a volume of rock (Putnis & Austrheim, 2010). Thereby, typical alteration reactions between the minerals and the fluid take place. Therefore, a mass transfer between the rock volume and the entered fluid occurs on a local scale (open-system). The mass transfer distinguishes metasomatism from metamorphism (see Sec. 2.1.3). Further, metasomatism is rather driven by the change of the chemical environment (by the fluid), metamorphism by the change of pressure and/or temperature on a larger, mostly geodynamic scale (Putnis & Austrheim, 2010).

Reaction mechanisms include typical alteration reactions. The change of the fluid by metasomatic alteration reactions and the transport out of the system, inevitably results in the disturbance of the geochemical environment of another volume of rock (another system) (Putnis & Austrheim, 2010).

### 2.1.3 METAMORPHISM

*Metamorphism* is the process of the re-equilibration of a mineral assemblage to changed physical conditions by large-scale geological dynamics. It involves changes in the mineralogical and geochemical composition of a rock dominantly in the solid state. Thereby, the structure of the rock is modified (Bucher & Grapes, 2011). In strict sense, there is no mass transfer to or from the bulk system (closed system).

#### *METAMORPHIC PROCESSES*

Metamorphic processes are geochemical-mineralogical reactions between several mineral phases, which get in dis-equilibrium by changes of pressure and/or temperature to a new set of stable minerals at the new conditions. The lower temperature limit of metamorphic reactions is traditionally at about 150–300 °C. This boundary is set by the occurrence of a set of typical metamorphic minerals (e.g. pyrophyllite, paragonite, prehnite), which delineate metamorphic from diagenetic processes. The lower limit of metamorphic reactions strongly depend on the lithology, and can be at lower temperatures (Bucher & Grapes, 2011). The upper temperature limit of metamorphic processes is set by the beginning of igneous processes, which start in the range of 700–1150 °C depending on the rock composition and the presence of H<sub>2</sub>O. The lower pressure limit of metamorphic processes is close to ambient conditions, since ascending magma bodies lead to metamorphic reactions close to the surface (contact metamorphism). Concerning the upper pressure limit, metamorphic rocks can be formed at pressure much higher than 3 GPa.

Although the strict definition of metamorphism exclude a transfer of mass, metamorphic reactions only occur in the presence of a fluid (Putnis & Austrheim, 2010).

#### *METAMORPHIC FACIES*

The metamorphic facies concept was developed in 1915 by Eskola (1915). It divides characteristic mineral assemblages to groups and sub-groups, the facies, which occur at specific

temperature and pressure conditions. The concept was developed for basaltic rocks, where the rock type gives the name for the facies (e.g. greenschist facies). These facies were transferred to other lithologies, where different mineral assemblages may be stable and diagnostic (Bucher & Grapes, 2011).

In the context of hydrothermal alteration in geothermal applications, the relevant temperature field is between about  $<100\text{ }^{\circ}\text{C}$  as lower limit and about  $300\text{--}400\text{ }^{\circ}\text{C}$  for the upper limit. Pressure (fluid pressure) is generally low ( $\leq 50\text{ MPa}$ ) since high temperature gradients are expected in geothermal active areas and depth of geothermal bore holes are generally  $\leq 5\text{ km}$ . Therefore, the p-T area fills the “gap” between diagenetic processes, which are defined to maximum temperatures of up to  $\sim 100\text{ }^{\circ}\text{C}$ , and metamorphic processes, which traditionally take place at temperatures higher than  $300\text{ }^{\circ}\text{C}$  (Bucher & Grapes, 2011). But, since the reaction processes are similar to metamorphism, additional low-grade metamorphic facies have been defined in the “gap” between diagenetic processes and regional metamorphism (Coombs, 1973; Coombs et al., 1959).

**VERY LOW-GRADE METAMORPHIC FACIES** There are several approaches for definitions and further sub-divisions of the very low-grade metamorphic facies. The most general (and most prevalent) is the definition of one single *sub-greenschist facies* (e.g. Bucher & Grapes, 2011; Smulikowski et al., 2003). Since a differentiation of mineral assemblages to define sub-facies is not possible in every rock type, this is useful for most geological settings. A further bisection of the sub-greenschist facies into the *zeolite facies* at lower metamorphic grade, and a *prehnite-pumpellyite facies* at higher grade has been done by Coombs et al. (1959) (Fig. 2.1).

At least for basaltic and granitic rock compositions several zones can be observed and subdivided to various extent. Coombs (1973) and Coombs et al. (1959) developed two main facies, the *zeolite facies* at lowest p-T conditions, and a subsequent *prehnite-pumpellyite facies* at higher temperature and pressure on observation in the Taringatura area, New Zealand. The zeolite facies is marked by the appearance of zeolite phases in prograde metamorphic direction. The disappearance of zeolites at higher temperatures is the transition to the prehnite-pumpellyite facies (Coombs et al., 1959).

These two facies can be further divided to several sub-facies and zones, respectively. A split of the zeolite facies to a low- and a high-T sub-facies in the Na-Ca-Al-Si-H<sub>2</sub>O system can be realized by the occurrence of mordenite at the low temperature transition from the diagenetic zone, the assemblages analcime + heulandite/stilbite + quartz and laumontite + albite + quartz, and a wairakite zone at high temperature, low pressure conditions (Fig. 2.1; Coombs, 1973; Liou et al., 1991). In other geological settings different sub-facies and zonations has been defined, e.g. in Japan, (Miyashiro & Shido, 1970; Seki, 1969) or on Iceland (Walker, 1960).

The prehnite-pumpellyite facies is characterized by the absence of zeolite phases. It can be further divided into a prehnite-pumpellyite zone, a pumpellyite-actinolite zone at higher temperatures (Fig. 2.1; Arkai et al., 2003; Coombs, 1973).

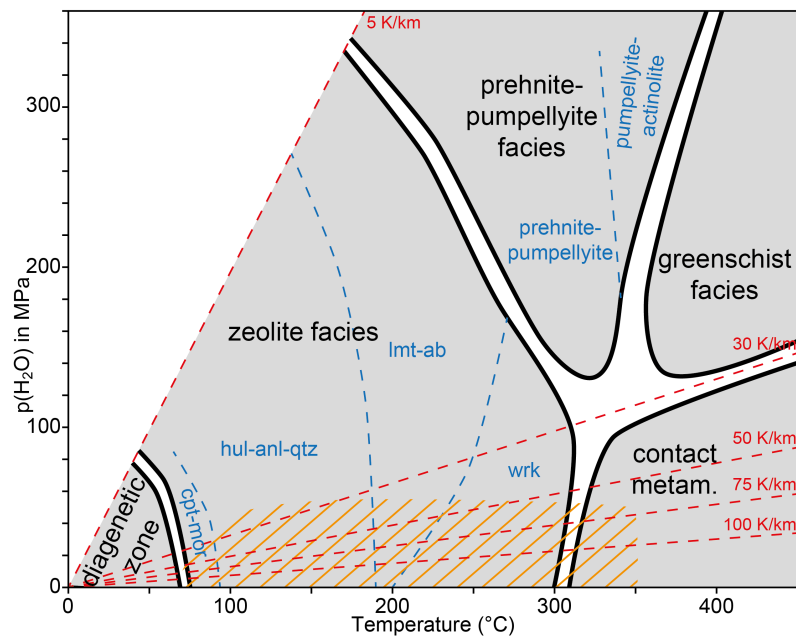


**Figure 2.1** – Metamorphic facies scheme for the low temperature and pressure area with temperature gradients (assuming hydrostatic pressure of pure water, red lines) and area of geothermal interest (orange shaded). Adapted from Bucher & Grapes (2011), Coombs (1973), and Utada (2001a).

#### 2.1.4 CHEMICAL WEATHERING

Reactions occurring during *chemical weathering* are similar to (hydrothermal) alteration and metasomatism, since they are mainly hydration reactions. But, the term weathering is commonly more used to alteration reactions close to the surface, where the rock is in contact with the atmosphere (e.g. Bauer & Velde, 2014; Putnis & Austrheim, 2010) and the influence of  $O_2$  and  $CO_2$  is high. Additionally, the bioactivity with several organic ligands, acids, and bases are part of the chemical weathering process close to the surface, which may influence mineral reactions to great extent (e.g. Bray et al., 2015; Wilson, 2004). The final result of the surface-near chemical weathering is the formation of soils.

#### 2.1.5 HYDROTHERMAL ALTERATION

Hydrothermal alteration is a process of alteration, where a (hydrothermal) fluid with an usually higher temperature as the rock body enters the system (open system). The chemical composition of the hydrothermal fluid commonly differs from a possibly present formation fluid. Hence, the entered fluid causes a change in temperature and chemical environment and, thus, a disequilibrium between the mineral assemblage of the rock and the fluid.

Consequently, hydrothermal alteration mostly is initiated in zones of higher hydraulic conductivity, i.e. fissures, veins, and fault zones, from where alteration reactions further proceed deeper into the adjacent rock body. The infiltration of the hydrothermal fluid and progression of the reaction front into the rock body cause a zonal distribution, dependent on the temperature of the fluid. Generally, temperature of the entering fluid decreases with distance to the heat source. Therefore, different alteration assemblages can be found and a characterization of zones be made.

An active fluid circulation is necessary for the processes of hydrothermal alteration. This can be driven by a heat source, which heats up relatively cold water. The density difference drives the fluid to rise up. Ascending magmatic fluids are a further possible source for hot fluids entering colder rock bodies. Furthermore, the circulation can also be morphological driven, where cold surface fluid enters a mountain ridge, heats up in deeper levels, and rises up again. Typical geological settings for this process are graben structures, as the URG (Fig. 1.2; Stober et al., 1999).

The entering of hydrothermal fluids delineates hydrothermal alteration from diagenesis and metamorphism, where temperature changes are on regional scale, and bulk chemistry is (on that scale) not changed (closed system; Utada, 2001b; Velde, 1995). Consequently, hydrothermal alteration is a type of the metasomatism.

#### CONDITIONS OF HYDROTHERMAL ALTERATION

Temperatures where hydrothermal alteration takes place range from few tens to several hundreds °C. An upper limit of hydrothermal alteration may emerge by the brittle ductile transition at temperatures at around >400 °C, which hamper the fluid flow since permeability generally decreases. The fluid circulation result in a mainly convective heat transport. The rising hot fluids can cause geothermal gradients of up to 200 K km<sup>-1</sup> and even higher (average is about 30 K km<sup>-1</sup>, Fig. 2.1).

The conditions of hydrothermal alteration intersect with the very low-grade metamorphic zones. Albeit the hydrothermal alteration contradict the strict definition of metamorphism, stable mineral assemblages produced by hydrothermal reaction are suitable to be arranged in the metamorphic facies scheme (see Sec. 2.1.3).

#### HYDROTHERMAL FLUID

The fluid has three important roles in the context of hydrothermal alteration. It is (1) transport medium for the chemical constituents to and from the alteration process, (2) it is reactant in most mineral reactions itself, and (3) it changes (increases) the temperature within the rock body.

Hydrothermal fluids are defined by an elevated temperature range of about 50 to >500 °C. Therefore, temperatures above the critical temperature of water (374 °C) are included. The term *fluid* is here used as umbrella term for liquid, gaseous, and supercritical aqueous solutions.

The sources of water are meteoric waters (rain, lakes, rivers, groundwater), sea water, connate, metamorphic, or juvenile water, but mostly a mixture of several sources (Pirajno, 1992). The low mineralized water is (depending on its source) heated up and enriched in dissolved solids by interaction with the surrounding lithologies.

The compositions of hydrothermal fluids are various. Some species are very common and part of nearly every natural hydrothermal solution. This includes Na<sup>+</sup>, K<sup>+</sup>, Ca<sup>2+</sup>, and Cl<sup>-</sup>, as well as SiO<sub>2,aq</sub> and HCO<sub>3</sub><sup>-</sup>. Others, are less common and its solubility is highly sensitive to the *pH* or *eH* of the fluid, e.g. Al<sup>3+</sup>, Fe<sup>2+</sup>, and Fe<sup>3+</sup>. Some typical species are correlated to a gaseous phase, as HCO<sub>3</sub><sup>-</sup>, SO<sub>4</sub><sup>2-</sup>, and CH<sub>4</sub>. In addition rare (earth-)alkalis as Ba<sup>2+</sup>, Li<sup>+</sup>,

Rb<sup>+</sup>, and Cs<sup>+</sup> can be constituents of a hydrothermal fluid. Hydrothermal solution connected to active magmatism (e.g. at mid-ocean ridges) or to (late stage) orogeny and other tectonic events are often enriched in metals as Mn<sup>2+</sup>, Zn<sup>2+</sup>, Cu<sup>2+</sup>, and many more (Pirajno, 1992).

The total dissolved solids (TDS) in hydrothermal fluids ranges from few ppm up to >50 wt.%. The *pH* of worldwide hydrothermal fluids can range at least between 2.4 to 9.6 (e.g. Ellis & Mahon, 1964; Pirajno, 1992).

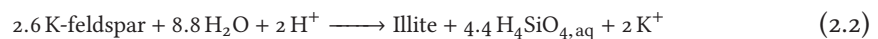
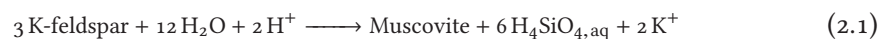
## 2.2 ALTERATION PROCESSES

The alteration process involves geochemical-mineralogical reactions, changing the bulk rock composition (open system), the mineral assemblage, the mineral composition, the texture of the rock and the fluid properties and composition (Ellis & Mahon, 1964; Pirajno, 1992).

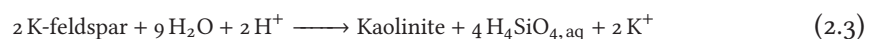
The conditions suitable for geothermal usage border the setting to a temperature range of about 100 to 350 °C. The maximum depth of the geothermal wells result in a pressure up to ~130 MPa lithostatically or ~50 MPa hydrostatically (Fig. 2.1). Wells deeper than about 5000 m are commonly not economically. Therefore a p-T area is formed, which overlap with the zeolite facies of the metamorphic facies concept.

The product of hydrothermal alteration reactions are mainly hydrous minerals (Velde, 1995), especially phyllosilicates and zeolites. Typical processes are hydration reactions proceeding during alteration of less-hydrous rocks with a hydrothermal fluid: Several common alteration processes are termed after the forming mineral phases, e.g. *sericitization*, *chloritization*, *serpentinization*, and *zeolitization*. All of them include a decomposition of water-free, or less hydrated, mineral phases to minerals with higher hydrated phases. Commonly, these hydration reactions release cations into the fluids and often consume H<sup>+</sup> from solution, changing the *pH* and the composition of the fluid.

Typical reactions in many lithologies (granites, gabbros, arkoses, ...) are the decomposition of feldspars forming muscovite, illite (sericitization)



or kaolinite (kaolinitization)

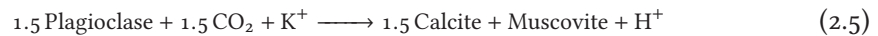


These reactions show the release of cations (K<sup>+</sup>) into the fluid, which increases the TDS and deliver them for further alteration reaction in the actual or a distant rock volume. For example the decomposition of plagioclase (anorthite) to muscovite may occur, if K<sup>+</sup> is available in the solution:



Furthermore, if CO<sub>2</sub> is present in the fluid, calcite can be formed additionally by the

transformation of plagioclase (anorthite) to muscovite:



Plagioclase to epidote (epidotization, saussuritization) is another typical alteration reaction.

Precipitation of quartz from solution is accompanied to many alteration reaction, which release  $\text{H}_4\text{SiO}_4$  to solution (Eq. 2.1–2.3). Omnipresent quartz fillings in fractures and veins show the prevalence of this process.



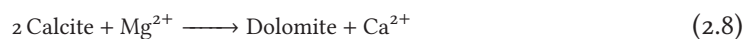
Lowering of temperature decrease the solubility of silicon species in respect to any silica phase and, therefore, support the precipitation of quartz (or another polymorph).

Additionally, biotite (phlogopite) is transformed to chlorite (e.g. clinochlore) by hydrothermal alteration reactions (chloritization), which further hydrates the precursor phases, and releases cations ( $\text{K}^+$ ) to the fluid, changing the fluid  $pH$  by consuming  $\text{H}^+$  (e.g. Ferry, 1979; Parry, 1982)



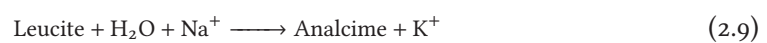
which is often accompanied by the formation of additional phases due to various compositional variations in the biotite (e.g. titanite or ilmenite by Ti). Chloritization of micas is one of the key reaction in alteration of granitic rocks, since the  $\text{Al}^{3+}$ -conservative reaction of, e.g. phlogopite to clinochlore, is accompanied with a decrease in volume (Parry, 1982). Therefore, this reaction has the potential to generate further fluid pathways accelerating the overall alteration process. Additionally, in more mafic rocks serpentization (olivine to serpentine), and chloritization of pyroxenes and amphiboles are common alteration reactions.

Furthermore, cation exchange induced by the composition of the fluid may change the mineral composition, e.g. dolomitization of calcite,



and albitization of anorthite.

Formation of zeolites is a further alteration process. It can be accompanied to transformation of clay minerals and to e.g. albitization of anorthite, where  $\text{Ca}^{2+}$  and  $\text{Al}^{3+}$  is released to the fluid (Weisenberger & Bucher, 2011). Typically, the easy access to cations, due to high concentrations in the fluid or the occurrence of volcanic glass favors the formation of zeolites. Hydration of feldspars and feldspathoids is a common alteration reactions, e.g. the transformation of leucite to analcime (Jamtveit et al., 2009)



### 2.2.1 CLASSIFICATION OF HYDROTHERMAL ALTERATION

Based on the cation-hydrogen ratio (activities,  $\text{Cat}/\text{H}^+$ ) in the hydrothermal fluid, Utada (1980) classified three major types of hydrothermal alteration. An acid-type with low  $\text{Cat}/\text{H}^+$ , an intermediate type with medium  $\text{Cat}/\text{H}^+$ , and an alkaline type with high  $\text{Cat}/\text{H}^+$  (Fig. 2.2; Utada, 2001b; Velde, 1995).

The acidic alteration type is characterized by a complete leaching of components other than  $\text{Al}_2\text{O}_3$ ,  $\text{SiO}_2$ , and  $\text{H}_2\text{O}$  from the rock body in the final stage of alteration, since the solution is initially low in solved cations. Therefore, typical alteration minerals include a  $\text{SiO}_2$ -polymorph, kaolinite, pyrophyllite, andalusite, corundum, and different Al-hydroxides (Velde, 1995). Alteration zones, subdivided by the occurrence of one reference clay mineral with a stable silica polymorph, are, with increasing temperature, (1) the halloysite zone, (2) the kaolinite zone, (3) the dickite + nacrite zone, and (4) the pyrophyllite zone (Fig. 2.2; Utada, 2001b). In silica deficient environments mineral assemblages with gibbsite, boehmite, and diasporite are stable.

Hydrothermal fluids in intermediate and alkaline alteration types contain initially a higher amount of (alkali, earth alkali) cations, on which a subdivision in K, Ca, and Na subtypes can be made by the predominant cation.

The intermediate type (K dominated) zones are grouped to (1) the smectite zone, (2) the mixed-layer clay mineral zone, (3a) the sericite or (3b) propylite zone, (4a) the K-feldspar or (4b) prehnite-pumpellyite zone, and (5) the biotite zone. The sub-types (b) are characterized by higher concentrations of Mg and Ca in the fluids (Utada, 2001b).

The alkaline type is dominated by zeolite phases instead of clay minerals. The Ca series is divided in (1) the chabazite-phillipsite zone, (2) the stilbite-heulandite zone, (3) the fibrous zeolite zone, (4) the laumontite zone, (5) the wairakite zone, and (6) the anorthite zone. The Na series in (1) the clinoptilolite zone, (2) the mordenite zone, (3) the analcime zone, and (4) the albite zone (Utada, 2001b).

The boundaries between the zones are wide and merge broadly. Differences between the hydrothermal regions, e.g. lithology, depth, fluid-rock ratio, lead to shifts in the temperature range and slightly divergent mineral assemblages. Nevertheless, the classification helps to compare the alteration stages of different hydrothermal active regions and to determine the alteration conditions in terms of temperature and fluid composition (Utada, 2001b; Velde, 1995).

### CONCLUSION

Conclusively, alteration processes involve the reaction of the solid mineral assemblage with the entering fluid. The fluid adds high amounts of  $\text{H}_2\text{O}$ , various chemical constituents, and heat into the system. Therefore, hydrothermal alteration can be considered as metasomatic processes, the resulting mineral assemblages can be graded reasonable to pressure-temperature conditions, and thus, into the metamorphic facies scheme.

Geochemical reactions highly depend on the parent mineral phases and on the composition of the fluid. Generally, hydrous minerals are formed by alteration reactions, which have fundamental different properties compared to the less-hydrous parent mineral assemblage.

Types		Zones					
Acidic type	Al series	Halloysite	Kaolinite			Dickite + nacrite	Pyrophyllite
Intermediate type	K series	Smectite		Mixed-layer clay minerals	Illite	K-feldspar	Biotite
	K series + Mg Ca				Propylite	Prehnite-pumpellyite	Amphibole
Alkaline type	Ca series	Chabazite + phillipsite	Stilbite + heulandite	Fibrous zeolites	Laumontite	Wairakite	Anorthite
	Na series	Clinoptilolite	Mordenite	Analcime	Albite		

Temperature

a(Cat) / a(H<sup>+</sup>) in solution

**Figure 2.2** – Alteration types and mineral assemblage zones dependent on temperature and the composition of the co-existing solution. Adapted from Utada (2001b).

The typical alteration reactions show the importance of the fluid itself (H<sub>2</sub>O) and its composition. On the other hand the alteration reaction may change the fluid properties and composition. The formed, mostly hydrous, minerals are suitable to classify the assemblages with respect to the type and degree of alteration and correlate it to specific pressure and temperature conditions. In the following section, groups of silicate minerals are introduced, which are of high importance as alteration product.

### 2.3 MINERAL GROUPS, IMPORTANT IN ALTERATION REACTIONS

The most important rock forming mineral class are the silicates, which constitute about 90% of the crustal rock material (Deer et al., 2013). The main building units of silicates are tetrahedra with one silicon atom in the center of four oxygens at the corners (SiO<sub>4</sub><sup>4-</sup>, Fig. 2.3). Besides, Al (AlO<sub>4</sub><sup>5-</sup>) and Fe (Fe<sup>3+</sup>O<sub>4</sub><sup>5-</sup>) often substitute Si in the tetrahedra.

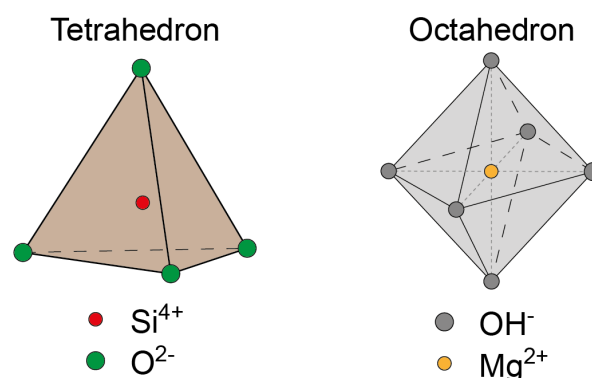


**Figure 2.3** – SiO<sub>4</sub><sup>4-</sup> tetrahedron: Silicon atom in the center and four oxygen atoms at the corners. Mg(OH)<sub>6</sub><sup>4-</sup> octahedron: Mg atom in the center and six hydroxides at the corners.

The tetrahedra build a framework by sharing oxygens at the tetrahedron corners. Depending on the extend of tetrahedra linking, it is negatively charged to varying degree.

Solely pure  $\text{SiO}_2$  frameworks are uncharged, of all  $\text{O}^{2-}$  tetrahedra corners are connected to framework  $\text{Si}^{4+}$ . Practically, this is the case only for quartz and its polymorphs. Substitution of  $\text{Si}^{4+}$  by  $\text{Al}^{3+}$  (and other elements) in most of the mineral phases, influence the charge of the tetrahedra framework. Thereby, aluminosilicate frameworks commonly are negatively charged, even if their cations ( $\text{Si}^{4+}$ ,  $\text{Al}^{3+}$ ) share every  $\text{O}^{2-}$  with other framework cations. Elements of nearly the entire periodic table can be incorporated into the aluminosilicate framework, maintaining different requirements, e.g. charge balance and ionic radius.

Based on the type of tetrahedra framework, silicates are subdivided into seven major groups:

- ◇ Nesosilicates (olivine, titanite)
- ◇ Sorosilicates (epidotes)
- ◇ Cyclosilicates (tourmaline)
- ◇ Inosilicates, single chain (pyroxenes)
- ◇ Inosilicates, double chain (amphiboles)
- ◇ Phyllosilicates (micas, chlorites, clay minerals)
- ◇ Tectosilicates (quartz, feldspars, feldspathoids, zeolites)

The arrangement results in a typical T : O ratio (T = Si,Al) for each silicate group, e.g. 2 : 5 for phyllosilicates and 1 : 2 for tectosilicates.

The structure of the framework results in tremendous differences in stability, chemical and physical properties, and shape. Consequently, thousands of different silicate minerals can be formed. Important alteration products are minerals of the phyllosilicate group, which include chlorites, micas, and clay minerals. In addition, tectosilicate minerals, in particular and zeolites, are commonly formed during alteration processes.

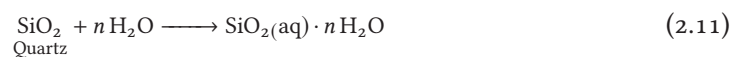
### 2.3.1 SIGNIFICANCE OF QUARTZ

Quartz and the other eight polymorphs of  $\text{SiO}_2$  form about 12 % of the Earth's crust (Dove & Rimstidt, 1994). Moreover silicon is component of 90 % of the crust minerals (silicates). Therefore quartz, and its  $\text{SiO}_2$  polymorphs, are the most important constituent in alteration reactions (Dove & Rimstidt, 1994). Naturally, this counts for geothermal systems, in particular in the URG, where sandstones and granitic rocks act as geothermal reservoir.

The simple quartz dissolution reaction can be written as



Nevertheless, the silica in solution is not strictly hydrated with two  $\text{H}_2\text{O}$ . Therefore formulations as



are used commonly, also with  $n = 0$ . Additionally, silica commonly forms polymers, which partly account for about 40 % of the dissolved silica complexes in solution.

**SOLUBILITY OF QUARTZ** The solubility of quartz is increased both with increasing temperature as well as with increasing pressure (Deer et al., 2004; Dove & Rimstidt, 1994).

The responsible mechanism is the interaction of the  $\text{OH}^-$  groups from the  $\text{H}_4\text{SiO}_4$  molecules with the surrounding dipolar  $\text{H}_2\text{O}$ . At higher pressure the number of  $\text{H}_2\text{O}$

molecules is higher (higher density), which can interact with the  $\text{OH}^-$  groups. Therefore, the number of molecules oriented in the most stable configuration is higher resulting in an enhanced solubility of the solid  $\text{SiO}_2$  phase (Dove & Rimstidt, 1994).

**IMPACT OF pH** The silica in solution is effected by the  $pH$  of the solution.  $\text{H}_4\text{SiO}_4$  is a weak acid, which first dissociates by the reaction



The  $pK_a$  of the reaction is 9.7 (Faure, 1998). The reaction can buffer natural systems where silica is in solution. On the other hand, if a (mineral-fluid) reaction consumes  $\text{H}^+$  from solution, the dissolution of quartz (or any other  $\text{SiO}_2$  polymorph) is triggered by the reaction



Consequently, the  $pH$  of any solution in contact with quartz, which is the case in most crustal geological environments, can not easily achieve values above the  $pK_a$  of reaction 2.12. At higher temperatures the quartz solubility rise dramatically with increasing  $pH$  (Dove & Rimstidt, 1994).

**EFFECT OF SOLUTION COMPOSITION** Beside temperature and  $pH$ , dissolved ions in the fluid have an influence on the quartz (and any other  $\text{SiO}_2$  polymorph) dissolution. Many experiments show an increasing quartz solubility with increasing ionic strength of the solution (*salting in* effect). This effect is tendentially enlarged at higher temperatures, but diminished at higher pressure (Newton & Manning, 2000; Xie & Walther, 1993).

At high ionic strength of a solution the effect will be reversed. The dissolved ions compete for the bipolar water molecules, which lowers the activity of the water, resulting in a lower solubility of quartz (*salting-out* effect). The impact of this effect decreases with increasing temperature (Newton & Manning, 2000; Xie & Walther, 1993).

The amount and type of cations in a solution have not only an influence on the solubility of silica, but also an effect on the dissolution rates on quartz and amorphous silica (Dove & Nix, 1997). Generally, the silica dissolution rate is enhanced proportional with the concentration of ions. Furthermore, the type of cations accelerate the dissolution to different extent (Dove, 1999), and dissolution rates may become more sensitive to the  $pH$  of the fluid (Dove & Elston, 1992).

### 2.3.2 PHYLLOSILICATES

Phyllosilicates (sheet silicates) occur in various geological environments. They are omnipresent in soils and weathered rocks, in sedimentary environments, and play a major role in the diagenesis of sedimentary and volcanic rocks. Beyond, they represent an important product of geothermal alteration reactions (e.g. Meunier, 2005; Velde, 1995). Micas are often a major components of initial unaltered rocks, in crystalline basement as granite and gneisses, as well as in immature sandstone formations. Chlorites are a common alteration product in every type of rock, where micas and/or feldspars occur. Clay minerals are omnipresent in alteration zones, fracture fillings and sandstone cementation.

## STRUCTURE OF PHYLLOSILICATES

The typical platy morphology is given by the silicate structure of this aluminosilicate group. The tetrahedra are linked together by sharing three of the four oxygens, forming a flat sheet. Hereby, the unlinked oxygens are all at the same side of the plane. The framework results in a lattice with hexagonal cavities in *c*-directions (Fig. 2.4a).

The second basic building unit of the sheet silicates are octahedra sheets, built by 6-fold coordinated cations connected to six oxygens and hydroxides (Fig. 2.3). In other words, one oxygen/hydroxide is linked to three cations in tri-octahedral type, or to two cations in di-octahedral types, where the third site is vacant. The result is also a hexagonal lattice (Fig. 2.4b-d).

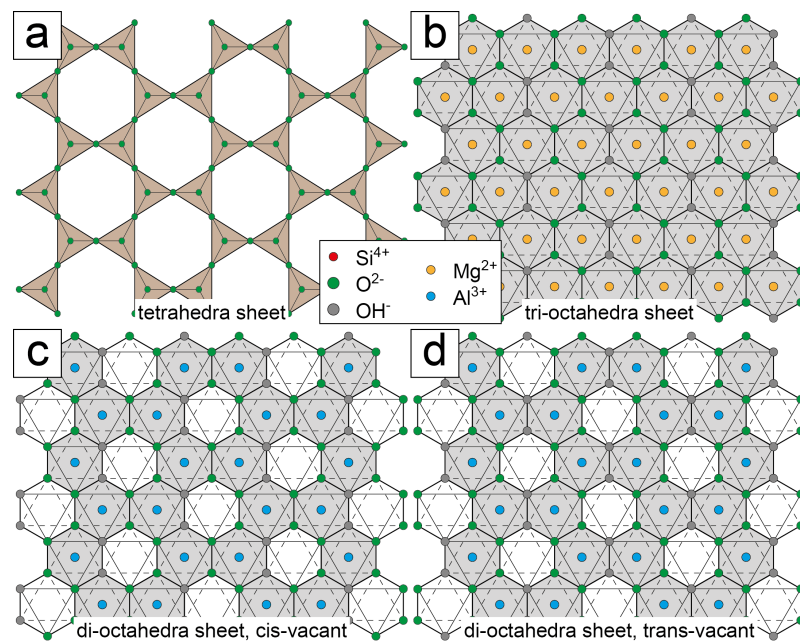


**Figure 2.4** – Schematic view of phyllosilicate sheets in *c*-direction. (a) Tetrahedra sheet (T) with un-connected O corners on one side (on the top) building a hexagonal plane. (b–d) Octahedra sheets (O). (b) O-sites completely occupied by  $Mg^{2+}$  (tri-octahedra sheet). (c) O-sites to 2/3 occupied by  $Al^{3+}$  and vacancies at the M2 position (cis-vacant di-octahedra sheet). (d) O-sites to 2/3 occupied by  $Al^{3+}$  and vacancies at the M1 position (trans-vacant di-octahedra sheet).

The vacancies of di-octahedral sheets are arranged in different ways with respect to the  $OH^-$ -groups. Trans-vacant di-octahedral sheets have vacant positions between the  $OH^-$ -groups ((M1; Fig. 2.4c). Whereas in cis-vacant sheets  $OH^-$ -groups are located at on “side” of the vacant positions (M1; Fig. 2.4d).

These framework building unites, tetrahedra (T) and octahedra (O, di and tri) sheets, give various possible combinations, which result in the different phyllosilicate types, i.e. chlorites, micas, and clay minerals. Furthermore, the inter-framework space can be filled by diverse elements and/or molecules, which result in various mineral phases with different properties.

The simplest ordering of T- and O-sheets is a T-O layer (1 : 1 layer), where all tetrahedra sites are filled with  $Si^{4+}$ , and all octahedra sites are filled with  $Mg^{2+}$  (or an other divalent cation; tri-octahedral) or with two  $Al^{3+}$  atoms (or an other trivalent cation; di-octahedral)

and one vacancy. The unconnected oxygen corners of the T-sheets bound to one side of the O-sheets. These bonds are rather strong, building a relatively stable unit. This results in the mineral antigorite (serpentine group) or kaolinite (kaolinite group), for a tri- or di-octahedral layer, respectively, in this simplest case. The resulting TO-layer is not charged. The single TO layers are connected to each other by weak OH–O bridges (Fig. 2.5).

Two T-sheets and one O-sheet form a TOT structure (2 : 1 layer), where the unconnected oxygen corners are linked to the O-sheet from both sides (Fig. 2.5). In the simplest way (Si at T positions, Mg or Al at M positions) the minerals talc and pyrophyllite are formed for tri- and di-octahedral O-sheets, respectively. Mineral groups with this TOT layers are micas, and clay minerals.

Substitutions in the T- and O-sheets result in a charge of the TOT layers.  $\text{Al}^{3+}$  and  $\text{Fe}^{3+}$  are common elements, substituting  $\text{Si}^{4+}$  in the T-sheets. Thus, the T-sheets of the TOT-layer are negatively charged. Different cations accumulate between the TOT layers, balancing the charge and holding the layers together by ionic bonds (Fig. 2.5). This sheet is called the interlayer sheet (I). Depending on the charge of the TOT layers, different types and amounts of cations (single atoms or small molecules) can be built into the phyllosilicate structure. The strength of the TOT layer binding is directly dependent on the ionic charge and radius of the interlayer cations.

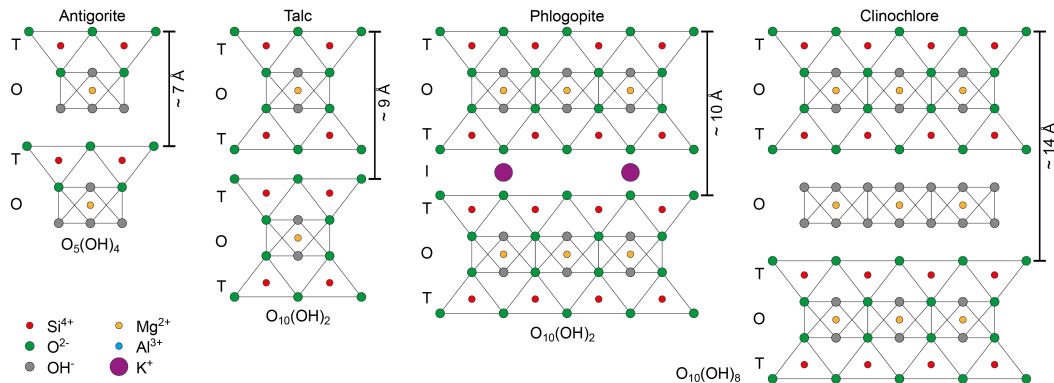


**Figure 2.5** – Schematic view of tri-octahedral phyllosilicates perpendicular to *c*-direction with typical layer distances: TO layers of antigorite (serpentine), TOT layers of uncharged talc, TOT-I layer of phlogopite (micas and clay minerals), and TOT'O layer of clinocllore (chlorite). Oxygens and hydroxides units per unit cell.

Phyllosilicates of the chlorite group are built by TOT unit structure, which are interconnected by an additional O-sheet (Fig. 2.5). This sheet can be described as brucite- or gibbsite-like sheets for tri- or di-octahedral layer types, respectively.

The unit cell of the different phyllosilicates depend mainly on the structure of the T-O units. The different unit structures have typical ranges of basal space (see Fig. 2.5) on which they can be identified by laboratory methods (e.g. XRD).

**LAYER CHARGE** The phyllosilicate groups (TO, TOT, TOT-I, TOT'O) are further sub-grouped, mainly by the layer charge and the amount and type of cations, balancing this charge. Especially the TOT phyllosilicates range largely in the layer charge. Therefore, a categorization is made on the charge per unit formula  $\xi$ . The main TOT layer sub-groups are, with increasing layer charge, the talc-pyrophyllite group with no layer charge, smectites, the vermiculite group, the interlayer deficient micas, the true micas, and the brittle micas

(Table 2.1).

**Table 2.1** – Division of phyllosilicates by layer type. Subdivision of TOT phyllosilicate based on layer charge  $\xi$ .

$\xi$	$d_{001}$	Subgroup	Tri-octahedral minerals	Di-octahedral minerals	Interlayer space
<b>T-O layer minerals</b>					
0.0	7 Å	Serpentine-kaolinite	antigorite, crysotile	kaolinite	–
<b>T-O-T layer minerals</b>					
0.0	9 Å	Talc-pyrophyllite	talc	pyrophyllite	–
0.2–0.6	10 Å	Smectites	saponite, hectorite	montmorillonite, beidellite, nontronite	Ca, Na, $\pm$ hydrated
0.6–0.9	10 Å	Vermiculite	vermiculite	vermiculite	Ca, Na, $\pm$ hydrated
0.6–0.75	10 Å	Interlayer deficient mica	–	illite, glauconite	K, not hydrated
0.9–1.0	10 Å	Micas	phlogopite, annite, celadonite (biotites)	muscovite, celadonite	K, Na, not hydrated
1.8–2.0	10 Å	Brittle mica	–	clintonite, margarite	Ca, not hydrated
<b>T-O-T O' layer minerals</b>					
variable	14 Å	Chlorites	clinochlore, chamosite	donbassite	gibbsite-, brucite-like

**SWELLABILITY** Phyllosilicates with a layer charge  $\xi$  between about 0.2 to 0.6 are able to incorporate small polar molecules (e.g. H<sub>2</sub>O) into their interlayer sheet. Thereby, this minerals enlarge their layer distances, the mineral swells. Typical swellable mineral are di- and tri-octahedral smectites and vermiculites (Meunier, 2005). Highly charged (micas, chlorites) and completely un-charged phyllosilicates (e.g. kaolinite, talc) cannot incorporate and exchange appreciable amounts of polar molecules.

**MIXED LAYER PHYLLOSILICATES** Often phyllosilicate layers are built by only one homogeneous TOT type. For example only illite TOT units are staged together, forming a pure illite crystal. But, different structure units can be alternating mixed, including different types of phyllosilicate groups (clay minerals, micas, chlorites). Mostly two, but also three and more different layer types can occur in one mineral. Thereby, the TOT units can repeat regularly or randomly. The randomly mixed-layer phyllosilicate often are a transition state between two pure different phyllosilicates. Changes in chemistry or temperature conditions may cause this transformation in the context of rock alteration (Meunier, 2005; Velde, 1995).

In regular mixed-layer phyllosilicates mostly two different layer types are inter-stratified, where a mixture of di- and tri-octahedral components are rare (Meunier, 2005). Regular mixed-layer minerals are able to built up stable phases, often related to hydrothermal alteration environments (Velde, 1995). Common mixed-layer phyllosilicates are e.g. illite-smectite and smectite-chlorite. Several of these phases are named as separate mineral phases. For example tosudite is a regularly mixed phyllosilicate of di-octahedral chlorite and smectite in the ratio 1 : 1, or hydrobiotite a regular 1 : 1 inter-stratification of vermiculite and biotite. A further mixed-layer phyllosilicate is corrensite, which is regularly built by tri-octahedral chlorite with either tri-octahedral vermiculite or tri-octahedral smectite (1 : 1 ratio).

*CHEMISTRY OF PHYLLOSILICATES*

Chemical composition and element substitutions of the phyllosilicates are mainly controlled by their structure. Occupation of the tetrahedra layer cation positions is mainly restricted to  $\text{Si}^{4+}$  and by  $\text{Al}^{3+}$  due to their ionic radii and coordination number. The octahedra positions can be occupied by a higher number of elements because of larger extend of these positions. Therefore,  $\text{Mg}^{2+}$ ,  $\text{Fe}^{2+}$ ,  $\text{Ni}^{2+}$ ,  $\text{Co}^{2+}$ ,  $\text{Zn}^{2+}$  and  $\text{Cu}^{2+}$  can substitute each other easily in tri-octahedral sheets, and  $\text{Al}^{3+}$  and  $\text{Fe}^{3+}$  in di-octahedral sheets (Meunier, 2005).

Different substitution types exist, especially in the octahedra sheets: (1) The homovalent substitution comprises the exchange of two cations with the same charge, e.g.  $\text{Fe}^{3+}$  for  $\text{Al}^{3+}$ , or  $\text{Fe}^{2+}$  for  $\text{Mg}^{2+}$ . (2) The heterovalent substitution comprises cations with different charge, e.g.  $\text{Fe}^{3+}$  for  $\text{Fe}^{2+}$ . (3) The di- to tri-octahedral transition substitutes a cation with a vacancy, e.g.  $\square$  for  $\text{Mg}^{2+}$ .

There is a much higher elemental variation in the interlayer sheet as in the T- and O-sheets. The high coordination number of this sites allows many, even large, cations to occupy these (e.g.  $\text{Sr}^{2+}$ ,  $\text{Ba}^{2+}$ ,  $\text{K}^+$ ,  $\text{Rb}^+$ , and  $\text{Cs}^+$ ). Furthermore, in swellable phyllosilicates hydrated interlayer sheets allow a relatively easy exchange of cations with ions in solution (Meunier, 2005).

*CONCLUSION*

The different types of phyllosilicate structures (TO, TOT, TOT-I, TOT'O), the various substitutions in all three layer units, as well as the mixing of different layers result in a high number of different phyllosilicates, which exhibit partly highly different properties.

Since the properties of clay minerals and chlorites vary tremendously from other silicates, alteration of lithologies where mainly tectosilicates are transformed to phyllosilicates the properties of the rock change to high extent.

*2.3.3 ZEOLITES*

Zeolites are known for a long time from amygdales and fissures, mostly in basic volcanic rocks. Nowadays, they are recognized as widespread and abundant authigenic silicate mineral in various sedimentary rocks as well as in low-grade metamorphic rocks (Deer et al., 2013; Hay & Sheppard, 2001).

Zeolites belong to the tectosilicates. They build up large frameworks with, partly, large cavities and channels within their crystallographic structure. The T : O-ratio is 1 : 2 according to the tectosilicate structure (Armbruster & Gunter, 2001; Gottardi & Galli, 1985). The center of the tetrahedra is mostly occupied by  $\text{Si}^{4+}$  and  $\text{Al}^{3+}$ , leading to a negatively charged aluminosilicate framework. Generally, the channels are filled with  $\text{H}_2\text{O}$  and large cations (mostly Na, Ca, and K), which balance the negative charge of the framework. The inter-framework  $\text{H}_2\text{O}$  and cations can be exchanged easily. This process is reversible and can take place already at low temperatures of  $<100^\circ\text{C}$  (Deer et al., 2013; Gottardi & Galli, 1985).

The zeolite structure resemble the structure of feldspars and feldspathoids. In feldspars the cations are strongly bounded to the oxygens of the aluminosilicate framework in

relatively small cavities, inter-framework channels are lacking (Fig. 2.6a). Therefore, ion exchange is only possible including the breaking of the framework bounds. Moreover, the exchange of Na or K by Ca has to involve a change in the Al : Si ratio of the framework. In contrast, the the Al : Si ratio of zeolites may remain fixed at cation exchange. Feldspathoid structure is more or less intermediate between feldspar and zeolite structures (e.g. nepheline, Fig. 2.6b). The aluminosilicate framework is more open and the inter-framework cations fill larger cavities, which could be connected channel-like (Deer et al., 2013). But, only the zeolite channels are large enough for water molecules entering the structure easily (e.g. garronite, Fig. 2.6c, and analcime, Fig. 2.6d). The extension of the cavities and channels in the different mineral groups result in discrete molar volume and density ranges: zeolites 2.0 to 2.3 g cm<sup>-3</sup>, feldspathoids 2.3 to 2.5 g cm<sup>-3</sup>, and feldspars 2.6 to 2.7 g cm<sup>-3</sup>.

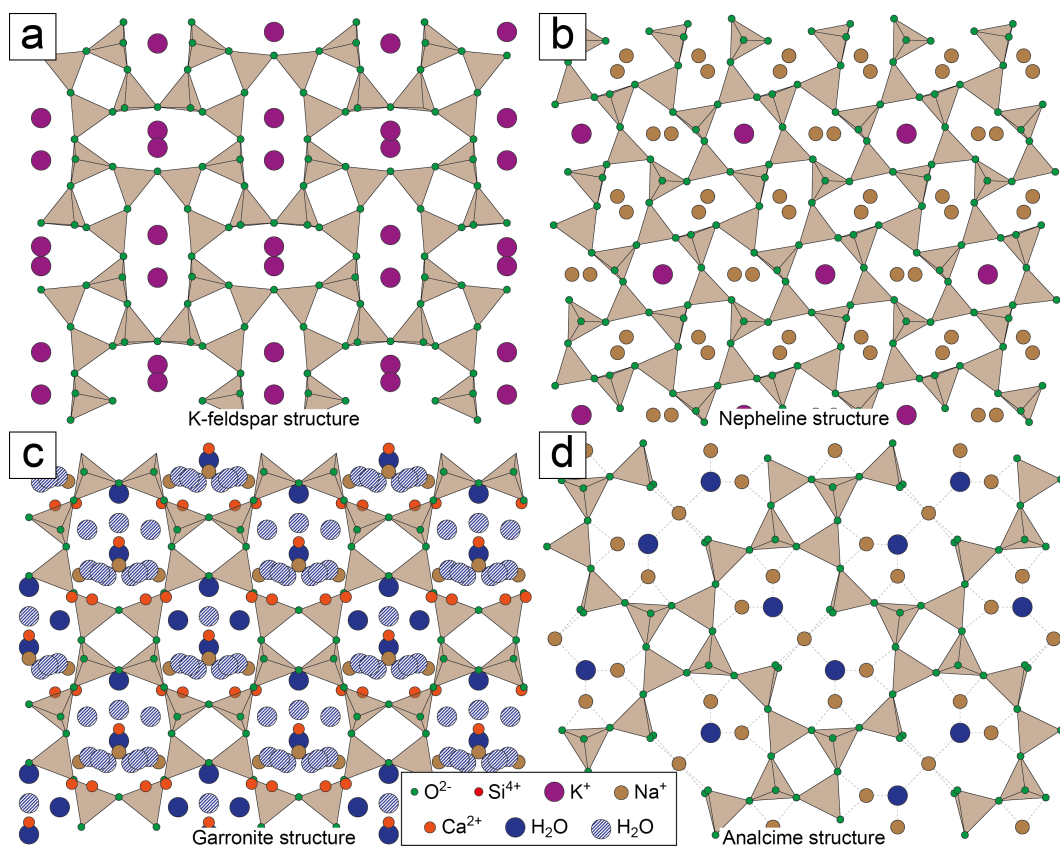


**Figure 2.6** – Schematic projection tectosilicate structures. (a) K-feldspar in *c* direction. (b) Nepheline in *c* direction. (c) Garronite structure in *a* direction. (d) Analcime structure. Figures adapted from Deer et al. (2013) and Deer et al. (2004).

### ZEOLITE STRUCTURE

**SECONDARY BUILDING UNITS** The secondary building units (SBU) are arrangements of 3 to 16 tetrahedra (the primary building unit, Fig. 2.3) to different units, e.g. single- or double-rings in various sizes. According to the *International Zeolite Association (IZA)* 23 SBUs exist (Baerlocher & McCusker, 2017). A selection of some SBUs is shown in figure 2.7. The type of SBUs in a zeolite framework have a direct influence on the topology of the zeolites and the physical and chemical properties (Deer et al., 2004). Every zeolite framework can be built by solely one SBU, but, a framework type often can be built by

different SBUs. For example the ANA framework can be built by the 6-2, 6, 4-[1,1], 1-4-1, or 4 SBUs (Fig. 2.7; Baerlocher & McCusker, 2017).

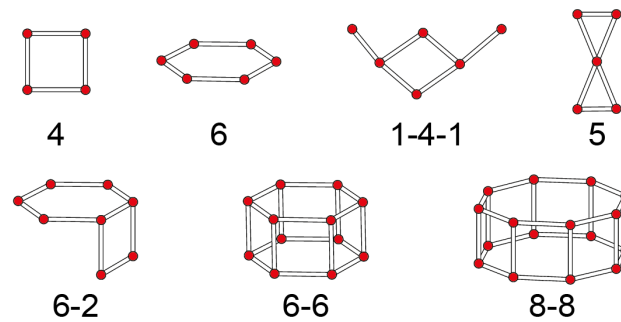


**Figure 2.7** – Selection of secondary building units (SBU). Red circles symbolize the T-site at tetrahedra centers. Adapted from Baerlocher & McCusker (2017).

**COMPOSITE BUILDING UNITS** The composite building units (CBU) are further structure units of zeolite frameworks. They are the basic unit which define the structure type (see next paragraph) of the zeolite frameworks by a periodic arrangement of them. Figure 2.8 shows some CBUs.

The ANA structure type can be built by the periodic arrangement of the *any* or the *kds* CBU (Fig. 2.8). In the *ana* CBU, on the top and the bottom of the building unit a 6-ring SBU can be recognized, respectively. Similarly, the *kds* CBU shows one 4 SBU at the top and the bottom, respectively. Another example is the GIS structure type. Here, the structure can be built by the periodic arrangement of the *gis* CBU. The same result will be a periodic arrangement of double crankshaft chain (dcc) CBU. The SBUs in the GIS framework could be 4, or 8, which can be recognized in the CBUs (Fig. 2.8).

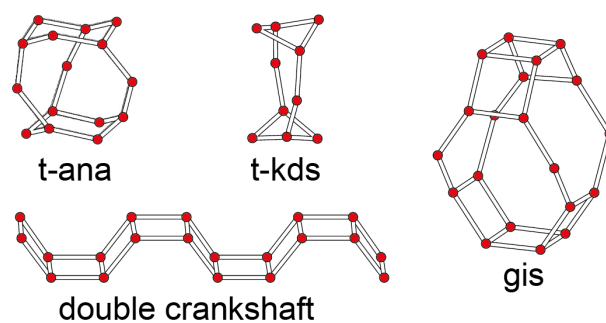


**Figure 2.8** – Selection of composite building units (CBU) for ANA and GIS structure types. Red circles symbolize the T-site at tetrahedra centers. Adapted from Baerlocher & McCusker (2017).

**STRUCTURE TYPES** Based on the CBUs zeolites are grouped to structure types, where several zeolites with the identical framework structure, differing only in the chemical composition and framework distortions, are combined. This classification lead to >230 different framework types (Baerlocher & McCusker, 2017), although many of them only occur as synthetic zeolites and only 41 are found in natural minerals (Deer et al., 2004). The structure types are labeled after a three letter code, which is based on one of the minerals (mostly the first discovered one; Armbruster & Gunter, 2001).

For example the framework structures of analcime, wairakite, leucite and pollucite are

identical. The structure code is ANA, named after analcime. The building units are four-membered tetrahedral rings, which are connected to form chains in three dimensions, resulting in strongly distorted eight-membered rings (Fig. 2.6d). There are six channel directions, parallel to  $\langle 110 \rangle$ . Therefore, the ANA structure type has a 3-D channel system.

Another example is the framework type GIS (Fig. 2.6c). This group, named after gismondine, further includes amicitite and garronite, among others. It is built by doubly connected four-membered rings forming crankshaft-like chains (similar to feldspars). The chains are connected building eight- and four-membered rings (Deer et al., 2013). Its channel system is three dimensional with a various width due to the flexible 8-ring system (Baerlocher & McCusker, 2017).

The structure of the zeolites lead to distinct properties of the actual zeolite phases, as ease of cation exchange, morphology of the crystals and hardness and fissility. For example fibrous zeolites: The single tetrahedron chains are connected parallel to each other and result in an elongated, fibrous crystal shape, which easily break on the cleavage planes (Armbruster & Gunter, 2001).

#### ZEOLITE CLASSIFICATION

Many zeolites share similar properties, mainly based on the framework structure. Therefore, different classification schemes have been evolved, considering structural data, density, crystal shape and symmetry, or the channel system.

**STRUCTURAL CLASSIFICATION** The most prevalent and current classifications of zeolites are based on the framework structure (Breck, 1974). The mostly used in the field of earth science consider mainly the secondary building units (SBU) and lead to six zeolite classes (Armbruster & Gunter, 2001; Baerlocher et al., 2007; Gottardi & Galli, 1985). In parentheses typical structure types are given.

1. Fibrous zeolites (NAT)
2. Zeolites with singly connected 4-ring chains (ANL, LAU)
3. Zeolites with doubly connected 4-ring chains (GIS, PHI)
4. Zeolites with 6-rings (single and double 6-rings; CHA)
5. Zeolites of the mordenite group (MOR, EPI)
6. Zeolites of the heulandite group (HEU, STI)

**DENSITY CLASSIFICATION** Also, a classification can be done based on the framework topology together with the framework density (Baerlocher et al., 2007; Meier et al., 1996). It divides zeolites by the number of T-atoms per  $1000 \text{ \AA}^3$ . Therefore, this classification also depends on the structure of the zeolites.

**SYMMETRY-BASED CLASSIFICATION** A first classification was made based on the symmetry of the zeolite phases. Three classes, fibrous zeolites (mainly pseudo tetragonal), (2) platy zeolites (pseudo-hexagonal), and (3) cubed zeolites (cubic and pseudo-cubic), exist.

**CHANNEL SYSTEM CLASSIFICATION** Another zeolite categorization can be made based on the type of channel system. One-dimensional channels are all in the same direction, which are not interconnected (e.g. LAU). Two-dimensional channel system connect each other in a platy system (e.g. STI, EPI, HEU). Three-dimensional channel systems (e.g. PHI, ANA, NAT) built up a network, interconnected in every direction.

### CHEMISTRY OF ZEOLITES

The general zeolite formula is  $M_xD_y[Al_{x+2y}Si_{n-(x+2y)}O_{2n}] \cdot mH_2O$ , where M stands for monovalent cations, D for divalent cations. The tetrahedra framework is represented by the part in squared brackets. It is negatively charged, where the degree of charge is directly coupled to the Si : Al ratio. The extra-framework space is filled by exchangeable cations, which balance the charge and water molecules, often coordinated to the extra-framework cations (Passaglia & Sheppard, 2001).

The variance of chemical compositions in zeolites is large. Mainly Ca, Mg, Ba, Na, K, and H are built into the zeolites, beside the framework elements O, Si, and Al. A minor role play Fe, Sr, Li, Be, Cs, Cu, and Pb. Generally, Si content has to be equal or larger than the Al content (*Loewenstein's rule*).

Two chemical properties are suitable for differentiation of zeolite phases: (1) The framework composition, and (2) the extra-framework content.

**FRAMEWORK COMPOSITION** The framework of zeolites is composed of nearly solely Si and Al. Therefore, the important (and single) chemical differences between zeolite frameworks is the ratio between the two components, expressed as Si/Al or  $R = Si/(Si + Al)$ . Since the *Loewenstein's rule* has to be complied the minimum value of  $R$  is 0.5. For example gismondine and thomsonite can have compositions reaching this low  $R$  value. Maximum values of  $R$  are <0.9. Heulandite and mordenite can reach high  $R$  values. The range of  $R$  ( $R_r$ ) can be very brought for some zeolite phases, e.g.  $R$  for chabazite is between 0.58 to 0.81 ( $R_r = 0.23$ ),  $R$  for phillipsite is between 0.57 to 0.77 ( $R_r = 0.20$ ) (Passaglia & Sheppard, 2001).

A classification based on  $R$  can be made. Here zeolites with an average  $R$  value <0.60 are grouped to Si-poor zeolites, 0.60 to 0.80 to zeolites with intermediate Si content, and >0.80 to Si-rich zeolites. The classification fits to the grouping by Coombs et al. (1959) based on field observations of mineral assemblages containing zeolite and silica phases. So, three groups can be arranged: (1) Zeolites which occur with opal, cristobalite or silica-rich glasses, and therefor are supersaturated with respect to quartz, (2) zeolites, which co-exist with quartz, and (3) zeolites, which are silica deficient with respect to quartz.

**EXTRA-FRAMEWORK CATIONS** The inter-framework cations locate in the voids of the framework and balance the negatively charged framework. Since the channels are open and wide, the cations can move and exchange easily within the zeolite lattice. Therefore, most zeolites integrate more than one cation as major constituent, and often solid solutions between single zeolite phases exists. For example heulandite has three different major cations: Ca, Na, and K, and additionally, Mg, Sr, and Ba are incorporated as minor constituents (Passaglia & Sheppard, 2001). Typical solid solutions are formed by the analcime–wairakite series.

**EXTRA-FRAMEWORK WATER** The content of extra-framework water is not a fixed characteristic of zeolites. Since the inter-framework space is connected to a channel network the amount of water can vary easily. The number of water molecules in the zeolite structure is related to both, chemical and structural properties. Tendentially, the amount of water is increasing with the extra-framework space, increasing  $R$ , and with an increasing

*D/M* ratio (Passaglia & Sheppard, 2001).

#### *OCCURRENCE AND STABILITY OF ZEOLITES*

Zeolites occur in different environments. Originally, they have been described in amygdules in basaltic lavas (Hay & Sheppard, 2001). But, also in fissures and fractures of granitic rocks zeolite assemblages are a common precipitation product from hydrothermal fluids, which heated up by circulation in basement rocks and are mineralized by the interaction with the rock material (e.g. Weisenberger & Bucher, 2010).

Additionally, zeolites have been recognized in various sedimentary rocks, where they may represent important rock-forming constituents. Hay & Sheppard (2001) list the occurrence of sedimentary zeolites into six environments: (1) saline, alkaline lakes, (2) soils, (3) deep-sea sediments, (4) low-temperature tephra systems, (5) burial diagenesis, and (6) hydrothermal alteration.

Various places with sandstones cemented by zeolites are reported. Examples are laumontite cement in the Pretty Hill sandstone formation of the Otway Basin, Australia (Higgs et al., 2015), wairakite cement in the Cerro Prieto geothermal system, Baja California, Mexico (Schiffman et al., 1985), authigenic heulandite cement in sandstone from Santa Cruz Country, California (Coombs et al., 1959), and analcime cementation in various sedimentary beds in Utah, Colorado, and Wyoming (Keller, 1952; Ross, 1941) and also in the Stuttgart Formation in Northeastern Germany (Förster et al., 2006).

Zeolite occurrences are often related to regions of high geothermal gradients and to hydrothermal activity as in New Zealand, The Geysers (California), the Yellowstone National Park, the Yugawara hot springs in Japan, and on Iceland (e.g. Coombs et al., 1959; Deer et al., 2013).

The stability field of zeolites fall directly in the *p*-*T* range of geothermal usage. In the URG elevated geothermal gradients in the range of 30 to 100 K km<sup>-1</sup> result in temperatures of up to ~250 °C in depth of >1000 m (see Fig. 2.1; e.g. Pribnow & Schellschmidt, 2000).

#### *FORMATION OF ZEOLITES*

Natural zeolites can be built from various precursor material as volcanic glass, aluminosilicate gels, and aluminosilicates including clay minerals, feldspathoids, feldspars, and other zeolites (Hay & Sheppard, 2001). Precipitation of zeolites is a rather fast process in comparison with the precipitation kinetics of other silicates. Therefore, zeolite assemblages may form meta-stably, even if they are not the thermodynamically most stable phase (Chipera & Apps, 2001). Low temperature conditions support non-equilibrium process and metastable phase precipitation (e.g. epistilbite, mordenite; Coombs et al., 1959).

**CHEMICAL REQUIREMENTS** For the formation of zeolites obviously all necessary chemical components have to be available. Accessibility to Al<sup>3+</sup> and SiO<sub>2(aq)</sub> in a hydrous environment are mandatory. High concentrations of (earth-)alkali elements are also a prerequisite. Low H<sup>+</sup> concentrations (high *pH*) further favor the formation of zeolites, but are not inevitably required. Rather a elevated (Na<sup>+</sup> + K<sup>+</sup> + Ca<sup>2+</sup>)/H<sup>+</sup> ratio is important for the formation of zeolites (Chipera & Apps, 2001; Hay & Sheppard, 2001). Albeit, elevated *pH*

support the formation of zeolites, since the solubilities of Si and Al species are higher in such an environment, making these elements accessible for the formation of zeolites.

Consequently, beside the p-T-conditions and the Si : Al ratio, the availability of extra-framework cations determines the type of zeolite forms, i.e. without any Na<sup>+</sup> in the system no analcime will be formed, even if all other prerequisites are fulfilled.

**TEMPERATURE** The stability of zeolite phases also dependent on temperature. Tendentially, more hydrous zeolites are stable at lower temperatures (e.g. chabazite, clinoptilolite, and stilbite), less hydrous zeolites at higher temperatures (e.g. analcime, laumontite, wairakite; Chipera & Apps, 2001; Hay & Sheppard, 2001). Nevertheless, temperature ranges are rather large for the stability of single zeolites. The occurrence of a zeolite phases often is more sensitive to the chemical components of the precursor mineral and the fluid composition (Hay & Sheppard, 2001).

**PRESSURE** Pressure plays a minor role for the stability of zeolites. Similar zeolite assemblages are found in surface-near geothermal area and in deep burial metamorphic settings (Chipera & Apps, 2001). Tendentially, zeolites with a lower H<sub>2</sub>O content and thus, a lower specific gravity are stable at higher pressure (Hay & Sheppard, 2001).

Consequently, p-T conditions for the formation of zeolites has to be fulfilled. But, fluid composition seems to be the crucial parameter for the type of zeolite formed, at same temperature and precursor composition (Chipera & Apps, 2001).

#### CONCLUSION

Zeolites are more wide-spread as they initially have been described and classified. Their structure vary fundamentally from other silicates and, therefore, show exceptional properties compared to other (silicate) minerals. They display a wide chemical variance. Their occurrence and stability field in typical geothermal environments make zeolites to alteration products, which should paid attention to in the circuits of geothermal installations.

---

---

## FUNDAMENTALS IN GEOCHEMISTRY

---

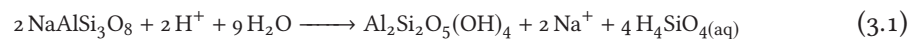
### 3.1 REACTION MECHANISMS

The infiltration of a fluid, change in temperature and/or pressure cause a geochemical disequilibrium between the mineral or mineral assemblage and the fluid. Fluid–mineral and mineral–mineral reactions occur to re-equilibrate the system to the new conditions. A dissolution process results, which provides ions to the fluid. The fluid may become super-saturated with respect to any mineral phases (Putnis, 2009).

#### 3.1.1 DISSOLUTION-PRECIPIATION REACTIONS

Alteration processes involve the replacement of a mineral assemblage by another one, stable at changed conditions. Putnis (2002) and Putnis (2009) showed, that the replacement of mineral phases by another one is rather a coupled dissolution-precipitation process than a diffusion or cation exchange reaction. The disequilibrium of the fluid to a mineral (assemblage) generally initiates a dissolution process. The accompanied release of ions to the fluid, may result in the super-saturation with respect to another phase, which therefore will tend to precipitate.

Consequently, the transformation of a mineral phase to another one, e.g. albite to kaolinite



can be split into two steps, the dissolution of albite



and the precipitation of kaolinite



Therefore, the solubilities of the phases in the coexisting fluid determine the reactions, which are dependent on the composition of the fluid as well as temperature and pressure (Putnis, 2002).

The replacement reaction commonly accompany with the formation of porosity in the product phase, which is mostly higher as molar volume changes can explain (Putnis, 2002). Hence, ions are released to the fluid during the replacement reactions.

---

Porosity in the precipitated mineral can be formed by different solubilities of the parent and the daughter minerals (higher solubility of the parent), and/or by different molar volumes of the mineral phases. The porosity in the product phase results in a maintaining of the reaction since fluid can reach the reaction interface and allows the transport of components. If no porosity is produced by the dissolution-precipitation process the reaction leads to a dense layer of the product phases, which covers the parent crystal and hampers its dissolution (Putnis, 2002).

The precipitation step (Eq. 3.3) begins, when the critical concentrations of ions for nucleation is reached. Between the single steps, fluid may be transported within the rock/fracture, and the precipitation of material is located in distance to the location of dissolution. Consequently, dissolution-precipitation process may occur at very small scale, or if transport of material in the fluid takes place, on larger scale, comprising other volumes of rock.

**CATION EXCHANGE** The term cation exchange is referred to a transformation of minerals, where some constituents are exchanged by others, but the main crystal structure remains preserved (Putnis, 2002). Typical cation exchange reactions are the albitization of K-feldspar and the transformation of leucite to analcime. However, oxygen isotope studies have shown, that the cation exchange is mostly accompanied with a small scale re-crystallization process of the aluminosilicate framework (e.g. O'Neil & Taylor, 1967; Putnis, 2002).

**LEACHING** Leaching of a mineral is the removal of several ions from the mineral phase, but, unlike cation exchange, with a modification of the crystal stoichiometry (Putnis, 2002).

**PSEUDOMORPHISM** By a pseudomorphic reaction a phase is transformed to another, preserving the shape of the parent crystal. Therefore, volume of the crystal remains constant. Consequently, the transformation reaction has to be iso-volumetric and chemical components exchange with the surrounding. The dissolution rate of the parent mineral has to be equal to the precipitation rate of the daughter crystal (Putnis, 2002). In this type of transformation reaction the crystallographic information are transferred from the reactant to the product crystal (Putnis & Austrheim, 2010).

### 3.1.2 REACTION INDUCED FRACTURING

Hydration reactions generally tend to increase the solid volume (e.g. Putnis & Austrheim, 2010). Alteration reaction can be preservative to different chemical elements, e.g. Si or Al, keeping these elements in the solid state. Additionally, volume balanced reactions may occur, where typically higher amounts of elements are released to and consumed from the fluid, but the molar volume of solid reactants and products is equal (Putnis & Austrheim, 2010). Consequently, the fluid properties and composition determines, if a iso-volumetric reaction is able to take place.

Common replacement reactions with an increase of solid volume are leucite to analcime, anhydrite to gypsum, olivine to serpentinite, and aragonite to calcite (Jamtveit et al., 2009; Shervais et al., 2005). An increase of >30 % can easily be reached by many of these reactions.

**ROCK FRACTURING** Mineral reactions with an increase of solid volume are able to generate stress to the rock fabric. Thereby, hydration reactions can produce stresses up to

300 MPa (Jamtveit et al., 2009; Røyne & Jamtveit, 2015). If the reaction exceeds the rock strength, it causes a fracturing of the mineral and rock fabric and produce pathways for fluid infiltration (Jamtveit et al., 2011; Putnis, 2009).

Reaction induced fracturing is a important process in alteration and weathering processes, where chemical hydration interacts directly with mechanical processes (Putnis, 2009). Fracturing produces pathways for further fluid infiltration into the rock material, enhancing the alteration process.

**CLOGGING OF OPEN SPACE** Porosity and fluid pathways may be reduced by alteration reactions. Obviously, precipitation of new minerals (e.g. quartz, calcite) reduce the open space for fluid flow. But besides, the expansion and transformation of mineral phases to highly hydrated phases may reduce pores and fissures. At combined reactions of volume increasing and volume decreasing reactions, the different reaction rates determine if a gain or loss of open space results in total (Røyne & Jamtveit, 2015).

**POROSITY GAIN** On the other hand, reactions with a decrease of solid volume, often produce highly porous minerals, which also have the potential for a higher permeability for fluids. Thus, also by this type of reactions the fluid flow and alteration processes can be enhanced.

## 3.2 FUNDAMENTALS OF AQUEOUS GEOCHEMISTRY

Water is omnipresent on the surface and the crust of the Earth. It plays an important role in geochemical-mineralogical reactions. Especially, alteration reactions occur in the presence of aqueous fluids. Fundamentals for alteration reactions include the most important properties of water, the equilibrium reaction mechanisms, and basics of thermodynamics.

### 3.2.1 WATER

Water has several functions in alteration reactions (see Sec. 2.1.5). It is transport medium for dissolved solids and energy, and furthermore, a reactant for many hydration reactions. Therefore, the properties of water play a major role for the interaction of any mineral phase with an aqueous fluid.

**POLARITY** The chemical composition of water is  $\text{H}_2\text{O}$ . The structure ( $104.48^\circ$  angle between the  $\text{H}-\text{O}-\text{H}$  bonds) and the different electronegativity of H and O are responsible for the di-polarity of water molecules. The O has a negative partial charge, the H atoms a partial positive charge. The water dipoles are attracted by weak hydrogen bondings, which are responsible for many properties of water (e.g. high heat capacity, negative thermal expansion, surface tension, low thermal conductivity; Faure, 1998).

Water molecules are attracted to charged mineral surfaces (e.g. clay minerals, quartz, calcite), which change the physical and chemical properties of the minerals (Velde, 1995). The attraction of water weakens ionic bonds in minerals (e.g.  $\text{Ca}^{2+}-\text{CO}_3^{2-}$  bonds in calcite; Faure, 1998). Thus, the aqueous fluid act as catalyst for mineral reactions (Putnis, 2002; Putnis, 2009).

Additionally, the formation of complexes of the bipolar water molecules with dissolved ions reduces the effective concentration (activity) of these species. Consequently, the

solubility of phases, which are in equilibrium with the species is increased (Merkel & Planer-Friedrich, 2008).

**HEAT CAPACITY** Water has a high heat capacity of  $4.2 \text{ kJ kg}^{-1} \text{ K}^{-1}$  (under standard conditions), which is a result of the dipole properties of the water molecules. Hence, circulating aqueous fluids are able to transport high amounts of heat energy, inducing hydrothermal alteration reactions (see Sec. 2.1.5) and high temperature gradients in convective geothermal systems.

### 3.2.2 GEOCHEMICAL REACTIONS IN AQUEOUS SOLUTIONS

Geochemical reactions mostly take place in the presence of water, which act as medium in which ions and molecule are able to interact with each other and with mineral phases. In aqueous solutions equilibrium reactions prevail, where mostly forward and backward reactions are possible. Equilibrium of a system depends on external factors as pressure, temperature, and volume. It is independent on the initial state and the history of the system (Ganguly, 2008; Misra, 2012).

#### LAW OF MASS ACTION

In a reversible chemical reaction the substances A and B react to the substances C and D.



where  $a$ ,  $b$ ,  $c$ , and  $d$  are the stoichiometric coefficients, which balance the reaction.

For the forward and reverse reactions of reaction 3.4 a reaction rate  $R$ , proportional to the concentrations  $[A]$ ,  $[B]$ ,  $[C]$ , and  $[D]$ , is given by

$$R_{\text{forward}} = k_{\text{forward}}[A]^a[B]^b \quad (3.5)$$

$$R_{\text{reverse}} = k_{\text{reverse}}[C]^c[D]^d \quad (3.6)$$

where  $k_{\text{forward}}$  and  $k_{\text{reverse}}$  are the rate constants for the reactions, respectively.

In the progress of the forward reactions starting with a mixture of only A and B,  $[A]$  and  $[B]$  is decreasing, whereas  $[C]$  and  $[D]$  is increasing. Consequently,  $R_{\text{forward}}$  decreases and  $R_{\text{reverse}}$  increases until  $R_{\text{forward}} = R_{\text{reverse}}$ . Then the chemical equilibrium of reaction 3.4 is reached.

Therefore, the reaction 3.4 is in chemical equilibrium, when the reaction rate of the forward reaction is equal to the rate of the backward reaction:

$$k_{\text{forward}}[A]^a[B]^b = k_{\text{reverse}}[C]^c[D]^d \quad (3.7)$$

which can be rearranged to the *law of mass action*

$$\frac{k_{\text{forward}}}{k_{\text{reverse}}} = \frac{[C]^c \cdot [D]^d}{[A]^a \cdot [B]^b} = K \quad (3.8)$$

where  $K$  is the equilibrium constant (solubility product). In real chemical mixtures the

concentrations of the substances have to be replaced by their activities (see below):

$$\frac{k_{\text{forward}}}{k_{\text{reverse}}} = \frac{a_C^c \cdot a_D^d}{a_A^a \cdot a_B^b} = K \quad (3.9)$$

$K$  is the theoretical value for reaction 3.4, when the forward and backward reactions are of the same intensity. Since chemical reaction rates depend on temperature and pressure, the equilibrium constants are only valid for specific conditions. If not given, they refer to the standard conditions at 298.15 K and  $1 \cdot 10^5$  bar.

**LE CHATELIER'S PRINCIPLE** A reaction (e.g. reaction 3.4) is in chemical equilibrium, when the rates of forward and backward reactions are equal. If this equilibrium is disturbed, e.g. by adding substance  $C$ , the system will re-equilibrate by, in this case, favoring the reverse reaction, resulting from the *law of mass action* (Eq. 3.9). This principle can also be applied on changes in temperature and pressure. Therefore, an increase in temperature would favor the reaction in the endothermic direction, whereas a decrease in temperature in the exothermic direction. Pressure affects the equilibrium reaction accordingly to changes in the volume.

#### GIBBS FREE ENERGY

The Gibbs free energy  $G$  is a measure for the probability of the proceeding of a reaction. It is composed by the enthalpy  $H$  and the entropy  $S$ :

$$G = H - T \cdot S \quad (3.10)$$

where enthalpy  $H$  is in J, temperature  $T$  is in K, and entropy  $S$  in  $\text{JK}^{-1}$ . The enthalpy  $H$  is the thermodynamic potential given by the internal energy  $U$ , the pressure  $p$ , and the volume  $V$  ( $H = U + pV$ ). The entropy  $S$  is a measure of the disorder and the irreversibility of a system.

The change of Gibbs free energy of a reaction is

$$\Delta G_r^0 = \Delta H_r^0 - T \cdot \Delta S_r^0 \quad (3.11)$$

for the standard state. It is composed by the Gibbs energy of formation  $G_f^0$  of the reactants and products by

$$\Delta G_r^0 = \sum \Delta G_{f,products}^0 - \sum \Delta G_{f,reactants}^0 \quad (3.12)$$

and can be calculated if  $G_f^0$  of the single phases are known. If  $\Delta G_r$  is negative the reaction proceeds spontaneously with the release of energy in the forward direction. If  $\Delta G_r$  is positive, additional energy is necessary for the reaction in forward direction, resp. the reaction runs in reverse direction spontaneously. Thus,  $\Delta G_r$  is a measure of the driving force of a reaction.

The change of the Gibbs free energy  $\Delta G_r$  of a chemical reaction (e.g. Eq. 3.4) is related to the change of energy of the activities of all reactants and products at standard state. Hence,

the Gibbs free energy can be combined with the law of mass action (Eq. 3.8) as

$$\Delta_r G = \Delta_r G^0 + RT \ln \frac{a_C^c \cdot a_D^d}{a_A^a \cdot a_B^b} \quad (3.13)$$

where  $R$  is the gas constant ( $8.314 \text{ J mol}^{-1} \text{ K}^{-1}$ ). At chemical equilibrium  $\Delta_r G$  is equal to 0 and therefore

$$\Delta_r G^0 = -RT \ln K \quad (3.14)$$

With these equations the equilibrium constant  $K$  of reactions can be calculated if the  $G_f^0$  of the reacting phases are known. Furthermore, equilibrium states for mineral assemblages are computable, which allows the construction of activity diagrams as a function of temperature, pressure and species activity. Hence, appropriate activity models are needed for a qualified calculation (see below).

#### SATURATION INDEX

The ion activity product  $IAP$  is the actual state of the reaction, also referred to reaction quotient. Assuming following dissolution reaction:



By measuring the concentrations (activities) of the involved species ( $A, B$ ) in solution the state/potential of the reaction can be calculated by

$$IAP = \frac{a_{A_a B_b}}{a_A^a \cdot a_B^b} \quad (3.16)$$

The comparison of the  $IAP$  for the reaction 3.15 with its equilibrium constant  $K$  gives information if the reaction is in equilibrium resp. saturated with respect to a phase ( $A_a B_b$ ). Therefore, the solution is saturated with respect to a phase if

$$\frac{IAP}{K} = 1 \quad (3.17)$$

and under-saturated if  $< 1$  or super-saturated if  $> 1$ .

Furthermore, the saturation state often is given by the *saturation index*  $SI$

$$SI = \log \left( \frac{IAP}{K} \right) \quad (3.18)$$

where  $SI < 0$  means unter-saturation,  $SI = 0$  saturation, and  $SI > 0$  super-saturation with respect to a phase ( $A_a B_b$ ).

#### ACTIVITY

In real mixtures interactions between the charged ions and molecules result in a deviation from the ideal behavior of the components and the thermodynamic quantities volume, internal energy, and enthalpy cannot be calculated by simple addition of the weighted mole fraction. The deviation generally increases with increasing concentrations and charge of the ions. Additionally, the activity of one species depend on temperature, pressure, and the

chemical composition of the whole system.

Therefore, instead of the concentration  $c$  the activity  $a$  is used, which considers the deviation from ideal behavior by the activity coefficient  $\gamma$ :

$$a = \gamma \cdot c \quad (3.19)$$

Thereby, the activity coefficient  $\gamma$  is 1 for ideal behavior, i.e. infinite dilution, and deviates at higher concentrations.

There are several conventions and approximations for the activity  $a_i$ :

- ◇ The activity of gaseous species  $i$  is approximately the partial pressure in a gaseous mixture:  $a_i = P_i$ .
- ◇ In a very dilute solution the activity of a specie  $i$  is approximately equal to molality of that specie:  $a_i = m_i$ , or the mole fraction of  $i$ . This results in the approximation of  $a_i = 1$  for a pure liquid.
- ◇ For pure solids the activity is equal to its mole fraction. So, for pure solids  $a_i = 1$ .

**ACTIVITY COEFFICIENTS** Several equations for calculating the activity coefficient  $\gamma$  have been established for different ionic strengths  $I$  (see below), temperature ranges, and background electrolytes.

One of the easiest activity models is the *Debye-Hückel* equation, which gives good results for  $I < 5 \cdot 10^{-3}$  (Faure, 1998):

$$\log \gamma_i = -Az_i^2\sqrt{I} \quad (3.20)$$

and an extended version for  $I < 0.1$ :

$$\log \gamma_i = -\frac{Az_i^2\sqrt{I}}{1 + Ba_i\sqrt{I}} \quad (3.21)$$

with  $A = 0.5085$  and  $B = 0.3281 \cdot 10^{10} \text{ m}^{-1}$  both at 25 °C ( $A$  and  $B$  are temperature dependent) and the ion-size parameter  $a_i$ . Both *Debye-Hückel* equations are valid for a wide range of temperatures (Appelo & Postma, 2005).

A further modification of the Debye-Hückel equation is the *B-dot equation* (Helgeson et al., 1969) for Na-Cl solutions up to 3 mol kg<sup>-1</sup> (Bethke & Yeakel, 2015) (but not accurate >0.5 mol kg<sup>-1</sup>).

$$\log \gamma_i = -\frac{Az_i^2\sqrt{I}}{1 + Ba_i\sqrt{I}} + \mathring{B}_i \cdot I \quad (3.22)$$

where  $a_i$  and  $b_i$  are ion-specific fit parameters and  $\mathring{B}_i$  is another temperature fitting parameter. It is used in several chemical modeling codes as *PhreeqC* (Ilnl database; Appelo & Postma, 2005; Parkhurst, 1990) and *The Geochemist's Workbench* *GWB* (Bethke & Yeakel, 2015).

Another approach are viral methods, where the specific properties of the ions, including the solvent, are considered, e.g. concentration, ion size, and affinity to interact (Bethke & Yeakel, 2015). These methods are suitable for high ionic strength, but restricted to relatively small temperature ranges and limited by the extend of the thermodynamic databases. One examples is the *Harvie-Möller-Weare* (HWM) formulation.

*IONIC STRENGTH*

The interaction of ions, anions and cations, results in a different behavior of dissolved species in the aqueous fluid. Thereby, the interaction is generally increasing with increasing concentrations and charge of the dissolved ions and can be estimated by the *ionic strength*  $I$

$$I = 0.5 \sum m_i z_i^2 \quad (3.23)$$

where  $m_i$  is the molar concentration and  $z_i$  the charge of a species  $i$ . The ionic strength is used for calculating the activity coefficients in real mixture (see above).

## 3.2.3 pH VALUE

The *pH* is defined as the negative base 10 logarithm of the  $H^+$  activity in a solution.

$$pH = -\log_{10}(a_{H^+}) \quad (3.24)$$

It is a measurement of the acidity of an aqueous solution and, therefore, one of the most important characteristic of a fluid (Faure, 1998).

Many fluid-mineral reactions are highly dependent on the *pH* value of the fluid phase. Many hydration reactions consume  $H^+$  from the fluid and are effected by its activity (see Sec. 2.2). Reversely, the mineral-fluid reactions modify the *pH* of the fluid, and partly may act as buffer in the system (e.g. calcite, or quartz (Eq. 2.10)).

Solubility of many species are highly sensitive to the *pH* value, namely Si has high solubilities at high *pH*s, whereas solubilities are low at intermediate and low *pH*. Another example is Al, which is soluble in appreciable amount at high and low *pH*, and poorly soluble at intermediate *pH*. Both elements are extremely important for fluid-mineral reactions. The solubilities of the species determine if some reactions are either iso-chemical or iso-volumetric, which may have a high impact on the alteration progress and the rock properties (see Sec. 3.1.2).

The *pH* value of pure water is 7 at 25 °C, given by the auto-dissociation of the water molecules to  $H^+$  and  $OH^-$  with  $K = 1 \cdot 10^{-14}$  at 25 °C.



It is the neutral value where the concentrations of  $H^+$  and  $OH^-$  are equal. At higher temperatures the neutral *pH* shifts to lower *pH*.

## 3.3 EXPERIMENTAL STUDIES

The complexity of geochemical-mineralogical reactions in natural systems is extremely high. Solid rock material varies highly in its mineral content and their modal ratios. Therefore, chemical and physical properties vary to high degree, sometimes direction-dependent for one single mineral phase. Rock type and its genesis (plutonic, volcanic, sedimentary, metamorphic) also influence the properties of the rock material, even if mineral phases and chemical composition might be the same, e.g. properties as grain size, pore space/density,

layering are different. Additionally, properties of one single mineral vary, partly to high extent, where solid-solutions, elemental substitutions, polymorphism, and transitional compositions occur.

The changes in multi-component mineral assemblages in coexistence with a (highly saline) fluid with various constituents at high temperature (and pressure) additionally contain lots of parameters and uncertainties. Furthermore, considering time, the kinetic of geochemical reactions may play an important role and modify the obtained mineral assemblage. Meta-stable phases (with a high reaction rate) further diverse possible mineral assemblages.

Geochemical modeling can give good results in relatively simple systems. It is able to calculate the fluid composition and species distribution, the saturation state of minerals in contact with the fluid as well as phase diagrams as a function of temperature, pressure, and composition. The results are in agreement with observations and measurements where the system contain few components, the interaction of the involved species is low, and the thermodynamic data for all components and phases are available.

The main limiting factors for the geochemical modeling in aqueous systems is the extent and quality of the thermodynamic databases. The available data basis of the thermodynamic databases is limited. Often data were estimated or extrapolated from correlated phases, if no real measurements have been available (Oelkers et al., 2009). Especially, thermodynamic data for many hydrous mineral phases as clay minerals and zeolites are still incomplete and improper (Velde, 1995). Furthermore, the internal consistency is not given for many databases, concerning the quality of the data (Oelkers et al., 2009).

Besides, the correct calculation of the activity coefficient (see Sec. 3.2.2) is limited for hydrothermal environments with highly saline brines, since all activity models are restricted either to low temperatures, or low salinities, or the necessary data for multi-component systems are incomplete.

Experimental studies approximate natural systems to relatively high degree, especially as numerical simulations remain relatively far from observations in natural systems, particularly if the number of mineral phases is high, and its composition differs from end-member composition. Elevated temperatures and highly saline brines hamper the uncertainties of numerical results of alteration processes additionally.

---

---

## EXPERIMENTAL INTERACTION OF HYDROTHERMAL Na-CL SOLUTION WITH FRACTURE SURFACES OF GEOTHERMAL RESERVOIR SANDSTONE OF THE UPPER RHINE GRABEN

---

This chapter is published as: Schmidt, R. B., Bucher, K., Drüppel, K. & Stober, I. (2017b): Experimental interaction of hydrothermal Na-Cl solution with fracture surfaces of geothermal reservoir sandstone of the Upper Rhine Graben. – in: *Applied Geochemistry* 81, pp. 36–52. – DOI: [10.1016/j.apgeochem.2017.03.010](https://doi.org/10.1016/j.apgeochem.2017.03.010).

### ABSTRACT

The Upper Rhine Graben (URG) is a Tertiary rift structure in central Europe offering favorable conditions for geothermal energy utilization. Relatively high heat flow combines with sufficiently high permeability of the hydrothermal reservoirs. One of the target stratigraphic levels is the lower Triassic sandstone formation (Buntsandstein), where hot water resources at temperatures up to 250 °C can be utilized. Extensional neotectonics and hydraulic stimulation form new fracture surfaces in the reservoir rocks (enhanced geothermal system, EGS). The exposed fresh rock fracture surface reacts with the highly saline reservoir brines (Na-Cl up to 200 g l<sup>-1</sup>) with consequences for the permeability of the reservoir.

In order to better understand the dynamic evolution of fault systems caused by fluid-rock interaction, we conducted batch-type experiments in a stirred autoclave system and reacted arkosic sandstone with synthetic 2 molal Na-Cl solution at temperatures of 200 °C and 260 °C. After 45 to 55 days reaction time altered rock samples were compared with the starting material and the geochemical-mineralogical processes were deduced with the help of XRD, SEM methods and EMP measurements. Fluid compositions were examined by ICP-MS, ICP-OES and IC.

The arkosic sandstones show a surprisingly high reactivity during the experiments. Quartz grain surfaces show deep dissolution features and all reaction fluids were saturated with respects to quartz. Illite and kaolinite from the primary sandstone cementation completely dissolved from the sample surface. Perfectly euhedral crystals of metastable analcime formed during the experiment as separate crystals on quartz, as groups or clusters and as surface covering mats. The overall net transfer process dissolves quartz + illite + kaolinite ± K-feldspar and precipitates analcime + chlorite ± albite. The process is accom-

---

panied by a total volume increase of the solids of 20–30 vol.%. K-feldspar dissolution is hampered by albitization rims shielding K-feldspar and efficiently preventing an equilibration of the Na–K exchange with the fluid. The experiments show changes on the rock surface, leading to an increase of the aperture of a single fracture during the early phases of reaction and later to a decrease as the fluid-rock reaction progresses. Alteration of the fracture surface also generates loose fragments and altered minerals. This fine material may efficiently reduce the fracture aperture at narrow points along the fracture.

#### 4.1 INTRODUCTION

The economic success of utilizing deep geothermal energy at a specific site depends on a maintainable high temperature of the heat transfer fluid and on a high permeability of the particular reservoir rock at target depth. Low enthalpy geothermal reservoirs reside typically at several km depth, e.g. Soultz-Sous-Forêts at 5 km depth and 200 °C (Genter et al., 2010; Gérard et al., 2006). The permeability of continental crust at several km depth is related to fractures and faults providing pathways for fluid migration (Bucher & Stober, 2010; Stober & Bucher, 2005), which are generally filled with saline fluid (Gascoyne et al., 1987; Hanor, 1994; Pauwels et al., 1993; Stober & Bucher, 2014).

Permeability of crustal rocks at reservoir depth is a dynamic property of the system (see several contributions in Gleeson & Ingebritsen, 2016). Permeability changes as a result of continuous mechanical deformation and ongoing chemical interaction between the fractured rocks and the fluid residing in the fracture porosity. This paper reports on the experimental geochemical alteration of fracture surfaces in sandstones resulting from fluid-rock interaction at reservoir temperatures (200 °C and 260 °C).

The Upper Rhine Graben (URG) in Central Europe, is an Oligocene rift structure (Behrmann et al., 2003; Illies, 1972; Illies & Greiner, 1978; Schwarz & Henk, 2005) offering favorable conditions for utilization of geothermal energy. Fluid temperatures are up to 250 °C at 4 km depth in the Permian and Triassic metasediments of the graben center (Dezayes et al., 2008; Sanjuan et al., 2016). Geothermal installation in these strata are e.g. Bruchsal, where in a depth of 1800–2500 m a fluid temperature of 128 °C is produced (Pauwels et al., 1993). Also at Rittershoffen two wells have been drilled to 2600 m and 3200 m in these sandstone reservoirs, where the saline fluid has a temperature of 170 °C (Baujard et al., 2017).

The URG fluids are Na-Cl dominated brines with a total of dissolved solids (TDS) up to 200 g l<sup>-1</sup> (Aquilina et al., 1997; Komninou & Yardley, 1997; Pauwels et al., 1993; Sanjuan et al., 2016; Stober & Bucher, 2014). Fracture surfaces created by neo-tectonics in the stressed graben or as a consequence of hydraulic stimulation of geothermal reservoirs (enhanced geothermal systems, EGS) result in an exposition of fresh sandstone mineral assemblages to the 200 ± 50 °C hot brine. Due to the disturbance of the equilibrated system in the reservoir formation, a reaction of the sandstone with the brine is highly presumable.

The geochemical-mineralogical dynamics in geological reservoirs have a major influence on the permeability and the lifetime of a geothermal system (Bertrand et al., 1994; Milodowski et al., 1989; Morrow et al., 2001). Dissolution of primary minerals increases frac-

ture apertures, whereas precipitation of secondary minerals from the brine seals fractures and joints reducing fluid flow permeability.

Fluid-rock interaction experiments at hydrothermal conditions mostly used powder or granulated samples as starting material (Savage et al., 1992; Shao et al., 2011; Xie & Walther, 1993) and typically with a reaction fluid of low salinity (Bertrand et al., 1994; Kuncoro et al., 2010; Moore et al., 1983; Vaughan et al., 1986). Recently several experimental fluid-rock interaction studies using high saline solutions were conducted in the context of the geological storage of CO<sub>2</sub> (Fischer et al., 2010; Fischer et al., 2011; Hu et al., 2011; Kaszuba et al., 2005; Lafay et al., 2014; Shao et al., 2011; Shiraki & Dunn, 2000). Experimental studies of fluid-rock interaction have been conducted on basement rocks and minerals (Hövelmann et al., 2010), sedimentary rocks (Bertrand et al., 1994; James et al., 2003) and specifically of rocks from the URG (Pauwels et al., 1992). In these studies, typically various clay minerals including illite and chlorite from hydrothermal alteration of basement rocks were produced.

In this paper we present an experimental study on the consequences of reaction of URG reservoir sandstone surfaces (rock surfaces) with a synthetic geothermal fluid with a salinity typical of URG reservoir fluids. We investigated rock samples from the Buntsandstein before and after these experiments. The analytical data permit an evaluation of reaction paths controlling the alteration of primary mineral assemblages at temperatures that are relevant for geothermal applications (200–260 °C).

The study focuses on the geochemical, mineralogical and textural changes of water-conducting joints and fractures (represented by fresh sample surfaces) from a fresh to an intensely altered sandstone surface, due to the reaction with highly saline solution. Additionally, consequences concerning the evolution of the reservoir permeability are deduced.

## 4.2 MATERIAL AND METHODS

### 4.2.1 ROCK MATERIAL

Two different sandstones have been used as representative reservoir rocks in the hydrothermal experiments: Pfinztal Sandstone (PfSst) and Tennenbach Sandstone (TenSst) as proxies for the lower Triassic Buntsandstein formation in the Upper Rhine Graben (URG). Both samples have been collected in local quarries, close to the URG, as blocks of about 30 × 30 × 40 cm<sup>3</sup>. In the laboratory cores of ~22 mm were drilled from the sandstone blocks. They were broken perpendicular to the core axis to get a fresh rock surface. Then, the core pieces were shortened to a height of 5–20 mm. Afterward, the samples were washed properly with deionized water and dried before use in the experiments.

### 4.2.2 COMPOSITION OF THE SOLUTION

A 2 molal Na-Cl solution (116.9 g kg<sup>-1</sup>) was prepared with deionized water and NaCl salt and used as reactive solution for the experiments, which approximate to the URG brines (TDS of 94–200 g l<sup>-1</sup>, Stober & Bucher, 2014). The pure Na-Cl solution used in the experiments

closely reflects the Na-Cl constitutes of 88–94 mol.% of the reservoir brines (Pauwels et al., 1993). This initial solution contained also a small amount of inorganic carbon given by the carbon exchange of the deionized water with the atmosphere (alkalinity of  $<0.1 \text{ mmol l}^{-1}$ ). Also, small quantities of  $\text{O}_2$  should be solved through contact with atmosphere. The initial pH of the solution was 5.5, measured at  $25^\circ\text{C}$ .

#### 4.2.3 EXPERIMENTAL SETUP AND PROCEDURE

Batch-type experiments in a stirred autoclave system (Limbo li, buechi) were performed (Fig. 4.1). In the autoclave we reacted sandstone surfaces with the 2 molal Na-Cl solution at elevated temperatures. One additional experiment has been conducted with 1.5 molal Na-Cl solution (PfsSt,  $260^\circ\text{C}$ ). The vessel and every component in contact with the solution is composed of stainless steel (X6NiCrTiMoVB25-15-2, EU standard 10269). The total volume of the vessel is 450 ml. Solution volume during the experiments was 350 ml with an atmospheric headspace. The stirrer speed was about 100 rpm. Three cylindrical solid samples were used in each experiment. From the anisotropic PfsSt samples broken surfaces, parallel as well as perpendicular to the bedding, were used.

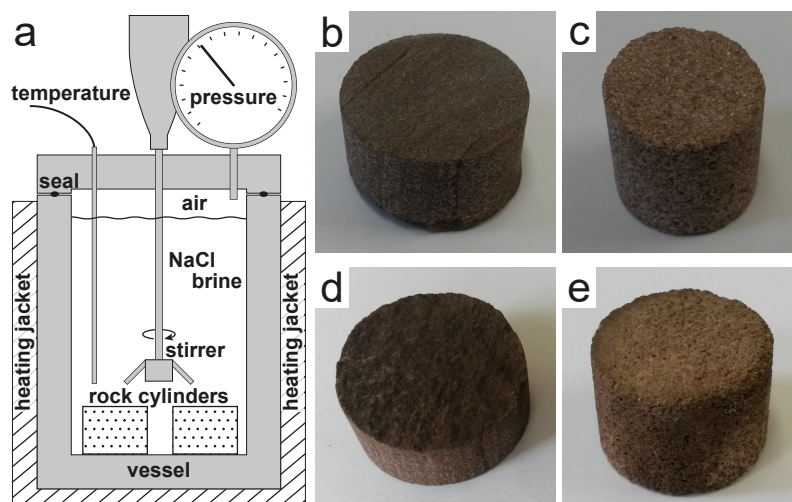


**Figure 4.1** – (a) Schematic illustration of the main components of the used autoclave system Limbo li (Buechi) during a running experiment. (b) Initial PfsSt sample. (c) Initial TenSst sample. (d) PfsSt sample and (e) TenSst sample, both after the  $260^\circ\text{C}$  experiment. Both samples are darker than the particular initial one, covered by a brownish layer. Quartz grains form morphological rises, more pronounced in the TenSst sample. All rock cylinders have diameters of 22 mm.

The duration of the experiments was 46 d for PfsSt and 54 d and 55 d for the TenSst. Temperatures during the experiments were  $200^\circ\text{C}$  and  $260^\circ\text{C}$  for both lithologies, respectively. These temperatures are reported (measured and maximum geothermometer temperatures) from reservoirs in the URG (Aquilina et al., 1997; Sanjuan et al., 2016). Experiments were carried out under pressures of  $\sim 16 \text{ bar}$  and  $\sim 44 \text{ bar}$  at  $200^\circ\text{C}$  and  $260^\circ\text{C}$ , respectively, given by the boiling conditions of the 2 molal Na-Cl solution.

#### 4.2.4 ANALYSIS OF THE FLUIDS

The fluid in the autoclave was cooled down rapidly after each experiment. Electric conductivity (Mettler Toledo Inlab 371) and pH (ProMinent PHER-112) were measured immediately. Carbonate alkalinity was determined by titration with 0.01 M HCl. The experiment solution was filtered with a 0.2  $\mu\text{m}$  cellulose acetate membrane for further fluid analyses. To prevent precipitation reactions, the fluid samples were diluted with ultra-pure water by a factor of 10 and, for cation measurements, acidified with distilled  $\text{HNO}_3$ . Samples were stored in 30 ml polyethylene bottles and preserved cool until analysis.

Major and minor cations were measured by inductively-coupled plasma mass spectrometry (ICP-MS) using a Thermo Fischer Scientific X-Series 2. Sample dilution was 1 : 100. Dissolved Si and Na concentration were analyzed by inductively-coupled plasma optical emission spectrometry (ICP-OES) with a Varian 715ES and a sample dilution of 1 : 200 for Si and 1 : 500 for Na. Ion chromatography (IC) was performed with a Dionex, ICS-1000 for dissolved anions. Due to high concentrations of Cl and a consequential need for high dilution of the sample (1 : 2000), it was not possible to detect other anions than Cl.

Quality of fluid measurements was verified by continuous measurement of standard solutions during analysis procedure. Accuracy of ICP-MS measurements is better than 3 % for main cations and better than 8 % for Al and Fe, for ICP-OES better than 5 % and for IC better than 4 %.

#### 4.2.5 ANALYTICAL METHODS SOLIDS

Rock samples has been removed from the vessel after solution extraction and washed with deionized water to prevent halite precipitation. Afterward, the samples have been dried at room temperature.

Characterization of the initial and post-experiment rock samples was performed with several analytical and imaging methods. The mineral content was identified by powder X-ray diffraction (XRD) measurements with a Siemens D500. System parameters were a Cu anode at 45 kV and 25 mA and a scintillation point detector. The scanning range was 3–63°, with a step size of 0.01° 2 $\theta$ . Unaltered samples were measured as representative bulk material, whereas only surface material of the altered samples was used to identify secondary phases formed during alteration. Mineral modes were calculated with the image processing program *ImageJ* based on SEM-BSE images of thin sections.

Alteration processes on sample surfaces and cross-sectional thin sections were detected and visualized by scanning electron microscopy (SEM) methods with a FEI Quanta 650 ESEM. Surface characterizations were made in secondary electron (SE) mode with an acceleration voltage of 10 kV. Additional, thin sections were examined for alteration reaction textures in the sample interior under back-scattered electron (BSE) mode at the same device setting. Mineral identification and qualitative analyses have been conducted with energy-dispersive X-ray spectroscopy (EDX, Bruker XFlash 5010 detector). Rock samples and thin sections were covered with carbon before SEM analyses.

Electron microprobe (EMP) measurements were carried out with a JEOL JXA-8530F. Calibration was performed on the following natural standards: Al:  $\text{Al}_2\text{O}_3$ , Ca + Si: wollas-

tonite, Fe:  $\text{Fe}_2\text{O}_3$ , Mn + Ti:  $\text{MnTiO}_3$ , K: orthoclase, Na: albite, Mg:  $\text{MgO}$ , F:  $\text{CaF}_2$  and Cl:  $\text{NaCl}$ . Measuring condition were an acceleration voltage of 15 kV, a beam current of 20 nA and a beam diameter of 1  $\mu\text{m}$  for all mineral phases except analcime (beam size of 2–4  $\mu\text{m}$  depending on grain size). Detection limit was 0.01 wt.%.

#### 4.2.6 GEOCHEMICAL MODELING AND CALCULATIONS

Geochemical modeling has been conducted with *The Geochemist's Workbench 10.0* (GWB, Bethke & Yeakel, 2015) and its standard database (thermo.dat), which based on LLNL data. Thereby, the activity coefficients were calculated by an extended Debye-Hückel equation (B-dot equation, Helgeson, 1969), which allows calculations of up to 3 molal Na-Cl in solutions, however with reduced accuracy at salinities higher than 0.5. Activity diagrams were created with the GWB program *Act2* for the experimental p-T conditions.

Measured pH were re-calculated to experiment temperatures with the GWB program *React*, with the complete data of measured fluid composition at 25 °C as input. Thus, the pH re-calculation considers the high salinity of the fluid as well as the total carbon in the system (alkalinity). Saturation states of relevant mineral phases for the solution composition after each experiment have been calculated with GWB (*GSS*), too.

### 4.3 RESULTS

Analyses of solid and fluid samples reveal significant differences between the starting material and the samples at the end of the experiments. Fluid composition changes, solid samples show alteration features from macroscopic to  $\mu\text{m}$  scale and in terms of chemical composition.

#### 4.3.1 INITIAL ROCK MATERIAL

**PFINZTAL SANDSTONE** The Pfinztal Sandstone (PfSst) has a grain size of 0.04–0.2 mm (typically >0.1 mm). It is a well sorted sandstone with angular and sub-spherical clasts (Fig. 4.2a). The volumetric modal composition is 49 % quartz, 16 % K-feldspar, 11 % muscovite, 15 % cementation, 1 % accessory phases and 8 % pore space (Table 4.1). The sandstone has a layered texture, caused by the orientation of sub-spherical feldspar grains and muscovite plates.

Quartz grains have smooth surfaces with few small holes and rarely often show dissolution edges (Fig. 4.2b). The feldspar is exclusively Na-free K-feldspar (Table 4.2). Chemical zonation or exsolution features are absent. Pitted alteration structures are visible on most K-feldspar grains (Fig. 4.2b). Broken K-feldspar grains at the surface of the initial rock samples show stepped and edged grain surfaces. Muscovite grains are platy, often bended and with kink bands (Fig. 4.2c). Samples, which are broken parallel to the sandstone bedding show intact muscovite grains on the sample surface. Whereas muscovite grains in samples, broken perpendicular to the sandstone bedding, are shattered to many small particles. The muscovite contains some Mg-Fe celadonite component (Table 4.3).

Original interstitial pore space is cemented with illite and hematite (Fig. 4.2b). Larger

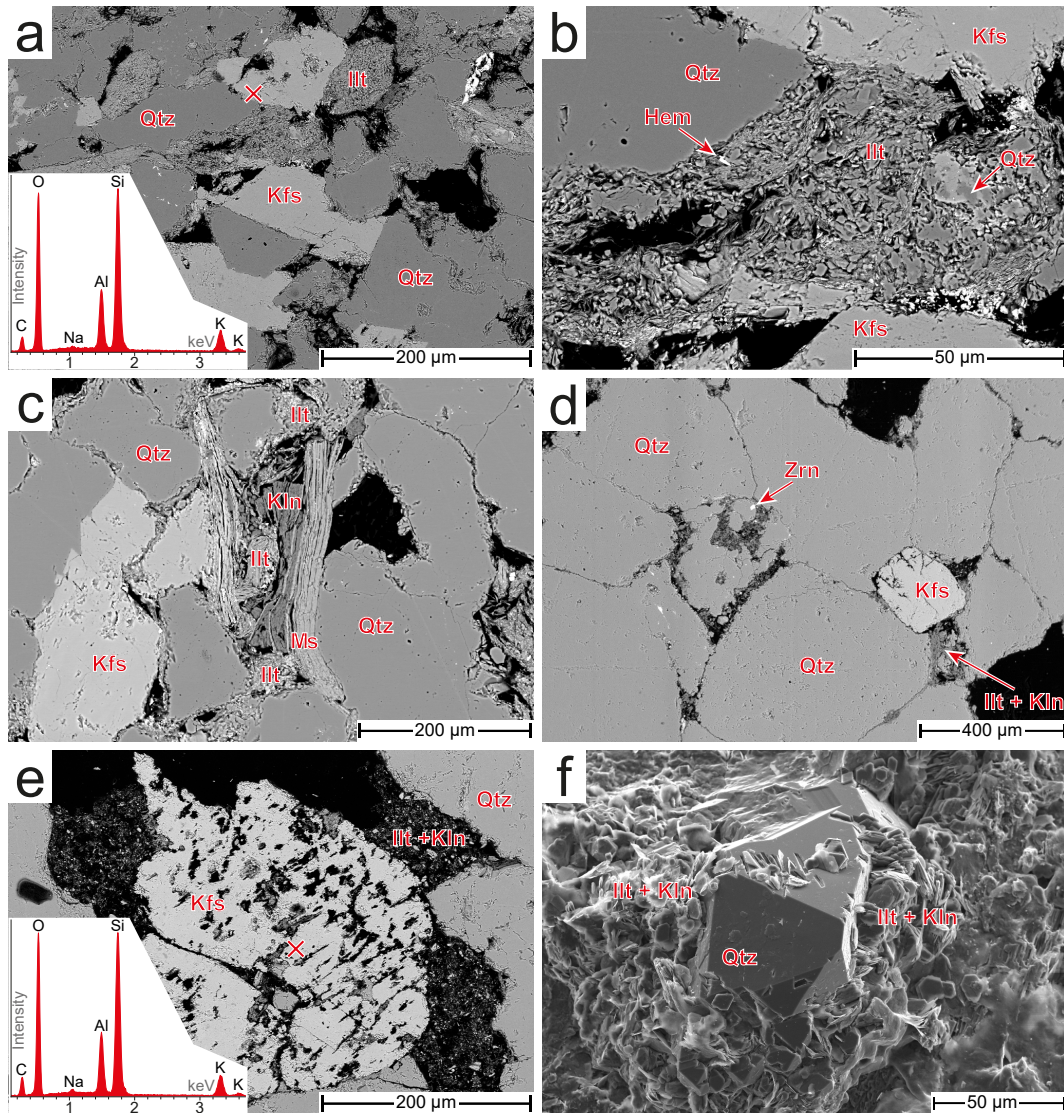


**Figure 4.2** – SEM images of initial Pfnztal and Tennenbach Sandstones (a) Texture of the initial Pfnztal composed of quartz, K-feldspar, muscovite and illite in the cementation. EDX spectrum of pure K-feldspar (measuring point marked with X). (b) Initial quartz and K-feldspar grains with interstitial illite and hematite in Pfnztal. (c) Muscovite grain with kink bands in vicinity to accessory kaolinite in initial Pfnztal. (d) Texture of the initial Tennenbach Sandstone composed of quartz, K-feldspar and illite and kaolinite in the cementation, and accessory zircon. (e) Skeletal K-feldspar in the initial Tennenbach Sandstone with EDX spectrum (measuring point marked with X). (f) Cementation of the initial Tennenbach Sandstone is composed of illite, quartz, kaolinite, and hematite (not in figure). (a)–(e) Thin section images, BSE mode, black color denotes pore space; (f) Surface image of broken rock fragment, SE mode.

**Table 4.1** – Mineral modes in volumetric percent in the initial samples and qualitative changes of phase occurrence on the sample surface during the experiments summarized for all experiments. ++ = strong increase, + = increase, o = no change, - = decrease, - - = strong decrease (on sample surface, not in the bulk sample!)

in vol. %	TenSst initial	PfSst initial	both Sst changes
Quartz	83	49	- -
K-feldspar	2	16	-
Albite	-	-	+
Muscovite	-	11	o
Chlorite	-	-	+
Analcime	-	-	++
Cementation	5	15	- -
Accessories	1	1	o
Pore space	9	8	+
Sum	100	100	

pores are filled by agglomerations of muscovite grains, often accompanied with chlorite, biotite and kaolinite (Fig. 4.2c). Accessory, calcite, rutile and apatite occur in the PfSst.

Interstitial illite is characterized, and distinguished from the muscovite clasts, by a lower K content on the interlayer site. The charge balance is probably maintained by higher Fe<sup>3+</sup> (Table 4.3).

**TENNENBACH SANDSTONE** The Tennenbach Sandstone (TenSst) has a coarser, well sorted grain size of 1–2 mm. The modal composition is 83 % quartz, 2 % K-feldspar, 5 % cementation, <1 % accessory phases and 9 % pore space (Table 4.1). The clasts are rounded and more spherical than those of the PfSst (Fig. 4.2d). The rock fabric seems to be isotropic, without any layering. The texture is grain-supported with relatively large pore space. Quartz grains are mostly solid with only few tiny holes (Fig. 4.2d). The feldspar is pure K-feldspar (Table 4.2) with skeletal dissolution textures (Fig 4.2e). Phyllosilicates occur in the Tennenbach Sandstone exclusively in the cementation.

Mainly illite, quartz, kaolinite and hematite make up the cementation of the TenSst. The cementation quartz grains are highly euhedral and embrace tiny (~100 µm) illite plates (Fig. 4.2f). Illite and kaolinite form hexagonal plates, 5–10 µm in diameter. Kaolinite plates tend to be thinner and less well crystallized than the illite plates. Chemical composition of phyllosilicates in the TenSst is listed in Table 4.3. Ilmenite, baryte, zircon, a Mn-oxide and svanbergite (SrAl<sub>3</sub>(PO<sub>4</sub>)(SO<sub>4</sub>)(OH)<sub>6</sub>) have been identified as accessory phases by SEM-EDX methods.

#### 4.3.2 SAMPLES AFTER THE EXPERIMENTS

After the experiments sandstone samples are covered by a brownish layer on their surface, which is darker than the initial sandstone surface (Fig. 4.1b–e). The quartz grains on the sample surface form macroscopically observable morphological rises in both PfSst and TenSst (Fig. 4.1d + e). The overall changes of mineralogy on the sample surface during the experiments are listed in Table 4.1, summarized for all experiments.

**Table 4.2** – Feldspar and analcime composition as determined by EMP analyses in sandstone samples (thin sections) prior to and after the experiments. Lower part: cations normalized to  $O_{96} \cdot 16 H_2O$  for analcime and  $O_8$  for feldspars. Kfs = K-feldspar, Afs = alkali feldspar, Anl = analcime, Hem = hematite. Anl + Hem are mixed analyses of analcime with included hematite particles.

Mineral Experiment Rock Grain	Kfs	Afs	Afs	Kfs	Afs	Kfs	Afs	Afs	Anl	Anl + Hem	Anl	Anl + Hem
	initial PfSst clast	260 PfSst albitiz.	260 PfSst albitiz.	260 1,5 M PfSst clast	260 1,5 M PfSst albitiz.	initial TenSst clast	260 TenSst albitiz.	260 TenSst albitiz.	260 PfSst precip.	260 PfSst precip.	260 TenSst precip.	260 TenSst precip.
SiO <sub>2</sub>	64.42	63.75	63.16	64.88	69.03	63.83	64.63	66.06	61.41	65.11	57.19	52.14
TiO <sub>2</sub>	0.03	0.02	0.01	0.03	0.02	<0.01	0.00	<0.01	<0.01	0.03	0.03	<0.01
Al <sub>2</sub> O <sub>3</sub>	18.07	18.26	18.18	18.30	20.37	18.40	18.92	19.44	22.06	21.79	22.15	20.23
FeO	0.05	0.05	0.03	0.05	0.14	<0.01	<0.01	0.05	0.32	2.30	0.32	1.85
MnO	0.01	<0.01	<0.01	<0.01	<0.01	<0.01	<0.01	0.01	<0.01	0.04	<0.01	0.03
MgO	<0.01	<0.01	<0.01	0.03	<0.01	<0.01	0.04	0.01	0.01	0.02	0.03	0.10
CaO	0.01	0.06	0.07	0.01	0.38	0.03	0.00	0.03	0.10	0.09	0.04	0.10
Na <sub>2</sub> O	0.07	1.31	1.20	0.11	8.46	0.47	1.14	1.16	7.16	2.04	9.08	6.00
K <sub>2</sub> O	16.17	14.22	14.56	16.15	0.04	16.09	15.51	14.42	0.22	0.45	0.07	0.05
Total	98.83	97.71	97.22	99.55	98.44	98.82	100.24	101.18	91.29	91.87	88.92	80.51
Si	3.01	3.00	2.99	3.01	3.02	2.99	2.98	2.99	34.82	36.10	33.73	33.88
Al	0.99	1.01	1.01	1.00	1.05	1.01	1.03	1.04	14.74	14.24	15.39	15.50
Ti	0.00	0.00	0.00	0.00	0.00	0.00	0.00	0.00	0.00	0.01	0.01	0.00
Mg	0.00	0.00	0.00	0.00	0.00	0.00	0.00	0.00	0.01	0.02	0.02	0.10
Fe	0.00	0.00	0.00	0.00	0.00	0.00	0.00	0.00	0.15	1.07	0.16	1.01
Mn	0.00	0.00	0.00	0.00	0.00	0.00	0.00	0.00	0.00	0.02	0.00	0.02
Ca	0.00	0.00	0.00	0.00	0.02	0.00	0.00	0.00	0.06	0.05	0.03	0.07
Na	0.01	0.12	0.11	0.01	0.72	0.04	0.10	0.10	7.87	2.20	10.38	7.55
K	0.96	0.85	0.88	0.95	0.00	0.96	0.91	0.83	0.16	0.32	0.05	0.04
Sum	4.98	4.98	5.00	4.97	4.81	5.01	5.02	4.96	57.82	54.02	59.78	58.17
Si + Al	4.00	4.01	4.00	4.01	4.07	4.00	4.00	4.02	49.57	50.34	49.12	49.38
Ca + Na + K	0.97	0.98	0.99	0.96	0.74	1.00	1.01	0.94	8.09	2.57	10.46	7.67
Na/K	0.01	0.14	0.13	0.01	292.21	0.04	0.11	0.12	49.02	6.93	200.00	182.22
An	0.00	0.00	0.00	0.00	0.00	0.00	0.00	0.00	-	-	-	-

#### ALTERATION FEATURES OF PRIMARY MINERALS

**QUARTZ (PfSST)** The initially conchoidal fracture surface of the quartz grains from the PfSst shows porous dissolution characteristics after the experiments. Small etch-pits and elongated ditches spread the quartz surfaces from both the 200 °C and 260 °C experiments. Additionally, quartz grains of the 260 °C sample show dissolution gashes, partly along crystallographic directions, deep into the grain interior (Fig. 4.3a). Quartz dissolution in the 200 °C samples is less pronounced, but initiations can be observed.

In accordance with the observed quartz dissolution on the sample surfaces, thin sections show, that quartz dissolution reaches up to ~3 mm into the sandstone samples. Dissolution features are located along the rims of the quartz grains, as well as within the grains (Fig. 4.3b).

**QUARTZ (TenSST)** Quartz dissolution in TenSst samples is similar to that of PfSst. Quartz surfaces are characterized by shallow dissolution features at samples from both experiment temperatures. Whereas deep dissolution is more pronounced in samples from the 260 °C experiments. Here wormhole-like dissolution features in the quartz grains are common (Fig. 4.3c).

**K-FELDSPAR (PfSST)** K-feldspar of the PfSst samples show no visible changes of the grain morphology after the experiment at both 200 °C and 260 °C. The stepped and edged grains remain mainly unchanged. However, there are partly rounded edges of K-feldspar grains from the 260 °C experiment (Fig. 4.3d, albitized K-feldspar). EDX indicates, that these K-feldspars incorporated variable amounts of Na (albitization) during the experiments (EDX in fig. 4.3d).

Occurrence of albite can also be detected in thin sections (Fig. 4.3f) of the 260 °C experiments. EMP measurements prove the occurrence of an albite component at K-feldspar margins (Table 4.2). K-feldspars also show smooth edges along the grain boundaries as

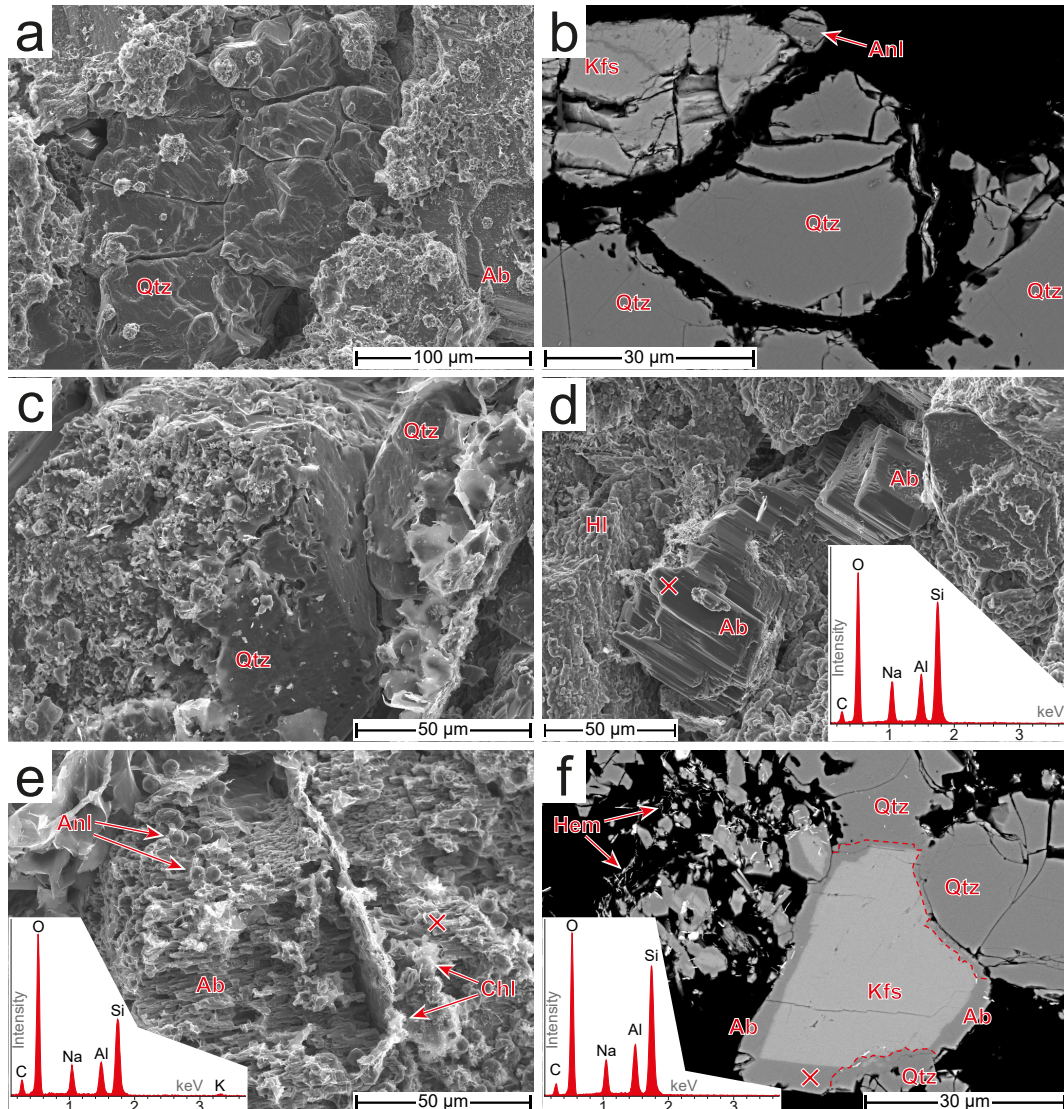


**Figure 4.3** – SEM images of Pfnztal and Tennenbach Sandstones after the 260 °C experiments. (a) Deep dissolution features on quartz grains at sample surface of PfSst. (b) Quartz dissolution along the grain boundaries and in the interior of the grains (holes in the initially compact Qtz grains; PfSst). (c) Deep wormhole-like dissolution phenomena in a quartz grain of a reacted TenSst sample. (d) Albitized K-feldspar with rounded, dissolved edges in the PfSst sample from the 260 °C experiment with corresponding EDX spectrum (measuring point marked with X). Halite precipitations around the feldspar. (e) Albitized K-feldspar in the TenSst sample from the 260 °C experiment with chlorite and analcime precipitations on top. EDX spectrum of the albitized K-feldspar (measuring point marked with X). (f) Albitized rim (EDX spectrum, measuring point marked with X) of a K-feldspar grain at the sample surface (on the left) in the PfSst sample of a 260 °C experiment with 1.5 M Na-Cl solution. Dashed line illustrate the grain boundary between quartz and albite. Bright particles are primary hematite. (a) + (c)–(e) surface images, SE mode, (b) + (f) thin section images, BSE mode, black color denotes pore space.

**Table 4.3** – Phyllosilicate composition as determined by EMP analyses in sandstone samples (thin sections) prior to and after the experiments. Mg# = Mg / (Mg + Fe) (in mol, all iron as Fe<sup>2+</sup>). Cations per O<sub>10</sub>(OH)<sub>2</sub> for mica, and O<sub>10</sub>(OH)<sub>8</sub> for chlorite. Ms = muscovite, Kln = kaolinite, Bt = biotite, Illt = illite, Chl = chlorite.

Mineral	Ms	Kln	Bt	Illt	Illt	Ms	Chl	Illt + Na	Illt	Illt + Na	Chl	Chl
Experiment	initial	initial	initial	initial	initial	260	260	260	initial	260	260	260
Rock	PfSst	PfSst	PfSst	PfSst	PfSst	PfSst	PfSst	PfSst	TenSst	TenSst	TenSst	TenSst
Grain	clast	clast	clast	matrix	matrix	clast	matrix	matrix	matrix	matrix	precip.	precip.
SiO <sub>2</sub>	46.92	46.55	38.42	51.45	50.51	47.37	32.11	44.48	48.66	49.50	21.13	20.04
TiO <sub>2</sub>	0.89	0.01	4.07	0.13	0.10	0.64	0.10	0.15	0.14	0.01	0.01	<0.01
Al <sub>2</sub> O <sub>3</sub>	35.13	39.04	16.30	30.50	30.92	31.26	19.82	33.64	33.23	30.65	10.47	10.03
FeO	1.62	0.21	15.65	2.24	2.43	2.16	19.34	2.05	1.43	1.54	18.70	18.45
MnO	0.02	<0.01	0.11	0.01	0.03	0.02	0.76	0.02	0.01	0.03	0.13	0.24
MgO	0.74	0.02	7.78	2.27	1.59	1.78	13.02	0.48	1.16	1.26	0.71	1.27
CaO	0.12	0.08	0.18	0.09	0.27	0.09	1.26	0.35	0.12	0.12	0.69	0.65
Na <sub>2</sub> O	0.50	0.01	0.22	0.48	0.17	0.28	0.16	1.94	0.37	2.19	0.32	0.44
K <sub>2</sub> O	9.24	0.03	7.93	7.94	8.77	10.14	0.32	6.00	8.42	4.63	0.11	0.12
F	<0.01	<0.01	<0.01	<0.01	<0.01	<0.01	<0.01	<0.01	<0.01	<0.01	<0.01	<0.01
Cl	0.01	<0.01	0.02	<0.01	<0.01	0.01	0.02	0.05	0.01	0.01	0.20	0.18
Total	95.18	85.95	90.66	95.08	94.77	93.74	86.90	89.16	93.54	89.94	52.43	51.38
Si	3.10	4.01	2.98	3.37	3.34	3.21	3.27	3.11	3.24	3.37	3.76	3.67
Al	2.74	3.96	1.49	2.36	2.41	2.50	2.38	2.77	2.61	2.46	2.20	2.16
Ti	0.04	0.00	0.24	0.01	0.00	0.03	0.01	0.01	0.01	0.00	0.00	0.00
Mg	0.07	0.00	0.90	0.22	0.16	0.18	1.98	0.05	0.12	0.13	0.19	0.35
Fe	0.09	0.01	1.01	0.12	0.13	0.12	1.65	0.12	0.08	0.09	2.78	2.82
Mn	0.00	0.00	0.01	0.00	0.00	0.00	0.07	0.00	0.00	0.00	0.02	0.04
Ca	0.01	0.01	0.01	0.01	0.02	0.01	0.14	0.03	0.01	0.01	0.13	0.13
Na	0.06	0.00	0.03	0.06	0.02	0.04	0.03	0.26	0.05	0.29	0.11	0.16
K	0.78	0.00	0.78	0.66	0.74	0.88	0.04	0.54	0.72	0.40	0.03	0.03
Sum	6.90	8.01	7.45	6.81	6.83	6.96	9.57	6.89	6.83	6.75	9.21	9.35
Si + Al	5.84	7.98	4.46	5.73	5.75	5.71	5.65	5.89	5.85	5.83	5.95	5.83
Ca + Na + K	0.85	0.01	0.83	0.73	0.78	0.92	0.21	0.83	0.77	0.70	0.27	0.31
Al <sup>IV</sup>	0.90	0.00	0.79	0.63	0.66	0.79	0.73	0.89	0.76	0.63	0.24	0.33
Al <sup>VI</sup>	1.84	3.96	0.70	1.73	1.75	1.71	1.65	1.89	1.85	1.83	1.95	1.83
Na/K	0.08	0.76	0.04	0.09	0.03	0.04	0.76	0.49	0.07	0.72	4.42	5.46
K/Al	0.28	0.00	0.53	0.28	0.31	0.35	0.02	0.19	0.27	0.16	0.01	0.01
Mg#	0.45	0.15	0.47	0.64	0.54	0.59	0.55	0.29	0.59	0.59	0.06	0.11

well as at cracks within the grains in thin sections (Fig. 4.3b).

**K-FELDSPAR (TENST)** The skeletal feldspar grains in the TenSst are preserved during the experiments at both temperatures (Fig. 4.3e). Only the sharp tips of the K-feldspar grains are sub-rounded, compared to the initial grains. Likewise, EDX measurements of the feldspar margins show a distinct Na signal (Fig. 4.3e). In thin sections occurrence of albite can be observed in BSE mode (Fig. 4.3f), as in the PfSst, and measured by EMP (Table 4.2). The initial grain shape of K-feldspar is preserved, but the sharp boundary between albite and K-feldspar progresses as a diffusion front into the grain interior.

**MUSCOVITE (PFSST)** Muscovite in the PfSst samples is relatively unaffected by the experiments. No changes in shape and surface structure can be observed on the sample surface with SEM for all samples at both temperatures. Nevertheless, qualitative EDX measurements on the sample surface indicate a small Na increase in muscovite at several spots on the sample surface. However, EDX and EMP measurements on thin sections show no change of the muscovite composition, neither for the large muscovite grains nor for the muscovite to illite of the cementation (Table 4.3).

**CEMENTATION PHASES (PFSST)** Minerals of the initial PfSst cementation cannot be observed after the experiments on the sample surface. Primarily illite has been removed from the surfaces during the experiments.

In thin sections, the cementation, which is at the surface of the sample and thus directly exposed to the solution, lack of illite whereas quartz, feldspar and muscovite fragments as well as hematite particles remain (Fig. 4.4a). Chemical changes in the remaining minerals cannot be measured by electron microscopy methods due to their tiny grain size. The mineral compositions are summarized in Table 4.3 for selected representative measuring

points.

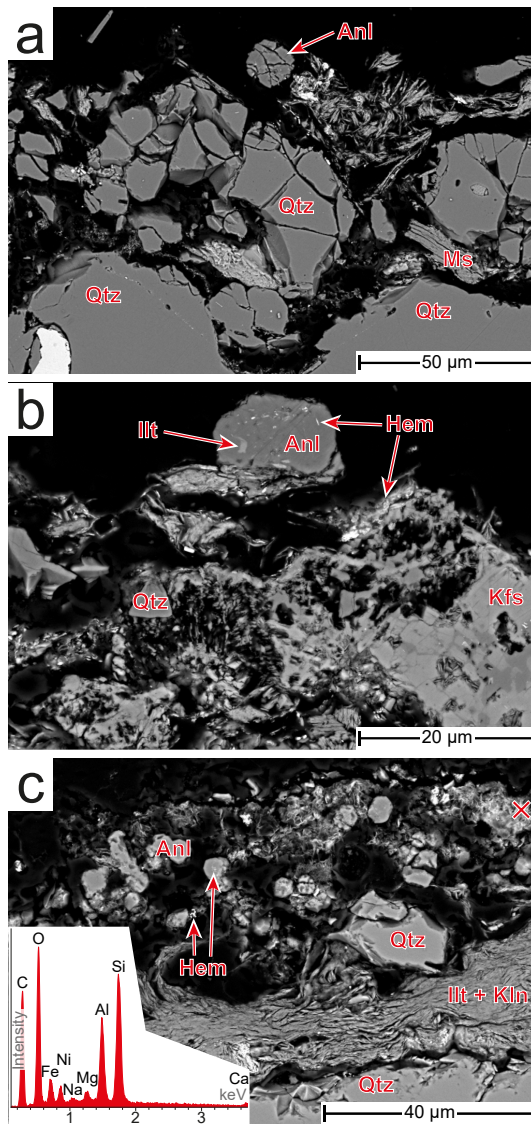


**Figure 4.4** – SEM thin section images of altered PfSst (a + b) and TenSst (c): (a) Dissolution of quartz results in smooth edges of the grain boundaries and in holes within the grains. Newly formed analcime crystal on the sample surface (top of the image). Most cementation minerals have been removed from the interstitial pore space. Muscovite grain shows a delamination of sheets. (b) Precipitated euhedral analcime crystal encloses pre-existing hematite particles and illite flakes. Cementation phases have been partly removed from the interstitial pore space. (c) Analcime precipitates with partly enclosed hematite particles. It is intergrown with product chlorite on the uppermost surface (EDX spectra, measuring point marked with X). Subsurface cementation minerals are preserved. Quartz dissolution results in rounded grain edges. (a)–(c) BSE mode, black color denotes pore space.

**CEMENTATION PHASES (TENST)** The primary cementation phases mostly disappeared from the sample surface, at both 200 °C and 260 °C (Fig. 4.3c + d). The euhedral quartz, illite and kaolinite grains from the cementation lack on sample surfaces after the experiments. The clasts of quartz and K-feldspar are now prominently exposed with relatively deep interstitial space.

The near surface disappearance of illite, kaolinite and quartz can also be observed in thin sections. EMP measurements of illites, deeper in the sample, indicate an incorporation of detectable amounts of Na (Table 4.3).

#### NEWLY PRECIPITATED MINERALS

**ANALCIME PRECIPITATION** Analcime has been detected by XRD as well as SEM methods (Fig. 4.4 + 4.5) on the surface of both sandstone samples during the experiments carried out at both 200 °C and 260 °C. The analcime crystals are pervasive throughout the sample surfaces (Fig. 4.5a, TenSst 200 °C; Fig 4.5c, TenSst 260 °C). Analcimes are mostly perfectly euhedral with a (pseudo-)cubic crystal habit (Fig. 4.5b, c + e). Besides, the samples of PfSst

(260 °C) and of TenSst (200 °C) are partly covered by a layer of analcime, which in some areas shows single subhedral crystals (Fig. 4.5d + f). Analcime occurs on the surface of every primary mineral (Fig. 4.5a + c), i.e. quartz, K-feldspar and in the case of PfSst on primary muscovite.

The diameter of the analcime crystals varies from 2.5–58 µm for both types of sandstones. Large diameters of 18–58 µm occur exclusively in samples of the additional experiment with PfSst and 1.5 molal Na-Cl solution at 260 °C. Here, the abundance of single analcime crystals is reduced, compared to the samples of the 2 molal Na-Cl experiments. For the 2 molal Na-Cl experiments, the grain shape of analcime is almost equigranular on TenSst samples, but more seriate on PfSst samples. The analcime diameters of PfSst range between 6–12 µm in samples from the 200 °C experiments and 3–17 µm in samples from the 260 °C experiments, with most grains having diameters between 6–7.5 µm. The anhedral to subhedral analcime crystals of the 260 °C experiment have diameters between 2.5–7 µm. The analcime diameters of the TenSst samples, vary between 3–7 µm for both 200 °C and 260 °C experiments.

In the vicinity of analcime co-precipitated phyllosilicate can be observed locally (Fig. 4.5b + c). Additionally, an overgrowth of primary hematite particles and residues of illite flakes by analcime can be observed, that occurs mainly in the center of the analcime crystals (Fig. 4.4b). Inclusions of hematite particles in analcime are more common in the PfSst. EMP measurements of the chemical compositions of analcime crystals are listed in Table 4.2.

**PHYLLOSILICATE PRECIPITATION** Precipitation of phyllosilicates took place during the experiments. Tiny flakes of it occur frequently in samples of the 200 °C experiments, independent of the type of sandstone. They are composed of Fe-Ni-(Na)-Mg-Al-Si-O (EDX measurements on surfaces and thin section) and can be classified as Fe-chlorite from EMP analyses (Fig. 4.4c, Table 4.3). The newly formed chlorite is spatially associated with analcime.

### 4.3.3 FLUID COMPOSITION

The fluid composition changed during the experiments. Cation concentrations of most elements increased with respect to the initial solution. Nearly all analyzed elements are higher concentrated in the fluids of the 260 °C experiments than in those of the 200 °C ones. The fluid compositions after the experiments are listed in Table 4.4.

**Table 4.4** – Composition of fluid as determined by ICP-MS, ICP-OES and IC. In-situ pH calculated with GWB and the thermo.tdat database (Bethke & Yeakel, 2015).

Rock	Temp. °C	Time d	Cond. mS cm <sup>-1</sup>	pH at 25 °C	pH in-situ	Alk. mmol l <sup>-1</sup> titr.	Na g l <sup>-1</sup> ICP-OES	K mg l <sup>-1</sup> ICP-MS	Ca mg l <sup>-1</sup> ICP-MS	Mg mg l <sup>-1</sup> ICP-MS	Fe mg l <sup>-1</sup> ICP-MS	Ni µg l <sup>-1</sup> ICP-MS	Al µg l <sup>-1</sup> ICP-MS	Si mg l <sup>-1</sup> ICP-OES	Cl g l <sup>-1</sup> IC	HCO <sub>3</sub> <sup>-</sup> mg l <sup>-1</sup> calc.
initial	–	0	136	5.77	–	<0.1	44.9	n.d.	n.d.	n.d.	n.d.	n.d.	n.d.	n.d.	67.2	<6
PfSst	200	46	120	6.03	6.66	0.7	38.0	39	77	n.d.	n.d.	27	47	125	57.4	43
PfSst	260	46	138	5.50	6.31	0.9	43.0	217	236	2	4.4	39	104	195	63.2	55
TenSst	200	55	142	6.50	6.81	0.4	47.7	57	104	0.2	1.6	80	100	98	68.5	24
TenSst	260	54	137	3.88	4.51	–	44.7	78	15	2	65	204	244	221	67.3	–

The pH is slightly acidic between 5.5 and 6.5 (at 25 °C). One exception is the markedly lower pH of 3.9 for the TenSst fluid from the 260 °C experiment. However, recalculation

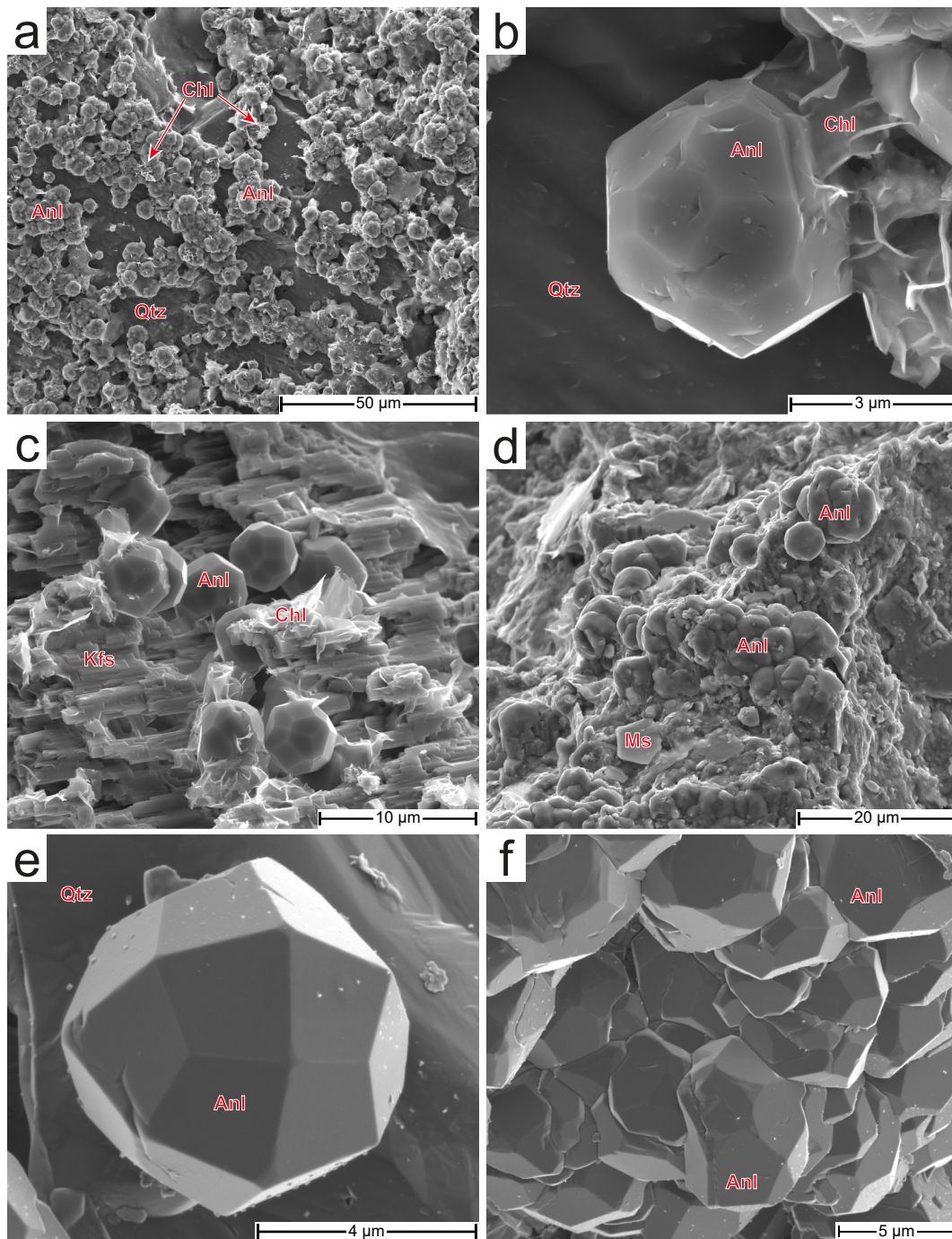


**Figure 4.5** – SEM surface images of analcime precipitates on the PfSst and TenSst samples after the experiments. (a) Massive precipitation of analcime crystals together with few chlorite particles on quartz grains with dissolved surfaces from the 200 °C experiment. (b) Euhedral analcime crystal intergrown with chlorite in the 200 °C experiment. (c) Euhedral analcime and chlorite precipitates on K-feldspar on the sample surface of the TenSst 260 °C experiment. (d) Analcime layer on the PfSst sample from the 260 °C experiment composed of shapeless material as well as euhedral crystals. (e) Euhedral analcime crystal on the surface of a primary quartz grain from the 260 °C experiment. (f) Anhedral to euhedral, intergrown analcime precipitates on the surface of the PfSst sample from the 260 °C experiment.

of pH values to the respective experimental temperature (GWB, Bethke & Yeakel, 2015) results in a near neutral pH (6.3–6.8) with the exceptions for the TenSst fluid (pH 4.5) at 260 °C (Table 4.4).

Sodium concentration remains in the range of the initial solution. Potassium is present in the fluids of all experiments, reaching values of 39–217 mg l<sup>-1</sup>. The K concentration of the 260 °C experiments are higher than the 200 °C experiments for both rock samples. Calcium concentrations range erratically from 15 to 236 mg l<sup>-1</sup>. The Mg concentrations in the fluid are generally very low (≤2 mg l<sup>-1</sup>) or below detection limit for all samples. Silica concentrations show consistent values of about 100 mg l<sup>-1</sup> and 200 mg l<sup>-1</sup> expressed as Si for 200 °C and 260 °C experiments, respectively. The chloride concentration of the initial solution remained nearly unchanged. Hydrogen carbonate concentration correlates with the Ca concentration (15–236 mg l<sup>-1</sup>). Based on alkalinity titration, the HCO<sub>3</sub><sup>-</sup> concentration has been calculated to 24–55 mg l<sup>-1</sup>.

## 4.4 DISCUSSION

Based on the analyses of solids and fluids as well as taking into account the results of the geochemical modeling, the main effects of reacting sandstone samples, typical of geothermal reservoirs in the URG, with a saline solution at hydrothermal conditions are (a) significant quartz dissolution, (b) dissolution of the cementation minerals kaolinite and illite, (c) minor dissolution of K-feldspar, (d) massive precipitation of analcime and some chlorite and (e) formation of albite replacing K-feldspar. The changes in the composition of the experimental fluid reflect the observed dissolution and growth of minerals.

### 4.4.1 MINERAL REACTIONS DEDUCED FROM THE EXPERIMENTS

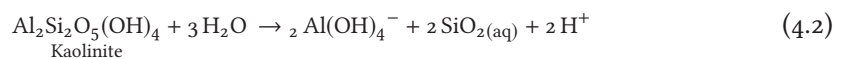
Both sandstone samples developed very similar surface features during the experiments and are discussed together in the following.

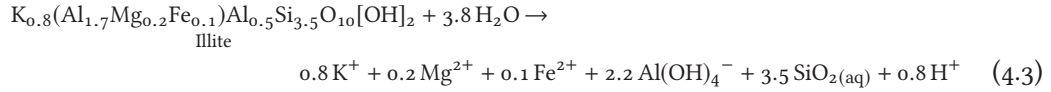
**QUARTZ DISSOLUTION** Quartz dissolution, both along grain margins and cracks, has been documented above for all samples. The aqueous Si concentration in the reacted fluids is close to quartz saturation (Table 4.7). Computed quartz saturation temperatures (Verma & Santoyo, 1997) are close to the experimental temperatures. This means that the quartz dissolution reaction (Eq. 4.1)



has reached equilibrium in less than experimental time (Table 4.4).

**DISSOLUTION OF KAOLINITE AND ILLITE** Dissolution of kaolinite and illite will increase SiO<sub>2(aq)</sub>, dissolved Al and, in case of illite, additional, K<sup>+</sup>, Mg<sup>2+</sup> and Fe<sup>2+</sup> in the fluid. The dominant Al species at all experimental conditions is Al(OH)<sub>4</sub><sup>-</sup> (GWB, Bethke & Yeakel, 2015). For measured (idealized) stoichiometric composition of kaolinite and illite (Table 4.5) the dissolution reactions can be written as:



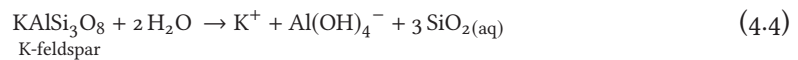


Progress of these reactions explain the observed absence of cementation illite and kaolinite in the near-surface zone of the reacted samples. The disappearance of cementation phases from the sample surface could also be a result of the mechanical removal by stirring in the autoclave. However, the solution after the experiments contain insufficient particles to explain a mechanical removal. Furthermore, the dissolution of the cementation phases is the only reasonable source of  $\text{Al}(\text{OH})_4^-$  for the precipitation reactions, outlined in 4.4.4.

**Table 4.5** – Mineral formulas calculated from EMP measurements, based on representative single measuring points. Lower part idealized compositions for use in the text. Acc. = accessory phase, cem. = cementation, preci. = precipitate.

Mineral	Rock	Sample	Grain	Formula
Muscovite	PfSst	initial	clast	$(\text{K}_{0.8}\text{Na}_{0.1})(\text{Al}_{1.8}\text{Mg}_{0.1}\text{Fe}_{0.1})\text{Al}_{0.9}\text{Si}_{3.1}\text{O}_{10}[\text{OH}]_2$
Muscovite	PfSst	260 °C	clast	$(\text{K}_{0.8})(\text{Al}_{1.7}\text{Mg}_{0.2}\text{Fe}_{0.1})\text{Al}_{0.8}\text{Si}_{3.2}\text{O}_{10}[\text{OH}]_2$
Kaolinite	PfSst	initial	acc.	$\text{Al}_4\text{Si}_4\text{O}_{14}[\text{OH}]_8$
Kaolinite	TenSst	initial	cem.	$\text{K}_{0.3}(\text{Al}_{3.9}\text{Mg}_{0.1})(\text{Al}_{0.2}\text{Si}_{3.8})\text{O}_{10}[\text{OH}]_8$
Illite	PfSst	initial	cem.	$(\text{K}_{0.7}\text{Na}_{0.1})(\text{Al}_{1.7}\text{Mg}_{0.2}\text{Fe}_{0.1})\text{Al}_{0.6}\text{Si}_{3.4}\text{O}_{10}[\text{OH}]_2$
Illite	PfSst	initial	cem.	$(\text{K}_{0.7})(\text{Al}_{1.7}\text{Mg}_{0.2}\text{Fe}_{0.1})\text{Al}_{0.7}\text{Si}_{3.3}\text{O}_{10}[\text{OH}]_2$
Illite	TenSst	initial	cem.	$\text{K}_{0.7}(\text{Al}_{1.9}\text{Mg}_{0.1}\text{Fe}_{0.1})\text{Al}_{0.8}\text{Si}_{3.2}\text{O}_{10}[\text{OH}]_2$
Illite	PfSst	260 °C	cem.	$(\text{K}_{0.5}\text{Na}_{0.3})(\text{Al}_{1.9}\text{Mg}_{0.1}\text{Fe}_{0.1})\text{Al}_{0.9}\text{Si}_{3.1}\text{O}_{10}[\text{OH}]_2$
Illite	TenSst	260 °C	cem.	$(\text{K}_{0.4}\text{Na}_{0.3})(\text{Al}_{1.8}\text{Mg}_{0.1}\text{Fe}_{0.1})\text{Al}_{0.6}\text{Si}_{3.4}\text{O}_{10}[\text{OH}]_2$
Chlorite	PfSst	260 °C	acc.	$(\text{Mg}_{2.0}\text{Fe}_{1.7}\text{Ca}_{0.1}\text{Mn}_{0.1})\text{Al}_{1.7}(\text{Al}_{0.7}\text{Si}_{3.3})\text{O}_{10}[\text{OH}]_8$
Chlorite	TenSst	260 °C	prec.	$(\text{Mg}_{0.2}\text{Fe}_{2.8}\text{Ca}_{0.1}\text{Na}_{0.1})\text{Al}_2(\text{Al}_{0.2}\text{Si}_{3.8})\text{O}_{10}[\text{OH}]_8$
Chlorite	TenSst	260 °C	prec.	$(\text{Mg}_{0.3}\text{Fe}_{2.8}\text{Ca}_{0.1}\text{Na}_{0.2})\text{Al}_{1.8}(\text{Al}_{0.3}\text{Si}_{3.7})\text{O}_{10}[\text{OH}]_8$
Analcime	PfSst	260 °C	prec.	$\text{Na}_{0.5}(\text{Al}_{0.9}\text{Si}_{2.2}\text{O}_6) \cdot [\text{H}_2\text{O}]$
Analcime	TenSst	260 °C	prec.	$\text{Na}_{0.7}(\text{Al}_{1.0}\text{Si}_{2.1}\text{O}_6) \cdot [\text{H}_2\text{O}]$
Idealized formula for reaction equations				
Muscovite	idealized	initial	clast	$\text{K}(\text{Al}_{1.8}\text{Mg}_{0.2})\text{Al}_{0.8}\text{Si}_{3.2}\text{O}_{10}[\text{OH}]_2$
Kaolinite	idealized	initial	cem.	$\text{Al}_4\text{Si}_4\text{O}_{14}[\text{OH}]_8$
Illite	idealized	initial	cem.	$\text{K}_{0.8}(\text{Al}_{1.7}\text{Mg}_{0.2}\text{Fe}_{0.1})\text{Al}_{0.5}\text{Si}_{3.5}\text{O}_{10}[\text{OH}]_2$
Chlorite	idealized	260 °C	prec.	$(\text{Mg}_2\text{Fe})\text{Al}_2(\text{Si}_4)\text{O}_{10}[\text{OH}]_8$
Analcime	idealized	260 °C	prec.	$\text{Na}_{0.6}\text{AlSi}_{2.1}\text{O}_6 \cdot [\text{H}_2\text{O}]$

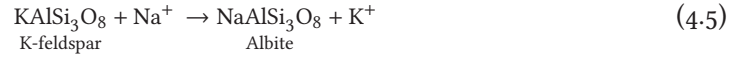
**DISSOLUTION OF K-FELDSPAR** The observed dissolution of K-feldspar in the samples of both sandstones increases  $\text{K}^+$ ,  $\text{Al}(\text{OH})_4^-$  and  $\text{SiO}_{2(\text{aq})}$  concentrations of the fluid (Eq. 4.4):



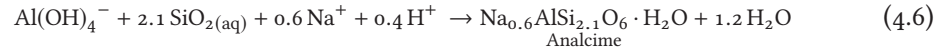
However, K-feldspar dissolution is a minor process in our samples, as evidenced by preserved crystal faces and shapes of K-feldspar fragments.

**FORMATION OF ALBITE** Albite is present at the rims of K-feldspar in all rock samples after experiments. Concerning the absence of Na-bearing feldspars in the initial samples two possible mechanisms could explain the formation of albite. (1) Albitization of existing K-feldspar by cation replacement ( $\text{K}^+$  by  $\text{Na}^+$ , Eq. 4.5), (2) Precipitation of albite directly from the fluid coating primary K-feldspar. The observations on the sample surface (with EDX data) as well as in thin sections (including EMP measurements) suggest, that albitization of existing K-feldspar is most probable (Fig. 4.3d–f, see 4.4.5 below). The total mass transfer

due to albitization of K-feldspar is small because of the small amount of modal K-feldspar, especially in TenSst. Furthermore, albite has been detected only at the outermost rims of K-feldspar grains.



**ANALCIME PRECIPITATION** Precipitation of analcime is a major process during the experiments. It is ubiquitous on the sample surfaces after the experiments. The analcime forming reaction using the analyzed analcime composition (Table 4.5) can be expressed as:

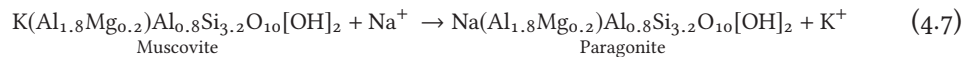


The reactant species in the fluid are provided by the dissolution of primary sheet silicates and quartz together with sodium from the solution.

**CHLORITE PRECIPITATION** Chlorite with an  $X_{Fe} = 0.45$  (Table 4.3) formed as a byproduct of illite (mica) alteration. Chlorite is the important sink for Mg released by illite breakdown (Eq. 4.3). Dissolved  $\text{Mg}^{2+}$  in the fluid is very low (Table 4.4) suggesting that Mg is directly transferred from illite to chlorite. Similarly, Fe from illite is captured by chlorite. However, material from the stainless steel container of the autoclave is an additional source of Fe in the fluid and in the chlorite precipitates, indicated by the presence of small amounts of Ni in chlorite. EDX measurements show a distinct Ni signal for the chlorite precipitates (Fig. 4.4c), which differ them from the original accessory chlorite in the non-reacted PfSst sample.

The macroscopically observed brownish layer on the samples after the experiments could be explained by the precipitation of analcime and chlorite. The reddish color presumably originate from iron-bearing phases, as already present in the initial samples.

**MUSCOVITE ALTERATION** Muscovite alteration is a very subordinate process. Muscovite dissolution textures are absent. Minor cation replacement ( $\text{K}^+$  by  $\text{Na}^+$ , Eq. 4.7) has been documented in the outermost layer of muscovite by EDX measurements. The lack of a Cl signal rules out that the Na signal originates from precipitated halite on muscovite.



#### 4.4.2 FLUID DATA AND pH VALUES

After experimental run time the reaction fluid contained solute species derived from the dissolution of quartz, feldspar, mica and clay minerals (illite and kaolinite). However it also contained elevated amounts of Ca, whose solid source is not obvious. A potential candidate is apatite, which has been identified in thin sections. But, bulk P is very low (Table 4.6) ruling out apatite as a Ca source. However, Ca correlates with total inorganic carbon (TIC) and carbon in the bulk rock (Table 4.6) of PfSst suggesting that it derives from unnoticed small amounts of calcite in veinlets and along grain boundaries of the used sandstone samples. TIC is the sum of  $\text{HCO}_3^-$  and dissolved  $\text{CO}_2$  computed from measured  $\text{HCO}_3^-$  and pH (Table 4.4). For the PfSst 200 °C experiment TIC is  $2.18 \text{ mmol l}^{-1}$  and matches very well

with  $1.93 \text{ mmol l}^{-1}$  Ca. For the PfSst  $260 \text{ }^{\circ}\text{C}$  experiment a TIC of  $7.28 \text{ mmol l}^{-1}$  compares to Ca  $5.9 \text{ mmol l}^{-1}$ , which is, given the uncertainties involved, a reasonably sound balance. The data suggest that Ca and TIC derive from calcite dissolution. Ca in the bulk of TenSst is very low but the fluid contains Ca and inorganic carbon. This apparent inconsistency could be caused by a calcite veinlet exposed on the sample surface. Furthermore, TIC is much lower than Ca for the TenSst  $200 \text{ }^{\circ}\text{C}$  experiment suggesting an additional Ca source to calcite dissolution.

**Table 4.6** – Whole rock composition of the initial sandstone samples as determined by XRF (in wt.%). LOI = loss on ignition.

	TenSst	PfSst
SiO <sub>2</sub>	94.62	82.04
TiO <sub>2</sub>	0.04	0.52
Al <sub>2</sub> O <sub>3</sub>	2.85	7.94
Fe <sub>2</sub> O <sub>3</sub>	0.50	1.87
MnO	0.01	0.01
MgO	0.03	0.38
CaO	0.03	0.93
Na <sub>2</sub> O	0.04	0.17
K <sub>2</sub> O	1.04	4.13
P <sub>2</sub> O <sub>3</sub>	0.02	0.07
LOI	0.83	2.00
Sum	100.02	100.05

The experimental fluid also contained various amounts of dissolved iron (up to  $64 \text{ mg l}^{-1}$ ). The iron derives partly from dissolved illite but probably mostly from the steel vessel. The surface of the autoclave vessel has been slightly tarnished during the experiments, building a passivation layer on its surface. The iron dissolution reaction consumes protons and controls the redox conditions during the experiments. It is difficult to separate the effect on the pH caused by the reaction of the fluid with the steel from the effects caused by the silicate alteration reactions. The steel vessel is responsible for reducing conditions during the experiment, which has the consequence that iron remains in solution as Fe<sup>2+</sup>-chloride.

The pH did not change significantly during the experiments. The initial pH of the 2 molal Na-Cl solution has been 5.5, measured at  $25 \text{ }^{\circ}\text{C}$  and a computed initial pH of 5.5 at both  $200 \text{ }^{\circ}\text{C}$  and  $260 \text{ }^{\circ}\text{C}$ . During the experiments pH changed to values of 6.3–6.8 at experimental temperatures, except for the TenSst  $260 \text{ }^{\circ}\text{C}$  experiment (i.e. pH of 4.5 at  $260 \text{ }^{\circ}\text{C}$ ).

The pH for the TenSst  $260 \text{ }^{\circ}\text{C}$  experiment is implausible for the system of progressing silicate reactions. It is distinctly lower than that of all other experiments, even for the same rock sample with an experiment temperature of  $200 \text{ }^{\circ}\text{C}$ . Thus, due to the same experimental setup for all experiments, it can not be explained by the oxidation of iron from the vessel. However, one possibility could be the oxidation of sulfides, accumulated in one of the rock cylinders used during this experiment. For modeling of the fluid data, a pH value for the TenSst fluid of the  $260 \text{ }^{\circ}\text{C}$  experiment was assumed of 6.7. This is in the range of the pH values of the other samples.

#### 4.4.3 MINERAL SATURATION STATES

The mineral saturation state *SI* for relevant minerals has been calculated using GWB (Bethke & Yeakel, 2015) and is listed in Table 4.7.

The experimental solutions are close to saturation with quartz and have no driving force to dissolve more quartz. The fluids are also close to equilibrium with K-feldspar and are undersaturated with respect to kaolinite and illite. The fluids are clearly oversaturated with analcime and albite and have a tendency to precipitate these minerals. The *SI* of analcime is lower than that of albite, indicating that albite is more stable than analcime under experimental conditions. Thus, analcime forms as a metastable phase. This conclusion is in good agreement with the observed quartz saturation of the experimental fluid. The assemblage analcime + quartz is metastable relative to the stable assemblage albite + quartz at all experimental conditions (Fig. 4.6a). K-feldspar does not show massive dissolution structures and only local and minor albitization. Kaolinite and illite are dissolving in the experimental fluid. Massive formation of metastable analcime in all experiments instead of stable albite suggests that the critical oversaturation for analcime is significantly below that of albite. At the critical oversaturation analcime starts to nucleate and grow spontaneously.

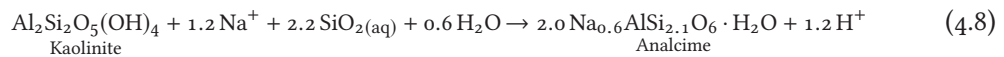
**Table 4.7** – Saturation Indices (*SI*) of selected minerals. Calculated from fluid data with GWB (Bethke & Yeakel, 2015). TenSst\* with adjusted pH value.

Rock Exp. T	PfSst 200 °C	PfSst 260 °C	TenSst 200 °C	TenSst 260 °C	TenSst* 260 °C
Quartz	0.15	0.09	0.04	0.15	0.15
K-feldspar	-0.14	-0.15	0.05	-0.42	-0.05
Albite	1.75	1.40	1.87	1.59	1.96
Muscovite	0.16	-0.43	0.74	2.91	-0.35
Paragonite	1.37	0.48	1.88	4.29	1.03
Kaolinite	-0.67	-1.46	-0.50	2.27	-1.36
Illite	-0.83	-0.70	0.00	1.40	-0.37
Analcime	1.33	0.96	1.55	1.09	1.46
Calcite	-0.56	-1.12	-0.47	-	-

The fluid compositions of the PfSst experiments are not far from saturation with respect to muscovite. The fluids are slightly oversaturated in the 200 °C samples and slightly undersaturated in the 260 °C samples. The respective Na-mica paragonite is oversaturated for both temperatures of the PfSst experiments. However, by taking in account all obtained data, K<sup>+</sup>-Na<sup>+</sup> ion replacement in muscovite in the samples after the experiments is very small.

#### 4.4.4 OVERALL NET MASS TRANSFER AT SAMPLE SURFACE

The dissolution of kaolinite (Eq. 4.2) and illite (Eq. 4.3) and the formation of analcime (Eq. 4.6) and chlorite can be combined to the following Al and Mg balanced equations:



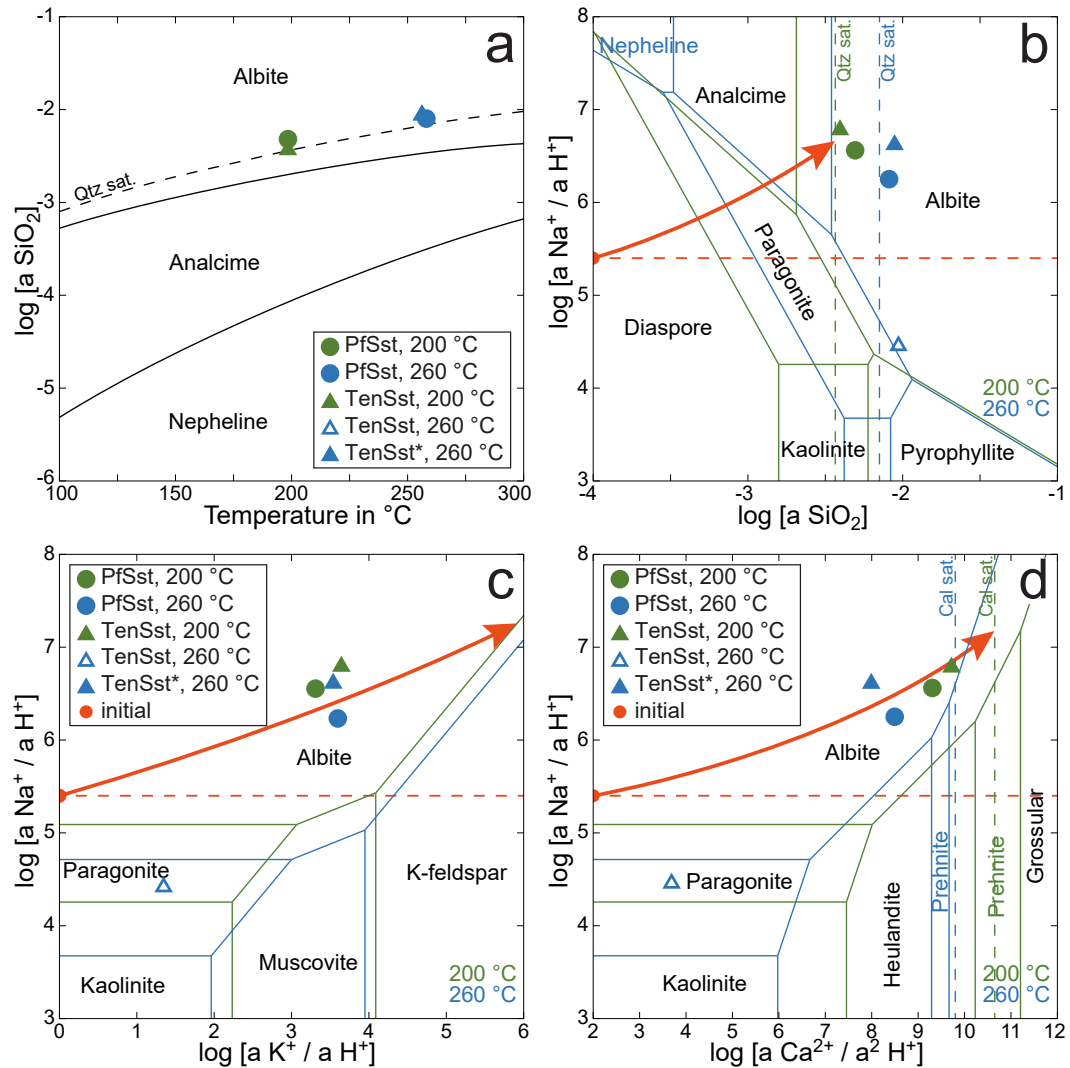
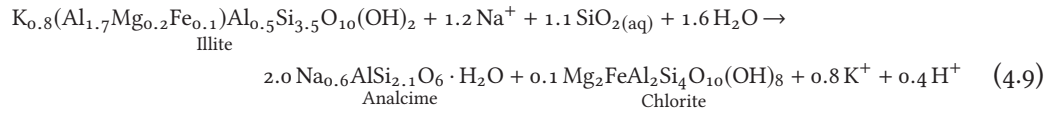


**Figure 4.6** – Activity diagrams for 200 °C (green) and 260 °C (blue) with data points of the experiment solutions showing Al balanced equilibria. Red points indicates the starting points of the reaction paths (red arrows). (a)  $\log [a_{\text{SiO}_2(\text{aq})}]$  vs. temperature, (b)  $\log [a_{\text{Na}^+} / a_{\text{H}^+}]$  vs.  $\log [a_{\text{SiO}_2(\text{aq})}]$  (legend similar to (b)), (c)  $\log [a_{\text{Na}^+} / a_{\text{H}^+}]$  vs.  $\log [a_{\text{K}^+} / a_{\text{H}^+}]$ , (d)  $\log [a_{\text{Na}^+} / a_{\text{H}^+}]$  vs.  $\log [a_{\text{Ca}^{2+}} / a_{\text{H}^+}^2]$ . Calculated with GWB (Bethke & Yeakel, 2015) and the LLNL database thermo.tdat. TenSst\* with adjusted pH value.

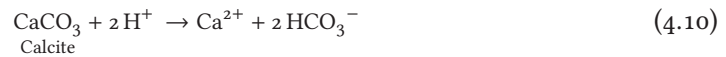


The reactions have been Al and Mg balanced because of the very low concentrations in the fluid implying that Al and Mg are locally redistributed from reactant to product minerals. The derived transfer reactions describe the deduced analcime and chlorite formation from primary diagenetic kaolinite and illite of the sandstones (Fig. 4.5a–c). Newly formed analcime crystals enclose diagenetic hematite particles and remains of clay minerals (Fig. 4.4b + c) from the sandstone cementation. The overgrowth textures, combined with the fact, that clay mineral dissolution is the only Al source in the system, give strong hints, for the consumption of illite and kaolinite by the formation of analcime.

The calculated amounts of quartz to reach quartz saturation (GWB, Bethke & Yeakel, 2015) in the fluid volume of the experiments (350 ml) are 27 mm<sup>3</sup> and 50 mm<sup>3</sup> for the 200 °C and 260 °C experiments, respectively. Comparing these values to surface area of quartz, which is exposed to the solution during the experiments, an alteration depth of few μm (about 7–30 μm) into the quartz grains is sufficient to produce a quartz saturated solution. The quartz surface area has been estimated by its modal volumetric percentage of the lateral area and one base area of the sample cylinders, which certainly is an assumption of a minimum quartz area in contact with the solution. Consequently, the observed deep dissolution features of the quartz grains (Fig. 4.3a–c), much deeper than ~30 μm, must be related to SiO<sub>2(aq)</sub> consuming processes such as the analcime formation described by the reactions Eq. 4.8 and 4.9.

The net transfer equations show that the deduced loss of SiO<sub>2(aq)</sub> can be explained by the formation of analcime. Both reactions lead to a net consumption of Na<sup>+</sup>, SiO<sub>2(aq)</sub> and H<sub>2</sub>O from the fluid. The illite to analcime reaction releases K<sup>+</sup> and produces a small amount of secondary chlorite as a byproduct. Both reactions produce H<sup>+</sup> and tend to decrease pH during reaction progress. The data shown in Table 4.4 are inconclusive with respect to pH changes because additional reaction between the fluid and the steel container probably masks the direction of proton transfer of the silicate reactions. Furthermore, the amount of H<sup>+</sup> produced as predicted by Eq. 4.8 and 4.9 depends on the stoichiometry of the analyzed analcime. The minerals tend to loose Na<sup>+</sup> during analysis under the electron beam. Precipitation of stoichiometric analcime would produce more H<sup>+</sup> and decrease pH.

The reaction fluid contains Ca<sup>2+</sup> and inorganic carbon derived from calcite dissolution:



Calcite dissolution efficiently controls and increases the pH during the progress of the experiments. Both silicate net reactions (Eq. 4.8 and 4.9) decrease pH, the carbonate reaction (Eq. 4.10) increases pH during reaction progress. Using the PfSst experiment as an example, the amount (Table 4.4) of dissolved calcium (from Eq. 4.10) and potassium (from Eq. 4.9) is 3.85 meq/l Ca<sup>2+</sup> and 1.3 meq/l K<sup>+</sup>, respectively. Therefore, during the experiment, illite dissolution produces 0.65 meq/l H<sup>+</sup> by Eq. 4.9, calcite dissolution consumes 3.85 meq/l H<sup>+</sup> by Eq. 4.10. Clearly calcite dissolution (Eq. 4.10) efficiently controls the pH at experimental

temperature. This is consistent with calculated pH values with and without calcite saturation in the system (calculated with PHREEQC and the LLNL database, Parkhurst & Appelo, 2013).

#### 4.4.5 REACTION MODELS AND CONSEQUENCES FOR RESERVOIR PERMEABILITY

Precipitation of metastable analcime in all experiments suggests that it nucleates and grows rather than albite, sodium mica or sodium zeolites (e.g. natrolite). Likewise, primary clay minerals, muscovite and K-feldspar are predicted to dissolve (Table 4.7). Additionally, albite is more stable than K-feldspar resulting in the observed formation of albite at the expense of K-feldspar (Fig. 4.3f).

These relationships can be depicted on standard activity diagrams (Fig. 4.6). The standard state used on the diagrams refers to unit activity for a hypothetical one molal solution at infinite dilution.

In the Na–Si system (Fig. 4.6b) the reaction path begins schematically at low  $\log[a_{\text{SiO}_2(\text{aq})}]$  and at  $\log[a_{\text{Na}^+}/a_{\text{H}^+}] \sim 5.4$  for both temperatures (indicated by a red dot on Fig. 4.6b). The reaction path closely follows the conditions given by the 2 molal Na-Cl solution (red horizontal dashed line). With increasing  $\text{SiO}_2(\text{aq})$  in the solution resulting from quartz dissolution and other silicate reactions analcime may start to form in its stability field. The mineral continues to grow along the path (red arrow) and continues growing as a metastable phase after the path crosses the boundary to the albite field. Although the transformation  $\text{Anl} \rightarrow \text{Ab}$  is tendentially favored based on *SI* calculations (Table 4.7) and the activity diagram (Fig. 4.6b) the reaction does not occur (is not detected) during the experiments. The path ends at the saturation conditions for quartz where metastable analcime coexists with stable quartz. The reaction path (red arrow) reflects the pH increase caused by calcite dissolution (Eq. 4.10).

The reaction path in the Na–K system for quartz saturation (Fig. 4.6c) predicts albite formation throughout. The observed analcime is a metastable phase at quartz saturation. The path ends at the albite–K-feldspar boundary if the system reaches equilibrium of reaction Eq. 4.5. However, the reaction does not reach equilibrium in our experiments. Computed Na-K temperatures (Verma & Santoyo, 1997) are far too low. At equilibrium the fluid would contain  $3.5 \text{ g l}^{-1} \text{ K}^+$  at  $200 \text{ }^\circ\text{C}$  and  $7.1 \text{ g l}^{-1}$  at  $260 \text{ }^\circ\text{C}$ . Also here, the path reflects the pH increase caused by calcite dissolution (Eq. 4.10).

Also in the Na–Ca system the reaction path, deduced by the measured fluid composition, crosses the albite field corresponding to the field of metastable analcime (Fig. 4.6d). Reaction ends before a stable Ca-silicate (prehnite at  $200 \text{ }^\circ\text{C}$ , grossular at  $260 \text{ }^\circ\text{C}$ ) starts precipitating. Calcite dissolution during progress of the overall reaction causes the pH to increase.

#### ALBITE FORMATION

For the formation of albite two possible mechanisms were introduced above. (1) Albitization of primary K-feldspar by cation replacement and (2) precipitation of albite from solution overgrowing the primary K-feldspar.

In our samples we observe albite rimming primary K-feldspar, measured by EDX on the

sample surface (Fig. 4.3d + e) and with EMP in thin sections (Fig. 4.3f). The grain shape and the morphology of the feldspars in samples after the experiments is similar to that of initial K-feldspar. The grain structure of the feldspar in Fig. 4.3f has an irregular surface with sub-rounded corners and edges, which match very well with the surrounding quartz clasts. This implies, that the initial grain shape has not changed much during the alteration experiments. Thus, albitization of primary K-feldspar occurs by ion replacement (Eq. 4.5) preserving the existing grain shape.

The albite rims on K-feldspar grow by diffusion of sodium into the primary feldspar and the counter-diffusion of potassium to the grain surface where it is released to the fluid. This slow transport limited process does not equilibrate reaction Eq. 4.5 (Fig. 4.6c). Equilibrium would require a large transfer of K to the fluid (equilibrium:  $3.5 \text{ g l}^{-1} \text{ K}^+$  at  $200^\circ\text{C}$  and  $7.1 \text{ g l}^{-1} \text{ K}^+$  at  $260^\circ\text{C}$ ). Our sandstone samples do not contain sufficient modal amounts of K-feldspar to ever reach feldspar exchange equilibrium with the given 2 molal Na-Cl solution.

#### MINERAL REACTION RATES

Mineral dissolution rates derived from experiments with high saline solutions differ significantly from those obtained from studies using pure water (e.g. feldspar: Stillings & Brantley (1995); quartz: Dove & Crerar (1990) and Newton & Manning (2000)). Dissolution features observed on quartz in our experiments are very prominent compared with K-feldspar and muscovite where these features are marginal (Fig. 4.3). The data suggest that the reaction rate of quartz is significantly increased in experiments with 2 molal Na-Cl solution relative to experiments using pure water.

Dissolution rate constants at  $25^\circ\text{C}$  in low TDS fluids show the order  $\text{Qtz} < \text{Ms} < \text{Kfs}$  (Dove & Crerar, 1990; Lasaga et al., 1994), our experiments suggest rate constants at elevated temperature and 2 molal Na-Cl in the sequence  $\text{Ms} < \text{Kfs} \ll \text{Qtz}$ . The observations are consistent with Stillings & Brantley (1995) who found a decrease of the dissolution rate for feldspars (K-feldspar and albite) with increasing  $\text{Na}^+$  concentration in the solution. The authors explain this by the competition of  $\text{Na}^+$  and  $\text{H}^+$  for the cation exchange sites at feldspar surface. Accordingly, Blake & Walter (1999) see an increase of quartz dissolution rate and a decrease of feldspar (orthoclase, albite) dissolution rates in experiments conducted with near-neutral Na-Cl solutions (up to 2 M) and temperatures of  $70\text{--}80^\circ\text{C}$ . Additionally, Dove (1994) showed the dependency of quartz kinetics on the  $\text{Na}^+$  concentration in solution (up to 0.3 M) at different pH and for temperatures up to  $300^\circ\text{C}$ . The quartz dissolution rate increased several orders of magnitude for Na-rich solutions compared to pure water. Dove & Crerar (1990) explained this circumstance by the disturbance of the mineral-solution interface (siloxane complexes) due to elevated alkali concentrations in the solution.

The details and extent of the observed rock alteration effects in our experiments are related to the used high salinity fluid. Using deionized water (11 d), Bertrand et al. (1994) observed no secondary precipitates in water-rock interaction experiments with sandstones at  $150^\circ\text{C}$ . The authors found that the major mass transfer process between the solid samples and fluid was the dissolution of illite, similar to our experiments. However, quartz dissolution, albitization of K-feldspar and analcime precipitation, observed in our experiments,

are different and can be attributed to the different compositions of the reaction fluid.

Rock alteration along fracture surfaces also depends strongly on temperature. The experimental reaction of sandstones (qtz, plg, kfs, ms, ilt, hem) with synthetic, highly saline solution at 40 °C by Fischer et al. (2011) did not dissolve quartz or muscovite. In the initial sandstone samples of Fischer et al. (2011) analcime is one of the cement minerals. It showed no reactivity during the experiments, including no further precipitation from solution. The authors found newly formed, euhedral albite crystals on the sandstone surface, however, only in experiments with CO<sub>2</sub> (Fischer et al., 2010).

#### *ANALCIME PRECIPITATION PROCESS*

Although the crystal structure of analcime resembles that of feldspathoids it is often discussed together with zeolites because of similar assemblages and analogous conditions of formation. In the following, the term zeolite includes analcime. Zeolite formation is typically linked to the alteration of volcanoclastic glass. Nevertheless, zeolites may also form in many other types of rocks and geologic environments include granitic rocks and very low grade metamorphism of crystalline basement (Bish & Ming, 2001). Zeolites typically replace clay minerals, feldspars and feldspathoids (Hay & Sheppard, 2001; Weisenberger & Bucher, 2010; Wilkin & Barnes, 2000).

Zeolitization of detrital authigenic minerals has been observed in sandstones and mudstones, reacting with, mostly alkaline, highly saline lacustrine fluids in low-T diagenesis (e.g. Do Campo et al., 2007; Hay & Sheppard, 2001). Analcime precipitation has also been reported from environments with near-neutral fluids with high concentrations of Na, Cl, SO<sub>4</sub> and TDS >200 mg l<sup>-1</sup> (English, 2001). Precipitation of analcime from a Na-rich brine has been described by English (2001), who postulated an analcime crystallization from an amorphous to gelatinous aluminosilicate precursor, which is an interim material from primary kaolinite, smectite and feldspar degradation at reaction temperatures of ambient conditions. Other examples for low-T diagenetic analcime formation by the reaction of clay minerals (illite, smectite) with saline fluids are given by Gall & Hyde (1989) (Carboniferous Rocky Brook Fm., Newfoundland, Canada). A direct reaction of montmorillonite and probably illite to analcime was observed by Hay & Sheppard (2001).

The formation of analcime in our experiments proceeds at the expense of authigenic kaolinite and illite (Eq. 4.8 + 4.9), which requires a degradation of these mineral phases. The high Na<sup>+</sup> concentration of our experiments causes an environment, where authigenic clay minerals become unstable. This can be easily discerned, considering stability diagrams of Fig. 4.6 (see also Do Campo et al., 2007). The experiments of Bauer et al. (1998) show as well increased kaolinite dissolution rates in high molar KOH solutions at 35 °C.

Conclusively, the high Na<sup>+</sup> concentration of the experimental fluid caused, on the one hand, the degradation of the primary kaolinite and illite providing the necessary Al(OH)<sub>4</sub><sup>-</sup> for the formation of analcime. On the other hand, the solution provides Na<sup>+</sup> and H<sub>2</sub>O for analcime precipitation. In addition, the high (Na<sup>+</sup> + K<sup>+</sup> + Ca<sup>2+</sup>)/H<sup>+</sup> ratio of the fluid supports the precipitation of zeolite phases and suppresses formation of secondary clay minerals (Hay & Sheppard, 2001). The type of phases forming, zeolites or clay minerals, is highly dependent on the activities of dissolved species in the fluid (English, 2001; Hay & Sheppard,

2001). Namely,  $H^+$ , alkali and alkaline-earth ions, silica and aluminum ( $Al(OH)_4^-$ ) are the determining factors.

At the temperature of 200 °C in our experiments the conditions are metamorphic (zeolite facies) rather than diagenetic (Bucher & Grapes, 2011). The Upper Rhine Graben reaches these conditions of burial metamorphism at a depth of about 5 km. The experiments show that at the beginning of metamorphism authigenic minerals in the sandstones are replaced by analcime or potentially Na-zeolites such as natrolite in the presence of saline formation fluids. In low-TDS fluids, the Ca-zeolites stilbite or heulandite (Fig. 4.6d) may form at the same temperature (Weisenberger & Bucher, 2010). The experimental temperature of 260 °C corresponds to the upper zeolite facies. Here, laumontite is the stable Ca-zeolite in fractured granitic rocks and sandstones together with low-TDS fluids. Together with Na-Cl-rich formation brine analcime will still be a stable sodic phase at quartz undersaturation. However, Na-zeolites may form alternatively depending on the individual solution composition (Chipera & Apps, 2001). In low-TDS or  $CO_2$ -rich fluids kaolinite is still stable together with quartz (Higgs et al., 2015). It will decompose to pyrophyllite at 270 °C. The boundary marks the upper limit of the zeolite facies and the beginning of prehnite pumpellyite facies metamorphism. We remain under the upper kaolinite boundary by 10 °C in our experiments. Pyrophyllite has not been reported to our knowledge from any core material in deep bores into sandstone formations of the URG. This suggests that the considered Permian and Triassic sandstones remained below 270 °C during the entire geological evolution of the region.

#### 4.4.6 EXPERIMENT RESULTS AT RESERVOIR SCALE

Albitization of K-feldspar and the presence of analcime have been reported from sandstone core samples of the Stuttgart Formation (Förster et al., 2010) and interpreted as diagenetic (hydrothermal) features. This mineral assemblage in a natural geothermal reservoir unit fits very well with the product phases of our experiments. Thus we conclude, the reactions in our experiments can be transferred to natural sandstone reservoirs. Requirements for these processes are (1) the occurrence of clay minerals as reactants together with quartz, (2) elevated temperatures, (3) a high saline brine and (4) fluid pathways throughout the reservoir rocks. All these conditions occur, or are even prospected for geothermal applications (high T, fluid pathways) in natural sandstone reservoirs.

The influence of the major alteration reactions (kln/ilt with qtz to anl) on the rock permeability can be estimated by a simple volume calculation of the involved solid phases. The reaction of 1 mol kaolinite to 2 mol of analcime, including the dissolution of the required 2.2 mol of quartz (Eq. 4.8), causes a volume increase of the solids of 27 %. The solid volume for the reaction of 1 mol illite with 1.1 mol quartz to 2 mol analcime and 0.1 mol chlorite (Eq. 4.9) increases by 20 %. The standard molar volume data are taken from Anthony et al. (2015).

The consequences of the fluid-rock interaction on the fracture permeability of the reservoir have been schematically summarized in Fig. 4.7. After fracture formation the pore space is filled with a saline brine residing in the reservoir (Fig. 4.7a). This brine migrates along the fracture as a result of topographically produced pressure heads in the Upper

Rhine Graben (Stober & Bucher, 2015; Stober et al., 1999). The permeability is given by the initial aperture distribution along the fracture. Along the flow path reactive authigenic minerals, kaolinite and illite, are exposed to the brine together with quartz and feldspar (Fig. 4.7a). The progressing reactions between the brine and the exposed solids continuously alter the structure of the fracture and the minerals exposed to the brine (Fig. 4.7b). Initially, dissolution of quartz produces additional porosity. Kaolinite and illite have been completely removed from the fracture surfaces along the flow path. This adds additional porosity to the fracture in early stages. Analcime nucleates after the solution becomes critically oversaturated with respect to this mineral. Our experiments show that numerous small crystals form if oversaturation is large and the nucleation rate is high. Fewer large analcime crystals grow from moderately oversaturated solutions where nucleation rate is low (see also Wilkin & Barnes, 2000). Massive analcime growth along the fracture reduces porosity in the successive stage. The net mass transfer among the solids causes a volume increase of the solids by 20 to 30 vol.% depending on the dominant reaction. Alteration of the fracture surface results in severe damage to the structural coherence of the rock surface. Small fragments of relict primary minerals can be detached from the surface and carried along with the fluid. These fines can accumulate along the flow path where fracture aperture narrows (Fig. 4.7) and clog the flow path. During reaction progress the aperture distribution is dynamically adjusted and the permeability evolution follows these adjustments. Stober & Bucher (2015) described that the permeability changes caused by a single fracture tends to first increase as a result of dissolution of primary minerals and to decrease later because of precipitation of new minerals. This general permeability development also follows from the experiments of this study for the geothermal reservoir sandstones typical of the URG containing reactive primary diagenetic minerals.

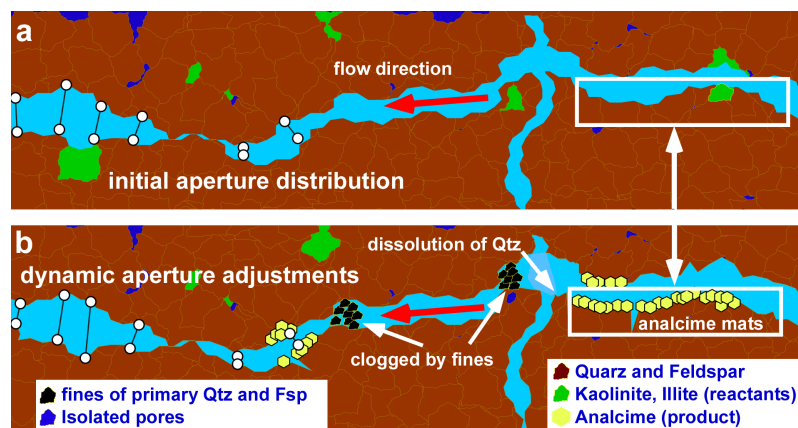


**Figure 4.7** – Schematic cartoon showing (a) the initial structure of a fracture system in sandstone and (b) the structure of the fracture system with permeability relevant features after reaction with a saline brine at reservoir temperatures as observed in the reported experiments. The white rectangle marks a possible portion of the fracture that has been used in the experiments.

## 4.5 CONCLUSION

The experimental data and observations show that significant geochemical, textural and mineralogical alteration of fracture surfaces in sandstone occurs after relatively short reaction time of less than 55 days at 200 °C and 260 °C. The saline formation solution represented by a 2 molal Na-Cl solution in the experiments proved chemically aggressive and reacted with the exposed sandstone vigorously. It dissolved primary minerals of the selected reservoir sandstones and readily precipitated analcime. The reactions also strongly modified the structure and texture of the fracture surface.

## ACKNOWLEDGMENTS

We thank the technicians and staff of the Department of Aquatic Geochemistry for their help and quick fluid analyses. Special thanks to H. Müller-Sigmund and S. Hirth-Walther for their support during the experiments at the Division of Mineralogy and Petrology, University of Freiburg. We are grateful to V. Zibat from the Laboratory for Electron Microscopy (KIT) for the SEM analyses. We would also like to thank U. Gerhards for her help with the electron microprobe at Institute for Micro Process Engineering (KIT). We thank three anonymous reviewers for their thorough and constructive comments which helped to improve our paper considerably. We acknowledge M. Kersten for his support and the editorial handling of the manuscript. This research has been supported by the project *StörTief* (“deep fault zones”) of the German Federal Ministry for Economic Affairs and Energy (BMW, no: 0325623C). The autoclave laboratory at the University of Freiburg has been funded by Baden-Württemberg Programme (PTKA-BWP) grants L75 12002 and L75 14003. We gratefully acknowledge the support of our research.

---

## EXPERIMENTS ON GRANITE ALTERATION UNDER GEOHERMAL RESERVOIR CONDITIONS AND THE INITIATION OF FRACTURE EVOLUTION

---

This chapter is published as: Schmidt, R. B., Bucher, K. & Stober, I. (2018): Experiments on granite alteration under geothermal reservoir conditions and the initiation of fracture evolution. – in: *European Journal of Mineralogy* 30 (5), pp. 899–916. – DOI: [10.1127/ejm/2018/0030-2771](https://doi.org/10.1127/ejm/2018/0030-2771).

### ABSTRACT

The Upper Rhine Graben (URG) hosts favorable conditions for geothermal energy usage in the crystalline basement, where temperatures higher than 200 °C were reached in 5 km depth. Formation fluids in the basement rocks are highly saline and Na-Cl dominated. Natural seismicity or artificial stimulation activity during geothermal reservoir development are able to produce fractures. Subsequently, unaltered rock surfaces get in contact with the brines and a geochemical-mineralogical alteration process will be initiated. The alteration products and the type of mineral reactions on the fracture surfaces have a major influence on the fracture permeability and, thus, the life-time of a geothermal installation.

Autoclave batch-type experiments were carried out to reproduce and comprehend the initial granite alteration processes under conditions found in the URG. We used granite samples with a fresh fractured surface and an intact rock fabric to represent natural fracture surfaces. A 1.5 and 2 molal Na-Cl solution has been used in the experiments, which is compositionally and in salinity strength close to natural URG basement brines. Experiment temperatures were 200 and 260 °C, inspired by maximum URG reservoir temperatures. Solid and fluid samples were investigated before and after the experiments.

One of the main mineral reaction is the dissolution of quartz at the (sub-)surface, weakening the rock fabric and increasing the permeability. Biotite chloritization is the most reactive process in the experiments. Partly chloritized biotites of the initial samples completely transformed into chlorites at sample surfaces. Thereby, hydrobiotite and a corrensite-like mineral phase occur as intermediate phases. The chloritization accompanies with a delamination of the phyllosilicate sheets and therefore, a volume expansion of the mineral grains. Feldspar shows only minor reactions in the experiments. During the autoclave experiments the initial solution changed considerably. It reflects the mineral reactions

---

during the experiments.

Comparison with natural deep basement rocks, e.g. from the German continental deep drilling project (KTB) and the Soultz-sous-Forêts geothermal project, show very similar processes at the beginning of fracture alteration in these settings. In accordance with the observations of alteration features in deep crystalline basement we derive, (1) quartz dissolution and biotite chloritization are the main mineral reactions in the early stages of fracture alteration in deep crystalline basement rocks under geothermal conditions. (2) In these early stages rock fabric will be further weakened by the mineral–brine reactions, resulting in a propagation of the fracture into the adjacent rock and thus, an increased fluid permeability in the early period of the fracture alteration.

## 5.1 INTRODUCTION

In Germany and France, the Upper Rhine Graben (URG) is one of the geological structures that offers favorable conditions for geothermal utilization due to its high heat flow and accordingly high temperatures (Pribnow & Schellschmidt, 2000). The underground in the URG hosts hot water resources at different stratigraphic levels with temperatures up to 250 °C (Sanjuan et al., 2016), which can be used for electricity production and heating purposes. Accordingly, several power plants have been installed in the URG, e.g. Soultz (Genter et al., 2010) and Rittershoffen (Baujard et al., 2017). The encountered URG fluids are usually Na-Cl dominated fluids with total dissolved solids (TDS) up to 200 g l<sup>-1</sup> (e.g. Sanjuan et al., 2016; Stober & Bucher, 2014), often saturated with respect to a range of different minerals (e.g. Pauwels et al., 1993; Sanjuan et al., 2016).

In geothermal settings with low natural permeability faults and fractures are essential for fluid migration through the reservoir. Generally, faults and fractures are associated with enhanced permeability zones and thus providing the necessary pathways for fluid flow. For the lifetime of geothermal facilities it is crucial to sustain the fluid circle in the fracture network of the reservoir rocks throughout the economic lifetime of the power plant. Therefore, it is important to understand the geochemical-mineralogical processes due to the reaction of the rock mineral assemblage with the highly saline brine, as water–rock interaction (WRI) can reduce or increase the effective permeability fundamentally (e.g. Milodowski et al., 1989; Morrow et al., 2001).

Creating new fractures artificially in the geothermal reservoir or naturally due to earthquakes, fracture evolution generally starts with an initial brittle fracture. Thereafter, a reaction period during which permeability increases occurs, which is followed subsequently by a period of decreasing permeability due to sealing with alteration products until the next re-opening of the fractures happen (Stober & Bucher, 2015). In that way, in the Soultz granite unaltered frame rock surrounds alteration zones laterally. The outer alteration zones are characterized by secondary chlorite and hematite precipitation, whereas the inner alteration zone in the fault center is marked by silicate dissolution and the formation of clay minerals and chlorites (Bartier et al., 2008; Schleicher et al., 2006). In the final stage of alteration evolution the faults often are sealed completely by mainly quartz, calcite, chlorites, and clay minerals (Genter & Traineau, 1996; Sausse, 2002).

In this experimental study, we simulate the first steps of alteration of initial fresh granite surfaces with a synthetic reservoir solution (2 molal Na-Cl, 200–260 °C) to understand in detail the WRI-processes at an early alteration stage of fracture surfaces and to deduce its influence on the geothermal fluid circle.

The individual mineral phases interact with each other, and mineral specific alteration reactions affect the rock fabric in different ways. Thus, we used solid granite samples with an intact rock fabric, to get an overall view of the alteration processes, the influence on the early evolution of fracture surfaces under geothermal conditions, and the impact of fluid composition. Relatively few experiments under geothermal reservoir conditions, e.g. highly saline solutions at enhanced temperatures have been conducted, which focus on solid rock samples with an intact fabric.

Many studies have been performed already in the 1980s and 1990s in the context of enhanced geothermal systems (EGS), and its former concept of hot dry rock (HDR) systems, using surface waters for experiment runs, as it was used as fracking, injection, or circulation fluid for these geothermal installations. Therefore, rather low TDS fluids (compared to URG reservoir fluids) were used in these experiments (e.g. Milodowski et al., 1989; Savage et al., 1993; Savage et al., 1992). Also, more recent studies carried out experiments with low TDS solutions (e.g. Kuncoro et al., 2010; Na et al., 2015).

Single mineral phase experiments with highly saline solutions were performed to determine dissolution rates in dependence of fluid TDS (e.g. Fu et al., 2009; Shao et al., 2010; Xie & Walther, 1993). These experiments show the dependency of single mineral-fluid reaction for different fluid salinities and compositions. Since these experiments were carried out with single mineral phases the inter mineral reactions in natural geothermal systems could not be described.

Additionally, many experimental studies were carried out with high saline brines, in the context of CO<sub>2</sub> storage in the subsurface (CCS) (e.g. Hu et al., 2011; Kaszuba et al., 2005; Shao et al., 2010; Shao et al., 2011; Shiraki & Dunn, 2000). Thereby the focus of these studies is on the removal of gaseous or dissolved CO<sub>2</sub> by solid mineral phases, rather than the influence of fluids reacting with the total mineral assemblage and the alteration of rock surfaces, e.g. dissolution and precipitation processes.

The impact of alteration concerning permeability in granitic rocks were studied in the context of radioactive waste disposal (HRWD) (e.g. Moore et al., 1983; Vaughan et al., 1986). But, the experimental conditions were much lower in temperatures and less saline solutions have been used.

Regardless of the topic, HDR, EGS, CCS, or HRWD, mostly granulated rock material or drill cuttings were used in the experiments (e.g. Kuncoro et al., 2010; Milodowski et al., 1989; Na et al., 2015) and rarely the experiments were carried out with rock pieces, large enough to represent the intact rock fabric.

The before mentioned experimental studies show major differences in the reactivity of mineral phases, the dissolution processes of primary minerals and the appearance, type, and amount of secondary minerals, depending mainly on fluid composition, temperature and type (grain size) of single mineral or rock material. The results of prior experimental investigations cannot be transferred directly to geothermal conditions and fluid composi-

tions found in the URG reservoirs. We conducted the experiments with solid rock samples with an intact rock fabric, since the interaction between solid mineral phases and the fluid solution on natural fracture surfaces is expected of crucial importance.

The present paper describes relevant processes under controlled laboratory conditions. It is an experimental research to investigate the reactivity of URG reservoir granite in contact with a synthetic geothermal fluid (1.5–2 molal Na-Cl) in order to determine the reaction paths that control the alteration of primary mineral assemblages, precipitation/formation of new minerals, and fluid evolution in a geothermally/relevant temperature spectrum (200–260 °C).

## 5.2 MATERIAL AND METHODS

### 5.2.1 ROCK MATERIAL

Granite has been used for the experiments as proxy for the crystalline basement rocks found in the deep URG reservoir. The granite has been collected as fresh blocks from a quarry in the Southern Black Forest (Malsburg Granite, MGr). The grain size is fine enough to ensure a representative mineral assemblage in the size of the samples used in the experiments. In the laboratory drill cores with a diameter of 22 mm and 30 mm have been drilled from the blocks, broken perpendicular to the core axis to get a fresh rock surface, and shortened to a height of ~10 mm. The rock cylinders were washed properly under a weak jet of deionized water and dried under laboratory conditions before use in the experiments.

### 5.2.2 SOLUTION COMPOSITION

A 2 molal Na-Cl solution (116.9 g kg<sup>-1</sup>) was prepared with deionized water and NaCl salt and used as reactive solution for the experiments, which approximate the salinity of the URG brines (TDS of 94–200 g l<sup>-1</sup>, Stober & Bucher, 2014). Additionally, a 1.5 molal solution was prepared to study possible influences of lower concentrations. The 2 molal Na-Cl solution already depicts the natural reservoir fluid composition chemically in the URG by 88–94 mol.% (Pauwels et al., 1993). Small amounts of inorganic carbon (alkalinity of <0.1 mmol l<sup>-1</sup>) and O<sub>2</sub> are solved in the initial solution due to contact with the atmosphere. The initial pH of the solution was 5.5 (at 25 °C).

### 5.2.3 EXPERIMENTAL SETUP AND PROCEDURE

Batch-type experiments in a stirred autoclave system (Limbo li, Buechi) were performed (Fig. 5.1). The autoclave vessel and its components in contact with the solution consists of stainless steel (X6NiCrTiMoVB25-15-2, EU standard 10269). The vessel volume is 450 ml, which allows a solution volume of 350 ml, with an atmospheric head space. During the experiments the solution was stirred with a speed of about 100 rpm. Three granite samples were used in each experiment.

The experiments were conducted at 200 °C with the prepared 2 and 1.5 molal solution, and additionally at 260 °C with the 2 molal solution. These temperatures are reported (measured and maximum geothermometer temperatures) from reservoirs in the URG (Aquilina et al.,

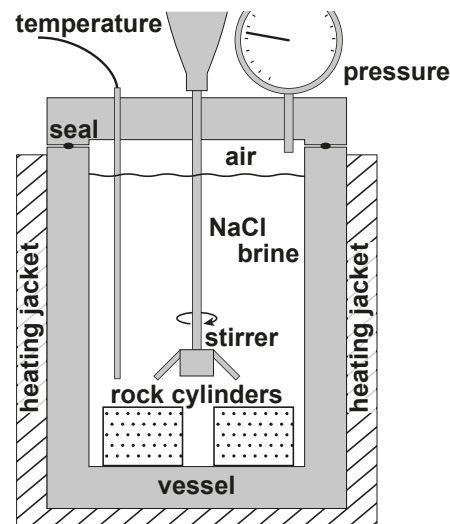


**Figure 5.1** – Schematic illustration of the main components of the used autoclave system Limbo li (Buechi) during a running experiment.

1997; Sanjuan et al., 2016). The pressure was given by the boiling pressures of the Na-Cl solutions at experiment temperatures ( $\sim 16$  bar and  $\sim 44$  bar, respectively). The duration of each experiment was 49 d (2 molal experiments) and 51 d (1.5 molal experiment).

#### 5.2.4 FLUID ANALYTICS

After the experiments the fluid was cooled to room temperature rapidly. Electrical conductivity (Mettler Toledo Inlab 371) and pH (ProMinent PHER-112) were measured immediately and carbonate alkalinity was titrated with 0.01 M HCl. For element analyses the solutions were filtered with 0.45  $\mu\text{m}$  cellulose acetate membranes. The fluid samples were diluted with ultra-pure water by a factor of 10 to ensure solution stability. Additionally, the solutions were acidified with distilled  $\text{HNO}_3$  for cation measurement. Samples were stored in 30 ml polyethylene bottles and preserved cool until analysis.

Major and minor cations were determined by inductively-coupled plasma mass spectrometry (ICP-MS) with a Thermo Fischer Scientific X-Series 2. Sample dilution was 1 : 100. Dissolved Si and Na concentration were analyzed by inductively-coupled plasma optical emission spectrometry (ICP-OES) with a Varian 715ES and a sample dilution of 1 : 200 for Si and 1 : 500 for Na. Ion chromatography (IC) was performed with a Dionex, ICS-1000 for dissolved anions. Due to high concentrations of Cl and a consequential need for high dilution of the sample (1 : 2000), it was not possible to detect other anions than Cl.

Continuously, standard solutions were remeasured during analysis procedure to ensure quality of measurements. Accuracy of ICP-MS measurements is better than 3 % for main cations and better than 8 % for Al and Fe, for ICP-OES better than 5 % and for IC better than 4 %.

#### 5.2.5 SOLID ANALYTICS

Rock samples have been removed from the vessel after solution extraction and washed two times with deionized water to prevent halite precipitation. After both washings, the

samples have been dried at laboratory temperature.

Characterization of the pre- and post-experiment rock samples was performed with several analytical and imaging methods. The mineral content was identified by powder X-ray diffraction (XRD) measurements with a *Bruker D8 Discover*. System parameters were a Cu anode at 40 kV and 40 mA and a silicon strip detector (lynxeye XE-T). The scanning range was 2–82°, with a step size of 0.01° 2 $\theta$ . Unaltered samples were measured as representative bulk material, whereas only surface material of the altered samples was used to identify secondary phases formed during alteration.

Alteration processes on sample surfaces and cross-sectional thin sections were detected and visualized by scanning electron microscopy (SEM) methods with a FEI Quanta 650 ESEM. Surface characterizations were made in secondary electron (SE) mode with an acceleration voltage of 10 kV. Additional, thin sections were examined for alteration reaction textures in the sample interior under back-scattered electron (BSE) mode at the same device setting. Mineral identification and qualitative analyses have been conducted with energy-dispersive X-ray spectroscopy (EDX, Bruker XFlash 5010 detector). Rock samples and thin sections were covered with carbon before SEM analyses.

Electron microprobe (EMP) measurements were carried out with a JEOL JXA-8530F. Calibration was performed on the following natural standards: Al: Al<sub>2</sub>O<sub>3</sub>, Ca + Si: wollastonite, Fe: Fe<sub>2</sub>O<sub>3</sub>, Mn + Ti: MnTiO<sub>3</sub>, K: orthoclase, Na: albite, Mg: MgO, Ba: baryte. Measuring condition were an acceleration voltage of 15 kV, a beam current of 20 nA and a beam diameter of 1  $\mu$ m for all mineral phases except analcime (beam size of 2–4  $\mu$ m depending on grain size). Detection limit was 0.01 wt.%.

#### 5.2.6 GEOCHEMICAL MODELLING AND CALCULATIONS

Measured pH were re-calculated to experiment temperatures with *The Geochemist's Workbench 10.0, react* (GWB, Bethke & Yeakel, 2015) and its standard database (thermo.dat). The complete data of measured fluid composition at 25 °C has been used as input. Thus, the pH re-calculation considers the high salinity of the fluid as well as the total carbon in the system (alkalinity). Saturation states of relevant mineral phases for the solution composition after each experiment have been calculated with GWB (GSS), too.

## 5.3 RESULTS

Analyses of solid and fluid samples reveal significant differences between the starting material and the post-experimental samples. Fluid composition changes, solid samples show alteration features from macroscopic to  $\mu$ m scale and in terms of geochemical composition.

### 5.3.1 INITIAL ROCK SAMPLE

The initial granite (MGr) is homogeneous and medium grained (1–2 mm) with a strong rock fabric (Fig. 5.2a). It is composed of plagioclase, K-feldspar, quartz, biotite, and chlorite. Chlorite occurs inter-stratified in slightly altered biotite. Accessory phases are muscovite, titanite, calcite, hornblende, rutile, apatite, pyrite, zircon, allanite, and monazite. The

mineral modes of rock forming phases are 45 % plagioclase, 22 % K-feldspar, 22 % quartz, 11 % biotite/chlorite, and <1 % accessory phases (Table 5.1). Whole rock composition is listed in Table 5.2. Mineral compositions were determined by EMP measurements (Table 5.3 + 5.4).

**Table 5.1** – Mineral modes in the initial samples (vol.%) and qualitative changes of mineral phases on post-experimental samples.

Rock material Exp. T Solution	bulk initial	surface 200 °C 1.5 M	surface 200 °C 2 M	surface 260 °C 2 M
Quartz	35	--	--	--
K-feldspar	40	-	-	-
Albite	10	+	+	+
Biotite/Chlorite	15	--	--	--
Hydrobiotite	-	++	+	+
Corrensite	-	o	+	++
Chlorite	-	++	++	++
Analcime	-	o	o	+
Sec. Phyllosilicate	-	++	+	+
Accessories	< 1	o	o	o
Sum	100			

++ = strong increase, + = increase, o = no change, - = decrease, -- = strong decrease (on sample surface)

**Table 5.2** – Whole rock compositions of the initial Malsburg Granite.

MGr	wt.%	MGr	ppm
SiO <sub>2</sub>	70.35	S	399
TiO <sub>2</sub>	0.31	Cl	205
Al <sub>2</sub> O <sub>3</sub>	15.05	Rb	217
Fe <sub>2</sub> O <sub>3</sub>	2.02	Sr	269
MnO	0.03	Ba	612
MgO	1.07	Y	10
CaO	1.37	Zr	118
Na <sub>2</sub> O	3.90	La	30
K <sub>2</sub> O	4.49	Ce	61
P <sub>2</sub> O <sub>3</sub>	0.14	Th	19
LOI	1.30		
Sum	100.02		

LOI = loss on ignition.

Feldspars are present in the initial samples as plagioclase and K-feldspar (Fig. 5.3). Former is mostly albite (An 4–8%). Additional oligoclase (An 11–26%) exists in the granite as core of the albite grains. Partly tiny K-feldspar inclusions occur in the albite grains. K-feldspars show albite lamella (Fig. 5.3 + 5.4a), typically for exsolution reactions (Putnis & McConnell, 1980). Initial feldspar compositions from EMP measurements are summarized Table 5.3.

Quartz grains in the initial sample are mostly compact and solid with only small dissolution features. They are closely interconnected with the surrounding mineral grains without any void space (Fig. 5.3).

Biotite is the only mica in the initial granite samples (Fig. 5.4b + b1). Its composition is within the phlogopite–annite solid solution. TiO<sub>2</sub> and BaO occur in minor amounts. Biotites are partly chloritized, where two types of chlorites can be identified in the samples

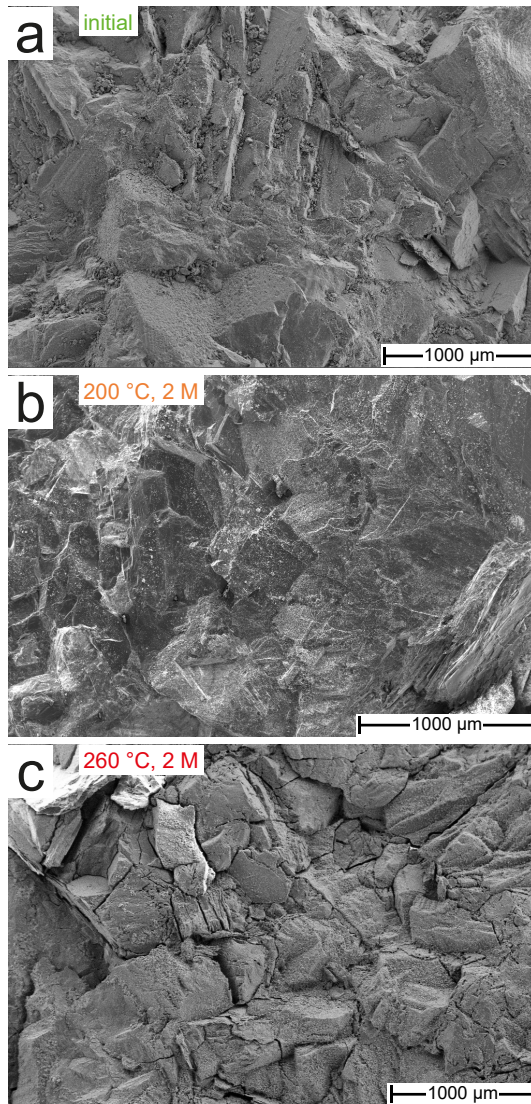


**Figure 5.2** – SEM images of sample surface: (a) Initial rock sample with broken surface, rock fabric appears compact and solid, minerals are sharp-edged. (b) Rock morphology seems to be only slightly modified after the 200 °C experiment (2 molal). (c) Rock fabric is significantly weakened by cracks, mineral edges are rounded in the 260 °C experiment sample.

**Table 5.3** – Mineral composition of feldspars from the initial samples.

Sample	030_15-01	030_15-02	030_15-03	030_15-04	030_15-05	030_15-06	030_15-08	030_15-09	030_15-10	030_15-11	030_15-12
Exp. T	initial	initial									
Mineral	ab	kfs	kfs	ab	ab						
Location	rim	rim	rim	rim	center	center	kfs	kfs	kfs	lamella in kfs	lamella in kfs
SiO <sub>2</sub>	67.93	67.37	66.97	68.06	64.48	64.93	64.53	64.74	64.90	67.88	68.39
TiO <sub>2</sub>	0.02	0.02	<0.01	<0.01	<0.01	<0.01	<0.01	0.03	0.02	<0.01	0.01
Al <sub>2</sub> O <sub>3</sub>	20.62	20.46	20.43	20.35	21.91	21.85	18.65	18.47	18.79	20.33	20.27
FeO	0.10	0.07	0.07	0.13	0.11	0.03	0.11	0.27	0.08	0.09	0.17
MnO	<0.01	<0.01	0.04	<0.01	0.01	<0.01	0.01	<0.01	<0.01	0.01	<0.01
MgO	<0.01	<0.01	<0.01	<0.01	<0.01	<0.01	0.01	0.01	<0.01	<0.01	<0.01
CaO	0.34	0.54	0.59	0.40	2.77	2.49	0.05	0.01	0.03	0.37	0.47
Na <sub>2</sub> O	10.70	10.94	10.93	11.32	9.78	9.92	1.04	0.96	0.88	7.58	6.21
K <sub>2</sub> O	0.16	0.45	0.20	0.19	0.42	0.36	14.63	14.94	13.58	3.71	3.78
BaO	<0.01	0.05	0.03	0.04	0.03	0.06	0.06	0.10	<0.01	0.01	0.08
Total	99.86	99.90	99.27	100.49	99.49	99.64	99.10	99.53	98.28	99.97	99.37
Cation distribution normalized to O <sub>8</sub>											
Si	2.97	2.95	2.95	2.96	2.86	2.87	2.99	3.00	3.01	2.99	3.01
Ti	0.00	0.00	0.00	0.00	0.00	0.00	0.00	0.00	0.00	0.00	0.00
Al	1.06	1.06	1.06	1.04	1.14	1.14	1.02	1.01	1.03	1.05	1.05
Fe	0.00	0.00	0.00	0.00	0.00	0.00	0.00	0.01	0.00	0.00	0.01
Mn	0.00	0.00	0.00	0.00	0.00	0.00	0.00	0.00	0.00	0.00	0.00
Mg	0.00	0.00	0.00	0.00	0.00	0.00	0.00	0.00	0.00	0.00	0.00
Ca	0.02	0.03	0.03	0.02	0.13	0.12	0.00	0.00	0.00	0.02	0.02
Na	0.91	0.93	0.93	0.96	0.84	0.85	0.09	0.09	0.08	0.65	0.53
K	0.01	0.03	0.01	0.01	0.02	0.02	0.87	0.88	0.80	0.21	0.21
Ba	0.00	0.00	0.00	0.00	0.00	0.00	0.00	0.00	0.00	0.00	0.00
Sum	4.96	5.00	4.99	5.00	5.00	5.00	4.98	4.99	4.92	4.91	4.84
An	0.02	0.03	0.03	0.02	0.14	0.12	0.03	0.01	0.02	0.03	0.04

Total Fe as FeO. ab = albite, kfs = K-feldspar, An = anorthite component.

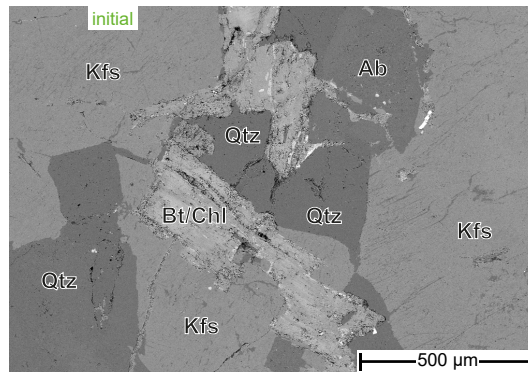


**Figure 5.3** – SEM image of the initial Malsburg Granite: solid rock fabric with major phases K-feldspar (Kfs), albite (Ab), quartz (Qtz) and partly chloritized (Chl) biotite (Bt). Quartz grains are compact and solid, K-feldspar shows albite exsolution lamella, and albite is often zoned with a Ca-richer core.

in terms of chemical composition. Type 1 is characterized by higher amounts of SiO<sub>2</sub>, lower concentrations of MgO and FeO, and higher TiO<sub>2</sub> and K<sub>2</sub>O contents, whereas chlorite type 2 has lower values of Si, higher concentrations of MgO and FeO, and lower concentrations of TiO<sub>2</sub> and K<sub>2</sub>O (Fig. 5.4b2 + b3). Both types of chlorite contain slight amounts of CaO.  $Mg\#$  ( $Mg / (Mg + Fe^{2+})$ ) is almost constant over all phyllosilicates, biotite and both types of chlorite (about 0.45–0.54). Type 1 chlorite is compositional closer to biotite and is located more inter-stratified with biotite, whereas chlorite type 2 is rather located at the rims of the mineral grains, but not exclusively. Thus we interpret, that chlorite type 1 is a potentially intermediate product of chloritization of primary biotite to type-2 chlorite (Fig. 5.4b1–b3). Chemical composition of the initial phyllosilicate series is summarized in Table 5.4. Geothermometer calculations for biotites, based on the Ti concentration and  $Mg\#$  (Henry, 2005), give formation temperatures of about 725 °C. Chlorite geothermometer temperatures (based on cation site occupancies, Cathelineau, 1988) are about 210–230 °C

**Table 5.4** – Mineral composition of biotite and chlorites from the initial samples.

Sample Exp. T Mineral	030_06-10 initial bt	030_06-11 initial bt	030_06-12 initial bt	030_06-19 initial bt	030_06-16 initial chl-T1	030_06-18 initial chl-T1	030_06-13 initial chl-T2	030_06-14 initial chl-T2	030_06-15 initial chl-T2	030_06-17 initial chl-T2
SiO <sub>2</sub>	36.75	36.63	36.04	36.67	30.08	29.36	28.26	28.05	27.51	27.11
TiO <sub>2</sub>	4.04	3.98	3.98	3.92	2.07	1.69	0.19	0.06	0.08	0.09
Al <sub>2</sub> O <sub>3</sub>	15.67	15.63	15.64	15.53	16.81	17.54	17.20	16.96	18.69	19.21
FeO	18.32	17.77	18.02	17.79	21.49	22.05	23.60	24.18	23.89	23.93
MnO	0.28	0.24	0.30	0.32	0.33	0.38	0.41	0.40	0.37	0.43
MgO	9.61	10.42	10.33	10.43	13.98	13.88	15.27	15.38	14.70	14.11
CaO	0.06	0.09	0.12	0.04	0.24	0.13	0.16	0.22	0.14	0.11
Na <sub>2</sub> O	0.19	0.24	0.21	0.24	0.07	0.03	0.02	<0.01	<0.01	<0.01
K <sub>2</sub> O	7.55	8.49	8.30	8.67	1.29	1.10	0.11	0.05	0.04	0.04
BaO	0.50	0.45	0.54	0.48	0.05	0.09	<0.01	0.02	0.01	<0.01
Total	92.97	93.92	93.48	94.08	86.40	86.27	85.21	85.31	85.43	85.03
Cation distribution normalized to O <sub>10</sub> (OH) <sub>2</sub> for micas, and O <sub>10</sub> (OH) <sub>8</sub> for chlorites.										
Si	2.84	2.81	2.79	2.82	3.16	3.10	3.04	3.02	2.95	2.92
Ti	0.23	0.23	0.23	0.23	0.16	0.13	0.02	0.00	0.01	0.01
Al	1.43	1.41	1.42	1.41	2.08	2.18	2.18	2.15	2.36	2.44
Fe	1.18	1.14	1.16	1.14	1.89	1.95	2.12	2.18	2.14	2.16
Mn	0.02	0.02	0.02	0.02	0.03	0.03	0.04	0.04	0.03	0.04
Mg	1.11	1.19	1.19	1.19	2.19	2.18	2.45	2.47	2.35	2.27
Ca	0.01	0.01	0.01	0.00	0.03	0.01	0.02	0.03	0.02	0.01
Na	0.03	0.04	0.03	0.04	0.01	0.01	0.00	0.00	0.00	0.00
K	0.74	0.83	0.82	0.85	0.17	0.15	0.01	0.01	0.01	0.01
Ba	0.02	0.02	0.02	0.02	0.00	0.00	0.00	0.00	0.00	0.00
Sum	7.60	7.69	7.70	7.71	9.73	9.76	9.87	9.90	9.87	9.85
Mg#	0.48	0.51	0.51	0.51	0.54	0.53	0.54	0.53	0.52	0.51
R <sup>2+</sup>	–	–	–	–	4.11	4.17	4.60	4.69	4.53	4.46
R <sup>3+</sup>	–	–	–	–	2.38	2.42	2.22	2.18	2.38	2.46

Total Fe as FeO. bt = biotite, chl-T1 = type-1 chlorite, chl-T2 = type-2 chlorite. Mg# = Mg / (Mg + Fe), R<sup>2+</sup> = Mg + Fe<sup>II</sup> + Mn, R<sup>3+</sup> =  $\frac{1}{3}(28 - 2R^{2+} - 4Si)$ .

and 250–280 °C for type-1 and type-2 chlorites, respectively.

Apatite is enclosed in quartz and K-feldspar grains, and it occurs near the phyllosilicates. Pyrite and titanite appear mostly in the vicinity of biotite/chlorite (Fig. 5.4b). Calcite is found in small fissures mostly near the phyllosilicates (Fig. 5.4b).

### 5.3.2 SAMPLES AFTER THE EXPERIMENTS

On a macroscopic scale the samples show marked alteration reactions. Biotite changed color completely from dark brownish to greenish-brown. The feldspar grains are of dull color. Brownish precipitates occur on the sample surface. Rock fabric of granite samples was weakened during the experiments (Fig. 5.2b + c) and the samples crumble easily.

#### QUARTZ

The initially smooth conchoidal quartz grains show intense dissolution features after the experiments under the electron microscope. Quartz dissolution is widespread over the whole surface of the exposed grains and reaches deep into the grain interior in all samples. In the samples of the 200 °C 2 molal experiment large parts of the quartz surface are covered by deep triangular etch pits with an extension of up to 40 μm (Fig. 5.5a). Whereas at samples from the 1.5 molal experiment the quartz surface shows wormhole-like dissolution features (Fig. 5.5b). Similarly, triangular etch pits are omnipresent in quartz grains of the 260 °C (2 molal) experiment (Fig. 5.5c). The intensive quartz dissolution into the sample interior can be observed in thin sections for both experiment temperatures (Fig. 5.5d). Here, quartz dissolution is located at grain boundaries as well as within the grain interior.

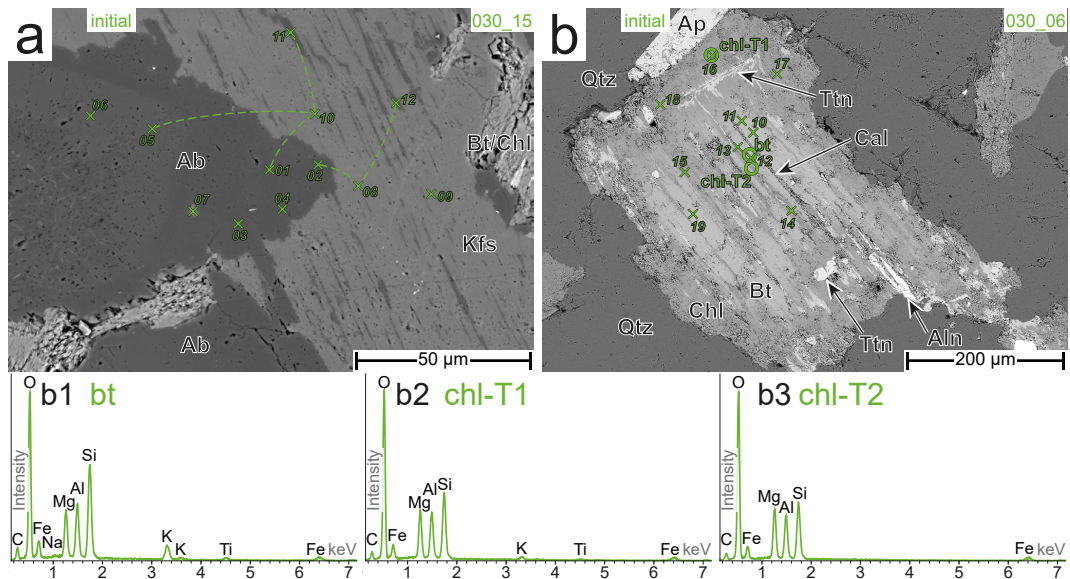


**Figure 5.4** – SEM image of the initial Malsburg Granite samples: (a) Initial feldspars: albite (Ab) show a zonation of slightly enriched Ca concentrations in the core. K-feldspar has exsolution lamella of albite. Green numbers correspond to EMP measuring points in Table 5.3. Dashed lines mark the two-feldspar geothermometer pairs. (b) Initial biotite/chlorite with EDX spectra of biotite (b1), type-1 chlorite (b2) and type-2 chlorite (b3). EDX measuring points marked with green circles, green numbers correspond to EMP measuring points in Table 5.4. Accessory apatite (Ap) titanite (Ttn), calcite (Cal) and allanite (Aln, Ca-REE-silicate) occur in the vicinity of the phyllosilicates.

#### FELDSPARS

The feldspars in the post-experiment samples show no morphological changes. The edges are still sharp and crystal faces well developed without any dissolution features. Some K-feldspars seems to be surrounded by albite at several spots of the mineral surfaces from the 260 °C experiment (Fig. 5.6), which could imply an albitization reactions of the K-feldspars at the outer-most rim of the sample–fluid interface. But, since the initial K-feldspar shows pre-experiment albite lamella due to exsolution reactions, albitization of K-feldspar cannot be verified by the observations in thin sections. The albite rim could also be an effect of coincidentally breaking through an albite lamella in K-feldspar during sample preparation. On the other hand, in the samples of the 200 °C experiments no albite rims at K-feldspar can be observed. Feldspar composition of post-experimental samples is listed in Table 5.5.

#### PHYLLOSILICATES

The primary (partly chloritized) biotite grains show alteration macroscopically. The biotite grains near the surface of the 200 °C experiment samples (1.5 and 2 molal) protrude above the former flat sample surface. They seem to be widened during the experiments, i.e. losing their interconnection and decomposing in separate sheets. Partly, other mineral grains were lifted out of the rock sample due to biotite alteration beneath. Accordingly, electron microscope images show the delamination of phyllosilicate layers in samples of the 200 °C experiments (1.5 and 2 molal). Figure 5.7a illustrates the uplift of surface-near material due to expansion of biotite/chlorite (200 °C, 2 M). Despite this delamination, the initial grain shape is more or less preserved during the 200 °C experiments (Fig. 5.7b).

On the contrary, biotites in the 260 °C samples forms morphological depressions, which

**Table 5-5** – Mineral composition of feldspars after the 260 °C, 2 molal experiment.

Sample	098_05-01	098_05-02	098_05-03	098_05-05	098_05-06	098_05-07	098_06-01	098_06-02	098_06-03	098_06-04	098_06-05	098_06-06	098_06-07	098_06-08	098_06-09	098_06-10	098_06-11
Exp. T	260	260	260	260	260	260	260	260	260	260	260	260	260	260	260	260	260
Mineral	ab	ab	ab	ab	kfs	kfs	ab	ab	ab	kfs	kfs	kfs	kfs	kfs	ab	ab	ab
Location	subsurf.	near-surf.	near-surf.	subsurf.	close to ab	close to ab	near-surf.	near-surf.	near-surf.	close to ab	close to ab	close to ab	close to ab	kfs	incl. in kfs	incl. in kfs	near-surf.
SiO <sub>2</sub>	68.47	68.02	69.70	68.03	65.51	64.99	68.99	69.42	70.20	65.33	65.25	65.28	64.81	64.54	68.82	67.84	69.14
TiO <sub>2</sub>	<0.01	0.01	0.01	0.01	<0.01	0.03	<0.01	0.01	0.03	0.02	<0.01	<0.01	<0.01	<0.01	0.01	<0.01	<0.01
Al <sub>2</sub> O <sub>3</sub>	20.28	20.52	20.66	20.70	18.66	18.84	20.87	20.74	20.63	18.40	18.74	18.84	18.72	18.72	20.27	20.52	19.92
FeO	0.03	0.04	0.08	0.06	<0.01	0.03	0.26	0.13	0.14	0.01	0.05	0.02	0.04	<0.01	0.03	0.03	<0.01
MnO	0.03	<0.01	<0.01	0.01	<0.01	<0.01	<0.01	0.02	<0.01	<0.01	<0.01	<0.01	0.02	<0.01	0.01	0.01	<0.01
MgO	<0.01	0.01	<0.01	<0.01	0.02	0.01	<0.01	<0.01	<0.01	<0.01	0.01	0.01	<0.01	0.01	<0.01	<0.01	<0.01
CaO	0.49	0.72	0.06	0.47	<0.01	0.01	0.17	0.14	0.10	<0.01	0.02	0.02	0.01	0.05	0.10	0.86	0.25
Na <sub>2</sub> O	11.10	11.09	11.13	11.04	0.34	0.06	9.56	8.43	7.71	0.22	0.79	0.26	0.51	0.67	11.34	11.06	11.47
K <sub>2</sub> O	0.12	0.12	0.01	0.10	15.63	14.98	0.24	0.06	0.57	15.51	14.94	13.62	15.70	14.83	0.12	0.15	0.68
BaO	0.01	<0.01	<0.01	0.03	0.22	0.16	0.02	0.02	0.05	0.20	0.16	0.21	0.09	0.14	0.05	<0.01	<0.01
Total	100.53	100.53	101.64	100.44	100.38	100.00	100.10	98.97	99.42	99.68	99.95	98.27	99.91	98.95	100.76	100.47	100.86
Cation distribution normalized to O <sub>8</sub>																	
Si	2.97	2.96	2.98	2.96	3.01	2.99	2.99	3.02	3.04	3.02	3.00	3.02	2.99	3.00	2.98	2.95	2.99
Ti	0.00	0.00	0.00	0.00	0.00	0.00	0.00	0.00	0.00	0.00	0.00	0.00	0.00	0.00	0.00	0.00	0.00
Al	1.04	1.05	1.04	1.06	1.01	1.02	1.07	1.06	1.05	1.00	1.02	1.03	1.02	1.02	1.03	1.05	1.02
Fe	0.00	0.00	0.00	0.00	0.00	0.00	0.01	0.00	0.00	0.00	0.00	0.00	0.00	0.00	0.00	0.00	0.00
Mn	0.00	0.00	0.00	0.00	0.00	0.00	0.00	0.00	0.00	0.00	0.00	0.00	0.00	0.00	0.00	0.00	0.00
Mg	0.00	0.00	0.00	0.00	0.00	0.00	0.00	0.00	0.00	0.00	0.00	0.00	0.00	0.00	0.00	0.00	0.00
Ca	0.02	0.03	0.00	0.02	0.00	0.00	0.01	0.01	0.00	0.00	0.00	0.00	0.00	0.00	0.00	0.04	0.01
Na	0.93	0.94	0.92	0.93	0.93	0.09	0.80	0.71	0.65	0.02	0.07	0.02	0.05	0.06	0.95	0.93	0.96
K	0.01	0.01	0.00	0.01	0.92	0.88	0.01	0.00	0.03	0.91	0.88	0.80	0.92	0.88	0.01	0.01	0.00
Ba	0.00	0.00	0.00	0.00	0.00	0.00	0.00	0.00	0.00	0.00	0.00	0.00	0.00	0.00	0.00	0.00	0.00
Sum	4.98	4.99	4.96	4.98	4.97	4.98	4.89	4.81	4.78	4.95	4.97	4.88	4.99	4.96	4.98	4.99	4.98
Si+Al	4.01	4.01	4.03	4.02	4.02	4.01	4.05	4.08	4.09	4.02	4.02	4.05	4.01	4.02	4.02	4.01	4.01
Na/K	142.99	140.47	2113.65	172.99	0.03	0.10	61.82	200.18	20.59	0.02	0.08	0.03	0.05	0.07	141.29	109.12	223.49
An	0.02	0.03	0.00	0.02	0.00	0.00	0.01	0.01	0.01	0.00	0.01	0.04	0.01	0.04	0.01	0.04	0.01

Total Fe as FeO, ab = albite, kfs = K-feldspar, An = anorthite component.

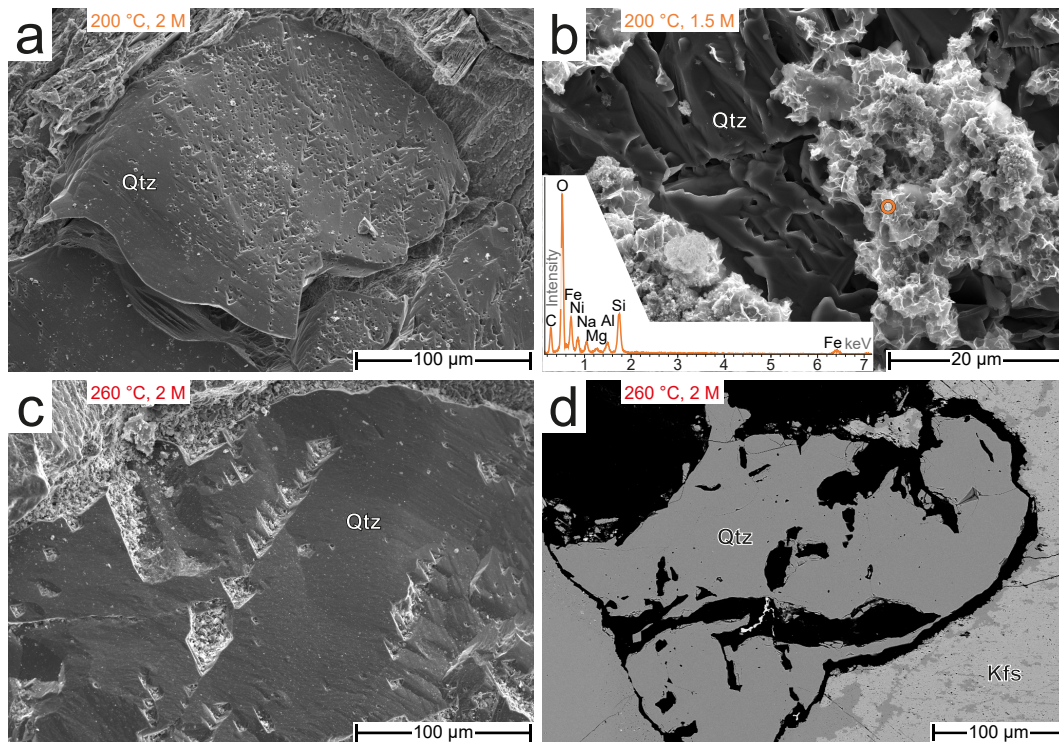


**Figure 5.5** – SEM images of quartz dissolution in post-experimental samples: (a) Triangular etch pits on the sample surface from the 200 °C, 2 molal experiment. (b) Wormhole-like dissolution features in the quartz surface with phyllosilicate precipitations (EDX spectra, measuring points marked with a circle) after the 200 °C, 1.5 molal experiment. (c) Triangular etch pits with precipitate fillings of secondary phyllosilicates after the 260 °C, 2 molal experiment. (d) Quartz dissolution at grain boundaries and within the interior in thin section (BSE image) after the 260 °C, 2 molal experiment.

are observable macroscopically on rock surfaces. The color of initially dark brownish biotites changed into a greenish-brown color during all experiments. Under the electron microscope phyllosilicates in the 260 °C experiment show evidences for dissolution or mechanical removal of delaminated material at the mineral–fluid interface (Fig. 5.7c + d). The observations in thin sections coincide with the macroscopical impressions of morphological uplifts or depressions. Similar to the 200 °C experiments sheet delamination is omnipresent in the 260 °C samples.

EDX measurements of post-experiment sample surfaces and in thin sections indicate significant lower concentrations of K in phyllosilicates at all sample surfaces (Fig. 5.7b). Moreover, in 260 °C samples, these elements are mostly totally absent in layers close to the mineral–fluid contact. EDX measurements detect Na in the phyllosilicates, which has not been found in the initial samples (Fig. 5.7b + 5.8a). Chemical compositions, measured by EMP, differ in some elements particularly in the type-1 chlorites from the initial ones. Especially, Na content increased in many type-1 chlorites and Ti concentrations are higher than in the initial chlorites. Whereas type-2 chlorites compositions are similar to the initial type-2 chlorite composition. Therefore, pre- and syn-experimental type-2 chlorites can not be discerned. Chemical analyses of post-experimental phyllosilicates are listed in Table 5.6 and 5.7.

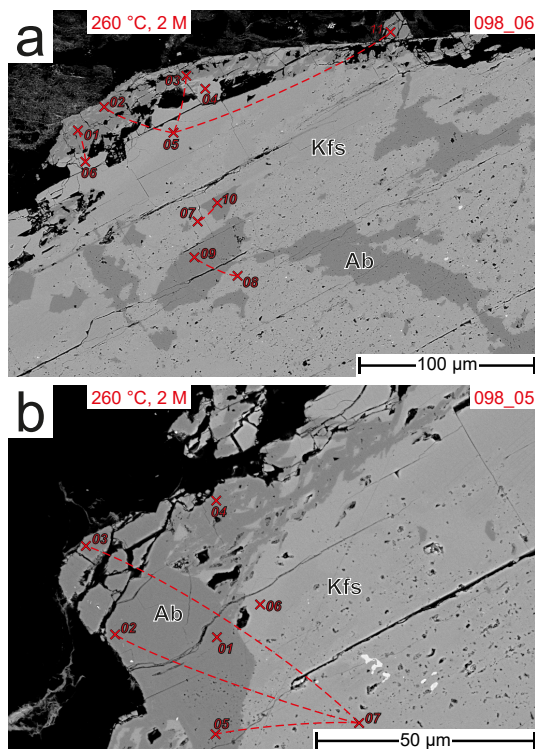


**Figure 5.6** – SEM images of feldspars in thin sections: (a) + (b) A rim of albite surrounds K-feldspar grains at the mineral–fluid contact after the 260 °C experiment. The pre-experimental albite exsolutions in K-feldspar are seen in the sample, too. Red numbers correspond to EMP measuring points in Table 5.5. Dashed lines mark the two-feldspar geothermometer pairs.

#### *PHYLLOSILICATE PRECIPITATION*

Phyllosilicates precipitated during the experiments on the sample surfaces. Especially on the samples of the 200 °C 1.5 molal experiment, comb-like flakes formed on the surface (Fig. 5.5b). EDX measurements on the sample surface show a qualitative composition of Fe-Ni-Na-Mg-Al-Si-O. Due to the tiny size (<1 μm) of the individual flakes, a mixed analysis of e.g. phyllosilicate and co-precipitated (Fe)-oxide can not be excluded. Their chemical composition could not be measured quantitatively, since the surface of the samples make up only the upper-most rim of thin sections, where the relatively loose precipitates were removed during preparation.

#### *ANALCIME*

A thin layer of analcime covers some areas of the 260 °C sample surface. In the samples of the 200 °C experiments analcime was not observed. The analcime consists mostly of anhedral aggregates covering all primary mineral phases. Few grains show a subhedral crystal habit, too (Fig. 5.8b). Analcime composition was determined by EDX measurements on sample surface (Fig. 5.8b) and verified by XRD investigation. In thin sections, no analcime layer could be observed, and therefore the analcime composition could not be measured by EMP.

#### *FURTHER SECONDARY PHASES*

Along with the phyllosilicate formation, unspecified Na-bearing Fe-oxides can be identified on the sample surface after the experiments by EDX. Additionally, halite occurs on the samples as a result of the evaporating of remaining Na-Cl solution on the samples.

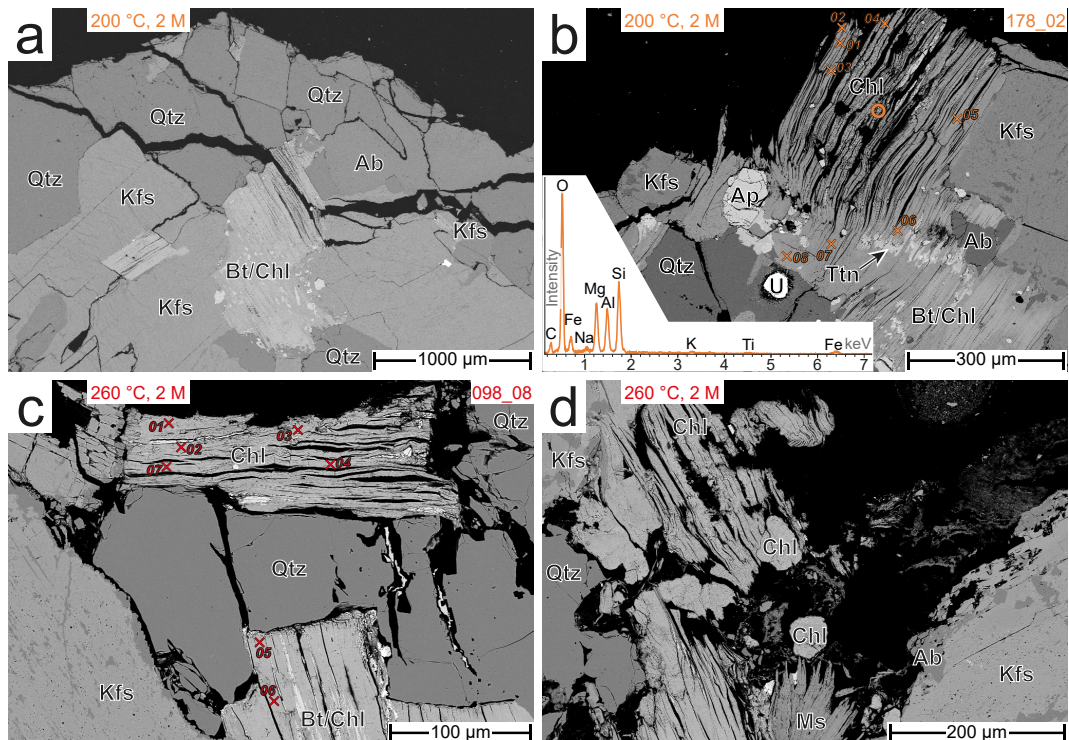


**Figure 5.7** – SEM thin section images (BSE mode) of post-experiment samples: (a) Delamination of biotite/chlorite and uplift of surface-near material after the 200 °C, 2 molal experiment; quartz dissolution at the grain boundaries near the mineral–fluid contact (black in the BSE image). (b) Biotite/chlorite in contact with the experiment fluid (200 °C, 2 molal) delaminates, leaches K, and incorporates small amounts of Na (EDX measuring point marked with an orange circle). Accessory phases are apatite, titanite, and an U-carbonate (U). (c) Weakened rock fabric after the 260 °C experiment due to quartz dissolution and biotite/chlorite delamination. Biotite in contact to the experiment fluid totally transformed to chlorite. (d) In the 260 °C samples surface-near chlorites show dissolution or mechanical removal of delaminated material. Orange and red numbers correspond to EMP measuring points in Table 5.6 and 5.7, respectively.

### 5.3.3 FLUID COMPOSITION

Rock alteration is preserved in the fluid composition after the experiment (Table 5.8). Cation concentrations of most elements are elevated with respect to the initial solution. Generally, solutes are higher concentrated in the fluid of the 260 °C than in those of the 200 °C experiments. Sodium is in the range of  $\sim 46 \text{ g l}^{-1}$  for the experiments with the 2 molal solution, and  $37 \text{ g l}^{-1}$  for the 1.5 molal one. Due to the high initial concentrations in the solution, slight variations in Na concentrations in the fluid can not be determined. Potassium is enriched in the fluids of all experiments to  $74\text{--}147 \text{ mg l}^{-1}$  with higher concentration in the 260 °C fluid and Ca ranges from 27 to  $59 \text{ mg l}^{-1}$ . Mg concentrations in the fluids are generally very low and close to detection limit ( $0.07\text{--}0.2 \text{ mg l}^{-1}$ ).

Iron concentrations in the fluids are in the range of  $\sim 100\text{--}250 \text{ } \mu\text{g l}^{-1}$ . Aluminum is close to or even below detection limit ( $\leq 89\text{--}140 \text{ } \mu\text{g l}^{-1}$ ). Silicon concentrations are in the range of  $\sim 100 \text{ mg l}^{-1}$  and  $\sim 150 \text{ mg l}^{-1}$  for 200 °C and 260 °C experiment solutions, respectively. Minor elements Li, Rb, Cs, Sr, and Ba were dissolved during the experiments and are thus enriched in the fluid. Where Ba is highly elevated to  $1300 \text{ } \mu\text{g l}^{-1}$ ,  $2170 \text{ } \mu\text{g l}^{-1}$ , and  $3670 \text{ } \mu\text{g l}^{-1}$  for the 200 °C 1.5 M, 200 °C 2 M, and 260 °C 2 M fluid, respectively. Chloride concentrations represent more or less the initial solutions:  $\sim 55 \text{ g l}^{-1}$  and  $\sim 68 \text{ g l}^{-1}$  for the 1.5 and 2 molal solutions, respectively. Similar to Na, slight changes in Cl concentrations caused by the

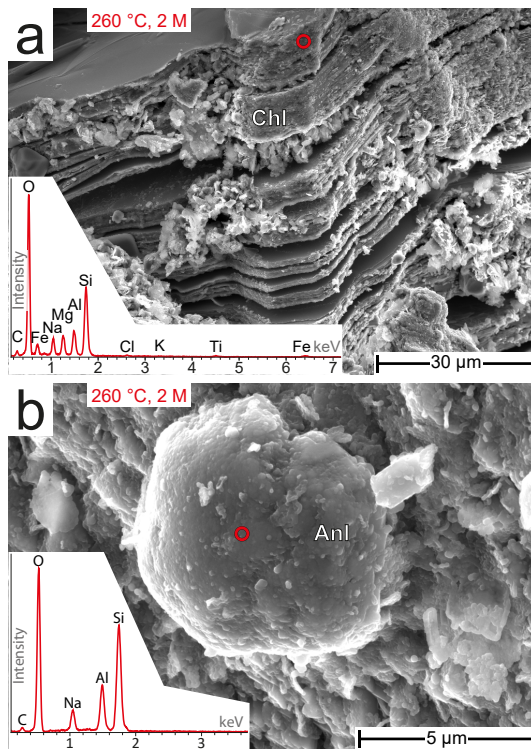


**Figure 5.8** – SEM surface images of post-experiment samples (260 °C): (a) Type-2 chlorite surface in direct contact with the fluid incorporates measurable amounts of Na and is delaminated after the experiment. (b) Anhedral analcime (Anl) layer covers the sample surface, sparsely single subhedral analcime occurs. EDX measuring points marked with a red circles.

experiments can not be examined.

pH measurements give slightly acidic to neutral values,  $\sim 6.4$  for the 200 °C fluid samples and 7.1 for the 260 °C one, measured at 25 °C. Recalculation of pH values to the respective experimental temperature (GWB, Bethke & Yeakel, 2015) results in pH values of  $\sim 6.8$  and 7.2, respectively (Table 5.8). Alkalinity is  $0.4 \text{ mmol l}^{-1}$  in the 200 °C 1.5 M fluid, and  $0.6 \text{ mmol l}^{-1}$  in the 200 °C 2 M and 260 °C 2 M ones.

## 5.4 DISCUSSION

The main characteristics of the alteration reactions in our experiments are: (1) deep holes in the near-surface quartz grains, (2) widening of biotite/chlorite sheets, (3) disappearance of biotite from the sample surface even forming depressions in the higher temperature experiments, and (4) formation of analcime in the 260 °C experiments (Table 5.1). But, no or hardly any reaction of K-feldspar was found. With these observations and the composition of the fluid after the experiments the proceeded mineral–fluid reaction can be deduced and compared with alteration reactions in natural settings and consequences for a granitic reservoir formation can be inferred.

### 5.4.1 ALTERATION REACTIONS DEDUCED FROM EXPERIMENTS

#### QUARTZ REACTIONS

Dissolution of quartz is obviously seen in the quartz grains exposed to the solution. This reaction is not surprising, since the initial experimental solutions are nearly free of  $\text{SiO}_{2(\text{aq})}$  (Table 5.7) and thus far from saturation with respect to quartz. Dissolution depth in the quartz grains in the rock samples reflects the higher quartz solubility at higher temperatures.

**Table 5.6** – Mineral composition of phyllosilicates after the 200 °C, 2 molal experiment.

Sample	178_02-01	178_02-02	178_02-03	178_02-04	178_02-05	178_02-06	178_02-07	178_02-08
Exp. T	200	200	200	200	200	200	200	200
Mineral	chl-T1	chl-T1	chl-T1	chl-T1	chl-T2	chl-T2	chl-T1	chl-T2
Location	near-surf.	near-surf.	near-surf.	near-surf.		subsurf.	subsurf.	subsurf.
SiO <sub>2</sub>	35.09	36.44	37.22	39.17	28.29	29.03	29.71	26.96
TiO <sub>2</sub>	3.87	3.74	3.60	3.73	0.09	0.18	1.97	0.05
Al <sub>2</sub> O <sub>3</sub>	13.56	15.26	15.56	16.18	18.43	16.55	17.93	19.32
FeO	18.18	17.58	18.32	17.78	24.59	24.08	21.96	24.30
MnO	0.23	0.26	0.28	0.27	0.37	0.44	0.41	0.39
MgO	8.49	10.42	9.25	10.39	14.27	15.36	13.63	14.66
CaO	2.39	0.73	2.58	1.60	0.15	0.20	0.19	0.06
Na <sub>2</sub> O	1.78	0.82	2.24	1.27	0.02	0.02	0.11	<0.01
K <sub>2</sub> O	1.62	6.55	0.22	3.73	0.02	0.05	1.36	0.01
BaO	0.04	0.12	0.04	<0.01	<0.01	0.05	<0.01	0.01
Total	85.25	91.92	89.31	94.12	86.23	85.96	87.27	85.76
Cation distribution normalized to O <sub>10</sub> (OH) <sub>8</sub> .								
Si	3.68	3.60	3.68	3.69	3.01	3.10	3.10	2.89
Ti	0.31	0.28	0.27	0.26	0.01	0.01	0.15	0.00
Al	1.68	1.78	1.81	1.80	2.31	2.08	2.20	2.44
Fe	1.60	1.45	1.51	1.40	2.19	2.15	1.91	2.18
Mn	0.02	0.02	0.02	0.02	0.03	0.04	0.04	0.04
Mg	1.33	1.53	1.36	1.46	2.26	2.44	2.12	2.34
Ca	0.27	0.08	0.27	0.16	0.02	0.02	0.02	0.01
Na	0.36	0.16	0.43	0.23	0.00	0.00	0.02	0.00
K	0.22	0.83	0.03	0.45	0.00	0.01	0.18	0.00
Ba	0.00	0.01	0.00	0.00	0.00	0.00	0.00	0.00
Sum	9.46	9.73	9.38	9.48	9.83	9.86	9.75	9.89
Mg#	0.45	0.51	0.47	0.51	0.51	0.53	0.53	0.52
R <sup>2+</sup>	2.95	3.01	2.90	2.88	4.48	4.63	4.07	4.55
R <sup>3+</sup>	2.46	2.53	2.50	2.49	2.33	2.12	2.49	2.45

Total Fe as FeO. chl-T1 = type-1 chlorite, chl-T2 = type-2 chlorite. Mg# = Mg / (Mg + Fe), R<sup>2+</sup> = Mg + Fe<sup>II</sup> + Mn, R<sup>3+</sup> =  $\frac{1}{3}(28 - 2R^{2+} - 4Si)$ .

Equally, SiO<sub>2(aq)</sub> concentrations in the fluid are close to or at quartz saturation: ~215 mg l<sup>-1</sup> for the 200 °C and ~320 mg l<sup>-1</sup> for the 260 °C experiments (Table 5.8). Accordingly, saturation indices (*SI*) of quartz are between -0.02 and 0.06, calculated with GWB (Bethke & Yeakel, 2015). So, the fluid reaches quartz equilibrium within experimental time.

#### PHYLLOSILICATE REACTIONS

**EVALUATION OF CHEMICAL DATA** Compositional diagrams of phyllosilicates (Fig. 5.9) show the chemical variance of the different phyllosilicates and elemental changes during the pre- and syn-experimental chloritization. The element concentrations in the diagrams are in atoms per (half) formula unit (apfu), on the basis of 11 oxygen (O<sub>10</sub>(OH)<sub>2</sub>) for biotites and 14 oxygen (O<sub>10</sub>(OH)<sub>8</sub>) for chlorites (all Fe is assumed as Fe<sup>2+</sup>).

In the R<sup>2+</sup> – Si diagram (Inoue et al., 2009; Wiewiora & Weiss, 1990) the type-1 and -2 chlorites can easily discerned (Fig. 5.9a). Here R<sup>2+</sup> represents octahedral cations (Mg + Fe<sup>2+</sup> + Mn), R<sup>3+</sup> trivalent cations ( $R^{3+} = \frac{1}{3}(28 - 2R^{2+} - 4Si)$ ) and □ stands for vacancy positions. Type-2 chlorites are compositionally close to the ideal clinocllore-chamosite solid solution composition with slightly higher vacancies and R<sup>3+</sup> values. In type-1 chlorites R<sup>2+</sup> content is lower and Si concentration higher than in type-2 chlorites, which results in higher vacancy positions in the chlorite unit cell. The type-1 chlorites can be subdivided in two groups, based on their position in the R<sup>2+</sup> – Si diagram: Type-1 from the initial samples and from measuring points more distant to the mineral–fluid interface located closer to the type-2 chlorites. The second sub-group of type-1 chlorites is richer in Si and poorer in R<sup>2+</sup>, accompanied with higher vacancies compared to the other sub-type-1 chlorites and the type-2 ones. All chlorites plot along a line of nearly constant R<sup>3+</sup> values (about 2.2–2.6). This trend with a constant R<sup>3+</sup> value correspond to a Si<sub>-1</sub>□<sub>-1</sub>R<sub>2</sub><sup>2+</sup> exchange vector, which is a combination of a di-trioctahedral and a Tschermak substitution (Bourdelle &

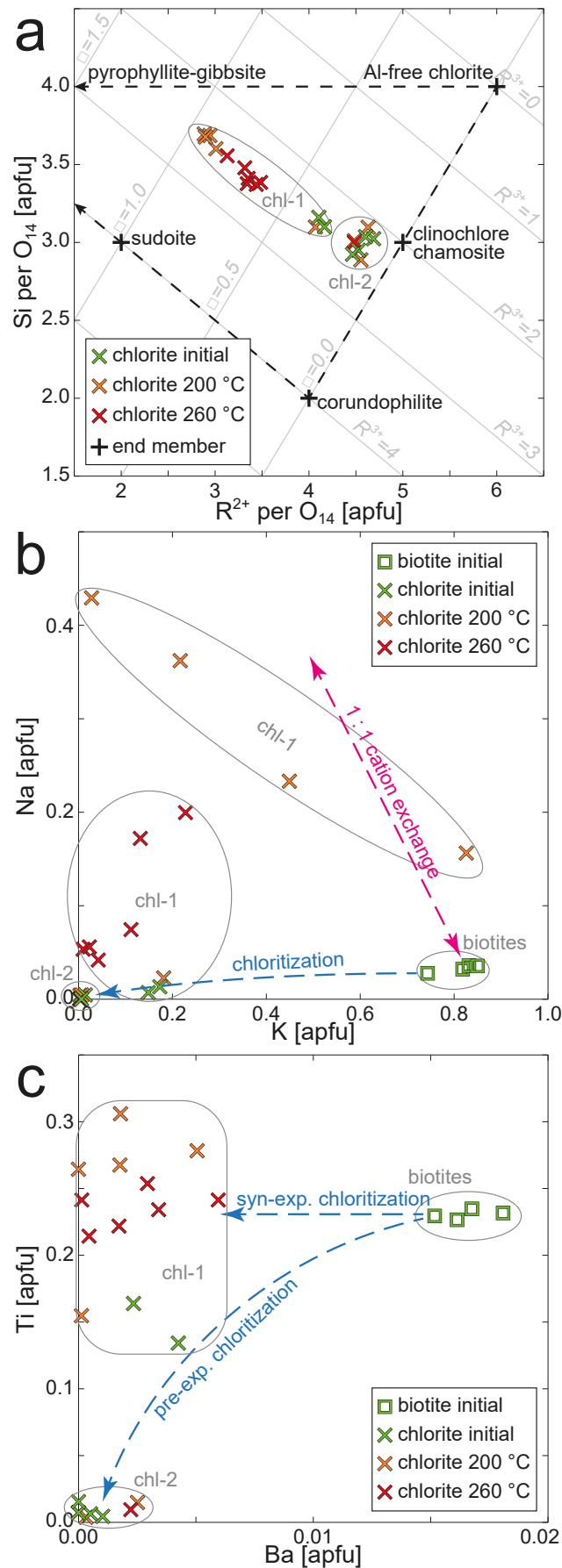


**Figure 5.9** – Compositional diagrams of phyllosilicates. All element compositions are atoms per formula unit (apfu), on the basis of 11 O (O<sub>10</sub>(OH)<sub>2</sub>) for biotites and 14 O (O<sub>10</sub>(OH)<sub>8</sub>) for chlorites. (a) R<sup>2+</sup> – Si diagram after Wiewiora & Weiss (1990) and Inoue et al. (2009). R<sup>2+</sup> represents octahedral cations Mg + Fe<sup>2+</sup> + Mn, R<sup>3+</sup> trivalent cations Al<sup>3+</sup> and □ vacancies. (b) K – Na diagram with phyllosilicate compositions. Biotites, type-1 and type-2 chlorite can be distinguished by K content. Type-2 chlorites show no compositional effect of the experiments, whereas type-1 chlorites are characterized by Na incorporation during the experiments. (c) The Ba – Ti diagram displays the different phyllosilicates by both their Ba and Ti concentrations. Syn-experiment biotite chloritization seem to leach Ba whereas Ti remain rather constant.

**Table 5.7** – Mineral composition of phyllosilicates after the 260 °C, 2 molal experiment.

Sample	098_08-01	098_08-02	098_08-03	098_08-04	098_08-06	098_08-07	098_08-05
Exp. T	260	260	260	260	260	260	260
Mineral	chl-T1	chl-T1	chl-T1	chl-T1	chl-T1	chl-T1	chl-T2
Location	near-surf.		near-surf.				
SiO <sub>2</sub>	33.67	33.18	33.75	31.68	32.81	32.84	27.64
TiO <sub>2</sub>	2.91	3.06	3.05	3.16	3.03	2.77	0.12
Al <sub>2</sub> O <sub>3</sub>	17.01	15.68	15.58	15.90	16.86	16.58	18.10
FeO	19.27	18.90	18.08	19.11	19.51	19.50	24.88
MnO	0.43	0.45	0.50	0.57	0.39	0.44	0.41
MgO	11.17	10.36	9.51	9.99	11.30	11.51	13.56
CaO	1.16	2.63	2.97	3.23	1.27	1.89	0.24
Na <sub>2</sub> O	1.02	0.21	0.27	0.26	0.86	0.37	<0.01
K <sub>2</sub> O	1.76	0.31	0.17	0.07	1.00	0.85	0.02
BaO	0.04	0.13	<0.01	0.06	0.08	0.01	0.05
Total	88.44	84.92	83.89	84.03	87.12	86.75	85.00
Cation distribution normalized to O <sub>10</sub> (OH) <sub>8</sub> .							
Si	3.41	3.48	3.55	3.38	3.37	3.38	3.00
Ti	0.22	0.24	0.24	0.25	0.23	0.21	0.01
Al	2.03	1.94	1.93	2.00	2.04	2.01	2.31
Fe	1.63	1.66	1.59	1.70	1.68	1.68	2.26
Mn	0.04	0.04	0.04	0.05	0.03	0.04	0.04
Mg	1.69	1.62	1.49	1.59	1.73	1.77	2.19
Ca	0.13	0.30	0.34	0.37	0.14	0.21	0.03
Na	0.20	0.04	0.06	0.05	0.17	0.07	0.00
K	0.23	0.04	0.02	0.01	0.13	0.11	0.00
Ba	0.00	0.01	0.00	0.00	0.00	0.00	0.00
Sum	9.57	9.36	9.28	9.41	9.53	9.49	9.84
Mg#	0.51	0.49	0.48	0.48	0.51	0.51	0.49
R <sup>2+</sup>	3.35	3.32	3.13	3.34	3.44	3.49	4.49
R <sup>3+</sup>	2.55	2.48	2.51	2.60	2.55	2.50	2.35

Total Fe as FeO. chl-T1 = type-1 chlorite, chl-T2 = type-2 chlorite. Mg# = Mg / (Mg + Fe), R<sup>2+</sup> = Mg + Fe<sup>II</sup> + Mn, R<sup>3+</sup> =  $\frac{1}{3}(28 - 2R^{2+} - 4Si)$ .

Cathelineau, 2015). This exchange trend is typical for datasets of low-T chlorites (Bourdelle & Cathelineau, 2015).

Figure 5.9b shows phyllosilicate compositions in a K-Na diagram. Biotite in the initial samples is high in K but below 1 per apfu. It incorporates only minor amounts of Na. In initial type-2 chlorites K and Na are nearly absent, which should be common in chlorites. But, type-1 chlorites from the initial sample are still slightly elevated in alkalis and plot on a line between biotite and chlorite-2 in the K–Na diagram. Thus, as mentioned before, type-1 chlorite constitutes an intermediate stage of biotite chloritization in the initial samples prior to the experiments.

After the experiments (200 °C and 260 °C) biotite is lacking at sample surface. Type-2 chlorite in the post-experiment samples are virtually identical in composition to the initial sample. Consequently, type-2 chlorite plot at the same place in the K–Na diagram (Fig. 5.9b). Thus, it cannot be stated from the alkali content, if some of the type-2 chlorite in the post-experiment samples has formed during the experiment, or if the whole type-2 chlorite already exists prior to the experiments. In contrast, Na content of type-1 chlorites from both, the 200 °C and 260 °C experiments, is generally higher than in the initial phyllosilicates. Starting from biotite composition in the K–Na diagram, type-1 chlorite from the 200 °C experiment plot on a line of K–Na-exchange (Fig. 5.9b), but do not exchange in a 1 : 1 ratio (pink arrow), but alkali content decreases in total. Type-1 chlorite from the sub-surface (Fig. 5.7b) has not changed in composition during the experiments and plot in the area of the initial type-1 chlorite composition. Surface-near type-1 chlorites from the 200 °C experiment are generally higher in alkalis as the ones from the 260 °C experiment, although an incorporation of Na is detectable. The type-2 chlorites from the 260 °C experiment are compositionally further away from initial biotite composition, in the sense of K content. Thus, the chloritization process (blue arrow in Fig. 5.9b) in the 260 °C experiment could

**Table 5.8** – Fluid compositions of initial 2 M Na-Cl solution, and fluids after the experiments. Re-calculation of pH to experimental temperature with GWB (Bethke & Yeakel, 2015).

Exp. T		initial	200 °C	200 °C	260 °C
Molality		2 M	1.5 M	2 M	2 M
Time	d	0	51	49	49
Cond.	mS/cm	136	59	139	145
pH	25 °C	5.77	6.48	6.31	7.14
pH	exp. T	–	6.82	6.86	7.17
Alk.	mmol/l	–	0.4	0.6	0.6
Na	g/l	44.9	36.7	46.0	47.1
K	mg/l	<0.04	74	87	147
Ca	mg/l	<0.03	27	35	59
Mg	mg/l	<0.002	0.07	0.07	0.2
Fe	µg/l	<0.5	252	149	103
Al	µg/l	<0.7	89	<0.7	141
Si	mg/l	–	99	103	151
Li	µg/l	10.8	731	899	1591
Rb	µg/l	3.0	695	945	1235
Cs	µg/l	<0.001	209	285	336
Sr	µg/l	1.8	293	128	346
Ba	µg/l	5.8	1302	2169	3674
Cl	g/l	67.2	54.5	67.9	68.6

have been accelerated due to the higher temperature. Conversely, the alkali exchange is subordinated in relation to the loss of cations induced by the chloritization process. Likewise, a complete/stoichiometric dissolution of the biotites could result in the absence of Na-enriched chlorites, which is in agreement with the observation of morphological depressions, seen macroscopically and in thin sections.

Figure 5.9c displays the different phyllosilicates compositions (in mol per apfu on the basis of 11 O ( $O_{10}(OH)_2$ ) for biotites and 14 O ( $O_{10}(OH)_8$ ) for chlorites) in a Ba-Ti diagram. In the initial samples, the biotites are characterized by the highest concentration of Ti and Ba. Type-1 and type-2 chlorites form a trend towards low concentrations of both Ti and Ba during pre-experimental chloritization (blue arrow in Fig. 5.9c). Titanite occurrence in the vicinity to initial type-2 chlorite (Fig. 5.4b) shows the segregation of Ti during pre-experimental chloritization from biotite. Syn-experiment biotite chloritization seems to leach Ba rapidly from the phyllosilicates whereas Ti remains rather constant in the time span of the experiments. Consequently, elevated Ba concentrations in the experimental fluids (Table 5.8) is a result of chloritization of phyllosilicates.

**XRD EVALUATIONS** Diffractograms ( $2\theta$   $CuK\alpha$ ) of initial granite and post-experiment surface material were compared for changes of phyllosilicates during the experiments. Therefore, the range of  $2-20^\circ 2\theta$  were considered in detail (Fig. 5.10). Direct comparison of the intensities and, therefore, the proportion of the individual mineral phases are prohibited, since the post-experiment material has been scratched from the sample surface and thus, does not correspond to the bulk sample. Thereby, sample material is very limited and a separation and treatment with ethylene-glycol of the phyllosilicates fraction was not possible.

The diffractogram of the initial sample has a well defined biotite peak at  $10.000 \text{ \AA}$  (001) and small ones at  $5.000 \text{ \AA}$  (002) and  $4.480 \text{ \AA}$  (Fig. 5.10). Chlorite reflections are at  $14.080 \text{ \AA}$

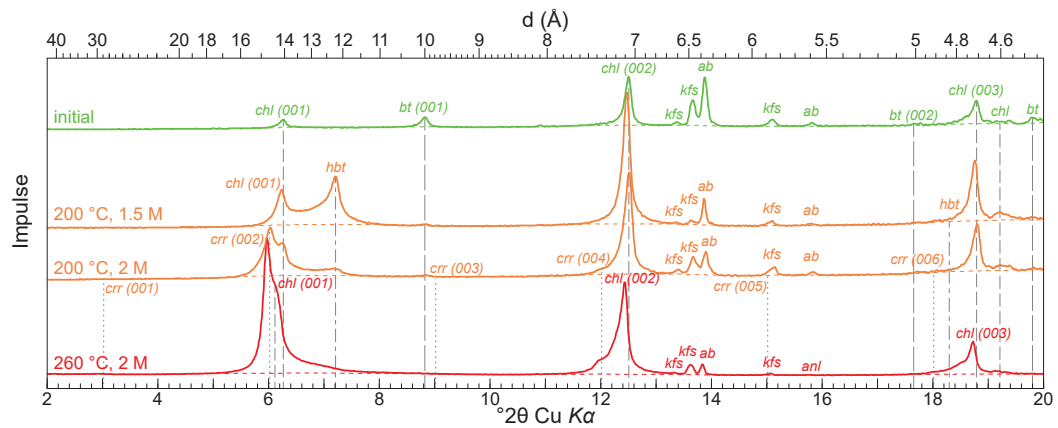


**Figure 5.10** – Diffractogram of the initial sample (green) and of surface material of the 200 °C (orange) and 260 °C (red) experiments. The relevant part from 2–20 ° 2 $\theta$  for phyllosilicate evaluation is shown. Pattern description is in the text. bt = biotite, chl = chlorite, hbt = hydrobiotite, crr = corrensite, ab = albite, kfs = K-feldspar, anl = analcime.

(001), 7.069 Å (002) and 4.717 Å (003). Additionally, K-feldspar (orthoclase) and albite peaks occur at the diffractogram.

The XRD pattern of the 200 °C 1.5 M surface material has only a minimal biotite peak at 10.000 Å (Fig. 5.10). Chlorite reflections have slightly shifted to higher d-values, 14.146 Å (001), 7.3086 Å (002), 4.725 Å (003). Peaks are widened, presumably more towards higher d-values. Additionally, a weak chlorite reflection at 4.613 Å arises. New peaks, which do not exist at the initial sample, occur at 12.239 Å and 4.843 Å. These correspond to hydrobiotite, the 1 : 1 regular inter-stratification of biotite and vermiculite. The 12.239 Å peak merge into the 001 reflection of chlorite. Feldspar peaks are the same as in the diffractogram from the initial sample.

Phases from 200 °C 2 M experiments changed again in comparison to the 1.5 M one, except for the feldspars. Biotite reflections are nearly absent. Chlorite *ool* reflections are at the same position as in the initial sample (14.080 Å, 7.069 Å, and 4.717 Å for 001, 002, and 003, respectively). Peak broadening, seen in the 1.5 M, exists in the 2 M diffractogram, too. The chlorite 001 reflection (14.080 Å) forms a plateau through the hydrobiotite peak at 12.239 Å. Peak intensity of the hydrobiotite of the 1.5 M sample is much smaller relatively to the peak height of the chlorite peaks than in the 2 M sample, both at 200 °C. In this sample reflections occur, which can be associated with a corrensite-like mineral phase (1 : 1 regular inter-stratification of chlorite and vermiculite). Peak positions are 29.207 Å, 14.621 Å, 9.700 Å, 7.300 Å, 5.901 Å, and 4.900 Å, where the odd *ool* peaks are very weak or nearly absent in our diffractogram. The peaks do not match exactly the d-values of corrensite from the literature, but, since corrensite is a mixed-layer phyllosilicates and the inter-stratification can vary from the ideal 1 : 1 ratio, variations in the d-values are not unexpected.

In the diffractogram of the 260 °C experiment biotite is totally absent (Fig. 5.10). The chlorite *ool* reflections shifted further to higher d-values (14.445 Å (001), 7.108 Å (002), 4.733 Å (003), 4.635 Å) and are highly broaden, more intense to higher d-values. Hereby all *ool* peaks overlap with reflections of the corrensite-like mineral phase, which tendentially place towards higher d-values as in the 200 °C 2 M sample. Hydrobiotite reflections are



Al<sup>3+</sup> (see below).

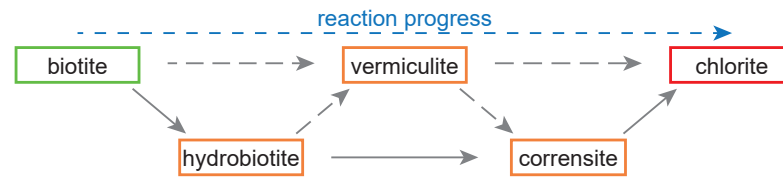


**Figure 5.11** – Phyllosilicate reaction in the experiments deduced from the evaluation of the XRD pattern and chemical data from EMP measurements. Initial biotite is transformed to chlorite in the experiments with intermediate hydrobiotite and a corrensite-like mineral phase.

#### FELDSPAR REACTIONS

Albite rims surrounding primary K-feldspar have been observed in thin sections of the 260 °C experiments (Fig. 5.6). However, albitization during the experiments is difficult to verify in the granite samples, since albite already exists in the initial samples and exsolution lamella could be exposed coincidentally to the sample surface. Exchange reactions could be possible, since the initial Na-Cl solution is far off the Na-K equilibrium of feldspars.

The mineral composition of K-feldspar and albite in lamella structures as well as from adjacent grain pairs (Fig. 5.4a and 5.6, Table 5.3 and 5.5) were used for the two-feldspar geothermometers of Putirka (2008) to discern pre- and potentially post-experimental albite in the samples. Feldspar pairs of the initial sample leads to temperatures of about 460–510 °C, clearly showing primary exsolution reactions (assuming a pressure of 2 kbar). Calculations with feldspar pairs from the sample surface–fluid interface of the 260 °C experiment (Fig. 5.6) give temperatures in the range of about 395–425 °C assuming the experimental pressure of 0.044 kbar. The temperatures are little lower than in the initial sample (independent on the different assumed pressure), but do not fit by far with the experimental temperature of 260 °C. Therefore we conclude, that the albite rimming at several K-feldspars could be an effect of coincidental exposition of pre-experimental albite lamella to the sample surface. However, the lower temperatures, calculated with the geothermometer show, that there is an influence of the experimental solution on the feldspar composition in mineral grains, which are in direct contact with the solution (possibly Ca loss to solution). EDX measurements of post-experimental K-feldspar surfaces mostly detect a Na signal, which support the conclusion of a slight incorporation of Na into K-feldspar from the solution.

SEM images of the surface and in thin sections imply no major dissolution reaction of K-feldspar, since the mineral grains show sharp edges very similar to the fresh fracture surface of the initial sample. Therefore, the dissolution of K-feldspar is considered as a minor process, which should have no significant influence on the K concentration measured in the experimental fluids. Conclusively, feldspars show a minor reactivity in our experiments at all. Probably the feldspar reaction is too slow in the time span of our experiments, compared to the high reactivity of the phyllosilicates (Nagy, 1995).

*PRECIPITATION OF SECONDARY MINERALS*

Analcime has been identified on the sample surface and in the XRD pattern of the 260 °C experiment. For its formation Na and H<sub>2</sub>O is provided from the initial experimental solution, and SiO<sub>2(aq)</sub> is added to solution by quartz dissolution, and chloritization of biotite releases Al<sup>3+</sup> to solution (Eq. 5.1). Analcime precipitation acts as suitable sink for the aqueous Al<sup>3+</sup>. The amount of analcime is limited by Al<sup>3+</sup> in solution, keeping it very low in the fluid phase. Since analcime has not been detected in the 200 °C experiments and the Al<sup>3+</sup> concentrations in the fluids are even so very low, the first step of biotite alteration to intermediate hydrobiotite has to be Al conservative. Once the chloritization process evolve to the transformation to corrensite and even pure chlorite, Al is released to the experimental fluid and analcime can form.



Since a minor dissolution of biotite/chlorite proceed in the 260 °C experiment observed in thin sections, and, at the same, the associated fluid sample contain only minor amounts of Mg and Fe these elements were removed from the fluid during the experiment. The composition of the tiny phyllosilicates, observed on the post-experiment samples with high amounts of Mg and Fe (Fig. 5.5b), matches as sink for these elements. The small grain size and the scarcity on the surface rule them out for a phase characterization by EMP or XRD. The process of clay mineral/phyllosilicate precipitation as sink for Mg has been described in other studies before. Savage et al. (1993) even observed a decrease of Mg concentration in fluids (stream and sea water) during experiments with granite at temperatures of 200 °C. Here, the precipitation of smectite and illite is responsible for the Mg consumption.

Summarizing, we deduce from our observations, that the chloritization of the biotites through intermediate hydrobiotite and a corrensite-like mineral phase, is the major reaction processes during the experiments (Eq. 5.1). The K release of this reaction controls its concentration in the experimental fluid. SiO<sub>2(aq)</sub> concentrations in the fluid are controlled by the quartz-solution equilibrium. Mg, Fe, and Al release of minor biotites/chlorite dissolution is consumed directly by precipitation of secondary chlorite-like phyllosilicates and analcime in the 260 °C experiment. Further minor processes are the Na incorporation during biotite chloritization and potentially Na integration in K-feldspar.

*IRON REDOX STATE*

We assume a relatively low O<sub>2</sub> fugacity in our experiments. The initial solution was in contact with the atmosphere before the experiments, but since the reactor material was a (stainless) steel, we think on rather reducing than oxidizing conditions. The Fe concentration in the fluid is too low (<300 µg l<sup>-1</sup>), especially in comparison to the high concentrations of Na and Cl (together 100 g l<sup>-1</sup>), to calculate the Fe state by ion balancing in the fluid. So, we assume iron as Fe<sup>2+</sup> in our solution. Chemical mineral compositions and XRD patterns fit well with Fe<sup>2+</sup> phases. The newly formed phyllosilicates are to large extent trioctahedral phyllosilicates (clinochlore-chamosite series, hydrobiotite, corrensite, vermiculite). Therefore, we assume again total Fe as Fe<sup>2+</sup> in the phyllosilicates, even though

the change of biotite color from dark brownish to greenish-brownish could be a result of oxidation of  $\text{Fe}^{2+}$ . The Fe-oxides found on the sample surface after the experiments cannot be analyzed by XRD methods due to the low proportion in the sample material.

#### 5.4.2 EXPERIMENTS EXTRAPOLATED TO RESERVOIR SCALE

##### *QUARTZ DISSOLUTION*

The quartz dissolution reaction in our experiments fits well with the early alteration stages found in natural basement reservoirs. Ledésert et al. (1999) described the hydrothermal alteration in the Soultz-sous-Forêts granite and found that early stages of granite alteration are characterized by quartz dissolution in the vicinity of faults. They explain the required quartz under-saturated fluids by the fluid migration in the graben structure. Relatively cold fluid descends into the granite reservoir, where it heats up during circulation (Stober & Bucher, 2015) increasing quartz solubility in the fluid. TDS of the fluid (mainly Na-Cl) increases due to dissolution reactions along the flow path (Stober & Bucher, 1999; Stober & Bucher, 2014). Therefore, our experimental conditions depicts well the early stages of granite joint alteration e.g. in the URG.

Furthermore, quartz dissolution occurred in deep crystalline basement rocks (up to 9100 m depth) of the German Continental Deep Drilling Program (KTB). Here, Pielow (1997) described triangular and V-shaped etch pits and deeper dissolution pits especially in minor altered areas of the drill hole. The quartz dissolution features has been formed by the reaction with deep Ca-Na-Cl solution.  $\text{SiO}_{2(\text{aq})}$  concentrations in these fluids have to be highly under-saturated with respect to quartz, to initiate etch pits on the quartz surface (Brantley et al., 1986). When the solution gets more and more  $\text{SiO}_{2(\text{aq})}$  saturated with respect to quartz, the etch pits evolve to deeper, branched networks (Pielow, 1997). Extend of quartz dissolution is triggered by the high salinity of the brines (salting-in), which increases the solubility of  $\text{SiO}_{2(\text{aq})}$  in the fluids (Dove & Rimstidt, 1994; Fournier et al., 1982).

The comparison of natural alteration features in quartz grains from relatively deep crustal crystalline rocks with the observations of dissolution features in our experimental samples shows, that our experiments describe well early alteration processes between unaltered crystalline rocks and high saline, quartz under-saturated brines. Therefore, we are able to transfer the alteration reactions of the other mineral phases, biotite, chlorite and feldspars, in our experiments to reservoir scale for the early stages of fracture alteration.

##### *BIOTITE REACTION*

The initially partly chloritization of biotites further progressed at (sub)-surface biotite grains during the experiments. So, no biotite occurs at the sample surfaces after the experiments anymore. Furthermore, XRD evaluations (Fig. 5.10) and SEM images of the sample surface (Fig. 5.8a) and most notably of thin sections (Fig. 5.7a–d) show a sheet delamination of the primary biotite/chlorite grains.

The observed fabric weakening, seen in our samples (Fig. 5.7a + c), is produced by phlogopite/chlorite delamination and expansion reactions during the experiments. The delamination triggers the crack propagation into adjacent mineral grains as many studies

have shown (Isherwood & Street, 1976; Rossi & Graham, 2010; Wahrhaftig, 1965). The uplift of mineral grains out of the sample due to sub-surface biotite/chlorite illustrates this process nicely.

Biotite delamination has been documented in soils by Mavris et al. (2012), where expansion and delamination increase permeability and fluid pathways, resulting in increasing alteration rates in the early stages of weathering. Thus, biotite alteration seen in our experiments is mainly responsible for fabric weakening and the driving force for continuing alteration further into the rock. But, although the rock fabric seems to be weakened during the experiments, the fluid appears not to enter the sample deeper than several 100  $\mu\text{m}$  (seen in thin sections) in the time span of our experiments.

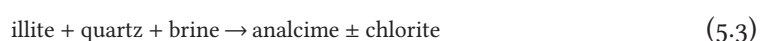
According to our experiments, dissolution of primary quartz and biotite can be seen in samples of Soultz granite (Bartier et al., 2008; Ledésert et al., 1999; Ledésert et al., 2010). Highly altered zones in the Soultz granite are characterized by the complete dissolution of quartz, and replacement of plagioclase and biotite with secondary phyllosilicates (illite, chlorite, tosudite) and carbonates. The first alteration stage of Soultz granite is initiated by the replacement of biotite by secondary chlorite (Komninou & Yardley, 1997). In particular the occurrence of tosudite (1 : 1 regular dioctahedral mixed-layer chlorite–smectite, Anthony et al., 2015) in the alteration zones of Soultz granite is in line with the formation of the corrensite-like mixed-layer phyllosilicate during our experiments. Tosudite represents the dioctahedral equivalent of the trioctahedral corrensite (Beaufort et al., 1997).

So, the simulated mineral-brine reactions in our experiments are in agreement with the early stage of reservoir rock alteration in granitic geothermal systems of the URG. Consequently, the delamination process of biotite/chlorite and the consequential disintegration of the rock fabric will occur, if fresh reservoir granite gets in contact with a highly saline reservoir brine. The influence of the alteration reactions on fluid migration into the geothermal circuit, will therefore promote the fault permeability, at least in the early stages of alteration.

#### 5.4.3 COMPARISON WITH ALTERATION PROCESSES IN SANDSTONE RESERVOIRS OF THE URG

The results of the performed experiments reveal a further propagation of (micro-)cracks in granitic reservoirs in contact with hot, highly saline brine, caused by quartz dissolution and biotite chloritization, delamination and partly dissolution. Appreciable formation of solid phases or phase conversions with a volume expansion of solids did not proceed during the experiments. Thus, joints will further tend to open during the early stages of alteration reactions of granitic rocks, under the simplified reservoir conditions used in the experiments.

This contrasts fundamentally with geochemical reactions in experiments under the same conditions with arkosic sandstone samples (Schmidt et al., 2017a). Here the sandstone cementation, composing of kaolinite and illite, reacts with the Na-Cl solution forming large amounts of analcime on sample surfaces. Following Schmidt et al. (2017a), the reactions:





caused an increase of solid volume of ~20 and ~30 %, respectively. The dissolution of clay minerals acts as source of Al, necessary for secondary analcime precipitation. Consequently, Al availability is the limiting factor for the formation of secondary silicates. Si is available in the fluids due to the omnipresence of quartz in both reservoir lithologies. In consequence, fresh fracture apertures in sandstones (with clay mineral matrix cementation) tend to decrease, whereas in granite reservoirs a rather increase of fluid pathways is expectable, at least in the early stages of alteration.

## 5.5 CONCLUSION

We could monitor the early stages of geochemical-mineralogical fault evolution with autoclave experiments. The simplified reservoir conditions we used in the experiments reflect well the temperature and fluid composition of URG fluids which induce the first steps of fracture alteration in granitic reservoirs. Comparison with natural alteration features in deep crystalline rocks, e.g. the KTB and Soultz-sous-Forêts geothermal drill cores, show clear similarities of the mineral alteration reactions seen in our experiments.

Therefore, in granite reservoirs fractures should tend to increase in permeability in the early stages of alteration, where quartz dissolution and biotite chloritization weaken the rock fabric fundamentally close the rock–brine interface and produce further pathways into the rock matrix. Thereby significant differences in mineral–brine reactions depending on the lithology could be found by comparison with alteration processes in sandstone reservoir rocks. Consequently, the exposed primary mineral assemblage is a crucial parameter for the mineralogical development of fresh fractures. In granitic reservoirs the phyllosilicates rather transform than dissolve completely. Whereas clay minerals in the sandstone cementation are highly reactive under these conditions and tend to dissolve in solution and act as starting material for secondary mineral phases, e.g. zeolites.

## ACKNOWLEDGMENTS

We thank the technicians and staff of the Department of Aquatic Geochemistry (KIT) and of the Division of Mineralogy and Petrology, University of Freiburg. We are grateful to K. Drüppel for discussion in the early stage of the study. Finally, we would like to thank editor C. Rodriguez-Navarro and two anonymous reviewers for their work and for improving our manuscript. This research has been funded by the projects *StörTief* and *Geofaces-SD* of the German Federal Ministry for Economic Affairs and Energy (BMW i, no: 0325623C, 0324025C), implemented by the Project Management Jülich (PtJ). The autoclave laboratory at the University of Freiburg has been funded by Baden-Württemberg Programme (PTKA-BWP) grants L75 12002 and L75 14003.

---

## EXPERIMENTS ON SANDSTONE ALTERATION UNDER GEOHERMAL RESERVOIR CONDITIONS AND THE FORMATION OF ZEOLITES

---

This chapter has been submitted as: Schmidt, R. B., Göttlicher, J. & Stober, I. (submitted): Experiments on sandstone alteration under geothermal reservoir conditions and the formation of zeolites. – in: *European Journal of Mineralogy* 31.

### ABSTRACT

The Upper Rhine Graben (URG), in the border area of southwestern Germany and eastern France, has suitable conditions for deep geothermal applications using enhanced geothermal systems (EGS). Sandstone formations are used as geothermal reservoirs, where highly saline in-situ brines contact directly the rock material at the surfaces of the fracture network. Alteration reactions influence the fluid flow in the geothermal reservoir, and therefore, play a major role in the sustainable operation of the geothermal installation.

For a better understanding on brine-rock interaction in EGS, batch experiments at reservoir conditions, with typical temperatures of 200 °C, have been conducted. We used sandstone samples with a natural rock fabric in our experiments, where the sample surface represents a fracture surface. Three different fluids with a composition close to natural URG brines have been prepared for the experimental series lasting up to 128 days: Na-Cl, Na-Ca-Cl, and Ca-Cl solutions all with an ionic strength of 2 mol kg<sup>-1</sup>.

Quartz dissolution and the removal of illite from the cementation are the main reaction processes of the primary mineral assemblage, independently of the experimental solution composition. K-feldspar shows a high degree of dissolution only in the Ca-Cl solution. Muscovite resists the solution in the main. The fluid compositions reflect the processes observed in the solid samples over time.

On the sample surface massive amounts of zeolites precipitated during the hydrothermal experiments. In the Na-Cl series analcime is the sole zeolite phase. Analcime and wairakite occur on samples from experiments with Na-Ca-Cl solution. In the Ca-Cl series wairakite is the dominant zeolite phase, accompanied with sporadic epistilbite crystals. The zeolite phases have been identified and characterized by electron microprobe analyses and the use of synchrotron X-ray diffraction.

Reaction mechanisms could be derived from the observations in the solid and fluid

---

samples. The governing reactions involve dissolution of quartz and illite, consumption of dissolved (earth-)alkali elements from solution, and result in the precipitation of zeolite phases, depending on the experimental solution composition. Based on the overall reactions, the volume of the solid phases increases. The observations in the experiments have been transferred to natural systems and are intensively discussed in the context of URG geothermal systems.

The experiments show the large influence of brine-sandstone interaction on surfaces of fracture networks in EGS. The observed processes have the potential to hamper the fluid flow and decrease the efficiency of geothermal installations.

## 6.1 INTRODUCTION

The lifetime of geothermal installations is highly dependent on the preservation of the subsurface fluid circuit. In enhanced geothermal systems (EGS) the reservoir brines circulate through a highly permeable fracture network. Sandstone formations can offer suitable properties necessary for a geothermal reservoir. Alteration of fracture surfaces in sandstone reservoirs have a major impact on the permeability of the circuit network and consequently on the efficiency and lifetime of geothermal installations (e.g. Griffiths et al., 2016).

In the Upper Rhine Graben (URG, France and Germany) sandstone formations are suitable targets for geothermal energy (Dezayes et al., 2008). The temperature gradient is elevated (Pribnow & Schellschmidt, 2000) and the reservoirs are in accessible depth. Therefore, several geothermal facilities have been build, using (also) sandstone reservoirs, e.g. Bruchsal (Pauwels et al., 1993) and Rittershoffen (Baujard et al., 2017). Formation brines are characterized by relatively high TDS ( $>100 \text{ g l}^{-1}$ ), compositionally dominated by Na-Ca-Cl (Sanjuan et al., 2016; Stober & Bucher, 2014). Temperatures of the reservoir formations are in the range of 120–220 °C (Sanjuan et al., 2016).

Based on the URG conditions, batch-type experiments with sandstone surfaces and pure Na-Cl solution have been performed in a previous study by Schmidt et al. (2017a) to investigate the beginning of alteration reactions. These experiments have shown a reaction of clay minerals (illite and kaolinite) from the sandstone cementation and quartz with sodium and water from the solution, forming massive amounts of analcime on the sample surfaces. These reactions result in a volume increase of solids by up to 30 %. Thus, a permeability reduction is highly conceivable, with negative effects on the geothermal circuit. In the previous study the experimental solution concentration match the ionic strength of the natural formation brines ( $\sim 120 \text{ g l}^{-1}$ , e.g. Pauwels et al., 1993; Sanjuan et al., 2016; Stober & Jodocy, 2011), but the composition is reduced to the main components  $\text{Na}^+$  and  $\text{Cl}^-$ . Nevertheless, the simplification of these experiments was crucial for the delimitation of single alteration reactions in order to better understand mechanisms of the natural alteration processes (in the geothermal circuit).

In the present study we carried out experiments with extended solution compositions (Na-Cl, Na-Ca-Cl, Ca-Cl) in time series to evaluate the initial processes in alteration reactions on fresh sandstone surfaces. All synthetic solutions have the same ionic strength of  $2 \text{ mol kgw}^{-1}$ . The Na-Ca-Cl solution with a Na : Ca ratio of 0.85 : 0.15 is close to the natural

URG reservoir brines. Additionally, experimental series with the end-member compositions, Na-Cl and Ca-Cl, have been performed, to identify the relevant (geochemical) parameters for the alteration processes and secondary mineral phases observed in the experiments. Thus, the initiation of alteration processes in sandstone reservoirs can be reproduced closer to natural conditions.

To track the initial progress of the alteration reactions, time series with a maximum duration of 60 days have been conducted. Additionally, two long-term experiments of > 120 days with Na-Cl and Ca-Cl solutions were carried out to track the reaction trends in later stages.

## 6.2 METHODS

### 6.2.1 ROCK MATERIAL

Pfingztal Sandstone (PfsSt) has been selected as proxy for the Triassic Buntsandstein formation in the Upper Rhine Graben (URG) and used in the hydrothermal experiments. The sandstone has been collected as fresh blocks from a local quarry close to the URG. In the laboratory drill cores with a diameter of 22 mm have been drilled from the blocks (in direction of the bedding), broken perpendicular to the core axis to get a fresh rock surface (perpendicular to the bedding), and shortened to a height of ~10 mm. The rock cylinders were washed properly under a weak jet of deionized water and dried under laboratory conditions before used in the experiments.

### 6.2.2 SOLUTION COMPOSITION

Three different solutions have been prepared for the experiments: Na-Cl, Na-Ca-Cl, and Ca-Cl, with concentrations of 2 mol kgw<sup>-1</sup>, based on the Cl concentration, respectively. The solutions have been prepared with deionized water and 116.9 g kgw<sup>-1</sup> NaCl salt for the Na-Cl solution, 86.4 g kgw<sup>-1</sup> NaCl and 29.0 g kgw<sup>-1</sup> CaCl<sub>2</sub> salt (38.4 g CaCl<sub>2</sub> · 2 H<sub>2</sub>O for 990.6 g H<sub>2</sub>O) for the Na-Ca-Cl solution, and 111.0 g kgw<sup>-1</sup> CaCl<sub>2</sub> salt (147.0 g CaCl<sub>2</sub> · 2 H<sub>2</sub>O for 982.0 g H<sub>2</sub>O) for the Ca-Cl solution. The ionic strength of these 2 molal solutions depicts the natural reservoir brines of the URG which is between 94 g l<sup>-1</sup> and up to 200 g l<sup>-1</sup> (Pauwels et al., 1993; Stober & Bucher, 2014). The molar Na : Ca ratio (0.85 : 0.15) of the Na-Ca-Cl solution reflects the ratio of these elements in natural URG brines. The pure Na-Cl and Ca-Cl solutions represent the end-member of the main components of natural URG brines.

Initial solution compositions are listed in table 6.1 (Na-Cl), 6.2 (Na-Ca-Cl), and 6.3 (Ca-Cl). They contain also small amounts of inorganic carbon given by the carbon exchange of the deionized water with the atmosphere.

### 6.2.3 EXPERIMENTAL SETUP AND PROCEDURE

Three experiment series have been conducted in un-stirred batch cells with a *Teflon* in-liner for each of the three different solutions (Na-Cl, Na-Ca-Cl, Ca-Cl). The experiments were performed with time steps of 3 : 5 : 10 : 15 : 30 : 45 and 60 d. For each time step and

**Table 6.1** – Fluid compositions of initial 2 M Na-Cl solution, and fluids after the experiments. Re-calculation of pH to experimental temperature with GWB (Bethke & Yeakel, 2015). bc = batch cells, as = autoclave system.

ID		101	217	218	219	220	221	222	223	224
Exp.		Na-Cl	PA03-1	PA03-2	PA05-1	PA05-2	PA10-1	PA10-2	PA15-1	PA15-2
System		–	bc							
Time	d	initial	3	3	5	5	10	10	15	15
Cond.	mS/cm	136	140	140	143	142	143	142	139	140
$pH_{25^\circ C}$	measured	5.77	7.78	8.13	7.54	7.65	7.01	7.17	7.75	7.92
$pH_{200^\circ C}$	calculated	6.25	7.44	7.57	7.39	7.42	7.29	7.35	7.44	7.50
Alk.	mmol/l	0.1	1.3	1.3	1.4	1.4	1.5	1.65	1.2	1.2
Na	g/l	44.9	45.8	45.5	44.1	42.7	45.5	44.8	45.5	44.9
K	mg/l	<4	36.4	37	50	44	52	47	53	51
Ca	mg/l	<3	81.3	81.5	94.8	83.9	118.8	102.6	122.6	117.9
Mg	mg/l	<0.2	<0.1	<0.1	<0.1	<0.1	<0.1	<0.1	<0.1	<0.1
Fe	µg/l	<50	<30	<30	89.4	<40	<40	<40	<30	<30
Al	µg/l	<70	80.6	91.1	499	80	193	100	45	23
Si	mg/l	b.d.l.	45	45	52	47	65	61	67	62
HCO <sub>3</sub> <sup>-</sup>	mg/l	6	79	79	85	85	92	101	73	73
Cl	g/l	67.21	69.45	66.53	69.10	69.00	67.30	68.40	68.55	69.76
ID		225	226	227	228	229	230	107	129	
Exp.		PA30-1	PA30-2	PA45-1	PA45-2	PA60-1	PA60-2			
System		bc	bc	bc	bc	bc	bc	as	as	
Time	d	30	30	45	45	60	60	46	125	
Cond.	mS/cm	145	143	145	145	144	144	120	136	
$pH_{25^\circ C}$	measured	8.48	7.95	8.25	8.41	8.12	8.05	6.0	6.5	
$pH_{200^\circ C}$	calculated	7.89	7.56	7.77	7.87	7.68	7.64	6.68	7.09	
Alk.	mmol/l	1.1	1.3	1.4	1.4	1.3	1.4	0.4	1.5	
Na	g/l	49.0	46.7	46.2	48.9	44.9	45.3	38.0	44.7	
K	mg/l	58	57	64	69	73.2	70.4	39.3	54.3	
Ca	mg/l	186.5	177.7	199.4	240.3	233.7	231.1	77.1	161.4	
Mg	mg/l	<0.1	<0.1	<0.1	<0.1	<0.1	<0.1	<0.2	<0.1	
Fe	µg/l	48.2	55.9	<40	<40	<40	<40	<40	293	
Al	µg/l	99.3	287.1	<30	<30	50.3	45.8	46.6	18.2	
Si	mg/l	109	90	112	115	114	111	138	121	
HCO <sub>3</sub> <sup>-</sup>	mg/l	67	79	85	85	79	85	42.7	92	
Cl	g/l	71.69	68.18	68.60	73.70	71.59	71.11	57.4	69.9	

**Table 6.2** – Fluid compositions of initial 2 M Na-Ca-Cl solution, and fluids after the experiments. Re-calculation of pH to experimental temperature with GWB (Bethke & Yeakel, 2015). bc = batch cells, as = autoclave system.

ID		124	231	232	233	234	235	236	237	238
Exp.		Na-Ca-Cl	PB03-1	PB03-2	PB05-1	PB05-2	PB10-1	PB10-2	PB15-1	PB15-2
System		–	bc							
Time	d	initial	3	3	5	5	10	10	15	15
Cond.	mS/cm	136	135	134	137	137	139	135	136	137
$pH_{25^\circ C}$	measured	6.56	6.74	6.93	6.28	6.74	7.1	6.45	7.08	7.77
$pH_{200^\circ C}$	calculated	6.16	6.52	6.56	6.37	6.50	6.59	6.41	6.64	6.88
Alk.	mmol/l	0.2	0.6	0.6	0.6	0.6	0.6	0.6	0.7	0.7
Na	g/l	32.29	33.4	33.5	32.7	33.5	33.9	33.6	34.2	33.8
K	mg/l	4.9	38.2	36.2	47.4	48.4	51.6	49.5	53.2	50.5
Ca	mg/l	10 118	10 560	10 640	10 500	10 710	10 910	10 950	10 910	10 930
Mg	mg/l	0.6	2.2	2	1.7	1.9	1.5	1.8	1.3	1.1
Fe	µg/l	48	46	62.4	86	50	49	43	53.1	82.2
Al	µg/l	<30	83.4	55	380	232	159	341	77.3	<20
Si	mg/l	b.d.l.	79	76	91	93	101	104	109	106
HCO <sub>3</sub> <sup>-</sup>	mg/l	12	37	37	37	34	34	34	43	43
Cl	g/l	70.58	69.24	67.04	69.50	67.10	67.90	71.40	69.79	69.83
ID		239	240	241	242	243	244	125		
Exp.		PB30-1	PB30-2	PB45-1	PB45-2	PB60-1	PB60-2			
System		bc	bc	bc	bc	bc	bc	as		
Time	d	30	30	45	45	60	60	60		
Cond.	mS/cm	138	140	145	142	142	141	153		
$pH_{25^\circ C}$	measured	7.91	8.15	8.07	7.9	7.82	7.77	5.98		
$pH_{200^\circ C}$	calculated	6.95	7.11	7.08	6.97	6.94	6.90	6.25		
Alk.	mmol/l	0.7	0.9	0.9	0.8	0.8	0.8	0.6		
Na	g/l	35.9	35.4	38.3	35.5	36.0	34.4	32.9		
K	mg/l	54.7	51.6	60.3	60.6	65.2	66.4	51.7		
Ca	mg/l	11 430	10 850	11 990	10 980	11 050	10 920	9882		
Mg	mg/l	0.8	0.8	0.7	0.9	0.8	0.8	0.6		
Fe	µg/l	87.4	61.2	63.9	68	53.6	66.8	102.7		
Al	µg/l	<10	<10	<10	<10	<20	<20	<30		
Si	mg/l	105	101	107	105	108	106	108		
HCO <sub>3</sub> <sup>-</sup>	mg/l	43	55	55	49	49	49	37		
Cl	g/l	70.32	72.66	76.61	71.11	73.48	73.27	72.78		

**Table 6.3** – Fluid compositions of initial 2 M Ca-Cl solution, and fluids after the experiments. Re-calculation of pH to experimental temperature with GWB (Bethke & Yeakel, 2015). bc = batch cells, as = autoclave system.

ID		128	245	246	247	248	249	250	251	252
Exp.		Ca-Cl	PC03-1	PC03-2	PC05-1	PC05-2	PC10-1	PC10-2	PC15-1	PC15-2
System		-	bc							
Time	d	initial	3	3	5	5	10	10	15	15
Cond.	mS/cm	124	122	123	126	127	127	127	127	126
$pH_{25^\circ C}$	measured	6.32	7.18	7.44	7.77	7.55	6.54	7.13	8.23	8.11
$pH_{200^\circ C}$	calculated	5.75	6.24	6.28	6.38	6.33	6.21	6.27	6.55	6.50
Alk.	mmol/l	0.3	1.0	1.0	1.2	1.1	1.3	1.1	1.5	1.4
Na	g/l	b.d.l.	0.1	0.0	b.d.l.	b.d.l.	0.1	0.1	0.1	0.0
K	mg/l	3.2	65.1	58.3	71.2	70.7	95.8	93	80.5	77.5
Ca	mg/l	39 640	40 630	39 130	38 860	38 630	38 730	39 960	41 390	40 880
Mg	mg/l	2	3.5	3.3	3	3.3	3.4	3.1	1.7	1.9
Fe	$\mu g/l$	173.6	147.4	147.1	147.8	147.9	140.3	164.3	152.8	153.3
Al	$\mu g/l$	<30	<20	<20	<30	<30	<30	<30	<20	<20
Si	mg/l	b.d.l.	82	77	86	86	98	98	100	101
$HCO_3^-$	mg/l	18	61	61	73	70	79	67	92	85
Cl	g/l	69.50	68.16	68.47	71.30	69.00	71.90	70.90	70.44	68.19
ID		253	254	255	256	257	258	126	259	
Exp.		PC30-1	PC30-2	PC45-1	PC45-2	PC60-1	PC60-2			
System		bc	bc	bc	bc	bc	bc	as	as	
Time	d	30	30	45	45	60	60	60	128	
Cond.	mS/cm	126	128	125	136	132	136	125	121	
$pH_{25^\circ C}$	measured	8.19	8.27	7.78	8.39	8.01	8.24	6.21	5.86	
$pH_{200^\circ C}$	calculated	6.56	6.61	6.42	6.66	6.53	6.61	6.03	5.88	
Alk.	mmol/l	1.6	1.8	1.4	1.9	1.7	1.8	1.0	1.2	
Na	g/l	b.d.l.	b.d.l.	b.d.l.	b.d.l.	0.2	0.1	b.d.l.	b.d.l.	
K	mg/l	86.5	94.3	112.6	104.5	136.6	136.9	125.5	137	
Ca	mg/l	40 660	41 830	40 260	43 120	40 490	40 760	40 291	40 291	
Mg	mg/l	1.3	1.2	1.9	1.1	1.1	1.0	0.9	0.2	
Fe	$\mu g/l$	206.8	223	208.6	269.4	181.7	157.2	268.7	489	
Al	$\mu g/l$	<10	<10	<10	<10	<20	<20	<10	40	
Si	mg/l	97	97	101	94	104	99	98.4	97.0	
$HCO_3^-$	mg/l	98	110	85	116	104	110	61	73	
Cl	g/l	70.77	72.90	70.95	80.04	75.73	76.48	71.28	67.00	

solution type two experiments have been carried out to ensure results and double the post-experiment rock and fluid material, since only one rock sample could be inserted to each batch cell. The experiments were conducted at 200 °C, which is a typical reservoir temperature in the URG (Aquilina et al., 1997; Sanjuan et al., 2016). The pressure was given by the boiling pressure of the prepared solutions at experimental temperature (~16 bar). The fluid volume in the batch cells was 60 ml with an atmospheric head space.

Additionally, long-term batch-type experiments in a stirred (~100 rpm) autoclave system (Parr Instruments) were performed to control and pursue the brine–rock interaction to later stages. The duration of these experiments have been 60 d and 128 d with a temperature of 200 °C. The vessel and every component in contact with the solution is composed of Hastelloy alloy C-276. Three rock samples have been inserted to each experiment. The total volume of the vessel is 600 ml. Solution volume during the experiments was 350 ml. Pressure has been the boiling pressure of the used solutions with an initial N<sub>2</sub> pressure of 5 bar to reduce fluid condensation at the vessel head.

#### 6.2.4 FLUID ANALYTICS

After the experiments the fluid was cooled to room temperature rapidly. Electrical conductivity (Mettler Toledo Inlab 371) and pH (ProMinent PHER-112) were measured immediately and carbonate alkalinity was titrated with 0.01 M HCl. For element analyses the solutions were filtered with 0.45  $\mu m$  cellulose acetate membranes. The fluid samples were diluted with ultra-pure water by a factor of 10 to ensure solution stability. Additionally, the solutions were acidified with distilled HNO<sub>3</sub> for cation measurement. Samples were stored in 30 ml polyethylene bottles and preserved cool until analysis.

Major and minor cations were determined by inductively-coupled plasma mass spectrometry (ICP-MS) with a Thermo Fischer Scientific X-Series 2. Sample dilution was 1 : 100. Dissolved Si and Na concentration were analyzed by inductively-coupled plasma optical emission spectrometry (ICP-OES) with a Varian 715ES and a sample dilution of 1 : 100 for Si and 1 : 100/1 : 1000 for Na. Ion chromatography (IC) was performed with a Dionex ICS-1000 for dissolved anions. Due to high concentrations of Cl and a consequential need for high dilution of the sample (1 : 2000), it was not possible to detect other anions than Cl.

Continuously, standard solutions were remeasured during analysis procedure to ensure quality of measurements. Accuracy of ICP-MS measurements is better than 3 % for main cations and better than 8 % for Al and Fe, for ICP-OES better than 5 % and for IC better than 4 %.

### 6.2.5 SOLID ANALYTICS

Rock samples have been removed from the vessel after solution extraction and washed two times with deionized water to prevent salt precipitation. After both cleanings, the samples have been dried at laboratory temperature.

Characterization of the pre- and post-experiment rock samples was performed with several analytical and imaging methods. The mineral content was identified by powder X-ray diffraction (XRD) measurements with a *Bruker D8 Discover*. System parameters were a Cu anode at 40 kV and 40 mA and a silicon strip detector (lynxeye XE-T). The scanning range was 2–82°, with a step size of 0.01° 2 $\theta$ . Unaltered samples were measured as representative bulk material, whereas only surface material of the altered samples was used to identify secondary phases formed during alteration.

Zeolites have been characterized by synchrotron X-ray micro diffraction. Crystals and crystal aggregates have been removed from sample surface directly to a Kapton tape. Some of them were crushed on the tape in order to increase distribution of crystallite orientation. Nevertheless, random orientation could not be achieved so that some deviations from theoretical Bragg peak intensity ratios may occur.

Micro focussed X-ray diffraction (*mu*-XRD) was carried out at the SUL-X beamline of the ANKA synchrotron radiation source (Karlsruhe Institute of Technology) using a CCD detector (Photonic Science XDI VHR-2 150) in symmetric transmission with a focused beam of about 100  $\mu\text{m}$  horizontal and 50  $\mu\text{m}$  vertical at sample position. The choice of 10 keV (about 1.257 Å X-ray wavelength) enable at a sample-detector distance of about 105 mm and a detector area of 80  $\times$  120 mm<sup>2</sup> a maximum diffraction angle of ca. 35° corresponding to a minimum lattice spacing  $d$  ca. 2.2 Å and to detect  $d$  values up to about 15 Å, sufficient for zeolite mineral identification. CCD frames were analyzed using Fit2D (Hammersley et al., 1996; Hammersley et al., 1994). Instrumental parameters were determined with a LaB6 NIST Standard (660b) and subsequently employed for integration of the sample frames into 1D diffractograms. For mineral identification the ICDD database (ICDD, 2016) has been used.

Alteration processes on sample surfaces and cross-sectional thin sections were detected and visualized by scanning electron microscopy (SEM) with a FEI Quanta 650 ESEM. Surface characterizations were made in secondary electron (SE) mode with an acceleration voltage

of 10 kV. Additionally, thin sections were examined for alteration reaction textures in the sample interior under back-scattered electron (BSE) mode at the same device settings. Mineral identification and qualitative analyses have been conducted with energy-dispersive X-ray spectroscopy (EDX, Bruker XFlash 5010 detector). Rock samples and thin sections were covered with carbon before SEM analyses.

Electron microprobe (EMP) measurements were carried out with a JEOL JXA-8530F. Calibration was performed on the following natural standards: Al:  $\text{Al}_2\text{O}_3$ , Ca + Si: wollastonite, Fe:  $\text{Fe}_2\text{O}_3$ , K: orthoclase, Na: albite, Mg: MgO, Ba: baryte. Measuring conditions were an acceleration voltage of 15 kV, a beam current of 20 nA and a beam diameter of 1  $\mu\text{m}$  for all mineral phases except zeolites. Detection limit was 0.01 wt.%. All iron has been assumed as  $\text{Fe}^{2+}$ . Zeolites were measured with the analysis protocol developed by Campbell et al. (2016) dedicated for this type of mineral phases. Acceleration voltage of 15 kV, a beam current of 2 nA, and a de-focused beam with diameter of 10  $\mu\text{m}$ . Campbell et al. (2016) suggested a beam diameter of 20  $\mu\text{m}$ , but our zeolite grains are too small or cracked into too small fragments for this beam size. Charge balance error was calculated after Passaglia (1970):  $E\% = 100 \times \frac{\text{Al} - (\text{K} + \text{Na}) - 2(\text{Mg} + \text{Ca} + \text{Sr} + \text{Ba})}{(\text{K} + \text{Na}) + 2(\text{Mg} + \text{Ca} + \text{Sr} + \text{Ba})}$  with an acceptable error of  $\pm 10\%$ .

## 6.3 RESULTS

### 6.3.1 INITIAL ROCK SAMPLE

The initial sandstone material is from a quarry in the Northern Black Forest (Pfinztal), which occurs in the URG in reservoir depth. Geothermal boreholes in Bruchsal, Croenbourg, Rittershoffen, and Brühl target Bunter formations in depths between 1800–3300 m.

The sandstone sample is fine grained (0.04–0.2 mm, mostly <0.1 mm). The clasts are well sorted and have an angular to sub-spherical shape. Sub-spherical feldspars and platy muscovites result in a layered texture. The main components of the sandstone are quartz (49%), pure K-feldspar (16%) and muscovite (11%). The cementation (15%) is made of illite, quartz and hematite in interstitial space. Open pore space is about 8%. Larger pores are filled with agglomerations of muscovite particles, and minor chlorite, biotite, and kaolinite. Further accessory minerals are calcite, rutile, and apatite.

Quartz grains have smooth surfaces with few small holes and rarely show dissolution edges. The feldspar is exclusively Na-free K-feldspar. Chemical zonation or exsolution features are absent. Pitted alteration structures are visible on most K-feldspar grains. Muscovite grains are platy, often banded and with kink bands. The muscovite contains a small Mg-Fe celadonite component. Interstitial illite is characterized, and distinguished from the muscovite clasts, by a lower K content on the interlayer site. The charge balance is probably maintained by higher  $\text{Fe}^{3+}$ . Chemical data for all initial mineral phases of the initial sandstone are published in Schmidt et al. (2017a).

### 6.3.2 SAMPLE AFTER THE EXPERIMENTS

Solid samples changed significantly close to the rock–fluid interface. Primary sandstone minerals reacted with the 2 M Na-Cl, Na-Ca-Cl, and Ca-Cl solutions. The observations on

the primary minerals are mostly very similar in all the experiment series, independently of the initial solution composition.

Quartz dissolution is ubiquitous at the mineral–fluid contact zone. In the outermost range, quartz dissolution result in etch pits within the single grains. Further, at grain boundaries, quartz dissolution, reaches up to ~1 mm into the rock sample (Fig. 6.1 a + b). Quartz dissolution in the Ca-Cl samples tend to be less intense (Fig. 6.1 c). Additional long-term experiments (125 d) with Na-Cl and Ca-Cl solution, respectively, show quartz dissolution progress further with experimental duration (Fig. 6.2).

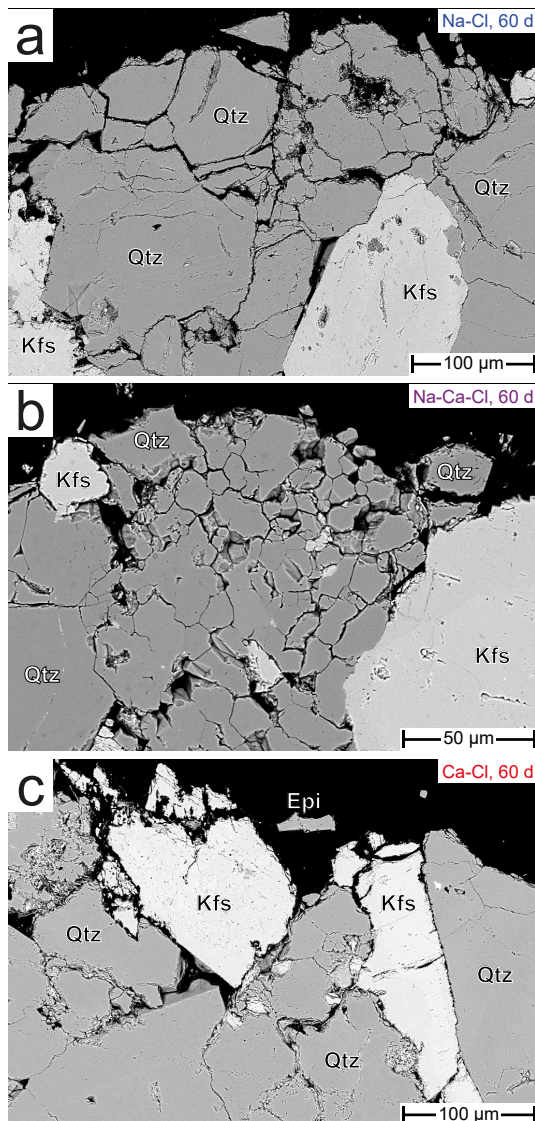


**Figure 6.1** – SEM-BSE image of thin sections after 60 days of experiment of samples from (a) the Na-Cl series, (b) the Na-Ca-Cl series, and (c) the Ca-Cl series. Quartz grains close to the rock–fluid interface show dissolution holes/etch pitches and intense dissolution along the grain boundaries. Illite removal from the sandstone cementation enhance the inter-clast pathways. K-feldspars in the Ca-Cl series is highly etched.

Reactions of the K-feldspars have not been observed in the experimental series with the Na-Cl and Na-Ca-Cl solutions, neither morphologically nor chemically (Fig. 6.1 a + b). K-feldspar grains seem to keep their diagenetic grain shape, indicated by direct grain contact between K-feldspar and quartz (Fig. 6.1 a + b), and crystallographic ideal edges at the sample surface. Whereas in the Ca-Cl series K-feldspars are dissolved at their grain boundaries and toward the grain centers (Fig. 6.1 c). The observations are more obvious in the long-term experiments, where K-feldspar dissolution is highly evolved in in the Ca-Cl experiments (Fig. 6.2). Whereas K-feldspars from the Na-Cl experiment still remain nearly

unaffected by the solutions.

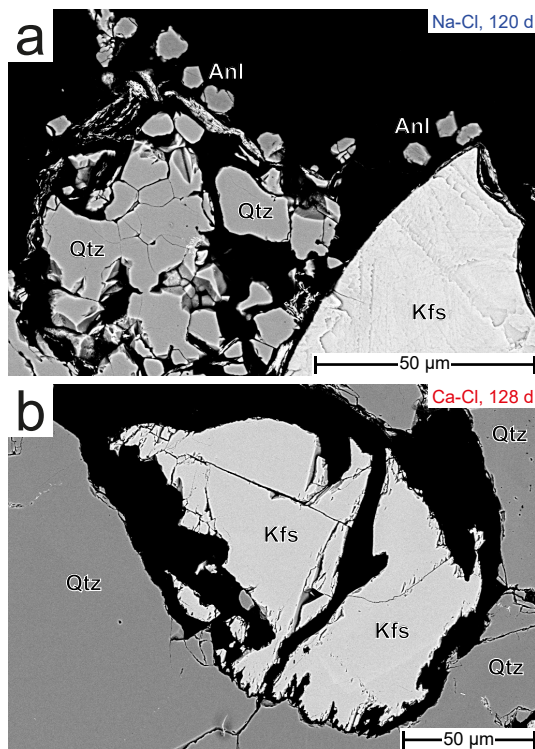


**Figure 6.2** – SEM-BSE image of thin sections after 128 days of experiment. (a) Na-Cl experiment: Quartz dissolution is highly proceeded, clay minerals nearly lack on sample surface, analcime crystals are very frequently, K-feldspar show no alteration features. (b) Ca-Cl experiment: quartz dissolution is in minor extent, cementation is rare, K-feldspar dissolution is highly proceeded.

Illite, constitute the cementation of the sandstone, has been removed from the sample surface. The removal propagates into the rock samples, forming inter-clasts space and channels up to a depth of  $\sim 1$  mm within the sandstone sample (Fig. 6.1 a). Muscovite grains show no morphological and chemical changes during all the experiments, independent on the experimental solution (Fig. 6.3 a).

#### *ZEOLITES IN THE NA-CL EXPERIMENTS*

Besides the changes in the primary mineral assemblage, new large spherical analcime crystals precipitate during the Na-Cl solution experiment series (Fig. 6.3 b). They are recognizable on the sample surface already from an experimental duration of 10 days by SEM (Fig. 6.3 c). Analcimes of the 10 day samples are spherical with only hinted crystal faces. The diameters are maximum 5 μm.

Analcime size increases with increasing experimental duration. The diameters reach up to 60 μm after 60 days of experiment (Fig. 6.3 d). Size distribution is very equigranular in samples of the same experimental duration (Fig. 6.3 b). The quantity of analcime crystals seems to stay constant over the experimental duration. Typical analcime crystal faces are observable, however, not well developed in samples of a longer experimental duration. Many edges and corners cover the crystal faces from the batch cells (Fig. 6.3 d).

In thin sections the intergrow of the analcimes with the primary minerals is observable (Fig. 6.3 e + f). The spherical analcimes grow on the surface of every mineral present in the initial sample (qtz, kfs, ms). They are partly firmly connected in edges and corners of the sample surface, taking shape of the adjacent mineral grains (Fig. 6.3 e), partly lie rather loose on the surface, building up a nearly perfect spherical shape (Fig. 6.3 f). Pieces

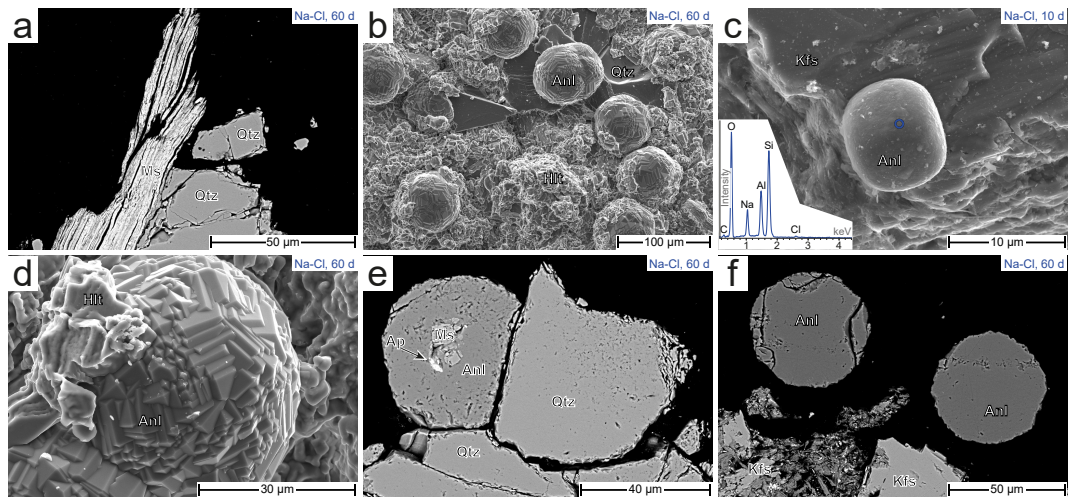


**Figure 6.3** – SEM-SE and -BSE images of samples after experiments with Na-Cl solution: (a) Muscovite grain at sample surface after 60 days of experiment. (b) Precipitated analcime crystals after 60 days of experiment. Halite precipitated from residue solution while drying. (c) Small analcime crystal after 10 day of experiment. Blue circle marks the measuring point of the EDX spectra. (d) Single analcime crystal after 60 days of experiment. The faces of the round crystal shape is built up by stepped and edged surfaces. (e) Cross-cut of a rounded analcime, crystallized on quartz grains with dissolution features on the (sub-)surface and along their grain boundaries. The Analcime enclose small muscovite and apatite particles in its center (60 d exp.). (f) Two round analcime crystals, precipitated on the sample surface, close to primary K-feldspar and remains of the initial sandstone cementation (ilt, hem, 60 d exp.).

of primary mineral grains are enclosed within the analcime crystals. In several analcimes quartz and K-feldspar particles are located in the center of the analcimes (Fig. 6.3 e). Also hematite and apatite has been found within the analcimes, whereas illite inclusions are absent. Inclusions are solely located in the center of the analcime crystals.

XRD measurements of surface material from sandstone samples of all experimental steps have been investigated (Fig. 6.4). Initially, quartz, K-feldspar, muscovite, hematite, and calcite have been identified. After the experiments, quartz, K-feldspar have been re-identified in the surface material. Hematite and calcite have not been detected in most of the samples. All diffractograms show the occurrence of halite, which should originate from residues of the experimental solution. Analcime is unequivocally detected with relatively high peak intensities. It is detectable in samples after 30 days of experimental duration (Fig. 6.4).

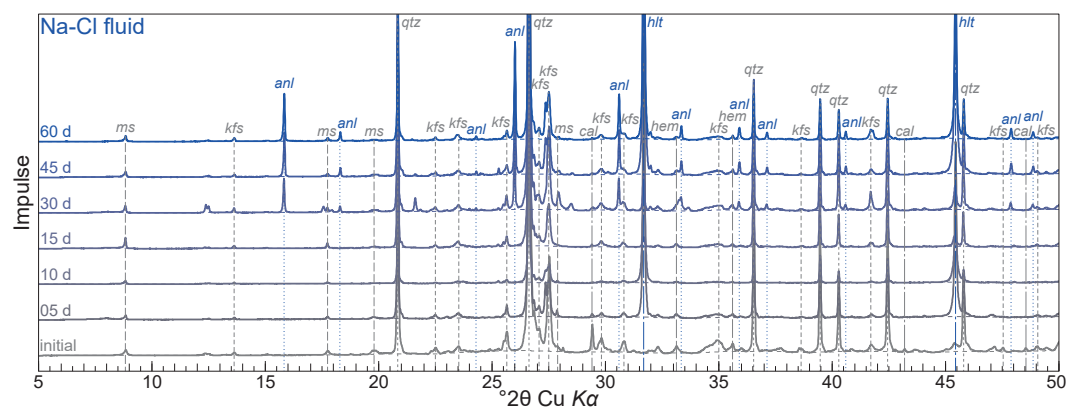


**Figure 6.4** – XRD pattern of the Na-Cl samples.  $2\theta\text{CuK}\alpha$  radiation (Wavelength 1.5406 Å). Dashed lines = background. qtz = quartz, kfs = K-feldspar, ms = muscovite, cal = calcite, hem = hematite, anl = analcime, hlt = halite.

The chemical composition of analcime was measured by EMP in the 60 day samples (Table 6.4). Na is the solely alkali cation in the analcimes of this experiment series (Na<sub>2</sub>O 11.5–12.2 wt.%). Ca and K is very low (CaO ≤ 0.13 wt.%, K<sub>2</sub>O ≤ 0.14 wt.%) and mostly close to detection limit. The molar Na/(Ca + Na) component is invariably ~1.00 (Table 6.4). The SiO<sub>2</sub> and Al<sub>2</sub>O<sub>3</sub> content is 55.4–57.4 wt.% and 19.6–22.3 wt.%, respectively. The mean composition gives an analcime formula of Na<sub>1.8</sub>Al<sub>1.8</sub>Si<sub>4.2</sub>O<sub>12</sub> · 2 H<sub>2</sub>O on the basis of 12 O (ideal composition: Na<sub>2</sub>Al<sub>2</sub>Si<sub>4</sub>O<sub>12</sub> · 2 H<sub>2</sub>O). Charge balance, given by *E*%, is between 0 and 6 (±10 is acceptable, Passaglia, 1970). Proportion of Si on tetrahedral framework sites  $R = \text{Si}/(\text{Si} + \text{Al})$  is 0.70–0.71, which is in the range of natural analcimes (0.60–0.74, Passaglia & Sheppard, 2001). Compositional variations from the center to the rims do not exist, thus, no compositional changes in time.

**Table 6.4** – Analcime composition (EMP measurements) of the Na-Cl (PA60) and Na-Ca-Cl (PB60) experiments after 60 d duration.  $R = \text{Si}/(\text{Si} + \text{Al})$ ,  $E = 100 \times (\text{Al} - (\text{K} + \text{Na}) - 2(\text{Mg} + \text{Ca} + \text{Sr} + \text{Ba})) / ((\text{K} + \text{Na}) + 2(\text{Mg} + \text{Ca} + \text{Sr} + \text{Ba}))$  (Coombs et al., 1997).

Mineral Experiment	anl PA60	anl PB60									
SiO <sub>2</sub>	55.44	56.15	54.90	57.24	57.40	56.42	56.49	55.64	56.19	56.02	56.29
Al <sub>2</sub> O <sub>3</sub>	20.01	20.13	20.32	19.57	19.59	20.31	20.38	20.59	20.61	20.43	20.22
FeO	0.05	0.24	0.00	0.20	0.07	0.00	0.18	0.00	0.02	0.10	0.00
MgO	0.00	0.00	0.02	0.01	0.00	0.00	0.01	0.00	0.02	0.04	0.01
CaO	0.03	0.05	0.03	0.07	0.13	0.00	0.78	0.80	0.83	0.82	0.79
Na <sub>2</sub> O	11.65	11.59	12.22	11.58	11.48	11.63	10.54	11.26	10.55	11.30	10.93
K <sub>2</sub> O	0.14	0.00	0.03	0.02	0.02	0.03	0.03	0.03	0.02	0.13	0.00
BaO	0.00	0.00	0.00	0.00	0.00	0.07	0.00	0.15	0.00	0.00	0.03
Total	87.32	88.15	87.52	88.69	88.69	88.46	88.41	88.46	88.24	88.83	88.26
Cation distribution normalized to O <sub>12</sub> · 2 H <sub>2</sub> O											
Si	4.22	4.23	4.18	4.28	4.28	4.23	4.23	4.19	4.21	4.20	4.23
Al	1.79	1.79	1.82	1.72	1.72	1.79	1.80	1.83	1.82	1.80	1.79
Fe	0.00	0.01	0.00	0.01	0.00	0.00	0.01	0.00	0.00	0.01	0.00
Mg	0.00	0.00	0.00	0.00	0.00	0.00	0.00	0.00	0.00	0.00	0.00
Ca	0.00	0.00	0.00	0.01	0.01	0.00	0.06	0.06	0.07	0.07	0.06
Na	1.72	1.69	1.80	1.68	1.66	1.69	1.53	1.64	1.53	1.64	1.59
K	0.01	0.00	0.00	0.00	0.00	0.00	0.00	0.00	0.00	0.01	0.00
Ba	0.00	0.00	0.00	0.00	0.00	0.00	0.00	0.00	0.00	0.00	0.00
Sum	7.75	7.73	7.81	7.70	7.69	7.72	7.64	7.72	7.64	7.73	7.67
Na / (Na + Ca)	1.00	1.00	1.00	1.00	0.99	1.00	0.96	0.96	0.96	0.96	0.96
<i>E</i>	3	5	0	2	2	6	8	2	9	1	4
<i>R</i>	0.70	0.70	0.70	0.71	0.71	0.70	0.70	0.70	0.70	0.70	0.70

#### ZEOLITES IN THE NA-Ca-CL EXPERIMENTS

Analcime crystals occur on the sample surface on the Na-Ca-Cl series, too (Fig. 6.5 a – c). Analcime could be observed by SEM on samples not before an experimental duration of 15 days. The size of the analcimes is ~60 μm on samples after 60 days of experiment. The shape of the analcimes is similar to the ones from the Na-Cl experiments, with slightly finer edges on the crystal faces (Fig. 6.5 c).

Large crystals with a size of about 200 μm are present on the sample surface from the 45 d and 60 d experimental duration (Fig. 6.5 a, b + d), which is presumably wairakite (see discussion in Sec. 6.4.1). First sporadic wairakite crystals could be seen in samples of the 10 day experiments, where the size is already ~30 μm.

The diffractograms of the Na-Ca-Cl experimental series show a similar pattern of the initial sandstone minerals as in the pure Na-Cl series (Fig. 6.6). Here again halite peaks occur due to precipitation from experimental solution during sample drying. Wairakite could be identified in the diffractograms of samples with an experimental duration of ≥30 days, whereas analcime could be detected not before a experimental duration of 45 days

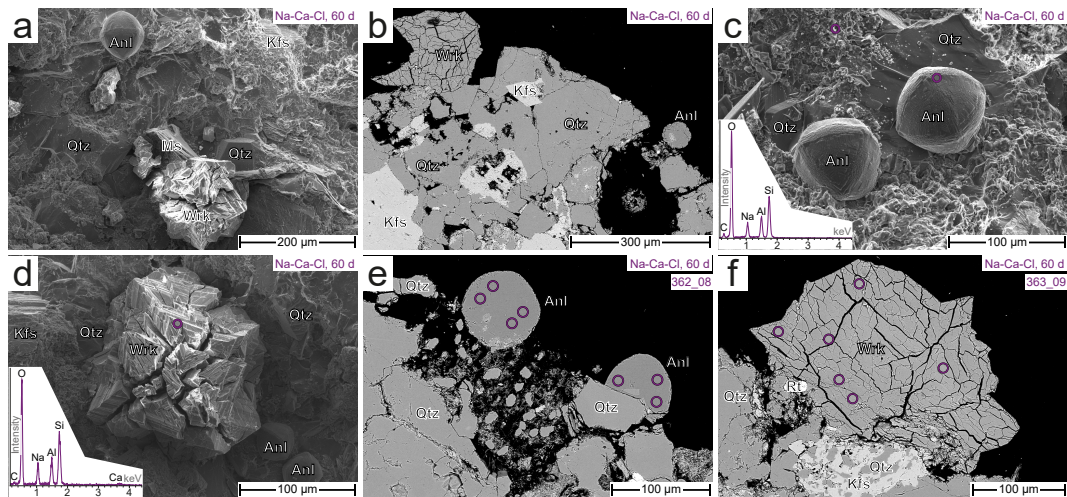


**Figure 6.5** – SEM-SE and -BSE images of samples after experiments with Na-Ca-Cl solution: (a) Sandstone surface after 60 days of experiment. Analcime and wairakite precipitations on initial quartz and K-feldspar. (b) Thin section image of the sub-surface after 60 days of experiment. Quartz show dissolution features within surface-near grains and along grain boundaries. Cementation has been removed during experiment. Wairakite and analcime occur at sample surface. (c) Spherical analcime on initial quartz. The crystal faces are recognizable, but covered with steps and edges. Purple circle marks the measuring point of the EDX spectra. (d) Wairakite crystal with smaller analcimes on a sample after 60 days of experiment. Cracks in the crystal are a result of the electron beam during image recording. Purple circle marks the measuring point of the EDX spectra. (e) Spherical analcime crystals at sample surface, enclosing quartz and hematite particles. Quartz dissolution features and residual cementation are seen below. (f) Cross-cut through a wairakite crystal. (d) + (f) EMP measuring points (Table 6.4 + 6.5) marked by circles (10  $\mu\text{m}$  beam size).

(Fig. 6.6).

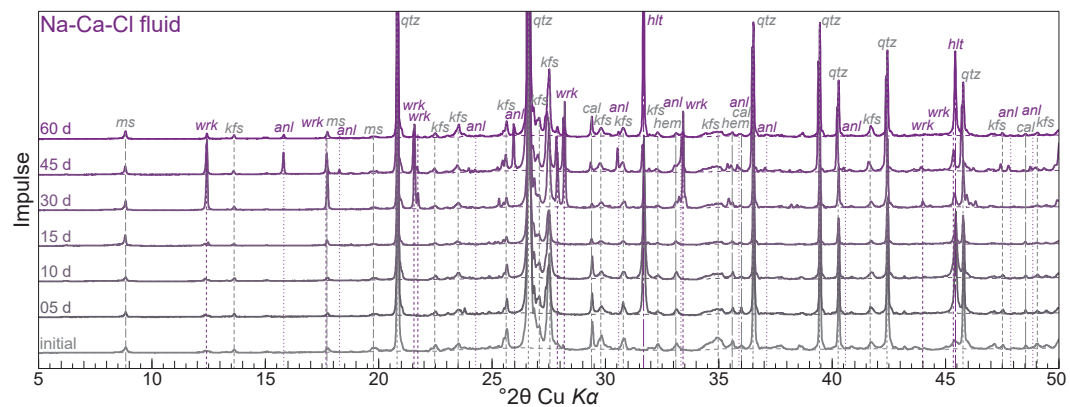


**Figure 6.6** – XRD pattern of the Na-Ca-Cl samples.  $2\theta\text{CuK}\alpha$  radiation (Wavelength 1.5406  $\text{\AA}$ ). Dashed lines = background. Abbreviations see Fig. 6.4, wrk = wairakite.

Chemical composition of the zeolites are listed in table 6.4 for analcime (Fig. 6.5 e) and table 6.5 for wairakite (Fig. 6.5 f). Analcime in the Na-Ca-Cl experiment series has Na concentrations in the range of  $\text{Na}_2\text{O}$  10.5–11.3 wt.%, and higher Ca contents ( $\text{CaO}$   $\sim$ 0.8 wt.%) than in the Na-Cl experiment. The molar  $\text{Na}/(\text{Ca} + \text{Na})$  ratio is  $\sim$ 0.96 (Table 6.4). K concentration is low ( $\text{K}_2\text{O} \leq 0.13$  wt.%). The alkali content of analcimes displays the fluid concentrations of Na, K, and Ca. The amount of Si and Al is given as  $\text{SiO}_2$  and  $\text{Al}_2\text{O}_3$  as 55.6–56.5 wt.% and 20.2–20.6 wt.%, respectively, leading to a  $R$  value of 0.70. The mean composition gives an analcime formula of  $\text{Na}_{1.6}\text{Ca}_{0.1}\text{Al}_{1.8}\text{Si}_{4.2}\text{O}_{12} \cdot 2\text{H}_2\text{O}$  on the basis of 12 O.  $E\%$  is between 1 and 9. Equally to the Na-Cl experiments, the analcime composition do not differ within one mineral grain, meaning with experimental duration.

**Table 6.5** – Wairakite composition (EMP measurements) of the Na-Ca-Cl (PB60) and Ca-Cl (PC60) experiments after 60 d duration.  $R = \text{Si}/(\text{Si} + \text{Al})$ ,  $E = 100 \times (\text{Al} - (\text{K} + \text{Na}) - 2(\text{Mg} + \text{Ca} + \text{Sr} + \text{Ba})) / ((\text{K} + \text{Na}) + 2(\text{Mg} + \text{Ca} + \text{Sr} + \text{Ba}))$  (Coombs et al., 1997).

Mineral Experiment	wrk PB60	wrk PC60										
SiO <sub>2</sub>	52.75	53.45	55.86	52.90	53.25	52.01	54.08	54.17	54.94	54.10	54.53	52.81
Al <sub>2</sub> O <sub>3</sub>	20.88	20.14	20.16	20.82	20.71	20.24	20.94	20.94	21.58	21.34	21.28	20.70
FeO	0.00	0.00	0.01	0.06	0.00	0.03	0.00	0.00	0.05	0.10	0.00	0.14
MgO	0.00	0.00	0.00	0.04	0.02	0.02	0.05	0.00	0.03	0.00	0.04	0.00
CaO	5.89	5.45	5.77	5.39	4.93	4.99	11.73	11.88	12.13	12.00	11.90	11.85
Na <sub>2</sub> O	5.23	5.04	4.61	5.53	6.11	5.43	0.05	0.08	0.19	0.05	0.00	0.11
K <sub>2</sub> O	0.74	0.76	0.86	0.96	0.99	0.92	0.10	0.09	0.10	0.04	0.05	0.01
BaO	0.00	0.00	0.00	0.00	0.04	0.00	0.00	0.00	0.03	0.00	0.07	0.02
Total	85.48	84.85	87.27	85.70	86.05	83.64	86.95	87.17	89.04	87.62	87.88	85.63
Cation distribution normalized to O <sub>12</sub> · 2 H <sub>2</sub> O												
Si	4.10	4.17	4.23	4.11	4.12	4.13	4.11	4.11	4.09	4.08	4.10	4.08
Al	1.91	1.85	1.80	1.91	1.89	1.87	1.87	1.89	1.89	1.90	1.89	1.89
Fe	0.00	0.00	0.00	0.00	0.00	0.00	0.00	0.00	0.00	0.01	0.00	0.01
Mg	0.00	0.00	0.00	0.00	0.00	0.00	0.01	0.00	0.00	0.00	0.00	0.00
Ca	0.49	0.46	0.47	0.45	0.41	0.42	0.95	0.97	0.97	0.97	0.96	0.98
Na	0.79	0.76	0.68	0.83	0.92	0.84	0.01	0.01	0.03	0.01	0.00	0.02
K	0.07	0.08	0.08	0.10	0.10	0.09	0.01	0.01	0.01	0.00	0.00	0.00
Ba	0.00	0.00	0.00	0.00	0.00	0.00	0.00	0.00	0.00	0.00	0.00	0.00
Sum	7.37	7.32	7.25	7.40	7.44	7.39	6.96	6.97	6.99	6.97	6.96	6.98
Na / (Na + Ca)	0.62	0.63	0.59	0.65	0.69	0.66	0.01	0.01	0.03	0.01	0.00	0.02
E	4	6	6	4	3	6	-3	-4	-4	-3	-3	-5
R	0.68	0.69	0.70	0.68	0.69	0.69	0.69	0.69	0.68	0.68	0.68	0.68

Wairakite in the Na-Ca-Cl experiments contains Ca as CaO in the range of 4.9–5.9 wt.% (Table 6.5). Na given as Na<sub>2</sub>O is mostly between 4.6–6.1 wt.%. The resulting molar Na/(Ca + Na) ratio varies highly between 0.59 and 0.69. K<sub>2</sub>O content of the wairakite is elevated and reaches 0.7 to 1.0 wt.%, which is the highest concentration in a zeolite precipitated in all experimental series. The SiO<sub>2</sub> and Al<sub>2</sub>O<sub>3</sub> content is 52.0–55.9 wt.% and 20.1–20.9 wt.%, respectively. *R* value is constant between 0.68 and 0.70 (natural samples 0.65–0.70, Passaglia & Sheppard, 2001). *E*% range between 3 and 6. A mean composition can be formulated by Ca<sub>0.5</sub>Na<sub>0.8</sub>K<sub>0.1</sub>Al<sub>1.9</sub>Si<sub>4.1</sub>O<sub>12</sub> · 2 H<sub>2</sub>O. The ideal wairakite composition is CaAl<sub>2</sub>Si<sub>4</sub>O<sub>12</sub> · 2 H<sub>2</sub>O.

#### ZEOLITES IN THE CA-CL EXPERIMENTS

In the Ca-Cl experiment series no analcime has been found. Wairakite precipitates on the sample surfaces of these series, too (Fig. 6.7 a). It is equigranular with a size of ~100–300 μm in the 45 and 60 day samples (Fig. 6.7 b). The crystals can be observed in samples after an experimental duration of 10 days by SEM.

Sporadically a stalky, fan-like mineral phase occurs on the sample surface of the 45 d and 60 d Ca-Cl experiments (Fig. 6.7 a + c), which has been identified as epistilbite by synchrotron XRD measurements (see below). It has a total size of up to ~70 μm, but with a stalk width of about 0.5 × 5 μm<sup>2</sup> (Fig. 6.7 d).

Similar to the other experimental series, XRD pattern of the Ca-Cl experiment show quartz, K-feldspar, muscovite, calcite, and hematite in samples from all experimental steps (Fig. 6.8). Halite is not present on the sample surfaces. Wairakite could be detected in samples after 30 days experimental duration. The occurrence of epistilbite is too rare to detect it with laboratory XRD.

The chemical composition of the wairakites from the Ca-Cl experiments is very homogeneous (Table 6.5, Fig. 6.7 e). Ca content is between 11.7–12.1 wt.% CaO, whereas Na and K occur in traces (≤0.19 wt.% Na<sub>2</sub>O and ≤0.10 wt.% K<sub>2</sub>O, resp.). Therefore, the molar Na/(Na + Ca) ratio is very low (≤0.02). The SiO<sub>2</sub> and Al<sub>2</sub>O<sub>3</sub> content is 52.8–54.9 wt.% and

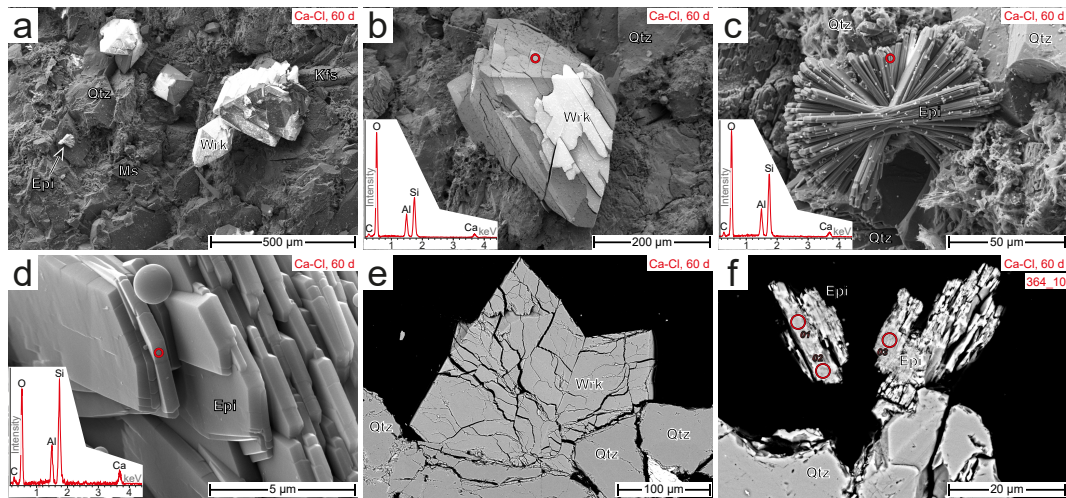


**Figure 6.7** – SEM-SE and -BSE images of samples after experiments with Ca-Cl solution: (a) Sandstone surface after 60 days of experiment with large wairakite precipitates and small fan-like epistilbite. (b) Large, euhedral wairakite crystal on quartz and K-feldspar. Cracks result from the electron beam. (c) Fan-like epistilbite with EDX spectra. (d) Stalk head of epistilbite with EDX spectra. (e) Cross-cut of wairakite, precipitated on quartz. (f) Cross-cut of epistilbite at sample surface. EMP measuring points (Table 6.6) marked by circles (2  $\mu\text{m}$  beam size). EDX measuring points marked with red circles.

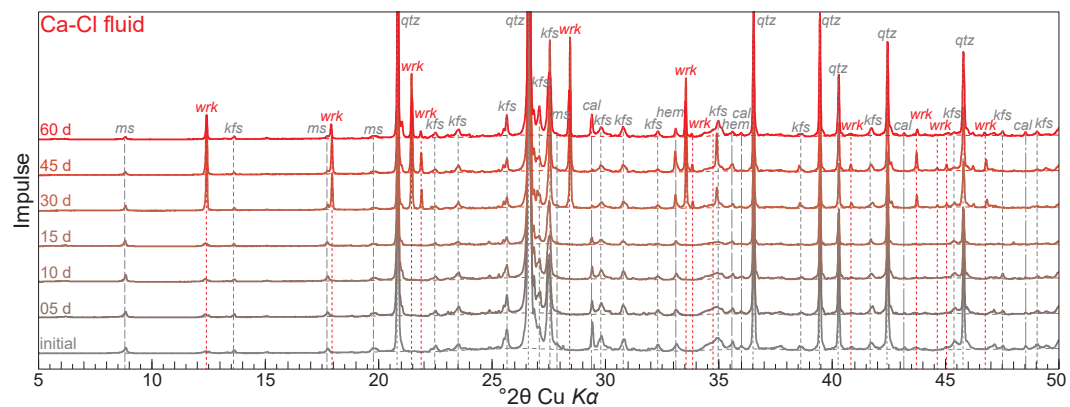


**Figure 6.8** – XRD pattern of the Ca-Cl samples.  $2\theta\text{CuK}\alpha$  radiation (Wavelength 1.5406  $\text{\AA}$ ). Dashed lines = background. Abbreviations see Fig. 6.4, wrk = wairakite, epi = epistilbite.

20.7–21.6 wt.%, respectively, which result in a  $R$  value of 0.68–0.69.  $E\%$  range between  $-5$  and  $-3$ . A mean composition of the Ca-Cl series wairakite is  $\text{Ca}_{0.95}\text{Al}_{1.9}\text{Si}_{4.1}\text{O}_{12} \cdot 2 \text{H}_2\text{O}$ , which is very close to the ideal formula ( $\text{CaAl}_2\text{Si}_4\text{O}_{12} \cdot 2 \text{H}_2\text{O}$ ).

EMP measurements of the fan-like zeolite (Table 6.6) give also a very consistent chemical composition of the epistilbite crystals (Fig. 6.7 f). CaO is by far the main (solely) alkali component with concentrations of 9.3–9.8 wt.%.  $\text{Na}_2\text{O}$  and  $\text{K}_2\text{O}$  contents are  $\leq 0.10$  wt.% and  $\leq 0.09$  wt.%, respectively. The resulting molar  $\text{Na}/(\text{Na} + \text{Ca})$  ratio is  $\leq 0.02$ . The  $\text{SiO}_2$  and  $\text{Al}_2\text{O}_3$  content is 57.3–62.9 wt.% and 16.9–18.3 wt.%, respectively, which give  $R$  values of 0.74–0.75 (natural samples between 0.73–0.77, Passaglia & Sheppard, 2001).  $E\%$  range between  $-1$  and  $2$ . The EMP data give a mean formula of  $\text{Ca}_{1.0}\text{Al}_{2.0}\text{Si}_{6.0}\text{O}_{16} \cdot 5 \text{H}_2\text{O}$ , which matches perfectly the ideal epistilbite composition (Anthony et al., 2015).

**Table 6.6** – Epistilbite composition (EMP measurements) of the Ca-Cl (PC60) experiments after 60 d duration.  $R = \text{Si}/(\text{Si} + \text{Al})$ ,  $E = 100 \times (\text{Al} - (\text{K} + \text{Na}) - 2(\text{Mg} + \text{Ca} + \text{Sr} + \text{Ba})) / ((\text{K} + \text{Na}) + 2(\text{Mg} + \text{Ca} + \text{Sr} + \text{Ba}))$  (Coombs et al., 1997).

Mineral Experiment	epi PC60					
$\text{SiO}_2$	60.40	60.88	62.86	58.04	57.32	58.75
$\text{Al}_2\text{O}_3$	17.39	18.31	17.82	17.16	17.32	16.92
FeO	0.04	0.00	0.08	0.09	0.03	0.00
MgO	0.01	0.00	0.02	0.01	0.00	0.00
CaO	9.28	9.83	9.78	9.40	9.38	9.27
$\text{Na}_2\text{O}$	0.03	0.10	0.02	0.00	0.02	0.04
$\text{K}_2\text{O}$	0.07	0.09	0.07	0.07	0.04	0.07
BaO	0.06	0.00	0.00	0.04	0.00	0.00
Total	87.34	89.20	90.66	84.83	84.12	85.04
Cation distribution normalized to $\text{O}_{16} \cdot 5 \text{H}_2\text{O}$						
Si	5.98	5.91	5.99	5.93	5.90	5.97
Al	2.03	2.09	2.00	2.07	2.10	2.03
Fe	0.00	0.00	0.01	0.01	0.00	0.00
Mg	0.00	0.00	0.00	0.00	0.00	0.00
Ca	0.98	1.02	1.00	1.03	1.03	1.01
Na	0.01	0.02	0.00	0.00	0.00	0.01
K	0.01	0.01	0.01	0.01	0.01	0.01
Ba	0.00	0.00	0.00	0.00	0.00	0.00
Sum	9.01	9.06	9.01	9.04	9.05	9.02
Na / (Na + Ca)	0.01	0.02	0.00	0.00	0.00	0.01
$E$	2	1	-1	-1	1	0
$R$	0.75	0.74	0.75	0.74	0.74	0.75

#### SYNCHROTRON X-RAY DIFFRACTION OF ZEOLITES

Synchrotron X-ray diffraction has been applied to identify and characterize the newly formed zeolites. Therefore, single zeolite crystals or crystal aggregates have been picked from the 60 d sample surfaces and measured as single crystal, crushed, or directly as aggregates (epistilbite). Figure 6.9 shows a selection of zeolite diffractograms from all experimental series.

Analcime from both, the Na-Cl and the Na-Ca-Cl series, fit very well with a cubic pattern (1a-3d,  $a = 13.707 \text{ \AA}$ , PDF 41-1478, Ferraris et al., 1972). There are no significant peak shifts in the analcimes of the Na-Cl compared to the Na-Ca-Cl series, despite their different chemical composition (Ca content).

Wairakite from the Ca-Cl series sample match rather good with the X-ray diffraction pattern of the tetragonal form ( $a = 10.010 \text{ \AA}$ ,  $c = 9.890 \text{ \AA}$ , PDF 15-0139, Barrer & Denny, 1961). The wairakites from the Na-Ca-Cl series have shifted peak positions compared to the peak positions in the Ca-Cl experiments. (See discussion in Sec. 6.4.1.)

The fan-like crystal aggregates (Fig. 6.10) in samples of the Ca-Cl series can be clearly

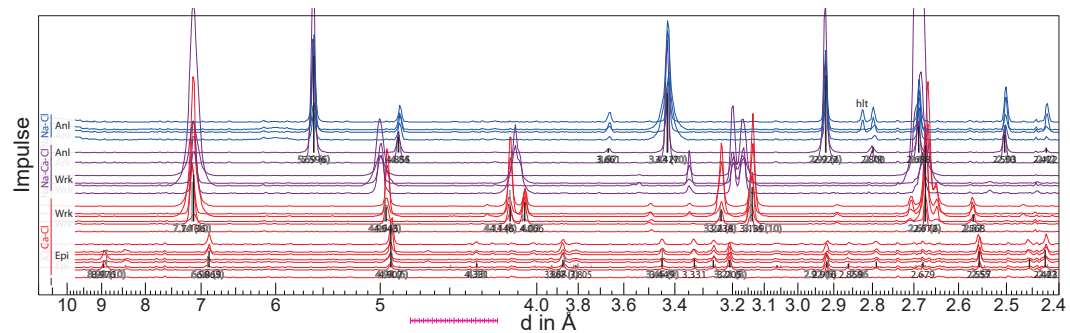


**Figure 6.9** – Synchrotron X-ray diffractogram of zeolites from the Na-Cl (blue), Na-Ca-Cl (purple), and Ca-Cl (red) experiments. Most intense peaks (d-spaces) below the diffractograms in Å. Background subtracted. Intensities not to scale. hlt = halite.

identified as epistilbite by synchrotron X-ray diffraction. Measurements of such aggregates show Bragg peaks that are in agreement with monoclinic epistilbite ( $C2$ ,  $a = 9.09 \text{ \AA}$ ,  $b = 17.747 \text{ \AA}$ ,  $c = 10.229 \text{ \AA}$ ,  $\beta = 124.650^\circ$ , PDF 39-1381, Yang & Armbruster, 1996).

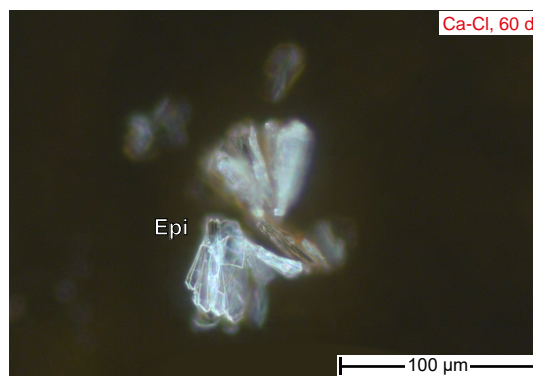


**Figure 6.10** – Microphotograph of epistilbite (Ca-Cl solution, 60 d, epi6k-st12) on a Kapton strip for synchrotron XRD measurements.

### 6.3.3 FLUID COMPOSITION

Fluid compositions are listed in Table 6.1, 6.2 and 6.3 for the Na-Cl-, Na-Ca-Cl-, and Ca-Cl-solution, respectively. The single measurements of the doubled experiments give very similar data. Fluids of the autoclave experiments match the compositions of the batch cells after 60 days and continue the trends in the > 120 d experiments.

#### *pH* VALUES

The pH was measured at laboratory conditions shortly after the experiments. These values have been calculated to the experimental temperatures of  $200^\circ\text{C}$  ( $pH_{200^\circ\text{C}}$ ) with the help of *The Geochemist's Workbench* (GWB, Bethke & Yeakel, 2015).

$pH_{200^\circ\text{C}}$  in the Na-Cl series rise quickly already after 3 days of experiment from 6.3 in the initial solution. In the following, the  $pH_{200^\circ\text{C}}$  slightly decreases until an experimental duration of 10 d. Afterwards,  $pH_{200^\circ\text{C}}$  increases to maximum values after 30 d and 45 d. Then,  $pH_{200^\circ\text{C}}$  tendentially decreases after 60 d of experiment. All  $pH_{200^\circ\text{C}}$  values after an experimental duration of 3 d are in the range of 7.3 and 7.9 (Fig. 6.11 a).

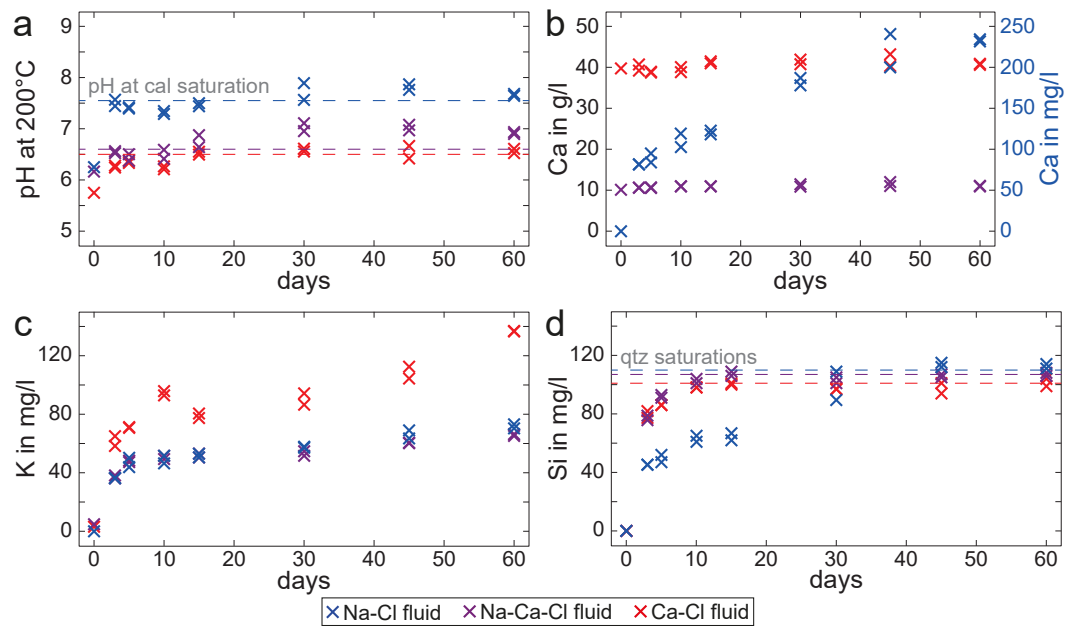


**Figure 6.11** – Fluid concentrations versus experimental time: (a) pH (at 200 °C) versus time; (b) Ca concentration versus time, Na-Cl fluids in  $\text{mg l}^{-1}$ , Na-Ca-Cl and Ca-Cl fluids in  $\text{g l}^{-1}$ , colors as in the other diagrams; (c) K concentration versus time; (d) Si concentration versus time with quartz saturation (dashed lines).

The  $pH_{200\text{ }^\circ\text{C}}$  values of the Na-Ca-Cl and Ca-Cl series follow a very similar trend as for the Na-Cl fluids (Fig. 6.11 a). The starting  $pH_{200\text{ }^\circ\text{C}}$  for the Na-Ca-Cl series is 6.2, for the Ca-Cl 5.6. The  $pH_{200\text{ }^\circ\text{C}}$  values in the total series are between 7.0 and 7.1 for the Na-Ca-Cl fluids and in the range of 6.6 for the Ca-Cl fluids. The  $pH_{200\text{ }^\circ\text{C}}$  values of the 60 d experiments tendentially decrease for both, the Na-Ca-Cl and Ca-Cl fluids.

#### ELEMENT CONCENTRATIONS

Calcium concentrations in the Na-Cl series increase with experimental duration over the whole time series (Fig. 6.11 b). The initial concentration is below  $3\text{ mg l}^{-1}$ . After 3 days it rises up to  $\sim 81\text{ mg l}^{-1}$  and constantly increases up to  $\sim 232\text{ mg l}^{-1}$  in the 60 day experiments. Both other experiment series have initially high Ca concentrations in the solution (Na-Ca-Cl  $10.1\text{ g l}^{-1}$  and Ca-Cl  $39.6\text{ g l}^{-1}$ ). Nevertheless, in both series a slight increase is measured. The Na/(Ca + Na) ratios of the Na-Cl, Na-Ca-Cl, and Ca-Cl fluids are 1.00, 0.84–0.85, and  $<0.01$ , respectively, and are very constant with experimental time. This is not surprising, since the high Na and Ca concentrations in the initial solutions mask minor changes, caused by fluid–mineral reactions in the experiments.

Potassium concentrations are very low in the initial solutions ( $<4\text{ mg l}^{-1}$ ,  $4.9\text{ mg l}^{-1}$ , and  $3.2\text{ mg l}^{-1}$  for Na-Cl, Na-Ca-Cl, and Ca-Cl, resp.). The concentrations in the Na-Cl and Na-Ca-Cl experiments are similar. The K concentration rises quickly up to  $\sim 37\text{ mg l}^{-1}$  after 3 days and to  $44\text{--}50\text{ mg l}^{-1}$  after 5 days (Fig. 6.11 c). Thereafter it increases linearly up to  $45\text{ mg l}^{-1}$  in the Na-Cl, and to  $65\text{--}66\text{ mg l}^{-1}$  in the Na-Ca-Cl series (both 60 days). The Ca-Cl experiments show an other behavior of the K concentration evolution. The early increase is much stronger,  $58\text{--}65\text{ mg l}^{-1}$  after 3 days, and up to  $93\text{--}96\text{ mg l}^{-1}$  after 10 days. But, the 15 day K concentrations are lower ( $78\text{--}81\text{ mg l}^{-1}$ ) and afterward a constant increase up to  $137\text{ mg l}^{-1}$  after 60 days has been measured.

All initial solutions are nearly free of silicon (below detection limit). The Si concentrations increase with the duration of the experiments (Fig. 6.11 d). In the Na-Cl experiments it stays constant at 110–115 mg l<sup>-1</sup> after 45 d experimental duration. The increase of Si concentration in the Na-Ca-Cl series is much faster as in the pure Na-Cl series. After 10 days a concentration of 101–104 mg l<sup>-1</sup> is reached, which stays virtually constant in the longer experiments (106–108 mg l<sup>-1</sup> at 60 days). In the Ca-Cl experiment series a constant Si concentration of ~100 mg l<sup>-1</sup> after 10 day is reached. The increase is very similar to the trend of the Na-Ca-Cl series, but with slightly lower end-concentrations. The stabilization of Si concentrations matches the equilibrium state with quartz for the Na-Cl (110 g l<sup>-1</sup>), Na-Ca-Cl (107 g l<sup>-1</sup>), and Ca-Cl (101 g l<sup>-1</sup>) solutions (Fig. 6.11 d).

## 6.4 DISCUSSION

### 6.4.1 COMMENTS ON ZEOLITE IDENTIFICATION

Different zeolites phases precipitated on the sample surfaces during the hydrothermal experiments (Table 6.7). Structural data are most suitable for the identification of mineral phases. Limited data, large compositional ranges, the special channel structure, and the varying water content of zeolites impede their characterization and delimitation. Chemically, zeolites can be classified and distinguished by their Si and Al ratio in the tetrahedral sites, defined as  $R = \text{Si}/(\text{Si} + \text{Al})$  (e.g. Coombs et al., 1997; Passaglia & Sheppard, 2001). Additionally, (earth-)alkali content provide further chemical information. Plotting both data in one diagram, zeolites can be discriminated reliably (Fig. 6.12).

**Table 6.7** – Zeolite occurrence and mean composition from EMP measurements. x = observed by SEM, bold X = detected by XRD.

Fluid	Zeolite	Days of experiments					Measured composition
		≤5	10	15	30	≥45	
Na-Cl	Analcime:	-	x	x	<b>X</b>	<b>X</b>	Na <sub>1.8</sub> Al <sub>1.8</sub> Si <sub>4.2</sub> O <sub>12</sub> · 2 H <sub>2</sub> O
Na-Ca-Cl	Analcime:	-	-	x	x	<b>X</b>	Na <sub>1.6</sub> Ca <sub>0.1</sub> Al <sub>1.8</sub> Si <sub>4.2</sub> O <sub>12</sub> · 2 H <sub>2</sub> O
	Wairakite:	-	x	x	<b>X</b>	<b>X</b>	Ca <sub>0.5</sub> Na <sub>0.8</sub> K <sub>0.1</sub> Al <sub>1.9</sub> Si <sub>4.1</sub> O <sub>12</sub> · 2 H <sub>2</sub> O
Ca-Cl	Wairakite:	-	x	x	<b>X</b>	<b>X</b>	Ca <sub>0.95</sub> Al <sub>1.9</sub> Si <sub>4.1</sub> O <sub>12</sub> · 2 H <sub>2</sub> O
	Epistilbite:	-	-	-	-	x	Ca <sub>1.0</sub> Al <sub>2.0</sub> Si <sub>6.0</sub> O <sub>16</sub> · 5 H <sub>2</sub> O

Stability conditions, i.e. temperature, pressure, fluid composition, of zeolites differ for many zeolites. Therefore, the environmental conditions limit the number of possible zeolites formed in our experiments.

#### ANALCIME

The precipitated analcime (Na-Cl and Na-Ca-Cl series) match well to a cubic analcime structure (Ia-3d (230),  $a = 13.73 \text{ \AA}$ , PDF 41-1478, Ferraris et al., 1972). Chemical data are in the range of natural and synthetic analcimes (e.g. Anthony et al., 2015; Gottardi & Galli, 1985; Seki & Oki, 1969, Fig. 6.12), morphology is typical for analcime (e.g. Tschernich, 1992), and formation conditions in our experiments are as reported from natural and synthetic occurrences (~60–300 °C, Chipera & Apps, 2001; Tschernich, 1992). Thus, there is no doubt about the existence of analcime in our samples

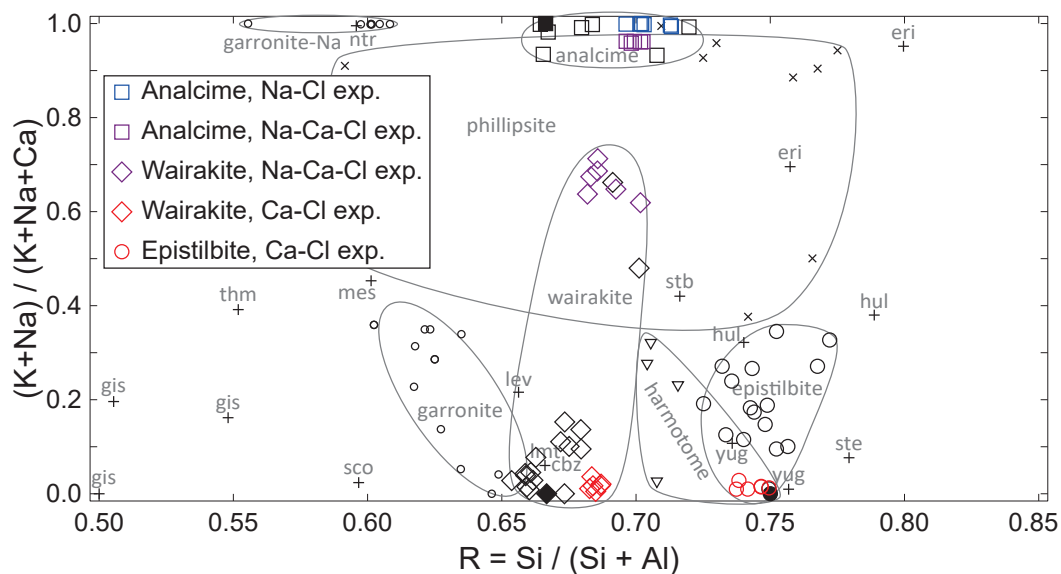


**Figure 6.12** – Zeolite discrimination diagram with measured chemical element ratios of zeolites. Squares = analcime, diamonds = wairakite, circles = epistilbite, small circles = garronite, x = phillipsite, triangles = harmotome (Ba as Ca), crosses = other zeolites; blue = Na-Cl exp., purple = Na-Ca-Cl exp., red = Ca-Cl exp., black = literature values; filled symbols = ideal composition. Literature data from Akizuki & Nishido (1988), Anthony et al. (2015), Artioli (1992), Galli & Rinaldi (1974), Gottardi & Galli (1985), Grice et al. (2017), Mehegan et al. (1982), Nawaz (1982), Okamoto & Makajima (1994), Schröpfer & Joswig (1997), Seki & Oki (1969), Seryotkin et al. (2003), Takeuchi et al. (1979), Walker (1962), and Weisenberger & Selbekk (2009). Mineral abbreviation after Whitney & Evans (2010).

#### WAIRAKITE

Synchrotron X-ray diffraction measurements of the zeolite mineral that we finally assigned as wairakite (Na-Ca-Cl and Ca-Cl series) give a diffractogram, which does not match perfectly to any published structural data. Three possible zeolite phases are worth considering: (1) tetragonal wairakite, (2) tetragonal garronite, and (3) harmotome-Ca or phillipsite-Ca.

**WAIRAKITE** The diffractogram of our zeolite (Fig. 6.9) match the best to a synthetic, tetragonal wairakite (PDF 15-0139, Barrer & Denny, 1961). But, the quality of the structural data for the synthetic, tetragonal wairakite is uncertain. A space group is not specified. Source of the structural data is Barrer & Denny (1961), who produced the zeolite synthetically from Ca aluminosilicate gels at  $\leq 220$  °C. The zeolite from the Na-Ca-Cl experiment has a similar diffraction pattern to the Ca-Cl one, but with shifted peak positions (Fig. 6.9). Elevated Na content could be responsible for this shift.

Chemical data fit very well to wairakite compositions from literature, both natural (Anthony et al., 2015; Gottardi & Galli, 1985; Okamoto & Makajima, 1994; Seki & Oki, 1969; Takeuchi et al., 1979) and synthetic (Seryotkin et al., 2003) samples (Fig. 6.12). Further, measured composition of the zeolite formed in the Ca-Cl experiment is close to the ideal chemical composition of the pure Ca wairakite. *R* ratio (Na-Ca-Cl 0.68–0.70, Ca-Cl 0.68–0.69) is close to the natural 0.65–0.70 (Passaglia & Sheppard, 2001). Na and Ca content of these zeolites differ, but are completely in the range of the analcime–wairakite solid solution (Seki & Oki, 1969, Fig. 6.12).

Formation conditions of natural wairakite (low *p*, <150–300 °C, Chipera & Apps, 2001; Tschernich, 1992) are in the same range as our experiments (200 °C and boiling pressure).

Wairakites typically occur in geological settings with high thermal gradient (Liou, 1970). Also laboratory wairakite syntheses were conducted at similar conditions (e.g. Ghobarkar, 1985; Liou, 1970; Wirsching, 1981). Here, many synthetic wairakites formed as a disordered variety of wairakite with a tetragonal, instead of an ordered monoclinic structure (Liou, 1970), where the ordering of Al and Si in the tetrahedral sites should be the responsible process. Liou (1970) showed that a transformation from the disordered to the monoclinic ordered structure is only a matter of experimental time. In his experiments monoclinic wairakite occurred after 1500 hours. Wirsching (1981) displayed a simultaneous formation of wairakite and epistilbite in hydrothermal experiments with a Na- and Ca-bearing solution at temperatures of 200–250 °C with rhyolitic glass as starting material.

Crystal morphology of our zeolite (Fig. 6.7 b) looks very similar to wairakite, synthesized at 200–270 °C by Ghobarkar (1985).

**GARRONITE** Bragg peak positions of the zeolite coincide to garronite (tetragonal,  $I-4m2$  (119), PDF 85-2567, Schröpfer & Joswig, 1997). But, several peaks of the measured diffractogram are not covered by the garronite pattern.

Chemically garronite composition is different to the EMP data for our zeolite phase.  $SiO_2$  concentrations of natural garronite is in the range of about 43–45 wt.%,  $Al_2O_3$  about 23–24 wt.% (e.g. Walker, 1962), which differ from our measurements (see Table 6.5). Consequently,  $R$  of garronite (0.60–0.65, Passaglia & Sheppard, 2001) is lower than our data, in particular for Na-bearing garronite and garronite-Na. Alkali ratios of the zeolites from the Ca-Cl experiment are close natural (ideal) garronite ones (e.g. Artioli, 1992), whereas the zeolites from the Na-Ca-Cl experiments do not plot in the area of natural garronite compositions (Fig. 6.12).

Formation conditions and the stability field of garronite in laboratory syntheses are about 200–250 °C and a pressure of about 1 kbar (Ghobarkar & Schäf, 1999b; Schröpfer & Joswig, 1997). However, natural garronites are thought to form at temperatures in the range of 65–90 °C (Tschernich, 1992). Morphology of our zeolite phase does not match well to typical garronite morphologies of natural and synthetic samples (e.g. Ghobarkar & Schäf, 1999a; Tschernich, 1992).

Although, some characteristics of our zeolite are consistent with natural and synthetic garronite (structural data), it seems not plausible that garronite has been formed in our experiments.

**PHILLIPSITE-CA/HARMOTOME-CA** Phillipsite forms a series with Harmotome-Ca, a Ca-bearing Ba zeolite (Coombs et al., 1997). Bragg peak positions of harmotome-Ca (monoclinic,  $P2_1$  (4), PDF 39-1376, Galli, 1972) are close to our zeolite data. But, the match is not better than for wairakite and garronite. Phillipsite-Ca (monoclinic,  $P2_1/m$  (11), PDF 39-1375, Gottardi & Galli, 1985) match even less to our zeolite.

The chemical compositions of phillipsite and harmotome do not fit to our zeolite. Generally, they contain relatively high amounts of K, whereas K content is very low in our zeolites, although it is available in our experimental fluids (Fig. 6.11 c). The Ba content in our zeolites are too low for a harmotome composition (>50 % Ba of exchangeable cations, Tschernich, 1992).  $R$  of our zeolite is in the range of phillipsite (0.57–0.77, Passaglia & Sheppard, 2001). But, regarding this large range,  $R$  is not a limiting criteria here.

Formation temperatures of natural phillipsite and harmotome are relatively low ( $\leq 85$  °C Tschernich, 1992). Typical morphology of phillipsite and harmotome differs strongly from the morphology of the zeolite phase in our samples (Tschernich, 1992).

Beside the match of the Bragg peak positions of our zeolite to phillipsite/harmotome data, there are no other indications for the existence of these mineral phases in our samples. Chemical, morphological and stability data clearly argue against phillipsite/harmotome.

Table 6.8 summarizes the most important properties of our zeolite sample and the discussed zeolite phases. In conclusion, the newly formed zeolite in the Na-Ca-Cl and Ca-Cl experiments is most probably a wairakite.

**Table 6.8** – Comparison of zeolite properties for the measured “wairakite” and literature values. D spacing in angstrom (selection), PDF#: wrk 15-0139, grn 85-2567, hrm 39-1376, phi 39-1375. R = Si / (Si + Al), M = morphology, SF = natural stability field.

Mineral	d spacings in Å					R	SiO <sub>2</sub>	Al <sub>2</sub> O <sub>3</sub>	M	SF
Measured	7.1362	4.9433	4.1459	3.1385	2.6722	0.68–0.69	53–55 wt. %	21–22 wt. %	–	200 °C
Wairakite	7.1400	4.9600	4.1400	3.1420	2.6740	0.65–0.70	53–57 wt. %	21–24 wt. %	yes	~150–300 °C
Garronite	7.1235	4.9365	4.1412	3.1345	2.6690	0.60–0.65	43–45 wt. %	23–24 wt. %	poss.	~65–90 °C
Harmotome	7.1350	4.9580	4.1100	3.1380	2.6900	0.70–0.75	46–50 wt. %	14–17 wt. %	no	$\leq 85$ °C
Phillipsite	7.1600	4.9400	4.1300	3.1290	2.6830	0.59–0.78	41–64 wt. %	15–24 wt. %	no	$\leq 85$ °C

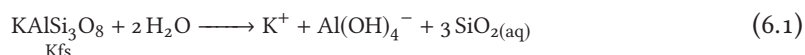
### EPISTILBITE

The occurrence of epistilbite is most likely. The fan-like zeolite match perfectly the ideal composition of epistilbite (Anthony et al., 2015), chemical ratios ( $R$ , alkalis, Fig. 6.12) are in the range of ideal and natural minerals (Passaglia & Sheppard, 2001), crystal morphology is typical for epistilbite (Tschernich, 1992), and Bragg peak positions coincide well the database entries (triclinic, C1 (1), PDF 39-1381, Yang & Armbruster, 1996).

#### 6.4.2 MINERAL REACTIONS

The results of all experiments with the different fluids show a disappearance of illite from the sandstone cementation close to the brine–rock boundary and the dissolution of initial quartz. From these observations reactions of the initial mineral assemblage with the brine forming zeolite phases can be deduced.

**K-FELDSPAR DISSOLUTION** K-feldspar in samples treated with Ca-Cl solution, show distinct dissolution features. Especially in samples of the additional 128 d experiments, K-feldspar is dissolved to high degrees and deep into the sample sub-surface ( $\geq 500$   $\mu\text{m}$ ). In contrast, no distinct changes of K-feldspars of samples treated with Na-Cl and Na-Ca-Cl solution are observable. Since dissolution at K-feldspar grains is clearly determined in the Ca-Cl experiments, a stoichiometric dissolution reaction can be assumed for K-feldspar:

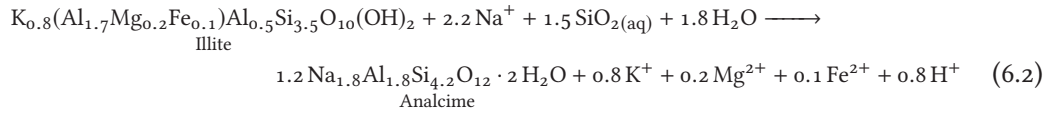


By this reaction  $\text{K}^+$  is released to the fluid, which fits well with the fluid composition (Table 6.3). The not observable (or minor) K-feldspar dissolution in the Na-Cl and Na-Ca-Cl experiments is therefore resulting in lower  $\text{K}^+$  concentrations in the respective fluids (Fig. 6.11 c).  $\text{Al}(\text{OH})_4^-$  concentrations do not differ between the Ca-Cl and both, the Na-Cl and Na-Ca-Cl solutions.  $\text{SiO}_2(\text{aq})$  match the respective quartz saturation concentration

(Fig. 6.11 d), independent of the K-feldspar dissolution. Therefore, concentrations of these components should not be controlled by the K-feldspar dissolution reaction significantly (Eq. 6.1). Meaning, other mineral reactions control the concentration of these elements in the fluids, i.e. a sink for  $\text{Al}(\text{OH})_4^-$  and  $\text{SiO}_{2(\text{aq})}$  has to occur.

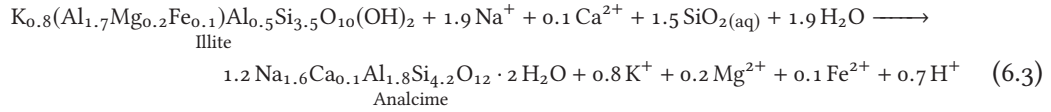
**ZEOLITE FORMATION** Three distinct zeolite minerals were detected on the post-experiment sample surfaces, partly with different compositions, depending on the brine composition. Based on the observations in the solid and fluid samples, the zeolite formation can be combined with the illite dissolution. Therefore, illite  $\rightarrow$  zeolite reaction equations can be developed for every zeolite phase. Initial illite composition is  $\text{K}_{0.8}(\text{Al}_{1.7}\text{Mg}_{0.2}\text{Fe}_{0.1})\text{Al}_{0.5}\text{Si}_{3.5}\text{O}_{10}(\text{OH})_2$  (measured in Schmidt et al., 2017a).

In the **Na-Cl** experiment analcime with a composition of  $\text{Na}_{1.8}\text{Al}_{1.8}\text{Si}_{4.2}\text{O}_{12} \cdot 2 \text{H}_2\text{O}$  has been formed. Therefore the reaction

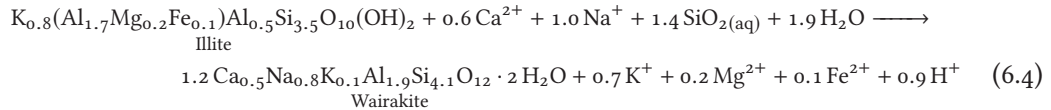


can be formulated, assuming Al remaining in the solid phase.

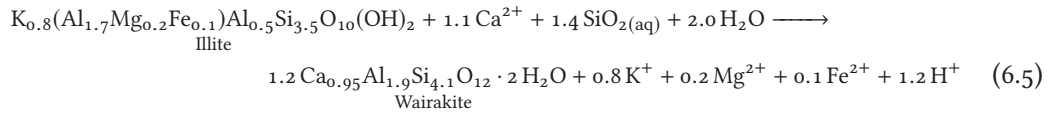
Similarly, the analcime ( $\text{Na}_{1.6}\text{Ca}_{0.1}\text{Al}_{1.8}\text{Si}_{4.2}\text{O}_{12} \cdot 2 \text{H}_2\text{O}$ ) formation in the **Na-Ca-Cl** experiments can be expressed by (O imbalance due to rounding):



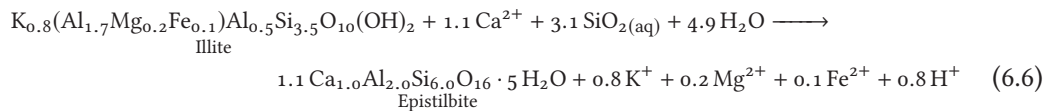
The formation reaction of wairakite ( $\text{Ca}_{0.5}\text{Na}_{0.8}\text{K}_{0.1}\text{Al}_{1.9}\text{Si}_{4.1}\text{O}_{12} \cdot 2 \text{H}_2\text{O}$ ) in the same experimental series is (O imbalance due to rounding)



and for wairakite in the **Ca-Cl** series ( $\text{Ca}_{0.95}\text{Al}_{1.9}\text{Si}_{4.1}\text{O}_{12} \cdot 2 \text{H}_2\text{O}$ ) is



Finally, the formation of epistilbite ( $\text{Ca}_{1.0}\text{Al}_{2.0}\text{Si}_{6.0}\text{O}_{16} \cdot 5 \text{H}_2\text{O}$ ) can be expressed by



The reactions consume  $\text{SiO}_{2(\text{aq})}$ , and, depending on the formed zeolite, Na and/or Ca from solution. The latter occur sufficiently in the initial fluids. Quartz dissolution replenish the  $\text{SiO}_{2(\text{aq})}$  concentration to its saturation limit during the experimental duration (Fig. 6.11 d), since quartz is omnipresent in the solid sample. Dissolution features in the quartz grains

indicate this effect.

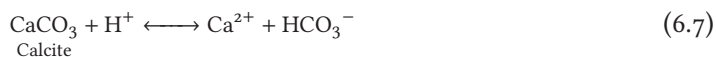
The dissolution of illite as starting material for zeolite precipitation should release K, Mg, and Fe to solution. Potassium in the fluids is increasing over the experimental series for all initial fluid compositions, which depict well zeolite formation reactions. The higher increase of K in the fluid from the Ca-Cl series, can be referred to the K-feldspar dissolution, seen primarily in the Ca-Cl experiments (Fig. 6.1 + 6.2).

Incorporation of K for Na in Na-bearing zeolites could be an additional possibility for the different  $K^+$  concentrations in the experimental fluids. But, chemical compositions of the zeolites (Table 6.4, 6.5, and 6.6) permit this explanation, if any, wairakites of the Na-Ca-Cl experiments have slightly elevated K contents.

The concentrations of Mg and Fe in the fluids are marginal, often lower than detection limit. But, their content in illite is in minor amounts, too. Thereby the reaction equations, with low release of Mg and Fe to the fluid, do not contradict with the fluid chemistry.

Attention should be paid on the behavior of  $H^+$  in these reactions. The formation of all zeolites (Eq. 6.2–6.6) releases  $H^+$  to the brine in all experiments. Assuming the reaction equations from above, the  $pH$  values should decrease by the reactions. But, fluid data (Table 6.1–6.3) indicate an increase of  $pH_{200\text{ }^\circ\text{C}}$  (Fig. 6.11 a). Furthermore,  $pH_{200\text{ }^\circ\text{C}}$  values of the Na-Cl series are definitely higher than of the other series and they tendentially increase during the experimental duration. In contrast,  $pH_{200\text{ }^\circ\text{C}}$  values of the Na-Ca-Cl and, especially, of the Ca-Cl series remain constant in later stages of the series.

**CALCITE REACTIONS** Presumable  $pH$  of the experimental fluids is rather controlled by equilibrium with respect to calcite, which occurs accessory in the initial samples. Small amount of carbon are solved in the initial solution due to the contact with atmosphere. The calcite dissolution can be written as:



We calculated the expected  $pH_{200\text{ }^\circ\text{C}}$  values for each experimental fluid with PHREEQC (Parkhurst & Appelo, 2013, LLNL database). The input parameter are the initial chloride solutions with the measured  $pH$  values, setting in equilibrium with atmospheric  $\text{CO}_2$ , and afterward heating to 200  $^\circ\text{C}$ . Conclusively we equilibrate the solution with respect to calcite, which we assume in excess. The calculated  $pH_{200\text{ }^\circ\text{C}}$  values are 7.6, 6.6, and 6.5 for the Na-Cl, Na-Ca-Cl, and Ca-Cl solutions, respectively. These values fit well with our measured data for the Na-Cl and Ca-Cl solutions (Fig. 6.11 a). But, measured  $pH_{200\text{ }^\circ\text{C}}$  of the Na-Ca-Cl solutions are higher as the calculated  $pH_{200\text{ }^\circ\text{C}}$  for equilibrium with calcite in this solution. Nevertheless, the calcite system is appropriate for controlling  $pH$  of our experimental solutions. Thus, the main differences are the various Ca concentrations in the fluid, which shift the equilibrium reaction (Eq. 6.7) to the left side in the case of initially high amounts of Ca in the solutions.

Calcite dissolution (Eq. 6.7) can also explain the rapid increase of the Ca concentrations in the Na-Cl fluids in the first experimental steps. The initially high amount of Ca in the Na-Ca-Cl and Ca-Cl solutions mask a potential increase (or decrease) of Ca in the fluids.

### 6.4.3 ZEOLITE STABILITY IN NATURAL HYDROTHERMAL SYSTEMS

We observe the formation of different zeolite phases by consumption of authigenic clay minerals as major process in our alteration experiments. The experimental conditions predestine the formation of zeolites: Chemical components, missing in the initial sandstone chemistry, are provided by the experimental solutions, namely water and large amounts of (earth-)alkaline elements. Temperature and pressure are likely for zeolite formation. The composition and texture of our solid samples are close to natural rock surfaces, since the morphology is rough and the original rock fabric is preserved. The occurrence and increase of zeolite material with progressing experimental duration (including the additional long-term experiments), show, that the formation of the zeolites is not a transitional process, at least within the duration of the experiments.

According to this, zeolites have been found in several sandstone formations worldwide as cementation phase (e.g. Coombs, 1965; Coombs & Whetten, 1967; Förster et al., 2010; Higgs et al., 2015; Ross, 1928; Ross, 1941; Schiffman et al., 1985). Hereby, Na- and Ca-zeolites have been described, reflecting the compositions of the respective formation fluids. Therefore, analcime is associated with highly saline Na-rich brines (e.g. English, 2001; Keller, 1952; Ross, 1941). Wairakite has been found as sandstone cementation, e.g. in the Cerro Prieto geothermal system, Baja California, Mexico (Schiffman et al., 1985). Also, diagenetic laumontite cementation has been reported for example in the Pretty Hill sandstone formation of the Otway Basin, Australia (Higgs et al., 2015).

#### *ZEOLITES IN THE URG SANDSTONES?*

In this way, zeolite phases should be found in natural systems as in the geothermally active Upper Rhine Graben (URG), to which conditions our experiments were inspired by. The p-T field of the URG reservoirs (and our experiments) match to the zeolite facies in the metamorphic petrology concept (Bucher & Grapes, 2011; Coombs, 1973; Coombs et al., 1959). Formations are saturated with H<sub>2</sub>O and the brines are rich in (earth-)alkali elements. SiO<sub>2(aq)</sub> and Al sources should be available in excess in sandstones. But, two main differences to the natural zeolite occurrences can be stated: (1) the sandstone reservoirs of the URG are in greater depth (higher pressure) (e.g. Dezayes et al., 2008), and (2) the reservoir brines are higher in inorganic carbon, dissolved in the fluid (HCO<sub>3</sub><sup>-</sup>, CO<sub>2(aq)</sub>) and/or as gaseous phase (e.g. Pauwels et al., 1993; Sanjuan et al., 2016; Stober & Bucher, 2014).

**(1) PRESSURE/DEPTH** Our experiments are conducted at water (brine) vapor pressure, i.e. ~16 bar at 200 °C. This results in a corresponding depth of about 200 m, assuming a water pressure for high porosity rocks of being 1/3 of the lithostatic pressure ( $P_{\text{H}_2\text{O}} \approx 1/3 P_{\text{lith}}$ , Coombs et al., 1959). Many natural zeolite occurrences are surface near, (e.g. Salt Lake Lewis, central Australia, English, 2001). But, zeolites cementations in sandstones have also been found in greater depth. Wairakite is stable up to depth of  $\leq 10$  km (Chipera & Apps, 2001), which means a pressure of about 850 bar (assuming  $P_{\text{H}_2\text{O}} \approx 1/3 P_{\text{lith}}$ ). Analcime has been reported being formed in burial depth of ~8500 m (~720 bar for  $P_{\text{H}_2\text{O}}$ , Coombs, 1965). Therefore, depth of geothermal reservoirs in the URG should lay within the stability field

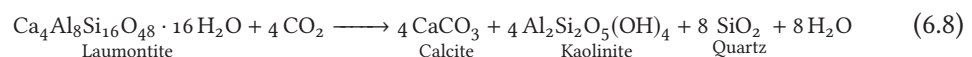
of zeolites. Besides, Chipera & Apps (2001) found, that pressure plays a minor role for a stable assemblage containing zeolites, in contrast to temperature and fluid composition.

**(2) INORGANIC CARBON** The total inorganic carbon (TIC) in our experiment is about  $\leq 110 \text{ mg l}^{-1} \text{ HCO}_3^-$ , based on alkalinity measurements for all used experimental fluid compositions. The natural zeolitic sandstone formations have low concentrations of  $\text{CO}_2/\text{HCO}_3^-$  in common.  $\text{HCO}_3^-$  in formation brines where zeolites occur is not higher than our experimental values, e.g.  $40\text{--}67 \text{ mg l}^{-1}$  for the Ketzin site (analcime cementation, Förster et al., 2006), and  $66 \text{ mg l}^{-1} \text{ HCO}_3^-$  in the brine of Lake Lewis (analcime cementation, English, 2001). Also the laumontite cementation in the Pretty Hill Formation occur in low  $\text{CO}_2$  areas (Higgs et al., 2015).

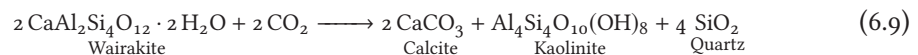
By contrast, many geothermal installations in the URG produce fluids with elevated TIC: the formation brine of the Bruchsal sandstone reservoir has a  $\text{HCO}_3^-$  concentrations of  $>500 \text{ mg l}^{-1}$  (Stober & Jodocy, 2011) and a gaseous phase, which is composed of  $\sim 90\% \text{ CO}_2$  (at a gas–liquid ratio of 23 %, Sanjuan et al., 2016). The Cronenbourg brine in the sandstone formation in 3200 m depth has a  $\text{HCO}_3^-$  concentrations of  $>300 \text{ mg l}^{-1}$  (Stober & Jodocy, 2011).

Liou (1970) reconstructed the effect of  $\text{CO}_2$  on Ca-zeolite stability experimentally. The author demonstrated the decomposition of laumontite and wairakite with different concentrations of  $\text{CO}_2$  in their experiments. A maximum content of 2 %  $\text{CO}_2$  in the fluid at vapor pressure for the formation of wairakite was evaluated as upper limit for the stability of the zeolite phases. Otherwise, the zeolites decompose to calcite and montmorillonite. Thermodynamic models show similar dependencies of the stability of zeolite assemblages on the activity of  $\text{CO}_2$  (e.g. Weisenberger & Bucher, 2010).

Higgs et al. (2015) and Watson (2012) stated the following reaction of laumontite with  $\text{CO}_2$  to an assemblage of calcite, kaolinite, and quartz



as a decomposition reaction of laumontite cement in  $\text{CO}_2$ -rich areas in the Pretty Hill sandstone formation. This relationship is applicable for wairakite, too. Therefore the reaction



limits the stability of wairakite depending on the availability of  $\text{CO}_2$  (representing total inorganic carbon).

Natural zeolite cementations in sandstones occur, where TIC is low. Higher concentrations result in stable assemblages of quartz, clay minerals, and calcite. For Ca-zeolites this connection is rather obvious. Thus Ca-zeolites, e.g. laumontite or wairakite, occur where  $p_{\text{CO}_2}$  is low. But, also in Na dominated formation brines Na-zeolites, as analcime, are part of stable mineral assemblages where TIC is low. A carbonate phase, which competes for Na-ions, has not been reported for the natural sedimentary formations.

We conclude, that zeolites are stable in natural sandstone formations of the URG. The reservoir conditions found ( $p$ ,  $T$ , fluid composition, rock material), are suitable for the formation of zeolites. The limiting factor is the availability or absence of carbon, dissolved

in the formation brine or as gaseous phase.

#### 6.4.4 ALTERATION PROCESSES INFLUENCE THE GEOTHERMAL CIRCUIT

According to Schmidt et al. (2017a), the change of solid volume for the alteration reactions of illite to the zeolite phases, seen in the experiments, can be calculated. Volume changes have been calculated for the actual experiments, using reactions Eq. 6.2, 6.5, and 6.6 for analcime, wairakite, and epistilbite formation, respectively. The calculations include the consumption of illite and quartz as primary phases and the precipitation of the zeolites as solid reaction products. The molar volume of the involved phases are collected from Anthony et al. (2015). The calculations give a net volume increase of all zeolite forming reactions: Analcime formation +20 %, wairakite formation +26 %, and epistilbite formation +35 %

Analcime and wairakite are formed to high amounts on the sample surface during the experiments. The long-term experiments imply a progression of the reactions under the experiment conditions. Consequently, the formation of the zeolite phases should have a high impact on the fracture aperture, which should result in a decrease of fracture permeability.

## 6.5 CONCLUSION AND PERSPECTIVE

The experiments show the large influence of brine-sandstone interaction on fracture surfaces of EGS networks. Quartz, illite, and K-feldspar dissolution have the potential for a weakening of the rock fabric and thus a slightly increasing of permeability. The formation of zeolites, on the other hand, are suitable to hamper the fluid flow and decrease the efficiency of geothermal installations, at least, where TIC is low. Natural zeolitic cemented sandstones show the relevance of the zeolite formation for the permeability in large scale environments.

Further studies on zeolite precipitation under geothermal conditions should incorporate the effect of CO<sub>2</sub> on the formation and stability of the zeolite phases and the mineral assemblage in total. Especially, in the case of analcime, where the relationship between CO<sub>2</sub> and the Ca-free zeolite phase is non-obvious.

## ACKNOWLEDGEMENTS

We thank the technicians and staff of the Department of Aquatic Geochemistry for their help and quick fluid analyses. Special thanks to V. Zibat from the Laboratory for Electron Microscopy (KIT) for the SEM analyses and U. Gerhards for her help with the electron microprobe at Institute for Micro Process Engineering (KIT). This research has been funded by the projects *StörTief* and *Geofaces-SD* of the German Federal Ministry for Economic Affairs and Energy (BMWi, no: 0325623C, 0324025C), implemented by the Project Management Jülich (PtJ).

---

## CONCLUSION

---

Geothermal energy can sustainably supply large amounts of heat and electrical energy. Particularly deep geothermal energy from enhanced geothermal systems (EGS) are able to generate large amounts of heat. In the URG deep geothermal reservoirs are mainly the Bunter sandstone formations and the crystalline basement. Elevated geothermal gradients in the URG allow temperatures of close to 250 °C in 4–5 km depth. The initial investment costs of deep drill holes are high, therefore the geothermal installations should operate for a long time period.

In EGS the mostly highly saline in-situ fluid is used as transport medium for the geothermal circuit. It is in direct contact with the reservoir rock during the circulation in the reservoir network. Alteration reactions between the reservoir lithologies and the fluid cause changes in the mineral assemblage influencing the rock properties and the fluid flow in the EGS. Therefore, a better knowledge of the alteration process in geothermal reservoirs are crucial for a sustainable operation and the lifetime of geothermal installations.

Aim of this research was to comprehend and evaluate alteration processes at fracture surfaces of different URG reservoir lithologies. Alteration experiments with hard rock samples and an intact rock fabric under geothermal conditions found in the URG are rare. Many experiments have been conducted with powder or granulated material (e.g. Savage et al., 1992) and often fluids with a low salinity has been used (e.g. Bertrand et al., 1994; Kuncoro et al., 2010). Nevertheless, several experiments on fluid-rock interaction with highly saline fluids have been conducted in the context of geological CO<sub>2</sub> storage (e.g. Kaszuba et al., 2005; Shao et al., 2011; Shiraki & Dunn, 2000). But here, often single mineral phases, or, again, granulated material was used at generally lower experimental temperatures.

The combination of a multi-phase mineral assemblage at temperatures  $\geq 200$  °C exposed to a highly saline brine merge many parameters far away from laboratory standard state. Present thermodynamic databases and numerical codes are still incomplete for satisfied computations of complex hydrothermal alteration processes. Especially since alteration products commonly are hydrous mineral phases (phyllosilicates, zeolites) for which thermodynamic data are incomplete (Velde, 1995). Consequently, experimental studies under geothermal conditions are suitable to explain geochemical-mineralogical processes in complex systems.

Effects on the fracture aperture and the permeability in the geothermal network by alteration reactions of a fresh rock surface with highly saline fluids have been demonstrated

---

in three studies. The first has been conducted with two different sandstones and pure 2 M Na-Cl solution at both 200 and 260 °C, the second with granite samples under the same conditions. The third one focused on the influence of various fluid compositions and the progress of the alteration reactions.

The studies (Ch. 4–6) pointed out the major alteration reaction at different lithologies under geothermal reservoir conditions of the URG. The observed processes gave implications on the influence of alteration reactions on the fluid circulation in an enhanced geothermal system.

## 7.1 MAJOR FINDINGS OF THE RESEARCH

Quartz dissolution occurs independently of the lithology, until its saturation for the 2 M fluid at experimental temperatures is reached. It is enhanced, where alteration reactions consume  $\text{SiO}_{2(\text{aq})}$  from solution. This is the case by the precipitation of zeolites, mainly in the sandstone experiments. The dissolution of quartz has been observed in natural boreholes in granitic basement rocks (KTB, Soultz-sous-Forêts), representing the initial step of hydrothermal alteration, when quartz under-saturated fluids contact the mineral assemblage in the geothermal reservoir (Ledésert et al., 2010; Pielow, 1997).

Independent on the lithology, feldspars show a minor reactivity of both K-feldspar (in granite and sandstones) and albite (in granite). If any, albitization of K-feldspar at the outermost layer and insignificant dissolution occur during the experiments at higher temperature (260 °C). However, in pure Ca-Cl solution K-feldspar dissolved to high degree at the sample surfaces (Ch. 6).

The studies emphasized the different alteration behavior of diverse lithologies. In sandstones (Ch. 4), cemented by clay minerals, the highly saline brine caused the destabilization of the clay minerals, resulting in their dissolution and the precipitation of a stable zeolite phases (analcime). In addition, the composition of the experimental solution (Ch. 6) determines which specific zeolite is formed, analcime at high to intermediate Na/Ca ratios and wairakite at intermediate to low Na/Ca ratios. Sporadic epistilbite formed in the pure Ca-Cl solution. The transformation of clay minerals to zeolites with the consumption of  $\text{SiO}_{2(\text{aq})}$  are the major process during the sandstone alteration. An increase of the total volume of the solid phases could be deduced from the transformation reactions. The consequences for the permeability in a geothermal reservoir have been highlighted in the studies (Ch. 4 + 6), as the zeolite formation have the potential to reduced the fluid pathways.

Completely different alteration behavior of granite, exposed to a brine with same chemical composition (Na-Cl) and at the same temperature and pressure conditions, is demonstrated in the second study (Ch. 5). Here, the rock fabric is weakened by the chloritization and partly dissolution of biotite, which is the major alteration process in the alteration experiments. The reaction progress from initial biotite to chlorite through an intermediate state, where the mixed-layer phyllosilicates hydrobiotite and corrensite have been formed, could be illustrated. The similarities of the chloritization process in this study to the phyllosilicate assemblage in natural granites (tosudite and chlorite in alteration zones of the Soultz-sous-Forêts granite) display, that the processes described in the experiments proceed in natural

geothermal system.

The weakening of the granite fabric by the alteration reactions, have the potential to effect the permeability in a geothermal reservoir. The chloritization process is able to further increase the fluid flow, in the initial state of fracture alteration the experiments dealing with. Nevertheless, a clogging of fluid pathways by debris, loosened during the alteration process may have a contrary effect.

The limiting factor for the formation of zeolite phases in hydrothermal fluids could be localized to the availability of  $\text{Al}^{3+}$ . In all experiments, on granite and sandstone samples,  $\text{H}_2\text{O}$  and (earth-)alkali elements are provided by the solutions.  $\text{SiO}_{\text{W(aq)}}$  has been added to the fluid by quartz dissolution, which is observed in all experiments. Zeolites formed in experiments, where the necessary  $\text{Al}^{3+}$  for the zeolite formation is provided by dissolution reactions. In the case of sandstones, zeolites precipitated to large extent, since the dissolution of clay minerals is the major process, providing high amounts of  $\text{Al}^{3+}$ . Whereas, in the granite experiments, a zeolite phase (analcime) has been formed only, where the chloritization process of biotite is further evolved and  $\text{Al}^{3+}$  is released to the fluid.

## 7.2 EFFECTS OF ALTERATION REACTIONS ON FLUID PERMEABILITY

Studies on the alteration of natural fractures and shear zones have shown that alteration processes have a high impact on the permeability (e.g. Bertrand et al., 1994; Evans et al., 1997; Morrow et al., 2001; Turpault et al., 1992). Depending on the mineral assemblage and the fluid involved, alteration reactions may result in increasing (e.g. Bartier et al., 2008) or decreasing permeability in fractures as well as in the rock matrix (e.g. Griffiths et al., 2016). The experiments of this research reproduced the first steps of fracture alteration under conditions of geothermal reservoirs in the URG.

The studies with sandstone samples (Ch. 4 + 6) show, that alteration reactions are responsible for several effects on the fracture surface (Fig. 7.1). The dissolution of the clay mineral and quartz cementation results in the disintegration of the sandstone fabric. Further pathways into the rock are created. Clasts from the weakened rock may be break out by the fluid flow and clog the fracture at other places. Furthermore, the dissolution of single mineral phases, e.g. feldspars in an arkose, result in a higher porosity in the rock. Uniform dissolution at the fracture surface obviously increase the rock aperture and the fluid pathway is enhanced. Precipitation of secondary minerals at fracture surfaces is able to decrease the aperture, possibly to its total sealing. The volume increase of the reaction from clay minerals to zeolites have the potential to influence the permeability of a reservoir rock negatively. Zeolite cemented sandstone formations illustrate the process in natural environments (e.g. Coombs & Whetten, 1967; Förster et al., 2010; Higgs et al., 2015).

In granitic reservoir rock (Ch. 5) some alteration processes are similar to the reactions seen in the sandstone sample. Quartz dissolution and minor changes in feldspars should increase the fluid permeability. These processes has been observed in the Soultz-sous-Forêts granite and associated to early stages of fracture alteration (Ledésert et al., 1999). The chloritization of biotite in the granite sample result in a disintegration of the rock fabric. Further, fluid pathways are created by this process, which accelerate the alteration reactions

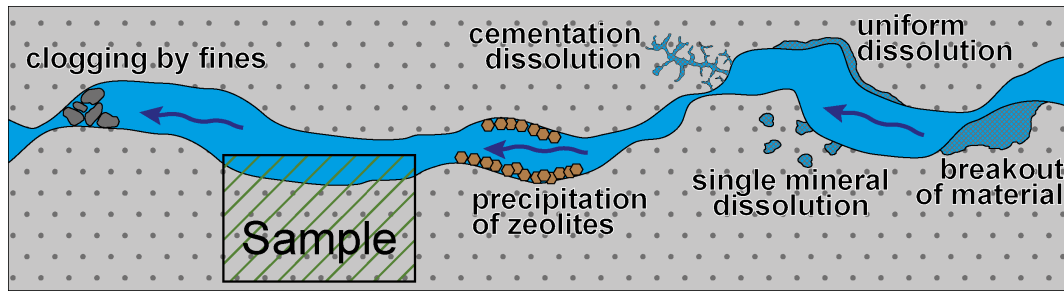


**Figure 7.1** – Schematic fracture in a sandstone reservoir with several alteration processes. Description in the text.

and progress it deeper into the adjacent rock material. Similar to the alteration processes in the sandstones, a clogging of loose material from the weakened rock fabric is feasible.

The studies illustrate, that the initial mineral assemblage is a crucial parameter determining which alteration process occur. The composition of single mineral phases are responsible for the availability of elements, additional to the components in a co-existing fluid, and therefore which secondary minerals are able to form.

Nevertheless, the initial fluid composition at certain temperature and pressure conditions depicts if a primary mineral is destabilized and which reactions take place to re-equilibrate the system. Certainly, the components and concentrations in the initial hydrothermal fluid are also a major factor for the type of alteration reactions proceeding.

Effects of the alteration processes, where a secondary mineral assemblage is formed, are various and go beyond a different geochemical behavior and the change of fluid permeability in fractures and fault zones. The different physical properties of typical hydrated alteration products, as clay minerals and zeolites, affect the mechanics, stress conditions, and seismicity in geothermal reservoirs (Meller & Kohl, 2014).

### 7.3 OUTLOOK

The experiments on rock alteration with highly saline solutions show the dependency of the alteration process on the lithology (mineral assemblage) and the fluid composition. Since, natural rock material was used, the solid material represents the natural environment to high extend. However, the fluid composition was simplified to the major constituent, occurring in URG reservoir brines (88–94 mol.%; Pauwels et al., 1993). To correlate geochemical-mineralogical reactions to single parameters in the experimental setting, the simplification was necessarily required. Further studies should adjust the experimental fluid step wise closer to natural composition. Especially,  $\text{SO}_4$  and  $\text{CO}_2$  play a fundamental role in URG reservoirs. Both constituents are able to produce precipitates which highly impact the circulation of geothermal installations, in the reservoir as well as in the technical facilities. For example baryte ( $\text{BaSO}_4$ ), if precipitated from solution, is nearly insoluble and may irreversibly decrease the reservoir permeability and clog parts of the geothermal circuit (e.g. Orywall et al., 2017).

Furthermore,  $\text{CO}_2$  is present in many URG brines, dissolved in the fluid and/or as gaseous phase. Since,  $\text{CO}_2$  in the gaseous phase is highly sensitive to pressure, changes of the pressure (especially decrease) in the reservoir and the technical installation are able to

decrease the solubility of carbonates tremendously resulting in the precipitation of these mineral phases, e.g. calcite, dolomite, and siderite. Furthermore, the activity of  $\text{CO}_2$  has a major influence on the stability fields of typical alteration products and determines for example if a clay mineral or a zeolite phase is formed (as discussed in Ch. 4 and 6).

The experiments further showed, that the alteration reactions do not coincide with mineral assemblages geochemical modeling predict under the geothermal conditions. An expansion of the thermodynamic databases to more minerals, especially hydrous phases, is of high importance for the development of appropriate geochemical-mineralogical models. Acquiring thermodynamic data needs sophisticated experiments and highly accurate measurements. If a good data basis exist, geochemical modeling may provide good results extrapolating experimental observations to larger scale, longer duration, and to advanced conditions.

---

## REFERENCES

---

- Akizuki, M. & Nishido, H. (1988): Epistilbite: Symmetry and twinning. – in: *American Mineralogist* 73, pp. 1434–1439.
- Anthony, J. W., Bideaux, R. A., Bladh, K. W. & Nichols, M. C. (2015): Handbook of Mineralogy. – ed. by Mineralogical Society of America.
- Appelo, C. A. J. & Postma, D. (2005): Geochemistry, groundwater and pollution. – 2nd ed.. – Leiden and New York: Balkema.
- Aquilina, L., Pauwels, H., Genter, A. & Fouillac, C. (1997): Water-rock interaction processes in the Triassic sandstone and the granitic basement of the Rhine Graben; geochemical investigation of a geothermal reservoir. – in: *Geochimica et Cosmochimica Acta* 61 (20), pp. 4281–4295. – DOI: [10.1016/S0016-7037\(97\)00243-3](https://doi.org/10.1016/S0016-7037(97)00243-3).
- Arkai, P., Sassi, F. P. & Desmons, J. (2003): Very low- to low-grade metamorphic rocks. – in: *Recommendations*. – ed. by IUGS Subcommission on the Systematics of Metamorphic Rocks. – vol. 5.
- Armbruster, T. & Gunter, M. E. (2001): Crystal Structures of Natural Zeolites. – in: *Reviews in Mineralogy and Geochemistry* 45 (1), pp. 1–67. – DOI: [10.2138/rmg.2001.45.1](https://doi.org/10.2138/rmg.2001.45.1).
- Artioli, G. (1992): The crystal structure of garronite. – in: *American Mineralogist* 77 (1-2), pp. 189–196.
- Baerlocher, C., McCusker, L. B., Olson, D. & Meier, W. M. (2007): Atlas of zeolite framework types. – 6th rev. ed.. – Amsterdam and Boston: Published on behalf of the Structure Commission of the International Zeolite Association by Elsevier.
- Baerlocher, C. & McCusker, L. B. (2017): Database of zeolite structures: <http://www.iza-structure.org/databases/>. – ed. by Structure Commission of the International Zeolite Association.
- Barrer, R. M. & Denny, P. J. (1961): Hydrothermal chemistry of the silicates. Part X. A partial study of the field CaO-Al<sub>2</sub>O<sub>3</sub>-SiO<sub>2</sub>-H<sub>2</sub>O. – in: *J. Chem. Soc.* 0 (0), pp. 983–1000. – DOI: [10.1039/JR9610000983](https://doi.org/10.1039/JR9610000983).
- Bartier, D., Ledésert, B., Clauer, N., Meunier, A., Liewig, N., Morvan, G. & Addad, A. (2008): Hydrothermal alteration of the Soultz-sous-Forets granite (Hot Fractured Rock geothermal exchanger) into a tosudite and illite assemblage. – in: *European Journal of Mineralogy* 20 (1), pp. 131–142. – DOI: [10.1127/0935-1221/2008/0020-1787](https://doi.org/10.1127/0935-1221/2008/0020-1787).
- Bauer, A. & Velde, B. (2014): Geochemistry at the Earth's surface: movement of the chemical elements. – movement of the chemical elements. – Berlin: Springer.
-

- Bauer, A., Velde, B. & Berger, G. (1998): Kaolinite transformation in high molar KOH solutions. – in: *Applied Geochemistry* 13 (5), pp. 619–629. – DOI: [10.1016/S0883-2927\(97\)00094-2](https://doi.org/10.1016/S0883-2927(97)00094-2).
- Baujard, C., Genter, A., Dalmais, E., Maurer, V., Hehn, R., Rosillette, R., Vidal, J. & Schmittbuhl, J. (2017): Hydrothermal characterization of wells GRT-1 and GRT-2 in Rittershoffen, France: Implications on the understanding of natural flow systems in the rhine graben. – in: *Geothermics* 65, pp. 255–268. – DOI: [10.1016/j.geothermics.2016.11.001](https://doi.org/10.1016/j.geothermics.2016.11.001).
- Beaufort, D., Baronnet, A., Lanson, B. & Meunier, A. (1997): Corrensite: A single phase or a mixed-layer phyllosilicate in the saponite-to-chlorite conversion series? A case study of Sancerre-Couy deep drill hole (France). – in: *American Mineralogist* 82 (1-2), pp. 109–124.
- Behrmann, J. H., Hermann, O., Horstmann, M., Tanner, D. C. & Bertrand, G. (2003): Anatomy and kinematics of oblique continental rifting revealed: A three-dimensional case study of the southeast Upper Rhine graben (Germany). – in: *AAPG Bulletin* 87 (7), pp. 1105–1121. – DOI: [10.1306/02180300153](https://doi.org/10.1306/02180300153).
- Bertrand, C., Fritz, B. & Sureau, J. F. (1994): Hydrothermal experiments and thermo-kinetic modelling of water-sandstone interactions. – in: *Chemical Geology* 116 (3-4), pp. 189–202. – DOI: [10.1016/0009-2541\(94\)90014-0](https://doi.org/10.1016/0009-2541(94)90014-0).
- Bethke, C. M. & Yeakel, S. (2015): The Geochemist's Workbench Release 10.0: GWB Essentials Guide. – GWB Essentials Guide. – Champaign, Illinois.
- Bish, D. L. & Ming, D. W. (2001): Natural zeolites: Occurrence, properties, applications. – Occurrence, properties, applications. – vol. v. 45. – Reviews in mineralogy and geochemistry. – Washington, DC: Mineralogical Society of America.
- Blake, R. E. & Walter, L. M. (1999): Kinetics of feldspar and quartz dissolution at 70–80 degree C and near-neutral pH: Effects of organic acids and NaCl. – in: *Geochimica et Cosmochimica Acta* 63 (13-14), pp. 2043–2059. – DOI: [10.1016/S0016-7037\(99\)00072-1](https://doi.org/10.1016/S0016-7037(99)00072-1).
- Bourdelle, F. & Cathelineau, M. (2015): Low-temperature chlorite geothermometry: a graphical representation based on a T - R<sub>2+</sub> - Si diagram. – in: *European Journal of Mineralogy* 27 (5), pp. 617–626. – DOI: [10.1127/ejm/2015/0027-2467](https://doi.org/10.1127/ejm/2015/0027-2467).
- Brantley, S. L., Crane, S. R., Crerar, D. A., Hellmann, R. & Stallard, R. (1986): Dissolution at dislocation etch pits in quartz. – in: *Geochimica et Cosmochimica Acta* 50 (10), pp. 2349–2361. – DOI: [10.1016/0016-7037\(86\)90087-6](https://doi.org/10.1016/0016-7037(86)90087-6).
- Bray, A. W., Oelkers, E. H., Bonneville, S., Wolff-Boenisch, D., Potts, N. J., Fones, G. & Benning, L. G. (2015): The effect of pH, grain size, and organic ligands on biotite weathering rates. – in: *Geochimica et Cosmochimica Acta* 164, pp. 127–145. – DOI: [10.1016/j.gca.2015.04.048](https://doi.org/10.1016/j.gca.2015.04.048).
- Breck, D. W. (1974): Zeolite molecular sieves: Structure, chemistry, and use. – Structure, chemistry, and use. – New York u.a.: Wiley.
-

- Bucher, K. & Grapes, R. H. (2011): Petrogenesis of metamorphic rocks. – 8. ed. – Berlin u.a.: Springer.
- Bucher, K. & Stober, I. (2010): Fluids in the upper continental crust. – in: *Geofluids* 10 (1–2), pp. 241–253. – DOI: [10.1111/j.1468-8123.2010.00279.x](https://doi.org/10.1111/j.1468-8123.2010.00279.x).
- Campbell, L. S., Charnock, J., Dyer, A., Hillier, S., Chenery, S., Stoppa, F., Henderson, C. M. B., Walcott, R. & Rumsey, M. (2016): Determination of zeolite-group mineral compositions by electron probe microanalysis. – in: *Mineralogical Magazine* 80 (5), pp. 781–807. – DOI: [10.1180/minmag.2016.080.044](https://doi.org/10.1180/minmag.2016.080.044).
- Cathelineau, M. (1988): Cation Site Occupancy in Chlorites and Illites as a Function of Temperature. – in: *Clay Minerals* 23 (4), pp. 471–485. – DOI: [10.1180/claymin.1988.023.4.13](https://doi.org/10.1180/claymin.1988.023.4.13).
- Chipera, S. J. & Apps, J. A. (2001): Geochemical Stability of Natural Zeolites. – in: *Reviews in Mineralogy and Geochemistry* 45 (1), pp. 117–161. – DOI: [10.2138/rmg.2001.45.3](https://doi.org/10.2138/rmg.2001.45.3).
- Coombs, D. S. (1965): Sedimentary analcime rocks and sodium-rich gneisses. – in: *Mineralogical Magazine and Journal of the Mineralogical Society* 34 (268), pp. 144–158. – DOI: [10.1180/minmag.1965.034.268.12](https://doi.org/10.1180/minmag.1965.034.268.12).
- Coombs, D. S. (1973): Present Status of the Zeolite Facies. – in: *Molecular sieves*. – ed. by W. M. Meier & J. B. Uytterhoeven. – vol. 101. – Advances in chemistry series. – Washington: American Chemical Society, pp. 317–327. – DOI: [10.1021/ba-1971-0101.ch024](https://doi.org/10.1021/ba-1971-0101.ch024).
- Coombs, D. S., Alberti, A., Armbruster, T., Artioli, G., Colella, C., Galli, E., Grice, J. D., Liebau, F., Mandarino, J. A., Minato, H., Nickel, E. H., Passaglia, E., Peacor, D. R., Quartieri, S., Rinaldi, R., Ross, M., Sheppard, R. A., Tillmanns, E. & Vezzalini, G. (1997): Recommended nomenclature for zeolite minerals: Report of the subcommittee on zeolites of the International Mineralogical Association, Commission on New Minerals and Mineral Names. – in: *Canadian Mineralogist* 35, pp. 1571–1606.
- Coombs, D. S., Ellis, A. J., Fyfe, W. S. & Taylor, A. M. (1959): The Zeolite Facies, with Comments on the Interpretation of Hydrothermal Syntheses. – in: *Geochimica et Cosmochimica Acta* 17 (1–2), pp. 53–107. – DOI: [10.1016/0016-7037\(59\)90079-1](https://doi.org/10.1016/0016-7037(59)90079-1).
- Coombs, D. S. & Whetten, J. T. (1967): Composition of Analcime from Sedimentary and Burial Metamorphic Rocks. – in: *Geological Society of America Bulletin* 78 (2), p. 269. – DOI: [10.1130/0016-7606\(1967\)78\[269:COAFSA\]2.o.CO;2](https://doi.org/10.1130/0016-7606(1967)78[269:COAFSA]2.o.CO;2).
- Deer, W. A., Howie, R. A. & Zussman, J. (2013): An introduction to the rock-forming minerals. – Third edition. – London: The Mineralogical Society. – DOI: [10.1180/DHZ](https://doi.org/10.1180/DHZ).
- Deer, W. A., Howie, R. A., Wise, W. S. & Zussman, J. (2004): Framework Silicates: Silica minerals, Feldspathoids and the Zeolites. – Silica minerals, Feldspathoids and the Zeolites. – 2. ed.. – London: The Geological Society.
-

- Dezayes, C., Genter, A., Thinon, I., Courrioux, G. & Tourli, B. (2008): Geothermal Potential Assessment of Clastic Triassic Reservoirs (Upper Rhine Graben, France). – Stanford, California.
- Do Campo, M., del Papa, C., Jiménez-Millán, J. & Nieto, F. (2007): Clay mineral assemblages and analcime formation in a Palaeogene fluvial–lacustrine sequence (Maíz Gordo Formation Palaeogen) from northwestern Argentina. – in: *Sedimentary Geology* 201 (1-2), pp. 56–74. – DOI: [10.1016/j.sedgeo.2007.04.007](https://doi.org/10.1016/j.sedgeo.2007.04.007).
- Dove, P. M. (1994): The dissolution kinetics of quartz in sodium chloride solutions at 25 degrees to 300 degrees C. – in: *American Journal of Science* 294 (6), pp. 665–712. – DOI: [10.2475/ajs.294.6.665](https://doi.org/10.2475/ajs.294.6.665).
- Dove, P. M. (1999): The dissolution kinetics of quartz in aqueous mixed cation solutions. – in: *Geochimica et Cosmochimica Acta* 63 (22), pp. 3715–3727. – DOI: [10.1016/S0016-7037\(99\)00218-5](https://doi.org/10.1016/S0016-7037(99)00218-5).
- Dove, P. M. & Crerar, D. A. (1990): Kinetics of quartz dissolution in electrolyte solutions using a hydrothermal mixed flow reactor. – in: *Geochimica et Cosmochimica Acta* 54 (4), pp. 955–969. – DOI: [10.1016/0016-7037\(90\)90431-J](https://doi.org/10.1016/0016-7037(90)90431-J).
- Dove, P. M. & Elston, S. F. (1992): Dissolution kinetics of quartz in sodium chloride solutions: Analysis of existing data and a rate model for 25°C. – in: *Geochimica et Cosmochimica Acta* 56 (12), pp. 4147–4156. – DOI: [10.1016/0016-7037\(92\)90257-J](https://doi.org/10.1016/0016-7037(92)90257-J).
- Dove, P. M. & Nix, C. J. (1997): The influence of the alkaline earth cations, magnesium, calcium, and barium on the dissolution kinetics of quartz. – in: *Geochimica et Cosmochimica Acta* 61 (16), pp. 3329–3340. – DOI: [10.1016/S0016-7037\(97\)00217-2](https://doi.org/10.1016/S0016-7037(97)00217-2).
- Dove, P. M. & Rimstidt, J. D. (1994): Silica-water interactions. – in: *Reviews in Mineralogy and Geochemistry* 29, pp. 259–308.
- Ellis, A. J. & Mahon, W. A. J. (1964): Natural Hydrothermal Systems and Experimental Hot-Water-Rock Interactions. – in: *Geochimica et Cosmochimica Acta* 28 (Aug), pp. 1323–1357. – DOI: [10.1016/0016-7037\(64\)90132-2](https://doi.org/10.1016/0016-7037(64)90132-2).
- English, P. M. (2001): Formation of analcime and moganite at Lake Lewis, central Australia: Significance of groundwater evolution in diagenesis. – in: *Sedimentary Geology* 143 (3-4), pp. 219–244. – DOI: [10.1016/S0037-0738\(01\)00063-X](https://doi.org/10.1016/S0037-0738(01)00063-X).
- Eskola, P. (1915): On the relations between the chemical and mineralogical composition in the metamorphic rocks of the Orijarvi region. – in: *Bull. Comm. Geol. Finlande* 44, pp. 109–143.
- Evans, J. P., Forster, C. B. & Goddard, J. V. (1997): Permeability of fault-related rocks, and implications for hydraulic structure of fault zones. – in: *Journal of Structural Geology* 19 (11), pp. 1393–1404. – DOI: [10.1016/S0191-8141\(97\)00057-6](https://doi.org/10.1016/S0191-8141(97)00057-6).
-

- Faure, G. (1998): Principles and applications of geochemistry: A comprehensive textbook for geology students. – A comprehensive textbook for geology students. – 2nd ed.. – Upper Saddle River, N.J.: Prentice Hall.
- Ferraris, G., Jones, D. W. & Yerkess, J. (1972): A neutron-diffraction study of the crystal structure of analcime,  $\text{NaAlSi}_2\text{O}_6 \cdot \text{H}_2\text{O}$ . – in: *Zeitschrift für Kristallographie* 135 (3-4), pp. 240–252. – DOI: [10.1524/zkri.1972.135.3-4.240](https://doi.org/10.1524/zkri.1972.135.3-4.240).
- Ferry, J. M. (1979): Reaction mechanisms, physical conditions, and mass transfer during hydrothermal alteration of mica and feldspar in granitic rocks from south-central Maine, USA. – in: *Contributions to Mineralogy and Petrology* 68 (2), pp. 125–139. – DOI: [10.1007/bf00371895](https://doi.org/10.1007/bf00371895).
- Fischer, S., Liebscher, A. & Wandrey, M. (2010):  $\text{CO}_2$ -brine-rock interaction - First results of long-term exposure experiments at in situ P-T conditions of the Ketzin  $\text{CO}_2$  reservoir. – in: *Chemie der Erde - Geochemistry* 70, pp. 155–164. – DOI: [10.1016/j.chemer.2010.06.001](https://doi.org/10.1016/j.chemer.2010.06.001).
- Fischer, S., Zemke, K., Liebscher, A. & Wandrey, M. (2011): Petrophysical and petrochemical effects of long-term  $\text{CO}_2$  -exposure experiments on brine-saturated reservoir sandstone. – in: *Energy Procedia* 4, pp. 4487–4494. – DOI: [10.1016/j.egypro.2011.02.404](https://doi.org/10.1016/j.egypro.2011.02.404).
- Förster, A., Schöner, R., Förster, H.-J., Norden, B., Blaschke, A.-W., Luckert, J., Beutler, G., Gaupp, R. & Rhede, D. (2010): Reservoir characterization of a  $\text{CO}_2$  storage aquifer: The Upper Triassic Stuttgart Formation in the Northeast German Basin. – in: *Marine and Petroleum Geology* 27 (10), pp. 2156–2172. – DOI: [10.1016/j.marpetgeo.2010.07.010](https://doi.org/10.1016/j.marpetgeo.2010.07.010).
- Förster, A., Norden, B., Zinck-Jørgensen, K., Frykman, P., Kulenkampff, J., Spangenberg, E., Erzinger, J., Zimmer, M., Kopp, J., Borm, G., Juhlin, C., Cosma, C.-G. & Hurter, S. (2006): Baseline characterization of the  $\text{CO}_2$ SINK geological storage site at Ketzin, Germany. – in: *Environmental Geosciences* 13 (3), pp. 145–161. – DOI: [10.1306/eg.02080605016](https://doi.org/10.1306/eg.02080605016).
- Fournier, R. O., Rosenbauer, R. J. & Bischoff, J. L. (1982): The solubility of quartz in aqueous sodium chloride solution at 350 degree and 180 to 500 bars. – in: *Geochimica et Cosmochimica Acta* 46 (10), pp. 1975–1978. – DOI: [10.1016/0016-7037\(82\)90136-3](https://doi.org/10.1016/0016-7037(82)90136-3).
- Fu, Q., Lu, P., Konishi, H., Dilmore, R., Xu, H., Seyfried, W. E. & Zhu, C. (2009): Coupled alkali-feldspar dissolution and secondary mineral precipitation in batch systems: 1. New experiments at 200 degree C and 300 bars. – in: *Chemical Geology* 258 (3-4), pp. 125–135. – DOI: [10.1016/j.chemgeo.2008.09.014](https://doi.org/10.1016/j.chemgeo.2008.09.014).
- Gall, Q. & Hyde, R. (1989): Analcime in lake and lake-margin sediments of the Carboniferous Rocky Brook Formation, Western Newfoundland, Canada. – in: *Sedimentology* 36 (5), pp. 875–887. – DOI: [10.1111/j.1365-3091.1989.tb01751.x](https://doi.org/10.1111/j.1365-3091.1989.tb01751.x).
- Galli, E. (1972): La phillipsite barifera (wellsite) di M. Calvarina (Verona). – in: *Periodico di Mineralogia* 41, pp. 23–33.
- Galli, E. & Rinaldi, R. (1974): The crystal chemistry of epistilbites. – in: *American Mineralogist* 59, pp. 1055–1061.
-

- Ganguly, J. (2008): *Thermodynamics in Earth and planetary sciences*. – Springer-Verlag. – DOI: [10.1007/978-3-540-77306-1](https://doi.org/10.1007/978-3-540-77306-1).
- Gascoyne, M., Davison, C. C., Ross, J. D. & Pearson, R. (1987): Saline groundwaters and brines in plutons in the Canadian Shield. – in: *Saline water and gases in crystalline rocks*. – ed. by P. Fritz & S. K. Frapes, pp. 53–68.
- Genter, A., Evans, K., Cuenot, N., Fritsch, D. & Sanjuan, B. (2010): Contribution of the exploration of deep crystalline fractured reservoir of Soultz to the knowledge of enhanced geothermal systems (EGS). – in: *Comptes Rendus Geoscience* 342 (7-8), pp. 502–516. – DOI: [10.1016/j.crte.2010.01.006](https://doi.org/10.1016/j.crte.2010.01.006).
- Genter, A. & Traineau, H. (1996): Analysis of macroscopic fractures in granite in the HDR geothermal well EPS-1, Soultz-sous-Forêts, France. – in: *Journal of Volcanology and Geothermal Research* 72 (1-2), pp. 121–141. – DOI: [10.1016/0377-0273\(95\)00070-4](https://doi.org/10.1016/0377-0273(95)00070-4).
- Gérard, A., Genter, A., Kohl, T., Lutz, P., Rose, P. & Rummel, F. (2006): The deep EGS (Enhanced Geothermal System) project at Soultz-sous-Forêts (Alsace, France). – in: *Geothermics* 35 (5-6), pp. 473–483. – DOI: [10.1016/j.geothermics.2006.12.001](https://doi.org/10.1016/j.geothermics.2006.12.001).
- Ghobarkar, H. (1985): Structural and morphological changes in hydrothermally grown wairakite. – in: *Crystal Research and Technology* 20 (9), K90–K92. – DOI: [10.1002/crat.2170200929](https://doi.org/10.1002/crat.2170200929).
- Ghobarkar, H. & Schäf, O. (1999a): Synthesis of gismondine-type zeolites by the hydrothermal method. – in: *Materials Research Bulletin* 34 (4), pp. 517–525. – DOI: [10.1016/S0025-5408\(99\)00052-5](https://doi.org/10.1016/S0025-5408(99)00052-5).
- Ghobarkar, H. & Schäf, O. (1999b): Effect of temperature on hydrothermal synthesis of analcime and viséite. – in: *Materials Science and Engineering B: Solid-State Materials for Advanced Technology* 60 (3), pp. 163–167.
- Gleeson, T. & Ingebritsen, S. E. (2016): *Crustal permeability*. – Chichester, UK and Hoboken, NJ: John Wiley & Sons.
- Gottardi, G. & Galli, E. (1985): *Natural zeolites*. – vol. 18. – Minerals and rocks. – Berlin: Springer.
- Grice, J. D., Rowe, R. & Poirier, G. (2017): Garronite-Na, A New Zeolite Species From Mont Saint-Hilaire, Québec. – in: *Canadian Mineralogist* 54 (6), pp. 1549–1562. – DOI: [10.3749/canmin.1600018](https://doi.org/10.3749/canmin.1600018).
- Griffiths, L., Heap, M. J., Wang, F., Daval, D., Gilg, H. A., Baud, P., Schmittbuhl, J. & Genter, A. (2016): Geothermal implications for fracture-filling hydrothermal precipitation. – in: *Geothermics* 64, pp. 235–245. – DOI: [10.1016/j.geothermics.2016.06.006](https://doi.org/10.1016/j.geothermics.2016.06.006).
- Hammersley, A. P., Svensson, S. O., Hanfland, M., Fitch, A. N. & Hausermann, D. (1996): Two-dimensional detector software: From real detector to idealised image or two-theta scan. – in: *High Pressure Research* 14 (4-6), pp. 235–248. – DOI: [10.1080/08957959608201408](https://doi.org/10.1080/08957959608201408).

- Hammersley, A. P., Svensson, S. O. & Thompson, A. (1994): Calibration and correction of spatial distortions in 2D detector systems. – in: *Nuclear Instruments and Methods in Physics Research Section A: Accelerators, Spectrometers, Detectors and Associated Equipment* 346 (1-2), pp. 312–321. – DOI: [10.1016/0168-9002\(94\)90720-X](https://doi.org/10.1016/0168-9002(94)90720-X).
- Hanor, J. S. (1994): Origin of saline fluids in sedimentary basins. – in: *Geological Society, London, Special Publications* 78 (1), pp. 151–174. – DOI: [10.1144/GSL.SP.1994.078.01.13](https://doi.org/10.1144/GSL.SP.1994.078.01.13).
- Hay, R. L. & Sheppard, R. A. (2001): Occurrence of Zeolites in Sedimentary Rocks: An Overview. – in: *Reviews in Mineralogy and Geochemistry* 45 (1), pp. 217–234. – DOI: [10.2138/rmg.2001.45.6](https://doi.org/10.2138/rmg.2001.45.6).
- Helgeson, H. C. (1969): Thermodynamics of hydrothermal systems at elevated temperatures and pressures. – in: *American Journal of Science* 267 (7), pp. 729–804. – DOI: [10.2475/ajs.267.7.729](https://doi.org/10.2475/ajs.267.7.729).
- Helgeson, H. C., Garrels, R. M. & MacKenzie, F. T. (1969): Evaluation of irreversible reactions in geochemical processes involving minerals and aqueous solutions-II. Applications. – in: *Geochimica et Cosmochimica Acta* 33 (4), pp. 455–481.
- Henry, D. J. (2005): The Ti-saturation surface for low-to-medium pressure metapelitic biotites: Implications for geothermometry and Ti-substitution mechanisms. – in: *American Mineralogist* 90 (2-3), pp. 316–328. – DOI: [10.2138/am.2005.1498](https://doi.org/10.2138/am.2005.1498).
- Herzberger, P., Münch, W., Kölbl, T., Bruchmann, U., Schlagermann, P., Hötzl, H., Wolf, L., Rettenmaier, D., Steger, H., Zorn, R., Seibt, P., Möllmann, G.-U., Sauter, M., Ghergut, J. & Ptak, T. (2010): The geothermal power plant Bruchsal. – in: *Proceedings World Geothermal Congress 2010*.
- Higgs, K. E., Haese, R. R., Golding, S. D., Schacht, U. & Watson, M. N. (2015): The Pretty Hill Formation as a natural analogue for CO<sub>2</sub> storage: An investigation of mineralogical and isotopic changes associated with sandstones exposed to low, intermediate and high CO<sub>2</sub> concentrations over geological time. – in: *Chemical Geology* 399, pp. 36–64. – DOI: [10.1016/j.chemgeo.2014.10.019](https://doi.org/10.1016/j.chemgeo.2014.10.019).
- Hövelmann, J., Putnis, A., Geisler, T., Schmidt, B. C. & Golla-Schindler, U. (2010): The replacement of plagioclase feldspars by albite: observations from hydrothermal experiments. – in: *Contributions to Mineralogy and Petrology* 159 (1), pp. 43–59. – DOI: [10.1007/s00410-009-0415-4](https://doi.org/10.1007/s00410-009-0415-4).
- Hu, Y., Ray, J. R. & Jun, Y.-S. (2011): Biotite-brine interactions under acidic hydrothermal conditions: fibrous illite, goethite, and kaolinite formation and biotite surface cracking. – in: *Environmental science & technology* 45 (14), pp. 6175–6180. – DOI: [10.1021/es200489y](https://doi.org/10.1021/es200489y).
- ICCD (2016): PDF-2 database. – International Centre for Diffraction Data, Newtown Square, PA, USA.
- Illies, J. H. (1972): The Rhine graben rift system-plate tectonics and transform faulting. – in: *Geophysical Surveys* 1 (1), pp. 27–60. – DOI: [10.1007/BF01449550](https://doi.org/10.1007/BF01449550).
-

- Illies, J. H. & Greiner, G. (1978): Rhinegraben and the Alpine system. – in: *Geological Society of America Bulletin* 89 (5), pp. 770–782.
- Inoue, A., Meunier, A., Patrier-Mas, P., Rigault, C., Beaufort, D. & Vieillard, P. (2009): Application of Chemical Geothermometry to Low-Temperature Trioctahedral Chlorites. – in: *Clays and Clay Minerals* 57 (3), pp. 371–382. – DOI: [10.1346/CCMN.2009.0570309](https://doi.org/10.1346/CCMN.2009.0570309).
- Isherwood, D. & Street, A. (1976): Biotite-induced grussification of the Boulder Creek Granodiorite, Boulder County, Colorado. – in: *Geological Society of America Bulletin* 87 (3), pp. 366–370. – DOI: [10.1130/0016-7606\(1976\)87<366:BGOTBC>2.0.CO;2](https://doi.org/10.1130/0016-7606(1976)87<366:BGOTBC>2.0.CO;2).
- James, R. H., Allen, D. E. & Seyfried Jr., W. E. (2003): An experimental study of alteration of oceanic crust and terrigenous sediments at moderate temperatures (51 to 350 degree C): insights as to chemical processes in near-shore ridge-flank hydrothermal systems. – in: *Geochimica et Cosmochimica Acta* 67 (4), pp. 681–691. – DOI: [10.1016/S0016-7037\(02\)01113-4](https://doi.org/10.1016/S0016-7037(02)01113-4).
- Jamtveit, B., Kobchenko, M., Austrheim, H., Malthe-Sørenssen, A., Røyne, A. & Svensen, H. (2011): Porosity evolution and crystallization-driven fragmentation during weathering of andesite. – in: *Journal of Geophysical Research* 116 (B12). – DOI: [10.1029/2011JB008649](https://doi.org/10.1029/2011JB008649).
- Jamtveit, B., Putnis, C. V. & Malthe-Sørenssen, A. (2009): Reaction induced fracturing during replacement processes. – in: *Contributions to Mineralogy and Petrology* 157 (1), pp. 127–133. – DOI: [10.1007/s00410-008-0324-y](https://doi.org/10.1007/s00410-008-0324-y).
- Kaszuba, J. P., Janecky, D. R. & Snow, M. G. (2005): Experimental evaluation of mixed fluid reactions between supercritical carbon dioxide and NaCl brine: Relevance to the integrity of a geologic carbon repository. – in: *Chemical Geology* 217 (3-4), pp. 277–293. – DOI: [10.1016/j.chemgeo.2004.12.014](https://doi.org/10.1016/j.chemgeo.2004.12.014).
- Keller, W. D. (1952): Analcime in the Popo Agie member of the Chugwater Formation. – in: *Journal of Sedimentary Research* 22 (2), pp. 70–82. – DOI: [10.1306/D42694C7-2B26-11D7-8648000102C1865D](https://doi.org/10.1306/D42694C7-2B26-11D7-8648000102C1865D).
- Kominou, A. & Yardley, B. W. D. (1997): Fluid-rock interactions in the Rhine Graben: A thermodynamic model of the hydrothermal alteration observed in deep drilling. – in: *Geochimica et Cosmochimica Acta* 61 (3), pp. 515–531. – DOI: [10.1016/S0016-7037\(96\)00358-4](https://doi.org/10.1016/S0016-7037(96)00358-4).
- Kuncoro, G. B., Ngothai, Y., O'Neill, B. K., Pring, A. S., Brügger, J. & Yanagisawa, N. (2010): Laboratory-scale study of fluid-rock interaction in the enhanced geothermal systems in cooper Basin, South Australia. – in: *Geothermal Resources Council Transactions* 34 (1), pp. 642–646.
- Lafay, R., Montes-Hernandez, G., Janots, E., Chiriach, R., Findling, N. & Toche, F. (2014): Simultaneous precipitation of magnesite and lizardite from hydrothermal alteration of olivine under high-carbonate alkalinity. – in: *Chemical Geology* 368, pp. 63–75. – DOI: [10.1016/j.chemgeo.2014.01.008](https://doi.org/10.1016/j.chemgeo.2014.01.008).
-

- Lasaga, A. C., Soler, J. M., Ganor, J., Burch, T. E. & Nagy, K. L. (1994): Chemical weathering rate laws and global geochemical cycles. – in: *Geochimica et Cosmochimica Acta* 58 (10), pp. 2361–2386. – DOI: [10.1016/0016-7037\(94\)90016-7](https://doi.org/10.1016/0016-7037(94)90016-7).
- Ledésert, B., Berger, G., Meunier, A., Genter, A. & Bouchet, A. (1999): Diagenetic-type reactions related to hydrothermal alteration in the Soultz-sous-Forêts granite, France. – in: *European Journal of Mineralogy* 11 (4), pp. 731–741.
- Ledésert, B., Hebert, R., Genter, A., Bartier, D., Clauer, N. & Grall, C. (2010): Fractures, hydrothermal alterations and permeability in the Soultz Enhanced Geothermal System. – in: *Comptes Rendus Geoscience* 342 (7-8), pp. 607–615. – DOI: [10.1016/j.crte.2009.09.011](https://doi.org/10.1016/j.crte.2009.09.011).
- Liou, J. G. (1970): Synthesis and stability relations of wairakite,  $\text{CaAl}_2\text{Si}_4\text{O}_{12} \cdot 2\text{H}_2\text{O}$ . – in: *Contributions to Mineralogy and Petrology* 27 (4), pp. 259–282. – DOI: [10.1007/BF00389814](https://doi.org/10.1007/BF00389814).
- Liou, J. G., Capitani, C. de & Frey, M. (1991): Zeolite equilibria in the system  $\text{CaAl}_2\text{Si}_2\text{O}_8 - \text{NaAlSi}_3\text{O}_8 - \text{SiO}_2 - \text{H}_2\text{O}$ . – in: *New Zealand Journal of Geology and Geophysics* 34 (3), pp. 293–301. – DOI: [10.1080/00288306.1991.9514467](https://doi.org/10.1080/00288306.1991.9514467).
- Mavris, C., Götze, J., Plötze, M. & Egli, M. (2012): Weathering and mineralogical evolution in a high Alpine soil chronosequence: A combined approach using SEM–EDX, cathodoluminescence and Nomarski DIC microscopy. – in: *Sedimentary Geology* 280, pp. 108–118. – DOI: [10.1016/j.sedgeo.2012.04.008](https://doi.org/10.1016/j.sedgeo.2012.04.008).
- Mehegan, J. M., Robinson, P. T. & Delaney, J. R. (1982): Secondary mineralization and hydrothermal alteration in the Reydarfjördur drill core, eastern Iceland. – in: *Journal of Geophysical Research* 87 (B8), pp. 6511–6524. – DOI: [10.1029/JB087iB08p06511](https://doi.org/10.1029/JB087iB08p06511).
- Meier, W. M., Olson, D. & Baerlocher, C. (1996): Atlas of zeolite structure types. – 4. rev. ed.. – vol. 17:1/2. – Zeolites. – London: Published on behalf of the Structure Commission of the International Zeolite Association by Elsevier.
- Meller, C. & Kohl, T. (2014): The significance of hydrothermal alteration zones for the mechanical behavior of a geothermal reservoir. – in: *Geothermal Energy* 2 (1), p. 2538. – DOI: [10.1186/s40517-014-0012-2](https://doi.org/10.1186/s40517-014-0012-2).
- Meller, C. & Ledésert, B. (2017): Is There a Link Between Mineralogy, Petrophysics, and the Hydraulic and Seismic Behaviors of the Soultz-sous-Forêts Granite During Stimulation? A Review and Reinterpretation of Petro-Hydromechanical Data Toward a Better Understanding of Induced Seismicity. – in: *Journal of Geophysical Research: Solid Earth* 122 (12), pp. 9755–9774. – DOI: [10.1002/2017JB014648](https://doi.org/10.1002/2017JB014648).
- Merkel, B. J. & Planer-Friedrich, B. (2008): Grundwasserchemie - Praxisorientierter Leitfaden zur numerischen Modellierung von Beschaffenheit, Kontamination und Sanierung aquatischer Systeme. – Springer-Verlag Berlin Heidelberg.
- Meunier, A. (2005): Clays. – Berlin and New York: Springer. – DOI: [10.1007/b138672](https://doi.org/10.1007/b138672).

- Milodowski, A. E., Savage, D. J., Bateman, K. & Hughes, C. R. (1989): The precipitation of solids from potential heat exchange fluids for use in a HDR geothermal system in granite. – in: *Geothermics* 18 (1-2), pp. 233–240. – DOI: [10.1016/0375-6505\(89\)90032-1](https://doi.org/10.1016/0375-6505(89)90032-1).
- Misra, K. C. (2012): Introduction to geochemistry: Principles and applications. – Principles and applications. – Chichester, West Sussex and Hoboken, NJ: Wiley-Blackwell.
- Miyashiro, A. & Shido, F. (1970): Progressive metamorphism in zeolite assemblages. – in: *Lithos* 3 (3), pp. 251–260. – DOI: [10.1016/0024-4937\(70\)90077-0](https://doi.org/10.1016/0024-4937(70)90077-0).
- Moore, D. E., Morrow, C. A. & Byerlee, J. D. (1983): Chemical reactions accompanying fluid flow through granite held in a temperature gradient. – in: *Geochimica et Cosmochimica Acta* 47 (3), pp. 445–453. – DOI: [10.1016/0016-7037\(83\)90267-3](https://doi.org/10.1016/0016-7037(83)90267-3).
- Morrow, C. A., Moore, D. E. & Lockner, D. A. (2001): Permeability reduction in granite under hydrothermal conditions. – in: *Journal of Geophysical Research* 106 (B12), pp. 30551–30560. – DOI: [10.1029/2000JB000010](https://doi.org/10.1029/2000JB000010).
- Na, J., Xu, T., Yuan, Y., Feng, B., Tian, H. & Bao, X. (2015): An integrated study of fluid–rock interaction in a CO<sub>2</sub>-based enhanced geothermal system: A case study of Songliao Basin, China. – in: *Applied Geochemistry* 59, pp. 166–177. – DOI: [10.1016/j.apgeochem.2015.04.018](https://doi.org/10.1016/j.apgeochem.2015.04.018).
- Nagy, K. L. (1995): Dissolution and precipitation kinetics of sheet silicates. – in: *Reviews in Mineralogy and Geochemistry* 31, pp. 291–351.
- Nawaz, R. (1982): A Chemical Classification Scheme for the Gismondine Group Zeolites. – in: *The Irish Naturalists' Journal* 20 (11), pp. 480–483.
- Newton, R. C. & Manning, C. E. (2000): Quartz solubility in H<sub>2</sub>O–NaCl and H<sub>2</sub>O–CO<sub>2</sub> solutions at deep crust–upper mantle pressures and temperatures: 2–15 kbar and 500–900 degree C. – in: *Geochimica et Cosmochimica Acta* 64 (17), pp. 2993–3005. – DOI: [10.1016/S0016-7037\(00\)00402-6](https://doi.org/10.1016/S0016-7037(00)00402-6).
- O'Neil, J. R. & Taylor, H. P. (1967): The oxygen isotope and cation exchange chemistry of feldspars. – in: *The American Mineralogist* 52 (9), pp. 1414–1473.
- Oelkers, E. H., Benezeth, P. & Pokrovski, G. S. (2009): Thermodynamic Databases for Water–Rock Interaction. – in: *Reviews in Mineralogy and Geochemistry* 70 (1), pp. 1–46. – DOI: [10.2138/rmg.2009.70.1](https://doi.org/10.2138/rmg.2009.70.1).
- Okamoto, M. & Makajima, W. (1994): Wairakites from Haga, Hyogo Prefecture, Japan. – in: *Journal of Mineralogy, Petrology and Economic Geology* 89 (11), pp. 433–438. – DOI: [10.2465/ganko.89.433](https://doi.org/10.2465/ganko.89.433).
- Orywall, P., Drüppel, K., Kuhn, D., Kohl, T., Zimmermann, M. & Eiche, E. (2017): Flow-through experiments on the interaction of sandstone with Ba-rich fluids at geothermal conditions. – in: *Geothermal Energy* 5 (1), p. 74. – DOI: [10.1186/s40517-017-0079-7](https://doi.org/10.1186/s40517-017-0079-7).
-

- Parkhurst, D. L. (1990): Ion association models and mean activity coefficients of various salts. – in: *Chemical modeling of aqueous systems II*. – ed. by D. C. Melchior & R. L. Basset, pp. 30–43.
- Parkhurst, D. L. & Appelo, C. A. J. (2013): Description of input and examples for PHREEQC version 3—A computer program for speciation, batch-reaction, one-dimensional transport, and inverse geochemical calculations. – vol. 6-A43. – U.S. Geological Survey Techniques and Methods. – Denver, Colorado.
- Parry, W. T. (1982): Geochemistry of Hydrothermal Chlorite Replacing Igneous Biotite. – in: *Clays and Clay Minerals* 30 (2), pp. 81–90. – DOI: [10.1346/CCMN.1982.0300201](https://doi.org/10.1346/CCMN.1982.0300201).
- Passaglia, E. (1970): The crystal chemistry of chabazites. – in: *American Mineralogist* 55 (7 + 8), pp. 1278–1301.
- Passaglia, E. & Sheppard, R. A. (2001): The Crystal Chemistry of Zeolites. – in: *Reviews in Mineralogy and Geochemistry* 45 (1), pp. 69–116. – DOI: [10.2138/rmg.2001.45.2](https://doi.org/10.2138/rmg.2001.45.2).
- Pauwels, H., Fouillac, C. & Fouillac, A. M. (1993): Chemistry and Isotopes of Deep Geothermal Saline Fluids in the Upper Rhine Graben - Origin of Compounds and Water-Rock Interactions. – in: *Geochimica et Cosmochimica Acta* 57 (12), pp. 2737–2749. – DOI: [10.1016/0016-7037\(93\)90387-C](https://doi.org/10.1016/0016-7037(93)90387-C).
- Pauwels, H., Fouillac, C. & Criaud, A. (1992): Water-rock interactions during experiments within the geothermal Hot Dry Rock borehole GPK1, Soultz-sous-Forêts, Alsace, France. – in: *Applied Geochemistry* 7 (3), pp. 243–255. – DOI: [10.1016/0883-2927\(92\)90040-A](https://doi.org/10.1016/0883-2927(92)90040-A).
- Pielow, H.-U. (1997): Korrodierte Mineralgrenzflächen als Indikatoren für die Migration salinärer Fluide im Kristallin am Beispiel des KTB. – in: *Göttinger Arbeiten zur Geologie und Paläontologie* 71, pp. 1–55.
- Pirajno, F. (1992): Hydrothermal mineral deposits: Principles and fundamental concepts for the exploration geologist. – Principles and fundamental concepts for the exploration geologist. – Berlin: Springer. – DOI: [10.1007/978-3-642-75671-9](https://doi.org/10.1007/978-3-642-75671-9).
- Pribnow, D. & Schellschmidt, R. (2000): Thermal tracking of upper crustal fluid flow in the Rhine graben. – in: *Geophysical Research Letters* 27 (13), pp. 1957–1960. – DOI: [10.1029/2000GL008494](https://doi.org/10.1029/2000GL008494).
- Putirka, K. D. (2008): Thermometers and Barometers for Volcanic Systems. – in: *Reviews in Mineralogy and Geochemistry* 69 (1), pp. 61–120. – DOI: [10.2138/rmg.2008.69.3](https://doi.org/10.2138/rmg.2008.69.3).
- Putnis, A. & McConnell, J. D. C. (1980): Principles of mineral behaviour. – vol. 1. – Geoscience texts. – Oxford, Boston and New York: Blackwell Scientific Publications.
- Putnis, A. (2002): Mineral replacement reactions: from macroscopic observations to microscopic mechanisms. – in: *Mineralogical Magazine* 66 (5), pp. 689–708. – DOI: [10.1180/0026461026650056](https://doi.org/10.1180/0026461026650056).
-

- Putnis, A. (2009): Mineral Replacement Reactions. – in: *Reviews in Mineralogy and Geochemistry* 70 (1), pp. 87–124. – DOI: [10.2138/rmg.2009.70.3](https://doi.org/10.2138/rmg.2009.70.3).
- Putnis, A. & Austrheim, H. (2010): Fluid-Induced Processes: Metasomatism and Metamorphism. – in: *Frontiers in Geofluids*. – Wiley-Blackwell, pp. 254–269. – DOI: [10.1002/9781444394900.ch18](https://doi.org/10.1002/9781444394900.ch18).
- Ross, C. S. (1928): Sedimentary analcite. – in: *American Mineralogist* 13 (5), pp. 195–197.
- Ross, C. S. (1941): Sedimentary analcite. – in: *American Mineralogist* 26 (10), pp. 627–629.
- Rossi, A. M. & Graham, R. C. (2010): Weathering and Porosity Formation in Subsoil Granitic Clasts, Bishop Creek Moraines, California. – in: *Soil Science Society of America Journal* 74 (1), pp. 172–185. – DOI: [10.2136/sssaj2009.0146](https://doi.org/10.2136/sssaj2009.0146).
- Røyne, A. & Jamtveit, B. (2015): Pore-Scale Controls on Reaction-Driven Fracturing. – in: *Reviews in Mineralogy and Geochemistry* 80 (1), pp. 25–44. – DOI: [10.2138/rmg.2015.80.02](https://doi.org/10.2138/rmg.2015.80.02).
- Sanjuan, B., Millot, R., Innocent, C., Dezayes, C., Scheiber, J. & Brach, M. (2016): Major geochemical characteristics of geothermal brines from the Upper Rhine Graben granitic basement with constraints on temperature and circulation. – in: *Chemical Geology* 428, pp. 27–47. – DOI: [10.1016/j.chemgeo.2016.02.021](https://doi.org/10.1016/j.chemgeo.2016.02.021).
- Sausse, J. (2002): Hydromechanical properties and alteration of natural fracture surfaces in the Soultz granite (Bas-Rhin, France). – in: *Tectonophysics* 348 (1-3), pp. 169–185. – DOI: [10.1016/S0040-1951\(01\)00255-4](https://doi.org/10.1016/S0040-1951(01)00255-4).
- Savage, D. J., Bateman, K., Milodowski, A. E. & Hughes, C. R. (1993): An experimental evaluation of the reaction of granite with streamwater, seawater and NaCl solutions at 200 degrees C. – in: *Journal of Volcanology and Geothermal Research* 57 (3-4), pp. 167–191. – DOI: [10.1016/0377-0273\(93\)90011-F](https://doi.org/10.1016/0377-0273(93)90011-F).
- Savage, D. J., Bateman, K. & Richards, H. G. (1992): Granite-water interactions in a flow-through experimental system with applications to the Hot Dry Rock geothermal system at Rosemanowes, Cornwall, U.K. – in: *Applied Geochemistry* 7 (3), pp. 223–241. – DOI: [10.1016/0883-2927\(92\)90039-6](https://doi.org/10.1016/0883-2927(92)90039-6).
- Schiffman, P., Bird, D. K. & Elders, W. A. (1985): Hydrothermal Mineralogy of Calcareous Sandstones from the Colorado River Delta in the Cerro Prieto Geothermal System, Baja California, Mexico. – in: *Mineralogical Magazine* 49, pp. 435–449.
- Schill, E. & Klingler, P. (2010): Increase of productivity in the Riehen geothermal system (Switzerland): Tracer test and reservoir model. – in: *Mitteilungen der Geotechnik Schweiz* 161, pp. 35–40.
- Schindler, M., Baumgärtner, J., Gandy, T., Hauffe, P., Hettkamp, T., Menzel, H., Penzkofer, P., Teza, D., Tischner, T. & Wahl, G. (2010): Successful hydraulic stimulation techniques for electric power production in the Upper Rhine Graben, Central Europe. – in: *Proceedings World Geothermal Congress 2010*.
-

- Schleicher, A. M., Warr, L. N., Kober, B., Laverret, E. & Clauer, N. (2006): Episodic mineralization of hydrothermal illite in the Soultz-sous-Forêts granite (Upper Rhine Graben, France). – in: *Contributions to Mineralogy and Petrology* 152 (3), pp. 349–364. – DOI: [10.1007/s00410-006-0110-7](https://doi.org/10.1007/s00410-006-0110-7).
- Schmidt, R. B., Bucher, K., Drüppel, K. & Stober, I. (2017a): Experimental interaction of hydrothermal Na-Cl solution with fracture surfaces of geothermal reservoir sandstone of the Upper Rhine Graben. – in: *Applied Geochemistry* 81, pp. 36–52. – DOI: [10.1016/j.apgeochem.2017.03.010](https://doi.org/10.1016/j.apgeochem.2017.03.010).
- Schmidt, R. B., Bucher, K., Drüppel, K. & Stober, I. (2017b): Experimental interaction of hydrothermal Na-Cl solution with fracture surfaces of geothermal reservoir sandstone of the Upper Rhine Graben. – in: *Applied Geochemistry* 81, pp. 36–52. – DOI: [10.1016/j.apgeochem.2017.03.010](https://doi.org/10.1016/j.apgeochem.2017.03.010).
- Schmidt, R. B., Bucher, K. & Stober, I. (2018): Experiments on granite alteration under geothermal reservoir conditions and the initiation of fracture evolution. – in: *European Journal of Mineralogy* 30 (5), pp. 899–916. – DOI: [10.1127/ejm/2018/0030-2771](https://doi.org/10.1127/ejm/2018/0030-2771).
- Schmidt, R. B., Göttlicher, J. & Stober, I. (submitted): Experiments on sandstone alteration under geothermal reservoir conditions and the formation of zeolites. – in: *European Journal of Mineralogy* 31.
- Schröpfer, L. & Joswig, W. (1997): Structure analyses of a partially dehydrated synthetic Ca-garronite single crystal under different T, PH<sub>2</sub>O conditions. – in: *European Journal of Mineralogy* 9 (1), pp. 53–66. – DOI: [10.1127/ejm/9/1/0053](https://doi.org/10.1127/ejm/9/1/0053).
- Schwarz, M. & Henk, A. (2005): Evolution and structure of the Upper Rhine Graben: Insights from three-dimensional thermomechanical modelling. – in: *International Journal of Earth Sciences* 94 (4), pp. 732–750. – DOI: [10.1007/s00531-004-0451-2](https://doi.org/10.1007/s00531-004-0451-2).
- Seki, Y. (1969): Facies series in low-grade metamorphism. – in: *The Journal of the Geological Society of Japan* 75 (5), pp. 255–266. – DOI: [10.5575/geosoc.75.255](https://doi.org/10.5575/geosoc.75.255).
- Seki, Y. & Oki, Y. (1969): Wairakite-analcime solid solutions from low-grade metamorphic rocks of the Tanzawa Mountains, Central Japan. – in: *Mineralogical Journal* 6 (1-2), pp. 36–45. – DOI: [10.2465/minerj1953.6.36](https://doi.org/10.2465/minerj1953.6.36).
- Seryotkin, Y. V., Joswig, W., Bakakin, V. V., Belitsky, I. A. & Fursenko, B. A. (2003): High-temperature crystal structure of wairakite. – in: *European Journal of Mineralogy* 15 (3), pp. 475–484. – DOI: [10.1127/0935-1221/2003/0015-0475](https://doi.org/10.1127/0935-1221/2003/0015-0475).
- Shao, H., Ray, J. R. & Jun, Y.-S. (2010): Dissolution and precipitation of clay minerals under geologic CO<sub>2</sub> sequestration conditions: CO<sub>2</sub>-brine-phlogopite interactions. – in: *Environmental science & technology* 44 (15), pp. 5999–6005. – DOI: [10.1021/es1010169](https://doi.org/10.1021/es1010169).
- Shao, H., Ray, J. R. & Jun, Y.-S. (2011): Effects of salinity and the extent of water on supercritical CO<sub>2</sub>-induced phlogopite dissolution and secondary mineral formation. – in: *Environmental science & technology* 45 (4), pp. 1737–1743. – DOI: [10.1021/es1034975](https://doi.org/10.1021/es1034975).
-

- Shervais, J. W., Kolesar, P. & Andreasen, K. (2005): A Field and Chemical Study of Serpentinization—Stonyford, California: Chemical Flux and Mass Balance. – in: *International Geology Review* 47 (1), pp. 1–23. – DOI: [10.2747/0020-6814.47.1.1](https://doi.org/10.2747/0020-6814.47.1.1).
- Shiraki, R. & Dunn, T. L. (2000): Experimental study on water-rock interactions during CO<sub>2</sub> flooding in the Tensleep Formation, Wyoming, USA. – in: *Applied Geochemistry* 15 (3), pp. 265–279. – DOI: [10.1016/S0883-2927\(99\)00048-7](https://doi.org/10.1016/S0883-2927(99)00048-7).
- Smulikowski, W., Desmons, J., Fettes, D. J., Harte, B., Sassi, F. P. & Schmid, R. (2003): Types, grades and facies of metamorphism. – in: *Recommendations*. – ed. by IUGS Subcommission on the Systematics of Metamorphic Rocks. – vol. 2.
- Stillings, L. L. & Brantley, S. L. (1995): Feldspar dissolution at 25 degree C and pH 3: Reaction stoichiometry and the effect of cations. – in: *Geochimica et Cosmochimica Acta* 59 (8), pp. 1483–1496. – DOI: [10.1016/0016-7037\(95\)00057-7](https://doi.org/10.1016/0016-7037(95)00057-7).
- Stober, I. & Bucher, K. (1999): Origin of salinity of deep groundwater in crystalline rocks. – in: *Terra Nova* 11 (4), pp. 181–185.
- Stober, I. & Bucher, K. (2005): The upper continental crust, an aquifer and its fluid: Hydraulic and chemical data from 4 km depth in fractured crystalline basement rocks at the KTB test site. – in: *Geofluids* 5 (1), pp. 8–19. – DOI: [10.1111/j.1468-8123.2004.00106.x](https://doi.org/10.1111/j.1468-8123.2004.00106.x).
- Stober, I. & Bucher, K. (2012): Geothermie. – Berlin [u.a.]: Springer.
- Stober, I. & Bucher, K. (2014): Hydraulic and hydrochemical properties of deep sedimentary reservoirs of the Upper Rhine Graben, Europe. – in: *Geofluids* 15 (3), pp. 464–482. – DOI: [10.1111/gfl.12122](https://doi.org/10.1111/gfl.12122).
- Stober, I. & Bucher, K. (2015): Hydraulic conductivity of fractured upper crust: Insights from hydraulic tests in boreholes and fluid-rock interaction in crystalline basement rocks. – in: *Geofluids* 15 (1-2), pp. 161–178. – DOI: [10.1111/gfl.12104](https://doi.org/10.1111/gfl.12104).
- Stober, I. & Jodocy, M. (2011): Hydrochemie der Tiefenwaesser im Oberrheingraben: Eine Basisinformation fuer geothermische Nutzungssysteme. – in: *Zeitschrift fuer Geologische Wissenschaften* 39 (1), pp. 39–57.
- Stober, I., Richter, A., Brost, E. & Bucher, K. (1999): The Ohlsbach plume; discharge of deep saline water from the crystalline basement of the Black Forest, Germany. – in: *Hydrogeology Journal* 7 (3), pp. 273–283.
- Takeuchi, Y., Mazzi, F., Haga, N. & Galli, E. (1979): The crystal structure of wairakite. – in: *American Mineralogist* 64 (9-10), pp. 993–1001.
- Tschernich, R. W. (1992): Zeolites of the world. – Phoenix, Ariz.: Geoscience Press.
- Turpault, M.-P., Berger, G. & Meunier, A. (1992): Dissolution-precipitation processes induced by hot water in a fractured granite; Part 1, Wall-rock alteration and vein deposition processes. – in: *European Journal of Mineralogy* 4 (6), pp. 1457–1475.
-

- Utada, M. (1980): Hydrothermal alteration related to igneous acidity in Cretaceous and Neogene formations of Japan. – in: *Mining Geol. Jpn Spec Issue* 8, pp. 67–83.
- Utada, M. (2001a): Zeolites in Burial Diagenesis and Low-grade Metamorphic rocks. – in: *Reviews in Mineralogy and Geochemistry* 45 (1), pp. 277–304. – DOI: [10.2138/rmg.2001.45.9](https://doi.org/10.2138/rmg.2001.45.9).
- Utada, M. (2001b): Zeolites in Hydrothermally Altered Rocks. – in: *Reviews in Mineralogy and Geochemistry* 45 (1), pp. 305–322. – DOI: [10.2138/rmg.2001.45.10](https://doi.org/10.2138/rmg.2001.45.10).
- Vaughan, P. J., Moore, D. E., Morrow, C. A. & Byerlee, J. D. (1986): Role of cracks in progressive permeability reduction during flow of heated aqueous fluids through granite. – in: *Journal of Geophysical Research* 91 (B7), pp. 7517–7530. – DOI: [10.1029/JB091iB07p07517](https://doi.org/10.1029/JB091iB07p07517).
- Velde, B., ed. (1995): Origin and mineralogy of clays. – Berlin and Heidelberg: Springer. – DOI: [10.1007/978-3-662-12648-6](https://doi.org/10.1007/978-3-662-12648-6).
- Verma, S. P. & Santoyo, E. (1997): New improved equations for  $\text{Al}_2\text{SiO}_5$  and  $\text{SiO}_2$  geothermometers by outlier detection and rejection. – in: *Journal of Volcanology and Geothermal Research* 79 (1-2), pp. 9–23. – DOI: [10.1016/S0377-0273\(97\)00024-3](https://doi.org/10.1016/S0377-0273(97)00024-3).
- Wahrhaftig, C. (1965): Stepped Topography of the Southern Sierra Nevada, California. – in: *Geological Society of America Bulletin* 76 (10), pp. 1165–1189. – DOI: [10.1130/0016-7606\(1965\)76\[1165:STOTSS\]2.0.CO;2](https://doi.org/10.1130/0016-7606(1965)76[1165:STOTSS]2.0.CO;2).
- Walker, G. P. L. (1962): Garronite, a new zeolite, from Ireland and Iceland. – in: *Mineralogical Magazine* 33 (258), pp. 173–186.
- Walker, G. P. L. (1960): Zeolite Zones and Dike Distribution in Relation to the Structure of the Basalts of Eastern Iceland. – in: *The Journal of Geology* 68 (5), pp. 515–528. – DOI: [10.1086/626685](https://doi.org/10.1086/626685).
- Watson, N. M. (2012): Natural  $\text{CO}_2$  accumulations as analogues for  $\text{CO}_2$  geological storage and  $\text{CO}_2$ -induced diagenesis in the Otway Basin, Australia. – Ph.D. thesis. – Adelaide, Australia: The University of Adelaide.
- Weisenberger, T. B. & Bucher, K. (2010): Zeolites in fissures of granites and gneisses of the Central Alps. – in: *Journal of Metamorphic Geology* 28 (8), pp. 825–847. – DOI: [10.1111/j.1525-1314.2010.00895.x](https://doi.org/10.1111/j.1525-1314.2010.00895.x).
- Weisenberger, T. B. & Bucher, K. (2011): Mass transfer and porosity evolution during low temperature water-rock interaction in gneisses of the Simano nappe: Arvigo, Val Calanca, Swiss Alps. – in: *Contributions to Mineralogy and Petrology* 162 (1), pp. 61–81.
- Weisenberger, T. B. & Selbekk, R. S. (2009): Multi-stage zeolite facies mineralization in the Hvalfjörður area, Iceland. – in: *International Journal of Earth Sciences* 98 (5), pp. 985–999. – DOI: [10.1007/s00531-007-0296-6](https://doi.org/10.1007/s00531-007-0296-6).
-

- Whitney, D. L. & Evans, B. W. (2010): Abbreviations for names of rock-forming minerals. – in: *American Mineralogist* 95 (1), pp. 185–187. – DOI: [10.2138/am.2010.3371](https://doi.org/10.2138/am.2010.3371).
- Wiewiora, A. & Weiss, Z. (1990): Crystallochemical classifications of phyllosilicates based on the unified system of projection of chemical composition: II The chlorite group. – in: *Clay Minerals* 25, pp. 83–92.
- Wilkin, R. T. & Barnes, H. L. (2000): Nucleation and growth kinetics of analcime from precursor Na-clinoptilolite. – in: *American Mineralogist* 85 (10), pp. 1329–1341. – DOI: [10.2138/am-2000-1001](https://doi.org/10.2138/am-2000-1001).
- Wilson, M. J. (2004): Weathering of the primary rock-forming minerals: Processes, products and rates. – in: *Clay Minerals* 39 (3), pp. 233–266. – DOI: [10.1180/0009855043930133](https://doi.org/10.1180/0009855043930133).
- Wintsch, R. P., Christoffersen, R. & Kronenberg, A. K. (1995): Fluid-rock reaction weakening of fault zones. – in: *Journal of Geophysical Research* 100 (B7), pp. 13, 021.
- Wirsching, U. (1981): Experiments on the hydrothermal formation of calcium zeolites. – in: *Clays and Clay Minerals* 29 (3), pp. 171–183.
- Xie, Z. & Walther, J. V. (1993): Quartz solubilities in NaCl solutions with and without wollastonite at elevated temperatures and pressures. – in: *Geochimica et Cosmochimica Acta* 57 (9), pp. 1947–1955. – DOI: [10.1016/0016-7037\(93\)90086-C](https://doi.org/10.1016/0016-7037(93)90086-C).
- Yang, P. & Armbruster, T. (1996): (010) disorder, partial Si,Al ordering, and Ca distribution in triclinic (C1) epistilbite. – in: *European Journal of Mineralogy* 8 (2), pp. 263–272. – DOI: [10.1127/ejm/8/2/0263](https://doi.org/10.1127/ejm/8/2/0263).
-

---

## DECLARATION OF AUTHORSHIP

---

### EXPERIMENTAL INTERACTION OF HYDROTHERMAL Na-CL SOLUTION WITH FRACTURE SURFACES OF GEOTHERMAL RESERVOIR SANDSTONE OF THE UPPER RHINE GRABEN

Schmidt, R. B., Bucher, K., Drüppel, K. & Stober, I. (2017b): Experimental interaction of hydrothermal Na-Cl solution with fracture surfaces of geothermal reservoir sandstone of the Upper Rhine Graben. – in: *Applied Geochemistry* 81, pp. 36–52. – DOI: [10.1016/j.apgeochem.2017.03.010](https://doi.org/10.1016/j.apgeochem.2017.03.010).

This research has been funded by the projects *StörTief* of the German Federal Ministry for Economic Affairs and Energy (BMWi, no: 0325623C), implemented by the Project Management Jülich (PtJ).

In this study I set up the conception of the laboratory experiments and defined the experimental setup and procedure. I selected the rock material, prepared the solid and fluid samples, and conducted the laboratory experiments. I chose the analytical methods for solid and fluid samples, and conducted the sample preparation for both. I performed all solid analytics and the immediate part of the fluid analyses. I evaluated all data, visualize them, and did the interpretation. I processed the fluid data and calculated the stability diagrams. Finally, I wrote the manuscript.

### EXPERIMENTS ON GRANITE ALTERATION UNDER GEOTHERMAL RESERVOIR CONDITIONS AND THE INITIATION OF FRACTURE EVOLUTION

Schmidt, R. B., Bucher, K. & Stober, I. (2018): Experiments on granite alteration under geothermal reservoir conditions and the initiation of fracture evolution. – in: *European Journal of Mineralogy* 30 (5), pp. 899–916. – DOI: [10.1127/ejm/2018/0030-2771](https://doi.org/10.1127/ejm/2018/0030-2771).

This research has been funded by the projects *StörTief* and *Geofaces-SD* of the German Federal Ministry for Economic Affairs and Energy (BMWi, no: 0325623C, 0324025C), implemented by the Project Management Jülich (PtJ).

In this study I set up the conception of the laboratory experiments and defined the experimental setup and procedure. I selected the rock material, prepared the solid and fluid samples, and conducted the laboratory experiments. I chose the analytical methods, for solid and fluid samples, and conducted the sample preparation for both. I performed all solid analytics and the immediate part of the fluid analyses. I evaluated all data, visualize them, and did the interpretation. I processed the data and carried out all calculations. Finally, I wrote the manuscript.

---

## EXPERIMENTS ON SANDSTONE ALTERATION UNDER GEOTHERMAL RESERVOIR CONDITIONS AND THE FORMATION OF ZEOLITES

Schmidt, R. B., Göttlicher, J. & Stober, I. (submitted): Experiments on sandstone alteration under geothermal reservoir conditions and the formation of zeolites. – in: *European Journal of Mineralogy* 31.

This research has been funded by the projects *StörTief* and *Geofaces-SD* of the German Federal Ministry for Economic Affairs and Energy (BMWf, no: 0325623C, 0324025C), implemented by the Project Management Jülich (PtJ).

In this study I developed the conception of the laboratory experiments, and defined the experimental setup and procedure. I selected the rock material, prepared the solid and fluid samples, and conducted the laboratory experiments. I chose the analytical methods, for solid and fluid samples, and conducted the sample preparation for both. I performed all solid analytics and the immediate part of the fluid analyses. I evaluated all data, visualize them, and did the interpretation. I processed the data and carried out all calculations. I interpreted the results, and classified them into the context. Finally, I wrote the manuscript.

---

## PUBLICATIONS

---

### PUBLICATIONS IN PEER-REVIEWED JOURNALS

- Schmidt, R. B., Bucher, K., Drüppel, K. & Stober, I. (2017a): Experimental interaction of hydrothermal Na-Cl solution with fracture surfaces of geothermal reservoir sandstone of the Upper Rhine Graben. – in: *Applied Geochemistry* 81, pp. 36–52. – DOI: [10.1016/j.apgeochem.2017.03.010](https://doi.org/10.1016/j.apgeochem.2017.03.010).
- Schmidt, R. B., Bucher, K., Mundhenk, N. & Stober, I. (2017b): Reactivity of Geothermal Reservoir Rocks under Temperature Conditions Found in the Upper Rhine Graben (Germany). – in: *Procedia Earth and Planetary Science* 17, pp. 881–884. – DOI: [10.1016/j.proeps.2017.01.006](https://doi.org/10.1016/j.proeps.2017.01.006).
- Schmidt, R. B., Bucher, K. & Stober, I. (2018a): Experiments on granite alteration under geothermal reservoir conditions and the initiation of fracture evolution. – in: *European Journal of Mineralogy* 30 (5), pp. 899–916. – DOI: [10.1127/ejm/2018/0030-2771](https://doi.org/10.1127/ejm/2018/0030-2771).
- Schmidt, R. B., Göttlicher, J. & Stober, I. (submitted): Experiments on sandstone alteration under geothermal reservoir conditions and the formation of zeolites. – in: *European Journal of Mineralogy* 31.
- Schmidt, R. B., Seithel, R., Bucher, K. & Stober, I. (2015c): Fluid-rock interaction in deep fault systems and the influence on permeability in typical rocks of the Upper Rhine Graben, Southwest Germany. – in: *Proceedings World Geothermal Congress, Melbourne, Australia*.

### PRESENTATIONS WITH ABSTRACTS

- Barth, F., Görner, T., Schmidt, R. B., Drüppel, K., Grimmer, J. C. & Stober, I. (2017): Experimental investigation of the hydrothermal alteration of granite and monzonite from the Black Forest, Germany. – Poster presentation. – 5th European Geothermal Workshop Karlsruhe, 12–13 October 2017.
- Schmidt, R. B., Bucher, K., Mundhenk, N. & Stober, I. (2016a): Reactivity of geothermal reservoir rocks under temperature conditions found in the Upper Rhine Graben (Germany). – Oral presentation. – 15th Water-Rock Interaction International Symposium, WRI-15, Évora, Portugal.
- Schmidt, R. B., Bucher, K. & Stober, I. (2014a): Geochemical reactions of fresh granite with in-situ fluids under geothermal reservoir conditions in the crystalline basement of the Upper Rhine Graben. – Poster presentation. – 3rd European Geothermal Workshop Karlsruhe, 15–16 October 2014.
-

- Schmidt, R. B., Bucher, K. & Stober, I. (2016b): Alteration of primary minerals from geothermal reservoirs in the Upper Rhine graben. – Poster presentation. – GeoTherm 2016, Offenburg.
- Schmidt, R. B., Bucher, K. & Stober, I. (2016c): Alteration products of reservoir rocks from the Upper Rhine Graben under geothermal conditions. – Poster presentation. – European Geothermal Congress 19-24 September 2016, Strasbourg, France.
- Schmidt, R. B., Bucher, K. & Stober, I. (2016d): Alteration products of reservoir rocks from the Upper Rhine Graben under geothermal conditions. – Poster presentation. – Workshop Geothermische Fluide in salinaren Systemen, Karlsruhe.
- Schmidt, R. B., Bucher, K. & Stober, I. (2016e): Alteration products of reservoir rocks of the Upper Rhine Graben under geothermal conditions. – Poster presentation. – 25. Meeting of the German Association for Hydrogeology, KIT, 13-27 April 2016.
- Schmidt, R. B., Bucher, K. & Stober, I. (2017c): Alteration products of reservoir rocks from the Upper Rhine Graben under geothermal conditions. – Poster presentation. – GeoTHERM Offenburg.
- Schmidt, R. B., Göttlicher, J. & Stober, I. (2018b): Formation of zeolites in sandstone-brine interaction experiments under geothermal conditions. – Oral presentation. – Goldschmidt Boston.
- Schmidt, R. B., Göttlicher, J. & Stober, I. (2018c): Sandstone-brine interaction and the formation of zeolites in experiments under geothermal conditions. – Oral presentation. – GeoBonn.
- Schmidt, R. B., Mundhenk, N., Bucher, K. & Stober, I. (2015a): Alteration of primary minerals from geothermal reservoirs in the Upper Rhine Graben. – Poster presentation. – 4th European Geothermal Workshop Strasbourg, 19–20 October 2015.
- Schmidt, R. B., Seithel, R., Bucher, K. & Stober, I. (2015b): Fluid-rock interaction in deep fault systems and the influence on permeability in typical rocks of the Upper Rhine Graben, Southwest Germany. – Poster presentation. – World Geothermal Congress, Melbourne, Australia.
- Schmidt, R. B., Seithel, R. & Stober, I. (2014b): From Laboratory Experiments to Modelling Fault Structures – Geomechanical Characterization and Water Rock Interactions of Geothermal Reservoirs in the Upper Rhine Graben (URG). – Poster presentation. – European Geothermal PhD Days 2014, Darmstadt.
- Schmidt, R. B. & Stober, I. (2017): Experiments on sandstone-brine interaction with various solutions under geothermal conditions. – Poster presentation. – Goldschmidt Paris.
- Schmidt, R. B. & Stober, I. (2018): Sandstone-brine interaction with various solutions under Upper Rhine Graben conditions. – Poster presentation. – GeoTHERM Offenburg.
-

---

Schmidt, R. B., von der Handt, A., Grimm, C., Laukert, G. & Mojica, J. (2012): Petrology of the Alto Condoto ultramafic-mafic complex, Colombia. – Poster presentation. – European Mineralogical Conference 2012, Frankfurt am Main.

---

---

## ACKNOWLEDGMENTS

---

I like to say thank you to many people who have accompanied me throughout the time of my PhD and supported me writing this thesis.

First, I have to thank my supervisor Prof. Dr. Ingrid Stober. She supported me over the whole period of PhD and showed me the way to a real scientist. Thank you also for applying and organizing the research projects I worked on.

Thank you to Prof. Dr. Thomas Kohl for giving me the opportunity to work in the field of my interest and allowing so much geochemistry and mineralogy in his working group.

Thank you to PD Dr. Kirsten Drüppel for taking the responsibility of being co-supervisor and for helpful comments and discussions on my research.

Many thanks to Prof. Dr. Kurt Bucher for surrender his autoclave system to my salty swill at the University of Freiburg. Thank you also for the helpful comments and the fruitful discussions during my PhD.

Many thanks to Elisabeth Eiche, Claudia Mößner, Gesine Preuß, and Kristian Nikoloski for their uncomplicated support in laboratory issues and the measurement of my salty solution. Also thank you Hiltrud Müller-Sigmund and Sigrid Hirth-Walther for their help in the laboratory at the University of Freiburg.

I would like to thank Jörg Göttlicher for enabling the zeolites measurements at the SUL-X beamline (ANKA), and for his help handling the tiny crystals and interpreting the results.

I would also like to thank Volker Zibat from the Laboratory for Electron Microscopy (KIT) for the SEM analyses and Uta Gerhards for her help with the electron microprobe at the Institute for Micro Process Engineering (KIT).

Special thanks to Silke for assisting me through the bureaucratic jungle of KIT and all the chats around the floor.

My research has been enabled by the projects *StörTief* and *GeoFaces-SD* supported by the German Federal Ministry for Economic Affairs and Energy (BMWi, no: 0325623C, 0324025C) and implemented by the Project Management Jülich (PtJ). The autoclave laboratory at the University of Freiburg has been funded by *Baden-Württemberg Programme* (PTKA-BWP) grants L75 12002 and L75 14003.

Thank you Fabian, Sebastian, and Niklas for lots of discussions on geochemistry and everything else in the laboratory, coffee breaks, and ATMs.

Thank you Robin for the good office sharing in the first period of PhD and for the geological, scientific, and recreational trips in the near and far.

Thank you Sarah for being there all the time and for encouraging me in hard times.

Finally, I like to thank my parents for their unconditional support all along my way.

---